Thesis: Investigating the Low-Frequency Stability of BiSON's Resonant Scattering Spectrometers

G. R. Davies

A Thesis submitted for the degree of Doctor of Philosophy

School of Physics and Astronomy

University of Birmingham

February 2011

Abstract

The main focus of this thesis is the study of low-degree low-frequency solar p modes from the analysis of high-resolution power spectra generated from 20 years of high-quality data collected by the Birmingham Solar Oscillations Network (BiSON) Resonant Scattering Spectrometers (RSS). To that end we present a novel model of the RSS and its observations that allows for the determination of a significant improvement in calibration for ground-based Sun-as-a-star Doppler velocity observations.

We show that the previously neglected multiple scattering in the RSS vapour cell is significant and demonstrate its impact on the spatial weighting to the solar disk, combining the new instrumental weighting with a detailed treatment of terrestrial atmospheric effects and a model of the solar surface velocity field. The resulting simulation allows for the development of a new and successful correction for differential atmospheric extinction generating up to a 25% increase in the signal-to-noise ratio at low frequencies (0.8 to 1.3 mHz).

The improvement in signal to noise allows for the detection of low-frequency p modes with small associated errors in frequency and together with the fitting of mode structure, produces estimates of mode linewidth ($\Delta\nu$) and power. Over the frequency range $972 \geqslant \nu \geqslant 1850$ μHz we find the frequency-linewidth dependence to be $\Delta\nu \propto \nu^{7.5\pm0.4}$.

Acknowledgements

Firstly I must express my eternal gratitude to both my parents and my long suffering partner Liz. None of this would have been possible without the support they have given and the sacrifices they have made.

I would like to thank my two supervisors Yvonne Elsworth and Bill Chaplin for all their support and guidance. In addition I must give special thanks to Brek Miller for his hefty contribution to my work. All three have contributed to the rich environment I have enjoyed during my time at Birmingham.

I am grateful to all who I have shared time with in Birmingham. A far from exhaustive list begins with Ann-Marie Broomhall (who would be first in this list even if it were not in alphabetical order) followed by Barry Jackson, Christopher Karoff, Elizabeth Jarvis, Fred Baudin, Graham Verner, Ian Barnes, John Allison, Kym Goss, Neil Tarrant, Othman Benomar, Saskia Hekker, Steve Hale, and Steve Spreckley.

Contents

1 Helioseismology **1**
- 1.1 Introduction . . . 1
- 1.2 Solar Oscillations . . . 2
  - 1.2.1 Spherical harmonics . . . 3
  - 1.2.2 A dispersion relation . . . 3
  - 1.2.3 Pressure modes . . . 4
  - 1.2.4 Gravity modes . . . 8
- 1.3 Observations . . . 9
- 1.4 Time series analysis . . . 11
  - 1.4.1 Fourier analysis . . . 11
  - 1.4.2 The window function . . . 13
- 1.5 Solar structure and dynamics . . . 13
  - 1.5.1 What have the 'helioseismologists' ever done for us? . . . 14
- 1.6 Low-frequency modes . . . 18
- 1.7 Thesis structure . . . 19

2 The BiSON Network **21**
- 2.1 BiSON history . . . 21
- 2.2 Resonant scattering spectrometers . . . 22
- 2.3 Calibrating data . . . 25
  - 2.3.1 Velocity components . . . 26
  - 2.3.2 The R-V calibration . . . 28
  - 2.3.3 Low-frequency losses . . . 29
- 2.4 Combining data . . . 32
- 2.5 Selection of mode candidates . . . 33
- 2.6 Current Bison limits of detection . . . 36

3 Modelling Data **37**
- 3.1 Introduction . . . 37
- 3.2 The solar line function . . . 39
  - 3.2.1 Solar Fraunhöfer line . . . 39
  - 3.2.2 Doppler shifts . . . 41
  - 3.2.3 Differential Solar rotation . . . 42
  - 3.2.4 Limb darkening . . . 47
  - 3.2.5 Results . . . 48
- 3.3 Atmospheric extinction . . . 50

3.3.1 Atmospheric model . . . 51
3.3.2 Airmass . . . 51
3.3.3 Zenith Angle . . . 52
3.3.4 Parallactic angle . . . 54
3.3.5 Extinction across the solar disk . . . 55
3.3.6 Results . . . 56
3.4 Instrumental weighting . . . 60

4 Resonant Scattering Vapour Cells 61
4.1 Geometric Description of the optical systems . . . 61
4.1.1 Primary optical setup . . . 62
4.1.2 Detector optical setup . . . 65
4.2 Resonant Scattering . . . 69
4.2.1 Resonance radiation . . . 69
4.2.2 Energy levels and line profiles . . . 70
4.2.3 With a magnetic field . . . 71
4.3 Instrumental Optical Depth . . . 73
4.3.1 Monochromatic optical depth . . . 74
4.3.2 Number Density . . . 75
4.3.3 Scattering Cross Section . . . 76
4.3.4 A new definition: IOD . . . 76
4.4 The path of a photon through the cell . . . 77
4.4.1 Definition of axis . . . 78
4.4.2 Properties of Zeeman Resonant Scattering . . . 78
4.4.3 Angular Dependence . . . 84

5 Modelling multiple scattering 86
5.1 Introduction . . . 86
5.1.1 Optical depth of unity . . . 87
5.1.2 The Hoyng Approach . . . 88
5.1.3 The Broomhall approach . . . 89
5.2 A Monte Carlo approach . . . 91
5.2.1 Initialisation . . . 92
5.2.2 Source parameters . . . 93
5.2.3 Propagation . . . 95
5.2.4 Detection . . . 97
5.3 Results . . . 99
5.3.1 The importance of multiple scattering . . . 102
5.3.2 The character of the instrument . . . 104

6 Results From Sun and Instrument Simulations 110
6.1 Introduction . . . 110
6.2 Reproducibility of the model . . . 112
6.3 Instrument response to pseudo velocity input . . . 113
6.3.1 Alignment of rotation axis of the Sun . . . 114
6.3.2 Dark counts and atmospheric extinction . . . 115
6.3.3 Size of solar image in cell . . . 118

6.3.4 Potassium vapour temperature . . . 119
6.4 Daily data . . . 121
6.4.1 Intensity . . . 121
6.4.2 Ratio . . . 123
6.4.3 Differential extinction . . . 125
6.5 Modelled long term stability . . . 127

7 Correcting for atmospheric effects 132
7.1 Extinction coupled with dark counts . . . 132
7.1.1 Measuring dark counts . . . 133
7.1.2 Measuring atmospheric extinction coefficients . . . 135
7.2 A correction for differential extinction. . . . 141
7.2.1 Differential extinction model . . . 143
7.3 Correcting modelled data . . . 145
7.4 Correcting real data . . . 149
7.4.1 Trimming . . . 155
7.4.2 Time series . . . 157

8 BiSON inference on long timescales 159
8.1 Introduction . . . 159
8.2 Integrated solar line . . . 160
8.3 Inverse sensitivity . . . 163
8.3.1 Analytical treatment of inverse sensitivity . . . 165
8.4 The δV parameter . . . 169
8.4.1 Las Campanas 2009 δV . . . 169
8.4.2 Determining the unknown signal . . . 172
8.5 Long term solar signals . . . 177
8.6 Data Reduction . . . 179
8.7 Modelling the solar rotation signal . . . 182
8.8 Data Analysis . . . 185
8.8.1 Variation signal through solar cycle . . . 185
8.9 Implications on BiSON RSS stability . . . 187

9 Final time series analysis 189
9.1 Introduction . . . 189
9.2 Data preparation . . . 190
9.2.1 Weighted FFT . . . 192
9.2.2 Bin shifting . . . 193
9.3 Searching the power spectrum . . . 194
9.3.1 Significance testing . . . 195
9.4 Preliminary results . . . 197
9.5 Going beyond statistical significance . . . 200
9.5.1 Fitting individual modes . . . 200
9.6 Detections . . . 211
9.7 Future Prospects . . . 213

10 Conclusion 215

Appendices **218**

11 Appendix **219**
11.1 Modelling the solar velocity field 219
11.1.1 Stochastic oscillations 219
11.1.2 Granulation 220
11.2 The transformation method 221
11.2.1 Uniform deviates in spherical polar coordinates over a limited solid angle 221
11.2.2 Exponential random deviates 221
11.2.3 Random deviates for the σ transition angular dependence 222
11.2.4 Random deviates for the π transition angular dependence 223
11.3 Ray tracing through the detection optics 223
11.4 Orthogonal transformation matrix 229

List of Figures

1.1 Radial velocity spherical harmonics. Left to right: l=1, m=1; l=3, m=1; l=3, m=3; l=9, m=3; l=9, m=7; l=25, m=12. 3

1.2 Propagation diagram for a standard solar model. The solid and dashed curves represent $k_r^2 = 0$ for real frequencies plotted as a function of radius for $l = 1$. The hatched areas indicate p and g-mode areas of oscillatory propagation buffered by the evanescent region. The horizontal lines represent three types of mode: a p mode of frequency $\omega = 600$ μHz; a mixed mode of frequency $\omega = 280$ μHz; and a g mode of frequency $\omega = 150$ μHz. Image from Appourchaux et al. [2010]. 5

1.3 Results from a sound speed inversion showing the difference, in sound speed squared, between the Sun and a standard solar model. Taken from Christensen-Dalsgaard [2002]. 15

2.1 The Las Campanas dome in Chile. 22

2.2 Schematic of a typical BiSON spectrometer. Image: Brek Miller 23

2.3 Pictures of a typical BiSON spectrometer. Left: instrument with cover removed. Right: the vapour cell housing together with detection optics. Images: Brek Miller 24

2.4 Intensities diagram showing the solar absorption line together with the blue and red wing absorption lines. Left: No source-observer line-of-sight velocity. Right: Source-observer line-of-sight velocity of 550 m s^{-1}. 25

2.5 Simulation of a single stochastic solar oscillation with frequency $\nu_0 = 1$ mHz and damping time of 30 days. The cadence of the measurement is 40 s and time between successive excitation kicks is $\approx$ 8hours. 30

2.6 Power spectrum of a single simulated solar stochastic oscillation at 1 mHz with simulated granulation and super-granulation. 31

2.7 Simulated solar signal removed by the BiSON third-order polynomial velocity calibration process for different lengths of data set. Red: 1000 pts; green: 800 pts; blue: 600 pts; cyan: 400 pts; and pink: 200 pts. 31

3.1 Cartesian coordinates of the solar disk. 39

3.2 Solar differential synodic rotation map. 44

3.3 Plot showing position angle, P_a (solid line), and tilt angle, B_0 (dot-dash line), for days after 01/01/2008. 45

3.4 Solar differential synodic rotation map with position angle of 26.25 $^\circ$ and zero tilt angle. 46

3.5 Varying intensity due to limb darkening on the solar disk at $\lambda = 770$ nm. . 47

3.6 Weightings of the solar line function in position on the solar disk and wavelength. Left: blue wing positional weighting. Centre: red wing positional weighting. Right: wavelength-intensity full disk line profile with reference Gaussian absorption line (dot-dash)of depth, $d = 0.84$, and FWHM $\Gamma = 18$ pm. Top line: with solar Fraunhöfer line only. 2^{nd} line: addition of line-of-sight velocity. 3^{rd} line: including solar differential rotation. 4^{th} line: including position angle, $P_a = 26.25°$. Bottom line: with solar limb darkening. 49
3.7 Variation of solar zenith angle with time at the BiSON Las Campanas station. The plot shows the variation with respect to local time through the day, and the variation between summer and winter solstice. Each day between summer and winter solstice is traced to give the annual variation. 53
3.8 Variation of extinction with time. The plot shows the variation with respect to local time through the day, and the variation between summer and winter solstice. Atmospheric extinction coefficient set to $\kappa_{\text{atm}} = 0.1$. Each day between summer and winter solstice is traced to give the annual variation. 53
3.9 Diagram showing definition of parallactic angle on the solar disk. 54
3.10 Variation of parallactic angle through the day and year. Each day between summer and winter solstice is traced to give the annual variation. 55
3.11 Diagrams of atmosphere showing differential extinction for the BiSON Las Campanas station on 14/01/2009. Contour lines mark changes in intensity of 0.01%, except for the central plot which has the resolution increased to changes in intensity of 0.001%. Each map shows the solar disk at different times during the day. The local time from left to right then top to bottom: 06:00; 07:00; 08:00; 10:00; 12:00; 14:00; 16:00; 17:00; and 18:00. 57
3.12 Full disk line profiles for various times through the day at the BiSON Las Campanas station on 14/01/2009. Black lines show the whole disk solar line with a referenced dashed green line not subjected to extinction. Red and blue lines show the difference between the lines with and without extinction on either side of the line. The local time from left to right then top to bottom: 06:00; 07:00; 08:00; 10:00; 12:00; 14:00; 16:00; 17:00; and 18:00. 58
3.13 Asymmetry in full disk line for various times through the day at BiSON Las Campanas but with position angle suppressed. Variation in time (hours): 06:00 (red); 07:00; 08:00; 10:00; 12:00 (green); 14:00; 16:00; 17:00; 18:00 (blue). 59
3.14 Asymmetry in full disk line for various times through the day at BiSON Las Campanas. Variation in time (hours): 06:00 (red); 07:00; 08:00; 10:00; 12:00 (green); 14:00; 16:00; 17:00; 18:00 (blue). 60

4.1 Diagram of the primary optics for a 3^{rd} generation BiSON spectrometer. . 62
4.2 Plan view diagram of the detection optics for a 3^{rd} generation BiSON spectrometer. 65

4.3 Composite images of non-resonantly scattered light for the BiSON Sutherland instrument taken in 2008 with an infra-red sensitive CCD. The front entrance of the cell is located at the top of the image (see figure 4.4 for the geometry of the observation). The majority of non-resonantly scatter light comes from the front of the cell. The scale in the focal plane, that is the zy plane at the center of the cell, is shown for reference. 67
4.4 Diagram (plane view) illustrating the geometry of observation for figures 4.3 and 4.5. 67
4.5 Scale maps of the detection optics weighting for a cross section of the vapour cell in the xz-plane (see figure 4.4 for the geometry of the observation). The region shown represents the full dimensions of the cell, 15 mm^2. Lens is $L2$ placed at 58 mm from the cell centre on the right hand side of the diagram. The detector has an aperture mask with radius of 3.5 mm and 2.5 mm for the left and the right plots respectively. 68
4.6 Diagram of the energy levels for potassium D1 $^2S_{\frac{1}{2}}$to $^2P_{\frac{1}{2}}$resonant scattering 70
4.7 Diagram of line width with hyperfine components. The black line shows the sum of the four components. The blue line shows a Gaussian profile with FWHM of 700 ms^{-1} 71
4.8 Diagram of the energy levels for potassium RSS resonant scattering with magnetic field. 72
4.9 Chosen definition of spherical polar coordinates with a point described by the distance from the origin, θ the angle formed with respect to the z-axis, and ϕ formed with respect to the x-axis. 78
4.10 Images of the Stokes terms in $\phi - \theta$ space. Left to right: ϕ_I; ϕ_Q; ϕ_U; ϕ_V. . 84
4.11 Resonant scattering angular profiles in a magnetic field. The red line represents the σ components and the blue line the π. The black line is the sum of both components showing isotropy. 85

5.1 Diagram of Hoyng active region 88
5.2 Plots of gain against instrumental optical depth for different detection optics configurations. Black crosses are results from the Monte Carlo simulation while the red lines show the Hoyng model results normalised in intensity to match the Monte Carlo results. All plots have DL2 at 73 mm from the center of the cell. The radius of the aperture at the detector varies with: top left - 7.495 mm; top right - 3.5 mm; bottom left - 2.5 mm; and bottom right - 0.2 mm. 100
5.3 Plot of gain against instrumental optical depth for DL2 at 73 mm and detector aperture radius of 3.5 mm. The insert shows the region of optimal gain. Black crosses are results from the Monte Carlo simulation while the red lines show the Hoyng model results normalised in intensity to match the Monte Carlo results. 101
5.4 Number of scatters of detected photons for various instrumental optical depths. Detection optics setup with DL2 at 73 mm and detector aperture radius of 3.5 mm. Optical depths highlighted are: 1.0 in red; 2.0 in green; and 3.0 in blue. 103

5.5 Cumulative frequency of the number of scatters of detected photons for various instrumental optical depths. Optical depths highlighted are: 1.0 in red; 2.0 in green; and 3.0 in blue. Detection optics setup with DL2 at 73 mm and detector aperture radius of 3.5 mm. 104
5.6 Simulated temperature curves for detection optical setups with DL2 at 73 mm and detector apertures of radius 3.5 and 2.5 mm for left and right respectively. Black crosses show the Monte Carlo results and the red line displays the Hoyng model. 105
5.7 Narrabri temperature curve data from S. Hale's visit to site in February 2010. Left: intensity and oven temperature as a function of time. Right: intensity as a function of oven temperature with time indicated by the colour bar. 106
5.8 Instrumental profiles in wavelength for a simulated BiSON RSS at various IOD's and detector apertures. Optical depths highlighted are: 1.0 in red; 2.0 in green; and 3.0 in blue. Radii of detector aperture are: top left 7.495 mm; top right 3.5 mm; bottom left 2.5 mm; and bottom right 0.2 mm. 107
5.9 Predicted instrumental weightings to the solar disk for a detector positioned on the right hand side of the images. Left: simulated instrumental weighting integrated over the wavelength range of the resonant transition for an IOD of 2. Right: Broomhall instrumental weighting at optical depth of 2. 109

6.1 Modelled ratio for varying numbers of Monte Carlo events N in the simulation of the vapour cell. Port detector displayed on the right and starboard on the left. Weighted mean ratio for all values of N shown as blue dot-dash line. 113
6.2 Left panel shows the modelled change in ratio as a function of the solar position angle. Right panel shows the modelled change in ratio as a function of solar tilt angle. Standard convention is applied that dictates the port detector is displayed in red, starboard in green, and the mean of the two in black. 114
6.3 Change in modelled ratio as a function of atmospheric extinction coefficient with background counts at 2% of intensity. Port detector in red and starboard in green. 117
6.4 Change in ratio as a function of the image size at the centre of the RSS vapour cell. Port detector in red and starboard in green. 118
6.5 Change in ratio as a function of vapour temperature for two different line-of-sight velocities. Left panel with $v_{\mathrm{los}} = 0\,\mathrm{m\,s^{-1}}$ and right panel $v_{\mathrm{los}} = 1100\,\mathrm{m\,s^{-1}}$. Port detector in red and starboard in green. 120

6.6 Comparison of modelled intensity data and real intensity data for the Las Campanas station on 11 January 2009 and 20 August 2009. Intensities measured in the blue wing are shown in blue and the red wing in red. Left: Intensities for real data as solid lines, modelled data without atmospheric extinction as dashed lines, and modelled data with extinction coefficient $\kappa = 0.03$. Right: Difference between the the real data and data modelled with atmospheric extinction. Top to bottom: 11/01/2011 port detector; 11/01/2011 starboard detector; 20/08/2011 port detector; and 20/08/2011 starboard detector. 122
6.7 Ratios for modelled and real data for the Las Campanas station. Each panel shows real data as solid line, modelled without extinction as dashed line, and modelled data with an extinction coefficient of $\kappa = 0.03$. The modelled data with and without extinction lie over the top of each other. Left panels show port detector data and right panels starboard. Top line: 11/01/2011. Bottom: 20/08/2011. 123
6.8 The difference between real and modelled ratios for the Las Campanas station. Port detector shown in red and starboard in green. Left: 11/01/2011. Right: 20/08/2011. 124
6.9 Modelled differential extinction as a function of time through the day for different values of extinction coefficient. Line shown are for extinction coefficient starting at 0.0 and increasing in steps of 0.01. Lines highlighted in colour are: $\kappa = 0.0$ in red; $\kappa = 0.03$ in green; and $\kappa = 0.06$ in blue. . . . 126
6.10 Ratios at midday local time through the year for modelled (dashed line) and real Las Campanas (solid line) data 2009. The port detector data is displayed in red and starboard in green. 128
6.11 The difference between modelled and real ratios taken at midday local time for Las Campanas 2009. Port data is displayed in red and starboard in green. 129
6.12 Port-starboard separation in ratio through the year for modelled (dashed line) and real (solid line) Las Campanas 2009 data. 130
6.13 The port-starboard separation difference between modelled and real Las Campanas 2009 data. 130
6.14 Ratio as a function of line-of-sight velocity - an RV curve - for modelled (colour) and real (black) Las Campanas 2009 data. For aesthetic purposes only every tenth day is displayed. 131

7.1 Mean overnight dark count values (black) for Las Campanas in 2009 with the port detector left and starboard right. Over plotted in red are the mean daytime dark counts for 4 days where the dome did not open. 135
7.2 Simulated sums of $I_b + I_r$ as a function of airmass. Each line represents a different input extinction coefficient starting at $\kappa = 0.0$ and increasing in steps of 0.01, with the values 0.0,0.03,0.06 highlighted in red, green and blue respectively. 136
7.3 Instantaneous atmospheric absorption coefficient as a function of airmass. Each line represents a different extinction coefficient starting at $\kappa = 0.0$ and increasing in steps of 0.01, with the values 0.0,0.03,0.06 highlighted in red, green and blue respectively. 137

7.4 Atmospheric extinction coefficients through the year calculated from modelled RSS data with input extinction coefficient of 0.03. 138
7.5 Atmospheric extinction coefficients through the year calculated from real data of Las Campanas station year beginning 01/01/2009. 139
7.6 Inverse sensitivity reduction due to dark counts coupled with extinction through the year 2009 for Las Campanas A instrument, calculated at fixed ratio, $R = 0.2$. 140
7.7 The impact of changes in inverse sensitivity due to dark counts and atmospheric extinction in a season ratio-velocity curve. 141
7.8 Differential extinction signal generated from modelled data. Shown in the time domain (left) and the generated residual signal in the frequency domain (right). 142
7.9 Fits of the differential extinction model to the modelled RSS differential extinction signal for the Las Campanas station 14/01/2009 (left) and 11/06/2009 (right). 146
7.10 Fit of a third-order polynomial plus differential extinction correction to the modelled RSS ratio for the Las Campanas station 14/01/2009. Data and residuals in the time domain on the left and residuals in the frequency domain on the right. In the power spectrum residuals from: just the differential extinction signal (+); the fit of the correction to just the differential signal ($*$); and the fit of the third-order polynomial and correction to the modelled RSS ratio including differential extinction ($\diamond$). 147
7.11 Fit of a third-order polynomial plus differential extinction correction to the modelled RSS ratio for the Las Campanas station 10/06/2009. Data and residuals in the time domain on the left and residuals in the frequency domain on the right. In the power spectrum residuals from: just the differential extinction signal (+); the fit of the correction to just the differential signal (*); and the fit of the third-order polynomial and correction to the modelled RSS ratio including differential extinction. 147
7.12 Fit coefficients for a third-order polynomial and differential extinction correction applied to simulated data. Left: The alpha coefficient for the fit to differential extinction signal only (black) and the treatment of the full ratio including differential extinction (red). Right: The δV solution to the third-order polynomial for the fit to ratio with (red) and without (black) a differential correction. 148
7.13 Calibrated data for the Las Campanas station 14/01/2009. Top left: residuals calibrated without the differential extinction correction and shown in the time domain. Top right: residuals calibrated with the differential extinction correction , again shown in the time domain. Bottom: Comparison of the uncorrected (red) and corrected (black) data in the frequency domain.151
7.14 Fit coefficients for a third-order polynomial with differential extinction correction applied to real data. Left: δV the solution to the third-order polynomial, for the calibration with (red) and without the differential extinction correction. Right: histogram of the morning (black) and afternoon (blue) alpha coefficients from the calibration. 152

7.15 Noise parameter as a function of time from sunrise of the point of data rejection for calibration with (red) and without (black) differential extinction correction. . . . 153
7.16 Histogram of data points per day for two regimes of regions, traditional (black) and liberal (green) over the year starting 01/01/2009 for the Las Campanas station. . . . 154
7.17 Histogram of the noise populations in two different region regimes (traditional left and liberal right) calibrated with (red) and without (black) the differential extinction correction. . . . 155
7.18 Histogram of noise populations for three different region regimes: traditional in black; liberal in red; and trimmed in blue. . . . 156
7.19 Power spectra for the three calibration regimes: Top - traditional regions without differential extinction correction; middle - liberal regions with differential extinction correction; and bottom - trimmed (optimised) regions with differential extinction correction. . . . 158

8.1 Ratio as a function of line-of-sight velocity - an RV curve - for modelled (red - port, green - starboard) and real (black) Las Campanas 2009 data. For aesthetic purposes, only every tenth day is displayed. . . . 161
8.2 Intensity velocity (IV) curve for Las Campanas year starting 01/01/2009. Intensity wings are displayed split by the magnetic field strength, 2600 m s^{-1}, and with the fitted integrated solar line Gaussian. Right: port detector Left: starboard detector. . . . 162
8.3 Inverse sensitivity as a function of day of the year. Left: modelled data. Right: Las Campanas station 2009. Detectors shown port (red) and starboard (green). . . . 164
8.4 Inverse sensitivity as a function of orbital velocity. Left: modelled data. Right: Las Campanas station 2009. Detectors shown port (red) and starboard (green). . . . 165
8.5 Analytical model for inverse sensitivity. Left: predicted instrumental response. Right: Response at varying magnetic field strength with interval 400 m s^{-1}. Foreground: Magnetic field strengths of 2600, 3000, and 3400 m s^{-1} in read, green, and blue respectively. . . . 167
8.6 Las Campanas 2009 and analytically modelled inverse sensitivity as a function of velocity. Left: The mean of both detectors offset by 790 m s^{-1} with respect to the analytical model. Right: Port (red) and starboard (green) detectors offset by 680 and 900 m s^{-1} respectively. . . . 168
8.7 δV parameter for Las Campanas station 2009 as a function of day of the year. Left: The mean of both detectors. Right: the port (red) and starboard (green) detectors. . . . 170
8.8 δV for Las Campanas 2009 as a function of day of the year with the fitted model (red) and individual components (green, blue, and cyan) over plotted. Left: mean detector data. Centre: port detector. Right: starboard detector. . . . 170
8.9 ΔV signal as a function of time predicted by the δV signal divided by the calculated inverse sensitivity. . . . 173

8.10 Result of fitted ΔV signal as a function of day of the year for port (red) and starboard (green) detectors. 175
8.11 RV curves showing uncorrected (black) data and data corrected with the fitted ΔV signal. Left: port detector. Right: starboard detector. 175
8.12 Long term δV signals. Top left: Las Campanas. Top right: Izana. Bottom left: Sutherland. Bottom right: Narrabri. 178
8.13 Examples of the signal fitted and removed from the long term δV results to produce δV residuals. 180
8.14 Long term δV residuals. Top left: Las Campanas. Top right: Izana. Bottom left: Sutherland. Bottom right: Narrabri. 181
8.15 Simulated sunspot transit. 183
8.16 Modelled response in time and frequency domain's to a single persisting sunspot at varying latitudes on the solar disk. Latitudes top to bottom: equatorial; 15°; 25°; 45°. 184
8.17 Power spectrum of the long-term δV residuals. Top to bottom: Las Campanas; Izana; Narrabri; and Sutherland. 186
8.18 Variation in time of the Carrington harmonics with international sun spot over plotted. Horizontal blue lines show the frequency of the Carrington harmonics. 187

9.1 BiSON network performance described by low-frequency noise and time series duty cycle (fill) for the years: 2009 red; 2005 green; 2000 blue; 1995 cyan; 1991 pink. 191
9.2 Selected smoothed power spectra for structure near a predicted frequency of oscillation and $P \leqslant 0.1$. The number of bins over which the spectra are smooth are (in ascending frequency): 4,7,11,12,1,15,and 3. Over plotted are the $P \leqslant 0.01$ and $P \leqslant 0.1$ significance levels in blue and red respectively together with the predicted frequencies from Turck-Chièze et al. [2001]. Predicted frequencies are displayed by m value with $m = 0, 1$, and 2 displayed with squares, triangles and diamonds respectively. 198
9.3 Frequency differences between the modelled predicted mode frequencies of Turck-Chièze et al. [2001] and the observed frequency of structure detected in power spectra. 205
9.4 Mode widths as a function of frequency plotted on a ln-ln scale. Over plotted in red is the least squares fit linear model with the dashed line showing the (bin width) resolution limit. Right: Same plot but rejecting data with small line widths (cut off at dot-dash line). 208
9.5 Observed mode power as a function of frequency on a ln-ln scale. Over plotted are the least squares fit linear models for $l = 0$ green and $l = 1$ blue. 210
9.6 Predicted heights of low-frequency p modes for different lengths of observation time series. 20 year background levels displayed, prior to this thesis as a dot-dot-dash line and following the work done in this thesis as a dashed line. Each time series displayed is twice the length of the previous starting at 1 year with 8,16, and 32 years displayed in red, green, and blue respectively. 214

11.1 Diagram showing both cell and detection optics coordinate systems along with the cell and detection optics. 224

11.2 Diagram showing definition of the O' coordinate system. 227
11.3 Diagram showing vectors $\mathbf{S}$, $\mathbf{T}$, and $\hat{\mathbf{r}}$ in the O' coordinate system. b and d are the representations of $\mathbf{S}$ and $\mathbf{T}$ in this, the O', system. 227

List of Tables

3.1 Solar line properties as a function of position on the solar disk taken from de La Reza and Mueller [1975]. 40
3.2 Coefficients of a third order polynomial to describe the solar line properties as a function of position on the solar disk, r. 41
3.3 Station parameters required to calculate the solar zenith angle. 52

4.1 Stokes parameters for common states of fully polarised beams of light. . . . 80

8.1 Returned fit parameters for a Gaussian absorption line fitted to the Las Campanas 2009 IV curve. 163
8.2 Table of fitted ΔV coefficients. 174

9.1 Results from significance testing. 199
9.2 Results from fitting individually to structure observed in the power spectrum near a predicted frequency of oscillation. 203
9.3 Reported mode frequencies from this and other work. 207
9.4 Coefficients of the linear models fit to observed mode width and power in ln-ln space. 211
9.5 BiSON table of mode frequencies. 212

Chapter 1

Helioseismology

1.1 Introduction

Helioseismology is the study and measurement of Solar oscillations in order to infer the structure and dynamics of the solar interior. Knowledge of the solar interior is interesting in itself, but helioseismology provides a view of the Sun that enables us to ask questions and solve problems much deeper than "What is the solar structure and rotation?"

The Sun dominates our solar terrestrial environment and current interest in the solar activity cycle has been reinvigorated following an extended period of quiescence between solar cycles 23 and 24. In addition, the Sun provides an effective astrophysical laboratory that tested - to breaking point - the particle physics standard model in the solar neutrino problem. Finally but not exhaustively, the Sun is a star and is believed to be unremarkable in all but its proximity to Earth. Much of astrophysics as a subject relies upon theories of stellar structure and as such the Sun provides observational comparison with and constraint on solar models, solar models being only a small sub-set of all stellar models.

Despite many years of work on global helioseismology, the Sun has not yet given up its deepest secrets - detailed and accurate observation of the structure and dynamics of the core. This thesis aims to advance the observational techniques required to measure low-frequency pressure and buoyancy oscillations that hold the key to understanding the solar

core. Through a detailed model of the Sun-atmosphere-instrument interaction we aim to tailor a version of the BiSON (Birmingham Solar Oscillation Network) data calibration pipeline to the detection of scientifically interesting solar oscillations below the current frequency limit of around 1 mHz.

The community of helioseismologists may be divided into two: global and local. Global helioseismology, the subdivision that this thesis is concerned with, considers oscillations that are standing waves setup through the entire Sun. Local helioseismology, as the name suggests, observes waves confined in small volumes just beneath - or local - to the solar surface. This introductory chapter will set out the preliminaries of solar oscillations, observation and analysis.

1.2 Solar Oscillations

Solar oscillations were discovered in 1960 by Leighton [1960]. Using a spectroheliographic technique, Leighton detected a periodic velocity field on the solar surface. These oscillations, with periods of around five minutes, were thought to be local phenomena. Ulrich [1970] and Leibacher and Stein [1971] perhaps did not realise the full extent of the oscillations but produced a description of standing waves trapped in an acoustic cavity created by the solar interior. The truly global nature of the modes was revealed when Claverie et al. [1979] detected low-degree modes at discrete frequencies in full-disk solar observations. Furthermore, a milestone in the observation of the modes of oscillation was passed when Grec et al. [1983] obtained continuous observation over 5 days from the south pole which more clearly revealed the stochastic nature of the mode excitation. By contrast, in 2010 we are spoilt with high quality data sets of many years from a number of observing programs e.g. BiSON Broomhall et al. [2009a], Chaplin et al. [1996b], Global Oscillations at Low-Frequency (GOLF), García et al. [2010], Gabriel et al. [1995].

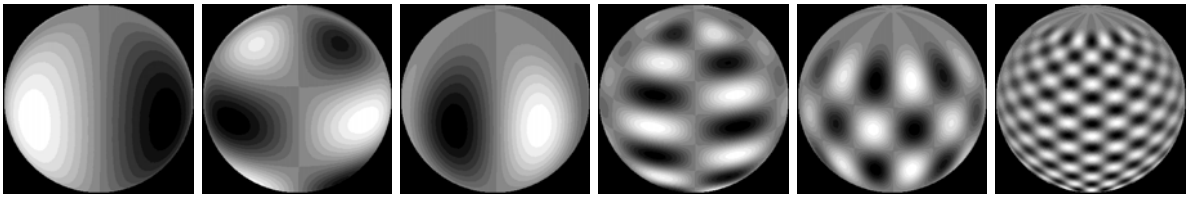

Figure 1.1: Radial velocity spherical harmonics. Left to right: l=1, m=1; l=3, m=1; l=3, m=3; l=9, m=3; l=9, m=7; l=25, m=12.

1.2.1 Spherical harmonics

As a preliminary to the discussion of solar oscillations, here we mention the natural modes of oscillation of a sphere. The angular structure of these modes can be expressed in terms of spherical harmonics $Y_l^m(\theta, \phi)$, where θ and ϕ are the co-latitude and longitude. The surface manifestation of each harmonic can be described by the degree l and the azimuthal order m. The degree l measures the horizontal wave number k_h on the surface and the azimuthal order gives the number of nodes along the equator. Figure 1.1 shows a selection of spherical harmonics as if measured in radial velocity and superimposed onto a sphere with polar axis pointing upwards just out of the plane of the page.

The description of oscillations as spherical harmonics is completed with the addition of internal structure. The order n, gives the number of nodes from the surface to the inner most turning point for a particular mode of oscillation. With this, any frequency of oscillation can be described in terms of degree, azimuthal order, and order or ν_{nlm}.

1.2.2 A dispersion relation

The Sun is a ball of gas in hydrostatic equilibrium and perturbations to the equilibrium will generate a restoring force. In broadly the same way that a piano string oscillates when struck by a hammer, the Sun oscillates when perturbed. By assuming linear adiabatic oscillations in a non-rotating Sun - and ignoring the perturbation of the gravitational potential, or in other words invoking the Cowling approximation - we can derive a dispersion relation [Stix, 2002].

The dispersion relation for an oscillation in an isothermal atmosphere with angular fre-

quency ω, wave speed c, acoustic cut-off angular frequency ω_{ac}, and radial wave number k_r is given by

$$k_r^2 = \frac{\omega^2 - \omega_{ac}^2}{c^2} + S_l^2 \frac{N^2 - \omega^2}{c^2 \omega^2}, \tag{1.1}$$

where S_l describes the horizontal component of a wave such that

$$S_l^2 = \frac{l(l+1)}{R_\odot^2} c^2 = k_h^2 c^2, \tag{1.2}$$

where l is the degree of the spherical harmonic that describes the surface manifestation of the wave, $R_\odot$ is the solar radius, and k_h is the horizontal wave number (related directly to l). Finally, N is the Brunt-Viäsälä frequency defined as

$$N^2 = \frac{g}{\rho} \left(\frac{\mathrm{d}p}{\mathrm{d}r} - \frac{\mathrm{d}\rho}{\mathrm{d}r} \right), \tag{1.3}$$

where p and ρ are the local density and pressure respectively and g is the gravitational acceleration.

This form of the dispersion relation can reveal three regimes of waves that propagate in the solar interior - oscillatory pressure waves, oscillatory gravity waves, and evanescent waves. Each regime is determined by the frequency of oscillation relative to either the acoustic cut-off frequency or Brunt-Väisälä frequency and will either be oscillatory with $k_r^2 > 0$ or evanescent with $k_r^2 < 0$. Figure 1.2 shows the so-called propagation diagram for a standard solar model. Horizontal lines represent modes of oscillation with regions of oscillatory propagation as solid lines and evanescent regions as dotted lines. Let us consider the regimes individually.

1.2.3 Pressure modes

Pressure modes or p modes are oscillatory waves with the gradient of pressure providing the required restoring force, just like for ordinary acoustic waves. Equation 1.1 can reveal the p mode regime if we consider frequencies of oscillation. First we expand equation 1.1

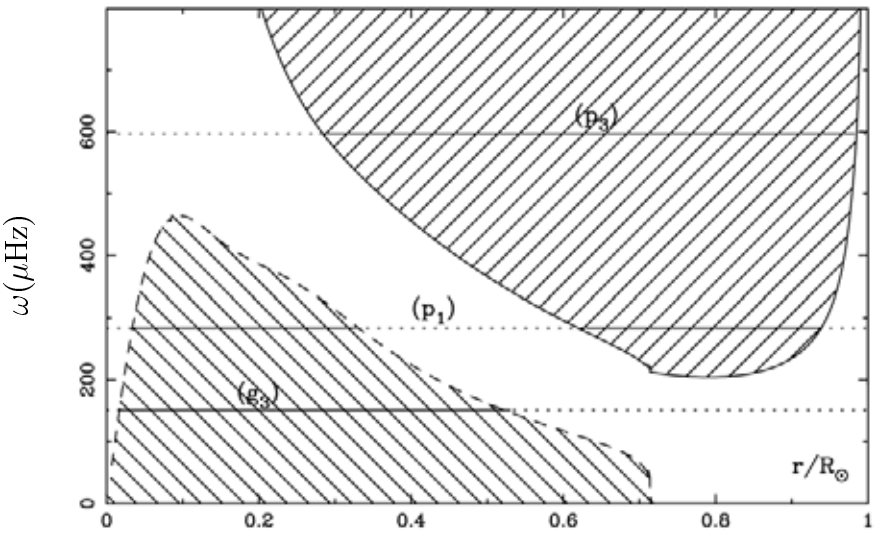

Figure 1.2: Propagation diagram for a standard solar model. The solid and dashed curves represent $k_r^2 = 0$ for real frequencies plotted as a function of radius for $l = 1$. The hatched areas indicate p and g-mode areas of oscillatory propagation buffered by the evanescent region. The horizontal lines represent three types of mode: a p mode of frequency $\omega = 600$ μHz; a mixed mode of frequency $\omega = 280$ μHz; and a g mode of frequency $\omega = 150$ μHz. Image from Appourchaux et al. [2010].

to give

$$k_r^2 = \frac{\omega^2 - \omega_{ac}^2}{c^2} + \frac{N^2 S_l^2}{\omega^2 c^2} - \frac{S_l^2}{c^2}. \tag{1.4}$$

We consider the regime where ω is large, or specifically that $\omega^2 \gg N^2$ and that ω^2 is large enough that we may disregard the acoustic cut-off frequency. Because $S_l^2 = k_h^2 c^2$ we can write equation 1.4 as

$$k_r^2 = \frac{\omega^2}{c^2} - k_h^2, \tag{1.5}$$

and rewrite in terms of ω^2, i.e.

$$\omega^2 = c^2 \left(k_r^2 + k_h^2\right), \tag{1.6}$$

which is the dispersion relation for acoustic waves.

So pressure waves may propagate in the solar interior, but we require additional information in order to describe these oscillations as modes. Firstly, we must define an acoustic cavity that traps pressure waves and allows for the creation of standing waves. Secondly,

if we wish to observe a p mode, the mode of oscillation must be excited by a source of acoustic energy. First we consider the acoustic cavity.

Reflection of an acoustic wave occurs at the boundary $k_r = 0$, which in equation 1.1 is determined by the acoustic cut-off frequency which varies with position in the solar interior. Near the solar surface density decreases rapidly, the density scale height (the distance over which the density decreases by a factor of e) is proportional to temperature which itself is falling off as the photosphere is approached. For a wave that has period longer than the time required to travel across a few scale heights, the whole atmosphere adjusts to smooth out the wave. Hence the energy of a wave is reflected in a process analogous to total internal reflection of a light wave or a quantum mechanical particle that does not have sufficient energy to climb a potential step. This analogy may be continued because just like a step potential, in the solar case, an evanescent wave propagates beyond the point of reflection. The reflection near the solar surface is defined as an upper turning point.

The lower turning point of a acoustic wave (for non-radial modes), while still a reflection at $k_r = 0$, may be described physically in terms of refraction. As an acoustic wave propagates into the solar interior, there will be a temperature gradient across its wavefront. Because sound speed is dependent on the temperature of the carrying medium T - in fact proportional to $\sqrt{T}$ - there is a sound speed gradient across the wavefront. This effect causes ray paths to be refracted away from the radial direction towards the horizontal direction, until all energy is contained in k_h. Hence, ray paths of acoustic waves resemble refractions with the lower turning point defined in terms of our original statement, $k_r = 0$. The consequence of the reflecting boundaries, the upper and lower turning points, is that we have defined an acoustic cavity. When waves are confined in a region with depth r, the possible number of vertical wave numbers becomes discrete:

$$k_r \approx \frac{n\pi}{r}, \tag{1.7}$$

for large k_r, where n is an integer. This gives a spectrum of oscillation frequencies that is discrete with equidistant frequency spacing. This is analogous to a musical instrument and it is common to find these p modes described as the 'music of the Sun'.

The excitation of trapped p modes is produced by acoustic energy generated across a broad band of frequencies, the source of which is convective turbulence. Parcels of gas moving up and down due to convection cause turbulent flow and release acoustic energy. This convective process is continually and randomly occurring and so p mode oscillations are described as stochastically forced or excited. But as sound travels through this convectively unstable medium, so the convection motion provides a kind of friction or damping. Hence we consider p modes to be stochastically excited and intrinsically damped by convective motion. Of course, there are additional forms of damping not mentioned here, i.e. absorption in the radiative zone.

Having introduced the spectrum of solar oscillations - discrete equally spaced peaks in the frequency domain - we can also consider the amplitudes of oscillations at the solar surface. It is clear that if an upper turning point is defined by the density scale height decreasing rapidly so that the atmosphere adjusts to smooth out an oscillation within a single period, then waves of increasing period - i.e. decreasing frequency - will be reflected at points that are lower in the solar atmosphere. This requires modes of lower frequency to propagate as evanescent waves for longer before reaching the height at which they are observed. As evanescent waves have energy that decays exponentially - returning to the analogy of a quantum particle being reflected at a potential barrier and the evanescent wave being analogous to quantum tunnelling - modes of lower frequency will be observed at the surface with reduced amplitude.

Waves at higher frequency suffer decreased observed mode height as the reflection mechanism of the solar surface loses efficiency at greater heights. In addition, the resonance of the p mode oscillations with the large-scale convective flow peaks around $3 - 4$ mHz, producing the maximum mode amplitude, with drop offs to either side. Hence the standing waves observed are not as well reinforced at higher frequencies.

These two reflection mechanisms at increasing depth and increasing height in the atmosphere and the resonance with granulation give the observed solar oscillations a mode height envelope with a maximum at around 3 mHz, dropping off to either side.

1.2.4 Gravity modes

Gravity modes or g modes, specifically internal g modes, propagate at low frequencies. Returning to equation 1.1 on page 4 and its expanded form, equation 1.4, we consider the regime where $\omega^2 \ll N^2$. When the first term on the right hand side of equation 1.4 is small, we can rewrite the equation as

$$k_r^2 = \frac{S_l^2 N^2}{c^2 \omega^2} - \frac{S_l^2}{c^2}, \tag{1.8}$$

which can be expressed as

$$k_r^2 = \frac{S_l^2}{c^2}\left(\frac{N^2}{\omega^2} - 1\right) = k_h^2\left(\frac{N^2}{\omega^2} - 1\right), \tag{1.9}$$

which gives the dispersion relation for internal gravity waves

$$\omega^2 = N^2 \frac{k_h^2}{k_r^2 + k_h^2}, \tag{1.10}$$

where N is the Brunt-Viäsälä frequency. These internal gravity waves, known as g modes have buoyancy as their restoring force.

The Brunt-Viäsälä frequency is the upper limit for the oscillatory propagation of internal gravity waves, as is obvious from equation 1.8. In real terms the Brunt-Viäsälä frequency describes the stratification of the medium and so is dependent on the position in the solar interior. When $N^2 > 0$ we have stable stratification. In conditions where a region is unstable to convective motion, a perturbation in terms of buoyancy will not return to equilibrium and so waves in this region cannot be oscillatory. Hence internal gravity

modes are confined to the radiative interior of the Sun and propagate as evanescent waves in the outer convective region. The consequence of this is that gravity waves provide only a small amplitude contribution to the velocity field observed at the solar surface. In fact, to date (2010) no unambiguous detection of solar g modes has been made [Appourchaux et al., 2010].

1.3 Observations

Observations of solar oscillations can be made in a number of ways. For example, observations can be made with photometry or in radial velocity. Observations may be either integrated over the whole solar disk or spatially resolved. And finally we can separate the method of producing long-term uninterrupted observation through either a network of ground-based stations or a space-based observatory. Each approach produces different characteristics in each observation and as such each combination of results is complementary to one and other.

Observations integrated over the whole solar disk, or spatially unresolved, often referred to as Sun-as-a-star measurements, are sensitive to low-degree modes. As signals are averaged over the whole disk, oscillations with smaller horizontal wavelength (larger l) cancel with regions of opposite phase. Consequently, Sun-as-a-star observations are sensitive only to low-degree modes or $l \leq 4$ [1].

Spatially resolved observations, in contrast, are sensitive from low-l up to as much as $l \approx 4500$. These observations record the intensity or velocity with respect to time of small patches on the solar disk. In order to extract information about particular modes, a spatial filter is applied to time series of resolved observations, normally at the post-processing stage. Modes of oscillation can be identified by decomposing resolved images into the coefficients of spherical harmonics, which create time series.

[1] All though Sun-as-a-star observations are typically limited to $l \leq 4$, for BiSON instruments $l = 5$ is observable because of visibility enhancement given by Doppler imaging discussed later in this thesis.

Observations of the solar velocity field measure radial velocity by considering the Doppler shifts of solar absorption lines. Irradiance measurements rely on the variation in intensity at the solar surface caused by compression - and hence heating and so increased emission - due to solar oscillations.

Velocity and intensity observations are complementary in the sense that results returned are sensitive in different ways to granulation. Velocity observations provide better signal-to-noise for solar oscillations than intensity measurements. Velocity measurements are less sensitive to solar granulation, particularly important when detecting modes at low frequencies, which is a source of noise. But intensity observations are more straightforward to implement and in a stellar context are the only current method of observing oscillations in many ($\gg 20$) different stars at the same time [Chaplin et al., 2010, Karoff et al., 2010].

Finally it is necessary to distinguish between ground and space-based observation. In order to overcome the day-night cycle, any ground based observation must make use of a network of (automated) telescopes spread across a range of longitudes around the world. Despite the redundancy produced by networks of, for example, six telescopes, which may produce as many as four simultaneously observing instruments, ground based networks cannot compete with the continuously high levels of 'fill' produced by space-based observatories. Using a simple statistical argument Chaplin et al. [1996a] showed that a network of six stations may expect a duty cycle of only 80% while fill in the mid-90% range might be achieved with a ten station network. While space-based instruments are saved from the noise produced by atmospheric extinction or 'seeing', the relative expense and no possibility of repair means that both approaches have been pursued.

1.4 Time series analysis

The preceding sections have considered the form of solar oscillations and introduced methods of how to detect the oscillations. In almost all applications it is necessary to transform data from the time domain to the frequency domain. It is in the frequency domain that we are able to identify the individual modes of oscillation and the most common procedure for performing this operation is an implementation of the discrete Fourier transform (DFT), the fast Fourier transform (FFT).

1.4.1 Fourier analysis

The standard Fourier transform is an operation that defines the relationship between a continuous signal in the time domain and its representation in the frequency domain. The operation is commonly expressed in terms of a function $f(t)$ in the time domain and its transform in the frequency domain $F(\nu)$

$$F(\nu) = \int_{-\infty}^{\infty} f(t) e^{-i2\pi\nu t} \mathrm{d}t. \tag{1.11}$$

In reality, observations of solar oscillations are integrated over small periods of time and this produces a data set that is discrete rather than continuous. For a data set with N regularly spaced (as is the case throughout this thesis) points in the time series, the discrete Fourier transform (DFT) is

$$F_\nu = \frac{1}{N} \sum_{x=0}^{N-1} f(x) e^{\frac{-2\pi\nu x}{N}}. \tag{1.12}$$

In the discrete case, F_ν is an approximation of the representation of the underlying signal in the frequency domain. The information contained in such a transform is limited by the discrete bin width in the frequency domain. Or in other words, a DFT assumes that a signal repeats at the end of the measurement time, T, consequently the frequencies that

it can represent are $\frac{n}{T}$ for integer n. This means the bin width $\delta\nu$ must be

$$\delta\nu = \frac{1}{T}. \tag{1.13}$$

The DFT provides frequency information up to the Nyquist frequency ν_{nq}, which is defined as

$$\nu_{nq} = \frac{1}{2\Delta t}, \tag{1.14}$$

where Δt is the cadence of the time series.

A frequency-power spectrum $P(\nu)$ is used to display the frequency domain information obtained from a DFT. In the simplest sense the power spectral density is defined as

$$P_\nu = |F_\nu|^2. \tag{1.15}$$

While the frequency determination of a mode is independent of the power scaling, a comparison of amplitudes requires sensible choices for the power scaling. The scaling used in this thesis is set to give a power spectrum scaled as power per unit frequency and in addition compensated once for reduced fill. Reduced fill occurs due to a number of reasons, primarily weather or instrument failure interruption. Missing data in the time domain is replaced by zeros to maintain an equally spaced time cadence. But, we define the total power in the spectrum as equal to the sum of the squares of the velocity residuals divided by the fill, to allow for this missing data. This choice is made to conform with Parseval's theorem, at least under the assumption that the variance of missing data should be the same as the variance of present data. This choice of scaling is suitable for comparing incoherent noise levels.

The impact of missing data is more subtle than just a reduction in power that can be easily compensated for. In reality gaps in data introduce undesirable spectral features.

1.4.2 The window function

The introduction of artifacts due to a window function in the time domain is a well known phenomenon. Gaps appearing in data may be categorised as either random or quasi-periodic. Both random and quasi-periodic window functions suffer from power leakage, power is redistributed (in the frequency domain) into nearby frequency bins. This is important in low signal-to-noise modes, where the height of a peak above the noise is reduced by this leakage.

Further to power leakage, quasi periodic gaps - i.e. gaps dominated by the day-night cycle - redistribute power into a series of sidebands that sit at multiples of ± 11.57 μHz from the main peak. The presence of these sidebands interferes with the $l = 0,\ 2$ spacing which is of order ≈ 11.5 μHz at 2.1 mHz. This interference introduces systematic errors into the estimates of central frequencies when fitting modes. At lower frequencies and hence lower signal to noise, sidebands cannot be distinguished from noise and contribute to background noise levels.

1.5 Solar structure and dynamics

The primary results of global helioseismic observations are the frequencies of the modes of oscillation of the Sun. As measurements of a quantity with units of inverse time, we must input additional information to make inference on solar internal structure and dynamics with units of anything more than time. In the simplest sense, we can construct a solar model with various input parameters in order to predict observed frequencies of oscillation, and then make comparison - this is direct modelling.

However, there is a well known difference between observed and computed frequencies of oscillation for the Sun [Christensen-Dalsgaard et al., 1988, Kjeldsen et al., 2008]. This systematic offset is known to arise from improper modelling of the near surface layers, or failure to account for non-adiabatic effects and the breakdown of convection near the surface. To compensate it is necessary to introduce a surface term. This surface term is

an empirical correction and because the term is independent of angular degree - at least for $l \lesssim 100$ while waves move approximately vertically near the surface and so there is little difference in the horizontal components in the near surface layers - the correction is most easily determined for radial modes and then applied to all modes.

However, the uncertainties in the near-surface layers makes it difficult to test models by directly comparing observed and modelled frequencies. The disagreement in frequency due to near-surface effects is often larger than that due to differences in structure. By using the differences in frequency and selecting modes of oscillation equally sensitive to the near surface layers the deep solar structure can be tested.

Differences in frequency are typically inverted in order to determine the differences in structure. Inversion techniques take observable outputs of a physical system and infer the properties that bring about those observables, that is with suitable constraints on the input physics, i.e. sound speed or density profiles as a function of solar radius must be continuous in the first and second derivatives. A number of techniques have been developed for solving the inverse problem [Gough and Thompson, 1991, Christensen-Dalsgaard, 2002].

Applying this process of inversion it is possible to infer conditions in the solar interior. Particularly, the depth dependent internal sound speed, the depth of the convection zone, and solar internal rotation.

1.5.1 What have the 'helioseismologists' ever done for us?

Helioseismology has seen useful application in and beyond solar physics. Applications include topics such as cosmology and the standard model of particle physics. Here we briefly consider some milestones in the subject.

A sensible, and therefore common, starting point for global helioseismology is the internal profile of sound speed. Gough [1986] showed that the internal sound speed could be used to directly determine the depth of the convection zone, an important parameter in solar physics, especially when considering the mixing of elements due to convection. Following

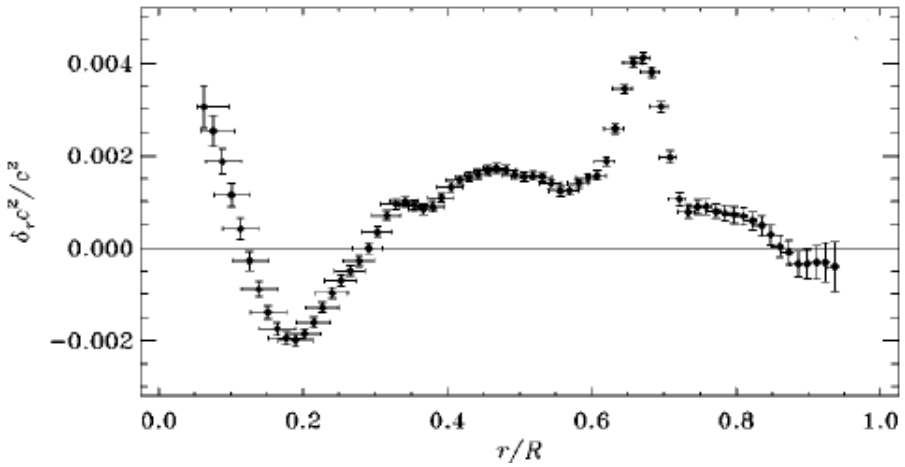

Figure 1.3: Results from a sound speed inversion showing the difference, in sound speed squared, between the Sun and a standard solar model. Taken from Christensen-Dalsgaard [2002].

on from this Christensen-Dalsgaard et al. [1991] used observations to show that the depth of the convection zone is 0.287 ± 0.003 solar radii. Figure 1.3 shows the difference between the sun and a standard model in sound speed squared. The feature at around 0.7 solar radii is associated with the convection zone and allows an accurate determination of the depth. More recent results have confirmed this with Basu and Antia [2004] reporting a well constrained value of 0.2867 ± 0.0005 solar radii. The depth of the convection zone determined by helioseismology is some 50% deeper than predicted by conventional models of the 1970's.

Helioseismology has determined the solar internal rotation rate. The frequency degeneracy of a mode of oscillation is broken by rotation so frequencies are rotationally split, with each frequency probing different layers of the solar interior. Rhodes and Ulrich [1977], Gough [1981], Thompson [1990] have shown with increasing accuracy that the differential rotation, witnessed through sunspots, on the solar surface continues to the depth of the tachocline - just beneath the base of the convection zone - after which solid body rotation dominates. This layer of shear at the tachocline is believed to be responsible for the dynamo that drives the 11-year solar cycle [Antia et al., 2008]. Using helioseismic

measurements Fletcher et al. [2010] suggest that a shorter 2-year cycle may be attributed to shear layer at a depth of only 0.05 solar radii.

The solar neutrino problem, now resolved, tested and strained the standard model of particle physics. Earth based observations of the solar electron-neutrino flux, a sensitive measure of the conditions in the solar core, consistently returned values of one third the amount of flux predicted by solar models and nuclear physics. The resolution of this problem was found to be electron neutrinos changing flavour to muon neutrinos - and becoming undetectable by current instruments - while in transit from the Sun to the Earth. This high accuracy of helioseismic measurements thereby providing strong constraints on solar models forced particle physicists to modify their understanding. This application of the Sun as an astrophysical laboratory to test fundamental physics lead to the modification of the particle physics standard model based on the confidence in solar models [Elsworth et al., 1990].

The elemental composition of the solar interior is an important parameter in current solar physics and the formation of the Sun, which of course has implications on the modelling of the solar system, modelling of other stars, modelling of our galaxy, and therefore impact in cosmology. Abundances can be measured by photospheric spectroscopy, but this is only a measure of abundance at the solar surface, additional information is required to extrapolate to a value for solar abundance. We can believe that the convection zone is well mixed due to turbulence which allows us to believe that the surface abundance is a measure that is good down to the bottom of the convection zone. But a true solar abundance must consider the effect of gravitational settling on the heavy elements.

In addition, the helium abundance cannot be inferred from spectroscopy as the required spectral lines are formed in the chromosphere, where a lack of thermal equilibrium prevents accurate determination of the line parameters. Helioseismic results constrain solar models and therefore can be used to determine solar abundances.

Christensen-Dalsgaard and Gough [1980] used helioseismic data and a standard solar model to determine a value for the helium abundance and hence demonstrate that there

was no significant variation from the accepted helium abundance of the time. However, solar models are sensitive to the input parameters, the opacity as determined by the heavy element abundance, and recent work by Asplund et al. [2005b] revised the mass fraction of the heavy elements to hydrogen, Z/X, to 0.0176 from the previous value of 0.0229 given by Grevesse and Sauval [1998]. As standard solar models must satisfy the requirements of measured effective temperature and luminosity at the current solar age, a change in the opacity tables must be compensated for. The required solution is a revision downwards of the metalicity Z and helium abundance Y, but these new abundances reduce the agreement displayed between solar models and helioseismic results [Asplund et al., 2005a].

As yet this 'solar model problem' (or 'solar abundance problem', depending on ones perspective) has not yet been resolved [Serenelli et al., 2009]. The depth of the base of the convection zone is predicted by models with the revised abundances as 0.724 solar radii from the solar centre, while helioseismic results show 0.7133 ± 0.0005. The surface abundance of helium is determined by models with the new abundances as 0.231, while helioseismic results give 0.2485 ± 0.0035. Clearly there is no agreement here. In addition to these two parameters, the sound speed and density profiles from observation and modelling show reduced agreement with the revised abundances. Modelling the Sun was easier with the old abundances.

Progress in the solar model problem has continued with helioseismology. Basu et al. [2007] showed the solar models constructed with low metalicity to be incompatible with observations based on the conditions in the solar core. And Chaplin et al. [2007] obtained a seismic estimate for the solar metalicity of between 0.0252 and 0.03103 with uncertainties in the range of 12%-19%. These values are clearly much greater than the revised low-metalicity abundances. Work in this field continues.

Helioseismology continues to demonstrate its relevance in unlocking the information stored in the solar interior. The recent quiescence of the Sun at the end of solar cycle 23 sparked interest in the internal conditions with analysis of the dynamic [Howe et al., 2009, Antia and Basu, 2010, Basu and Antia, 2010] and the structural [Salabert et al., 2010] changes.

In addition, once again using the Sun as an astrophysical laboratory, probing of the solar dynamo [Jones et al., 2010], or using helioseismic constraints to infer the presence of dark matter in the Sun [Cumberbatch et al., 2010] show a bright future for science using helioseismology.

1.6 Low-frequency modes

Detection of solar oscillations below 1.3 mHz has proved a significant challenge to observers since the early days of helioseismology. With decreasing frequency, the noise due to solar granulation increases, and yet the signal from evanescent waves reaching the photosphere decreases. This region in frequency of low signal to noise contains the key to inference on the structure and dynamics of the solar core: low-degree and low-order g and p modes.

Solar gravity waves have the potential to provide unprecedented inference on the solar core [Appourchaux et al., 2010], inference that is not possible with the easily detectable p modes. Gravity modes have high displacement amplitudes in, and hence are very sensitive to, the solar core but are evanescent in the convective region. Consequently, g modes have very low amplitudes in the photospheric region. While there are currently (2010) no undisputed detections of individual g modes, there have been a number of claimed detections for example Severnyi et al. [1976], Delache and Scherrer [1983], Kotov [1985] and more recently Turck-Chièze et al. [2004]. Some of these claims of detection have been rebuffed as systematic instrumental noise [Elsworth et al., 1989], while others face criticism on grounds of plausibility, particularly given that noise levels in modern data are significantly improved and yet still no undisputed detections exist. However, even more recently, the GOLF team have perhaps found evidence of the ensemble signature of g modes [García et al., 2007] but again these results have not yet been independently confirmed.

If g modes are difficult to detect then perhaps the signal from the so called mixed modes

may reveal itself. Mixed modes are modes with a duality of nature, g mode while in the stably stratified solar interior but p mode in propagation through the convective zone, albeit with an evanescent buffer between the two regions. It is hoped that the oscillatory, rather than evanescent, nature of these modes while in the outer regions of the Sun will provide the required amplitudes to be detected at the solar surface. However, detections of mixed modes [García et al., 2001, Gabriel et al., 2002] have again not been yet been independently confirmed.

In the absence of g and mixed modes the low-degree low-order p modes become important to understanding the structure of the solar core [García et al., 2001]. Low-frequency p modes have very long life times which means that their spectral features are very narrow. The determination of the frequency of oscillation is then estimated with a high accuracy which places better constraints on fractional precision of physical quantities inferred with these observations. Since the properties of low-degree p modes are sensitive to the conditions in the deep solar interior, their frequencies act as a probe of this region. Detection of low-frequency p modes could place constraints on the structure of the solar core. Numerous low-degree p modes have been detected but current limits do not extend beyond $\approx$ 972 μHz. As has been described previously, the signal to noise of p modes falls off rapidly in the low-frequency region. Once again some detections have been claimed in the sub 1 mHz region but all await independent confirmation [Chaplin et al., 2002a, Broomhall et al., 2007].

1.7 Thesis structure

The thrust of thesis is work towards the improvement of signal to noise for the region of low-frequency g and p modes, where the scientific objective is to further constrain the structure of the solar core.

In order to achieve this goal, we start in the following chapter by giving an overview of the current BiSON network. In chapter 3 we start the construction of a model to describe the

observations made by BiSON Resonant Scattering Spectrometers (RSS). Having produced the required descriptions of the Sun and terrestrial atmosphere we continue in chapter 4 to describe the process of resonant scattering at the heart of an RSS. Chapter 5 presents the results of a model of an RSS which is combined with the solar and atmospheric components in chapter 6 and the full model is tested against real observations.

In the following chapters we look to exploit the model for the improvement of the calibration and concatenation of BiSON data. Chapter 7 develops a correction for the well known (at least in the helioseismic community) effect of differential extinction. Where previous attempts at a correction have shown the ability to correct only a single day of data, here we show how a correction can be applied to all BiSON data.

Chapter 8 examines the long-term stability of the BiSON network by looking for signals at very low frequency that degrade the signal-to-noise ratio in the p and g mode regions of scientific interest.

Chapter nine takes the improvement in signal to noise produced by the correction for differential extinction over the whole 20 year BiSON data set and examines the target low-frequency regions in the power spectrum. Modes of oscillation previously undetected by the BiSON network are uncovered and their properties are analysed. Finally the future prospects of uncovering further modes using the BiSON network are examined.

Chapter 2

The BiSON Network

The Birmingham Solar-Oscillations Network (BiSON) uses resonant scattering spectrometers to measure the spatially unresolved line-of-sight velocity of the solar surface. The aim of this thesis is the detection of low-degree, low-frequency solar oscillations and to that end we will pursue an increase in signal to noise in BiSON instruments. In this chapter we describe the current instrumentation and data analysis techniques used to observe solar oscillations with the BiSON network.

BiSON currently consists of 6 semi and fully automated stations dedicated to the collection of low-degree (Sun-as-a-star) helioseismic data. The stations are situated at sites around the globe to provide as near continuous observation of the Sun as possible. The six sites are Izaña in Tenerife, Las Campanas in Chile, Mount Wilson in California, Narrabri in New South Wales, Carnarvon in Western Australia, and Sutherland in South Africa.

2.1 BiSON history

The BiSON network came in to being in the summer of 1981 when 3 months of solar oscillation data were collected from two manually-operated, celeostat-fed instruments on Haleakala, Hawaii and Izaña, Tenerife. This basic network achieved a duty cycle of about 50% and continued episodic observations into 1984. In late 1984 the IAC, Tenerife started operating the Izaña instrument all year round and by the end of 1985 a third equatorially

Figure 2.1: The Las Campanas dome in Chile.

mounted instrument had been commissioned at Carnarvon, Western Australia. These three instruments, spread across a range of longitudes, provided a network capable (in theory at least) of generating continuous coverage of the Sun. In reality though, the best duty cycle achieved until 1990 was only 56% over a two month period.

In the early 1990's the network expanded with the addition of the Sutherland, South Africa station in 1990, Las Campanas, Chile (figure 2.1) in 1991, and Narrabri, Eastern Australia in 1992. The transfer of the instrument in Haleakala to Mount Wilson, California in mid 1992 completed the current geographical configuration of the BiSON network, although instruments have been regularly upgraded and transferred over the past 18 years. Network performance over the last 20 years allows for the study of high-quality multi-year time series with duty cycles of very nearly 80%. Hence, BiSON's observations are a powerful tool for inference on the structure and dynamics of the solar interior.

2.2 Resonant scattering spectrometers

Each BiSON station uses a Resonant Scattering Spectrometer (RSS) to measure the line-of-sight Doppler velocity of the solar surface. A detailed description of the resonant scattering vapour cell is given in Chapter 4, for now we detail the operation of an RSS and how it compares the Doppler shifted solar absorption line with a laboratory referenced atomic transition.

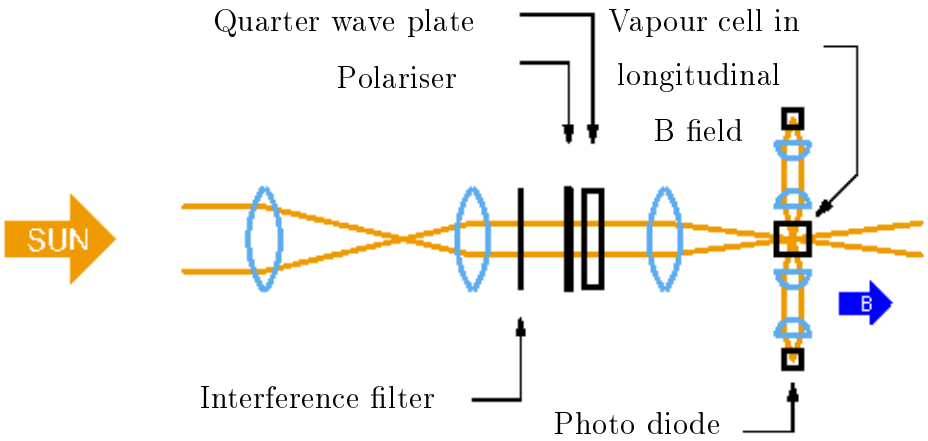

Figure 2.2: Schematic of a typical BiSON spectrometer. Image: Brek Miller

Figure 2.2 shows a schematic diagram of a typical BiSON RSS. Sunlight enters the instrument through the primary lens that forms part of a telescope with the second lens. A section of quasi-parallel light follows where components that are sensitive to off-axis angles are placed. First an interference filter, with a narrow pass band, reduces the through put of the instrument to a small range in wavelength that extends either side of the instrumental profile. Next a combination of a linear polariser and quarter wave plate act to modify the polarisation of the passed beam to that of circularly polarised light. In fact, the quarter wave plate is a Pockels cell, an opto-electric device that allows for the variation of the axis of birefringence, which may be modulated between each state and hence in combination with the linear polariser produces either left or right handed circularly polarised light. The passed light is then focused to an image at the center of the resonant scattering vapour cell. Further information on the operation of an RSS can be found in Brookes et al. [1978].

BiSON measurements are achieved by passing this incident solar light through a vapour of potassium atoms which resonantly scatter photons at energies matching atomic transitions. As light from this process is emitted isotropically, detectors placed away from the solar beam detect only resonantly scattered light. Because the line width of the vapour

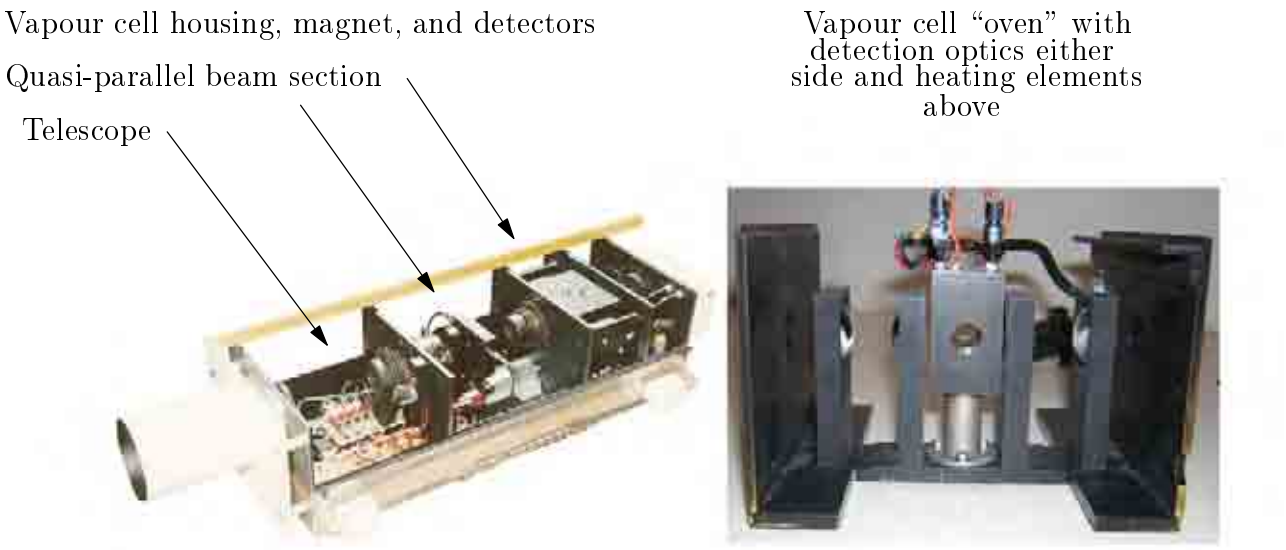

Figure 2.3: Pictures of a typical BiSON spectrometer. Left: instrument with cover removed. Right: the vapour cell housing together with detection optics. Images: Brek Miller

atomic transition is significantly smaller than that of the solar line, the intensity of light detected is proportional to the intensity of the light in a narrow wavelength band at a point on the solar absorption line.

The solar absorption line being studied is Doppler shifted by the line-of-sight velocity components between the source and observer. This places the narrow instrumental line away from the centre of the solar absorption line and changes the intensity detected. The sensitivity of the instrument to velocity signals can be maximised by placing the instrumental pass-band at the point of the solar line where the slope (in terms of wavelength) is greatest. This is achieved by placing the vapour in a longitudinal magnetic field.

The application of a longitudinal magnetic field produces Zeeman splitting of the instrumental pass-band. The splitting of the two resulting components that the RSS uses (the σ^+ and σ^-components) is proportional to the strength of the magnetic field applied and hence the sensitivity can be maximised. The typical magnetic field strength used by a BiSON RSS is 0.18 T, which produces a separation between the σ components of 13 pm or 5200 m s^{-1}.

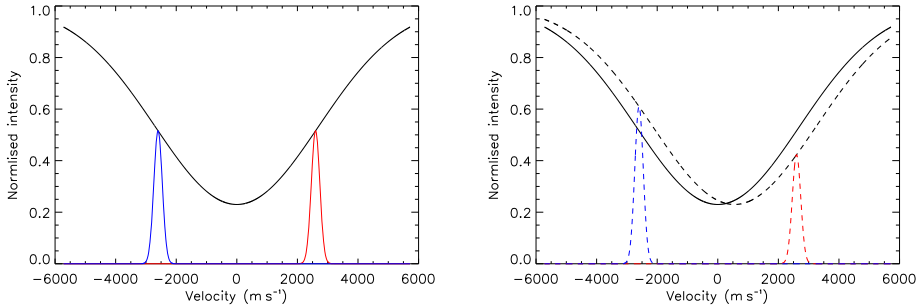

Figure 2.4: Intensities diagram showing the solar absorption line together with the blue and red wing absorption lines. Left: No source-observer line-of-sight velocity. Right: Source-observer line-of-sight velocity of 550 m s^{-1}.

In addition, because the blue shifted Zeeman σ component has an intrinsic circular polarisation of opposite handedness to the red component, the component detected can be isolated by supplying light of only left, or of only right, hand circular polarisation. This allows for the separate measurement of two intensities over narrow instrumental pass-bands either side of the solar absorption line, referred to here in as I_b and I_r. In application, measurements of each wing are taken as close to simultaneously as possible. In BiSON instruments the Pockels cell, and hence the handedness of polarisation and hence the wing scattered, are modulated at 50 Hz to minimise atmospheric and solar sources of noise. Figure 2.4 shows the classic picture of the intensity measurements.

Given that the basic measurement made by an RSS is an intensity, we require a calibration process that produces a measure of solar-surface velocities.

2.3 Calibrating data

Not all BiSON instruments share identical configurations and so rather than a modelled calibration process for each instrument, a common self-calibrating procedure is applied. This process takes advantage of what is a dominant Sun-observer line-of-sight velocity signal. Rather than calibrate intensities that are highly sensitive to atmospheric extinction noise, we use a ratio and hence create a differential measurement that is found to be a

linear measure, to a good approximation, of line-of-sight velocity.

The ratio R is defined as the difference in red and blue intensity measurements divided by the sum of the same measurements,

$$R = \frac{I_b - I_r}{I_b + I_r}. \tag{2.1}$$

The calibration of the ratio rather than an intensity significantly reduces the sensitives of measured velocities to atmospheric variation.

2.3.1 Velocity components

The Sun-observer line-of-sight velocity components can be described as a sum of five components: v_{spin} due to Earth's rotation; v_{orb} due to Earth's orbit; v_{grs} due to the gravitational red shift; v_{inst} due to instrumental effects; and finally v_{solar} due to solar velocity signals. This gives

$$v_{\text{total}} = v_{\text{spin}} + v_{\text{orb}} + v_{\text{grs}} + v_{\text{inst}} + v_{\text{solar}}. \tag{2.2}$$

The line-of-sight velocity component due to the Earth's spin is dependent on an observer's positional latitude ϕ_{obs} and the local time LT as well as the solar declination $\delta_{\odot}$, via:

$$v_{\text{spin}} = \omega_E R_E \cos\phi_{\text{obs}} \cos\delta_{\odot} \sin\left(\frac{\pi}{12} LT\right), \tag{2.3}$$

where ω_E is the Earth's angular velocity and R_E is the local perpendicular distance to the axis of the Earth's rotation. This component dominates daily data providing a change of around 800 m s^{-1} over the course of a day.

The Earth's elliptical orbit gives rise to a line-of-sight velocity component v_{orb}, between an observer and the solar surface. This velocity term is sensitive to the Sun-Earth interaction as well as components from lunar and planetary sources. While this velocity can

be modelled to a high accuracy it is sensible - and probably slightly more accurate - to take the velocity values generated from the JPL Ephemeris of solar system bodies. The orbital term has only small variation over a single day but changes by around 1000 m s^{-1} over a year.

In addition to the obvious velocity terms generated by the motion of the Earth, there are at least three additional components to consider. The first is the velocity component predicted by general relativity, the gravitational redshift. Gravitational redshift is a phenomena caused by photons experiencing energy loss as they leave the gravitational field of the Sun, which results in a shift in wavelength. The energy lost, and hence the magnitude of the redshift, is dependent on the change in the strength of the gravitational field. As a redshift can be described in terms of a velocity we can write

$$v_{\rm grs} = \frac{GM_\odot}{c}\left(\frac{1}{R_\odot} - \frac{1}{d}\right) - \frac{GM_E}{cR_E}, \tag{2.4}$$

where $M_\odot$, M_E, $R_\odot$, and R_E are the masses and radii of the Sun and Earth and d is the Earth-Sun distance. At a distance of 1 AU the magnitude of the velocity due to gravitational redshift is around -633 m s^{-1} and variation through the year is of order 0.1 m s^{-1}.

Artifacts that can be described as velocity signals are introduced by the RSS instrument $v_{\rm inst}$, for example most BiSON RSS's have two detectors that record the same measurement but with an offset due to a process referred to as Doppler imaging. Typically, calibration does not account for instrumental offsets or velocities but this will be discussed in detail towards the end of the thesis.

Finally, we arrive at the quantity of interest, the velocity signals of solar origin $v_{\rm solar}$. This signal includes the desired contribution from solar oscillations but also components from granulation and solar activity. Granulation is observed as both a signal from the convective turbulence and a blueshift produced by hotter and brighter convective material rising with cooler and so dimmer material falling away into the solar interior. The method

of calibration to extract the solar signals requires the determination of the known velocity contributions and the calculation of the sensitivity of the instrument. This allows the transformation of the ratio in to a velocity and then the known velocity contributions may be subtracted to leave velocities of solar origin.

2.3.2 The R-V calibration

Calibration of BiSON data is performed daily, in ratio-velocity (R-V) space. Standard data reduction approximates the relationship between the observed ratio $R_{\rm meas}$, and the computed observer velocity $v_{\rm obs}$, as a power series in velocity [Elsworth et al., 1995]. A third order polynomial function is selected which provides enough terms to follow the change in sensitivity through the day but does not become unstable. A linear least squares fit is performed to the measured ratio of the chosen function

$$R(v_{\rm obs}) = \sum_{i=0}^{3} a_i v_{\rm obs}^i, \tag{2.5}$$

where a_i are the fit coefficients and where the observer's velocity is the sum of the Earth's orbital and spin velocities

$$v_{\rm obs} = v_{\rm spin} + v_{\rm orb}. \tag{2.6}$$

The fit provides a function with good agreement to the observed ratio in order that the contribution from known velocity sources may be subtracted and the sensitivity of the instrument may be determined. It is implicit in the application of a least squares fit that the experimental errors are normally distributed. Although the distribution of the raw ideal intensity measurements should Poisson in nature, here the numerous sources of other "error" in the measurement (atmospheric effects, electronic noise, solar signals, etc.) combine, and under the central limit theorem approach a Gaussian distribution. This validates the application of a least squares fit and importantly allows the determination of the inverse sensitivity. The inverse sensitivity of the instrument, or the conversion factor between ratio and velocity, is then $\mathrm{d}v_{\rm obs}/\mathrm{d}R$.

The desired solar signal is the residuals of the third-order polynomial fit multiplied by the inverse sensitivity i.e.

$$v_{\rm resid} = \frac{R_{\rm meas} - \sum_{i=0}^{3} a_i v_{\rm obs}^i}{\sum_{i=1}^{3} i a_i v_{\rm obs}^{i-1}}. \tag{2.7}$$

But the signal obtained in $v_{\rm resid}$ is not composed completely of solar oscillations. Contributions remain from solar granulation and activity, and short timescale instrumental effects, both of which we will consider to be noise. In addition, it is not necessarily the case that all signals from solar oscillations have been retained by the calibration procedure. The fit performed may be considered as a high-pass filter, where low-frequency oscillatory signals are blocked. We consider this problem in the following section.

2.3.3 Low-frequency losses

The method of fitting and subtracting a third-order polynomial to the BiSON ratio is known to attenuate power at low frequencies in the final residuals. This is desirable when studying the five-minute modes as signal to noise in high-frequency regions is increased. However, at low frequencies the fit is able to follow the signal, which is then lost to the process when the fit is subtracted from the measured ratios. The question is, at what frequencies is this important?

The frequencies affected by the fitting of the third order polynomial are determined by the length of the time series under consideration. Although the fit is performed in R-V space, the Earth's spin velocity means that daily data produce a Sun-observer velocity that is monotonically increasing with time. This representation of time in the velocity axis means that very short data sets (a few points) will have almost all power removed by the fit, where as very long data sets will have only the very lowest of frequencies removed. We can crudely approximate the cut-off frequency by stating that the fit may remove a maximum of three periods in a data set. For a data set of 800 points with a cadence of 40 s this limit is around 100 μHz. We can produce a better test of the procedure by applying the fit to simulated data.

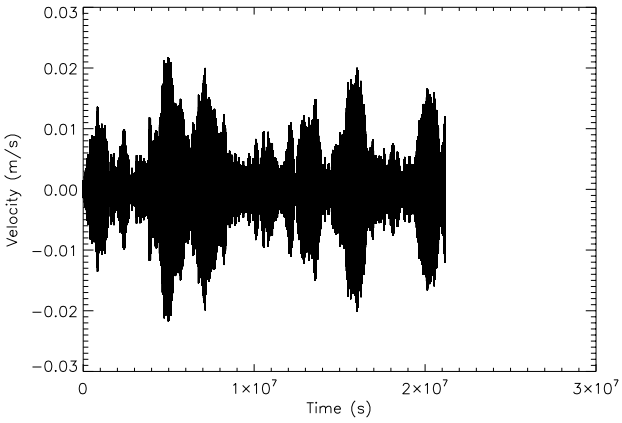

Figure 2.5: Simulation of a single stochastic solar oscillation with frequency $\nu_0 = 1$ mHz and damping time of 30 days. The cadence of the measurement is 40 s and time between successive excitation kicks is $\approx$ 8hours.

We start by generating simulated stochastic oscillations and granulation in terms of a velocity signal. This is done using the auto-regressive processes detailed in De Ridder et al. [2006] and reproduced in appendix 11.1(in addition to simulation in the time domain stochastic oscillations may be simulated in the frequency domain, see Anderson et al. [1990]). Adding the daily Sun-observer velocity and transforming from velocity to ratio gives a model for BiSON measured ratios. The calibration process can then be applied and comparison made between the input and output solar components. Figure 2.5 shows the results of a single simulated solar oscillation at 1 mHz with damping time of 30 days generated as described in appendix 11.1. Figure 2.6 shows the power spectrum of the simulated acoustic mode with simulated granulation. This solar component is added to the daily ratio variation modelled with the results of a typical day's third-order polynomial fit producing the simulated BiSON daily data.

To examine the impact of the third-order polynomial fit and its associated high-pass frequency filter effects, rather than consider a single mode of oscillation we simulate oscillations at a number of frequencies with amplitudes and lifetimes that match predictions. Using real data from the Las Campanas station for the third-order polynomial coefficients and length of data for each day, the simulated ratios are calibrated to produce residuals.

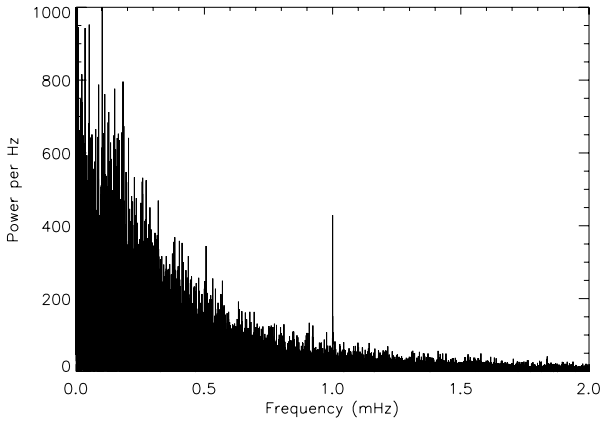

Figure 2.6: Power spectrum of a single simulated solar stochastic oscillation at 1 mHz with simulated granulation and super-granulation.

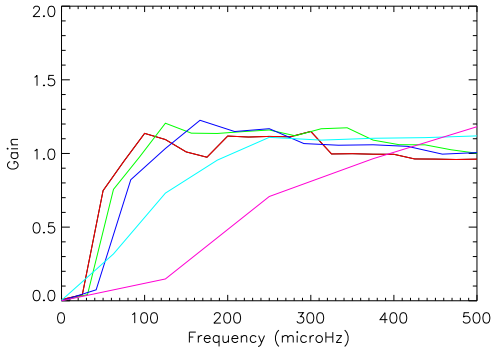

Figure 2.7: Simulated solar signal removed by the BiSON third-order polynomial velocity calibration process for different lengths of data set. Red: 1000 pts; green: 800 pts; blue: 600 pts; cyan: 400 pts; and pink: 200 pts.

Figure 2.7 shows the process gain (power output divided by power input) as a function of frequency for varying length data sets. The attenuation of power is clear at very low frequencies (< 100 μHz) while little attenuation occurs above this limit for longer data sets. This suggests that the current procedure is satisfactory for low-frequency p modes but may not be adequate for the detection of low-frequency (< 100 μHz) g modes or the study of very-low frequency variation in BiSON data.

2.4 Combining data

Once data have been calibrated into daily residual velocities, it is necessary to combine data from all six stations to produce a high-fill long-timescale data set. Here care is required as residual data from each station can be quite different in their noise characteristics. It is therefore sensible to combine data in such a way that strikes a compromise between the need for a high duty-cycle and optimum low-frequency noise.

The low-frequency noise can be parametrised as the mean power in the frequency domain over the range 0.8 to 1.3 mHz and so can be determined for each set of calibrated daily residuals. Firstly, this parametrisation allows for the rejection of data with unusually high low-frequency noise characteristics. Secondly, in the case of over-lapping data from stations observing simultaneously, the noise parameter allows for the selection of the best quality data and rejection of the inferior data. This is the historical BiSON method for combining data to form long time series.

This process appears wasteful, in that good-quality data may be rejected if there is better quality contemporaneous data. Clearly there are obvious advantages to combining data from two stations that contain coherent signal and incoherent noise. Chaplin et al. [1997] detail the merging of multi-site velocity residuals including the weighted combination of contemporaneous data and report gains in signal to noise if noise levels are comparable. However, to produce these gains large low-frequency trends in data sets must be removed. This is achieved by box-car smoothing the data set to remove signals below 1 mHz, which is clearly undesirable when studying low-frequency regions. BiSON data include large low-frequency trends that prevent the straightforward weighted combination of contemporaneous data. Worse still, BiSON data contain large trends at the beginning and end of the day due to a process called differential extinction (see Chapter 3). Because of the longitudinal spread of the network, the ends of the day are exactly the regions where the majority of overlaps occur. Hence, it is still the case that the BiSON data concatenation pipeline includes data of the best quality and rejects other overlapping data.

Long time series produced by the BiSON network are studied in the frequency domain to

find power due to solar oscillations. Next we present the statistical methods for evaluating observed power spectra structure in that domain.

2.5 Selection of mode candidates

Under conditions of low signal to noise i.e. the low-frequency region, it is necessary to determine the nature (signal or noise) of a prominent peak. Hence, a proper treatment of the probability of occurrence of prominent spikes, power confined to a single bin that might be regarded as a mode, is essential (see Appourchaux et al. [2010] for a comprehensive review on both the frequentist approach taken here and the alternative Bayesian approach). This treatment is dependent on the statistical distribution of power in the frequency domain.

If power in the frequency domain arises from a standard normally distributed noise source in the time domain, then the real and imaginary parts of the Fourier transform will be normally distributed, i.e. proportional to $\exp(-\chi^2/2)$, where χ^2 are the observed noise values or more generally the difference between the observed values and theoretical predictions. The probability that a result in the power spectrum (the sum of the squares of the real and imaginary parts) occurs between χ and $\chi + \mathrm{d}\chi$ depends on $\exp(-\chi^2/2)$, multiplied by χ, so

$$P(\chi) \propto \chi \exp(-\chi^2/2). \tag{2.8}$$

Changing variables from χ to χ^2 requires that we multiply by $\mathrm{d}\chi/\mathrm{d}\chi^2$ giving

$$P(\chi^2) = P(\chi)\frac{\mathrm{d}\chi}{\mathrm{d}\chi^2} \propto \chi \exp(\frac{-\chi^2}{2})\frac{1}{\chi} = \exp(\frac{-\chi^2}{2}). \tag{2.9}$$

This is the definition of a χ^2 with 2 degrees of freedom (d.o.f.) distribution and hence the power spectrum of Gaussian noise in the time domain will follow this negative exponential distribution.

While individual sources of noise may not necessarily be Gaussian in character, the central

limit theorem suggests that several noises sources, when combined, will tend to a normal distribution. Therefore, if we consider a small section in frequency of a power spectrum (≈ 100 μHz) and we assert that the background is flat and 'white', then power spectral density may be described by the χ^2 2 d.o.f. distribution.

Knowing the underlying distribution allows for the determination of the probability that a single spike is part of the background noise. So, let the relative height of a given spike be

$$s_\nu = \frac{\xi_\nu}{\langle \xi \rangle_\nu}, \tag{2.10}$$

where ξ is the power of the spike in question at frequency ν and where the mean background level is $\langle \xi \rangle_\nu$ also at frequency ν. Assuming that all bins are independent in the frequency domain, the probability of observing a peak of height s_ν or greater in any given bin is

$$p(s_\nu) = \exp\left(-s_\nu\right). \tag{2.11}$$

The probability of observing at least one spike that has relative height of s_ν or greater across N bins is

$$P_s(s_\nu) = 1 - \left(1 - p(s_\nu)\right)^N. \tag{2.12}$$

This serves as a measure of significance of a candidate detection, i.e. the lower the value of $P_s(s_\nu)$ the less chance a peak is due to noise. Of course, we do not know the probability that a spike is a mode, only the probability that it is part of the noise. Our ability to judge whether or not a spike may be considered as a p mode of oscillation depends upon not only the $P_s(s_\nu)$ but also its location in frequency. Predicted frequencies around 1 mHz are sufficiently well known so that we can ignore statistically significant peaks that disagree with predictions by more than 1 μHz. In addition, modes with $l \geqslant 1$ show characteristic multiplets, i.e. rotationally split multiplets that can increase our confidence in a detection. This information may be combined to determine whether or not a detection is plausible. For a spike to be considered as a candidate we require that $P_s(s_\nu) \leqslant 0.01$ when assessed across a frequency range of $\Delta p = 100$ μHz. The relative height threshold corresponding

to a low $P_s(s_\nu)$ can be found in the limit where $p(s_\nu) = \exp(s_\nu)$ is small. In this limit equation 2.12 can be approximated by [Chaplin et al., 2002a]

$$P_s(s_\nu) \approx Np(s_\nu) \approx \Delta_p T \exp(-s_\nu), \tag{2.13}$$

where T is the length of the time series and Δ_p is the range in frequency under consideration. Hence, rearranging gives the relative height threshold

$$s_\nu \approx \ln \Delta_p T - \ln P_s(s_\nu) \tag{2.14}$$

and substituting in $P_s(s_\nu) = 0.01$.

At low frequency, predicted mode widths are small compared to bin widths (unresolved), the regime change from resolved to unresolved occurring at around 900 mHz for a 10 year BiSON data set. Hence at low frequency, a modes height above the background may be increased using bin shifting, that is varying the length of a time series to place the centre of a bin in frequency closer to the central frequency of a narrow mode. The increase in visibility of a mode from bin shifting is clear if we consider a mode straddling two bins. In this case, the prominence of the mode above the background is reduced by approaching half in comparison to the case where the power is restricted to a single bin.

In addition to bin shifting there are gains to be found around the 1 mHz region and higher by applying power spectrum smoothing. Averaging N_s integer numbers of adjacent bins to produce a new bin with N_s times the width, but maintaining the independence of the new bins, changes the power spectrum statistics. The noise spectrum is smoothed and modified such that it follows a χ^2 $N_s + 1$ d.o.f. distribution. Hence the visibility of modes of oscillation that span several bins is improved. Adding power while smoothing the background produces an obvious reduction in probability that a peak is due to noise. The above methods of calibration, concatenation, and detection have been rigorously applied to BiSON data from the last 25 years. We conclude the introduction to the BiSON network by introducing the current limits of detection at low frequency.

2.6 Current Bison limits of detection

Low-frequency noise in BiSON data, primarily from granulation, limits the detection of solar p mode oscillations around 1 mHz. While the lower limit of detection is the $l = 0, n = 6$ mode at 972.6 μHz [Broomhall et al., 2009a], the lack of detections between this mode and the $l = 0, n = 8$ mode at 1263.2 μHz (also seen by GOLF) suggests that a typical limit of detection has been circumvented by additional excitation of the 972.6 μHz mode. Also reported in Broomhall et al. [2009a], the $l = 1, n = 7$ mode at 1185.6 μHz has been detected using BiSON data, but only the $m = -1$ component has been observed. This suggests that the typical BiSON limit of detection is around 1185 μHz.

The aim of this thesis is to reduce this limit of detection by improving the signal-to-noise ratio in the frequency domain. By reconsidering the process of BiSON residual velocity calibration and long time series concatenation we aim to lower the current mode frequency detection limit. The following chapter details a model of BiSON observations in order to isolate systematic noise in the BiSON power spectra.

Chapter 3

Modelling Data

The aim of this thesis is to present an improved approach to the detection of low-frequency p mode oscillations of the Sun. In the previous chapter we have seen that current data reduction techniques suppress oscillation amplitudes at low-frequencies. This means that the desired signal is lost in noise with things worsening with decreasing frequency. Here we will model observations made by BiSON instruments in order to study the problems of calibration and concatenation of raw data. We aim to improve the signal-to-noise ratio of oscillations in the power spectrum to increase the chance of detections of p modes at low frequency.

This chapter will proceed by forming a model of BiSON observations, without tackling the complexities of the instrumental effects. Following on from this, the next two chapters will deal with the processes and simulation of the RSS instrumental weighting. Finally, in chapter 6 on page 110 we present the results for the combined work. We start by producing an overall framework for the model.

3.1 Introduction

The BiSON network makes ground-based radial-velocity observations of the Sun as a star using a Resonant Scattering Spectrometer (RSS). The raw data returned by the

instrument is a measurement of intensity, taken from either side of the K1 solar absorption line, which is calibrated to produce a ratio. But what are the measured intensities I_m dependent on?

In order to measure radial velocity v_r the RSS compares the solar Fraunhöfer line as a function of wavelength $I_\odot(\lambda)$ to known laboratory atomic transitions. In addition, the RSS makes Sun-as-a-star measurements so intensities are integrated over the whole solar surface S. We can state this as a simple model:

$$I_m = \int_S \int_{\lambda_0-\delta\lambda}^{\lambda_0+\delta\lambda} I_\odot(v_r, \lambda)\, d\lambda\, dS, \tag{3.1}$$

where λ_0 is the central wavelength of the scattering atomic transition and $\delta\lambda$ describes the transition line width.

To achieve a more complete description of the system we must include atmospheric extinction suffered when making ground-based observations. Because the Sun is a discrete source and extinction is known to be differential across the solar surface, we must convolve the line function with an atmospheric function. By treating the the solar surface as a two dimensional disk, parametrised by x and y, we can include the atmospheric extinction T as a function of position on the solar disk, giving

$$I_m = \int_S \int_{\lambda_0-\delta\lambda}^{\lambda_0+\delta\lambda} I_\odot(v_r, \lambda) T(x, y)\, d\lambda\, dx, dy. \tag{3.2}$$

To complete the description we include a non-uniform instrumental response U. The scattering of light, required by the instrument to measure intensity, will only occur for wavelengths within the limits of the resonant scattering profile. In addition, the instrument has a non-homogeneous response to position on the solar disk, making U a function of wavelength and position $U(\lambda, x, y)$. Including the instrumental weighting in our simple model gives

$$I_m = \int_S \int I_\odot(v_r, \lambda)\, T(x, y)\, U(\lambda, x, y)\, d\lambda\, dx, dy. \tag{3.3}$$

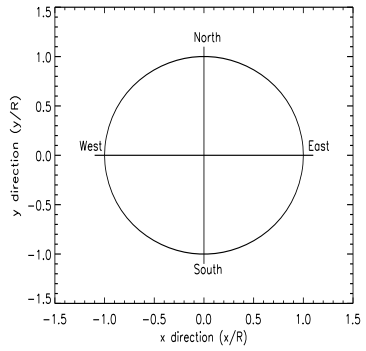

Figure 3.1: Cartesian coordinates of the solar disk.

This provides our framework to continue as we study each of the terms in the integral separately.

3.2 The solar line function

In this section we will consider the solar line function $I_\odot$ and its dependencies, one of which is the point of observation on the solar disk. In light of this, we start by defining a Cartesian coordinate system, with the origin at the centre of the disk. Figure 3.1 shows the coordinate system drawn with respect to the cardinal points, and normalised with respect to the solar radius $R_\odot$.

3.2.1 Solar Fraunhöfer line

In order to build a model for the solar line function we will consider the absorption line properties at each point on the solar disk. More specifically, we will consider the solar line observed at each point on the solar surface before integrating to obtain the Sun-as-a-star line measured by the RSS. The parameters of interest to us, with respect to line shape, are the line width and depth. The line width is sensitive to turbulence (granulation broadens the solar line by at least the same magnitude as thermal effects) and therefore line width is sensitive to the height of observation in the solar atmosphere. It is difficult, and therefore

μ	Γ (pm)	d
1.0	16.2	0.8399
0.8	16.8	0.8369
0.5	18.0	0.8361
0.3	19.0	0.8340
0.2	20.2	0.8321

Table 3.1: Solar line properties as a function of position on the solar disk taken from de La Reza and Mueller [1975].

beyond the scope of this work, to model the variation in line shape with height so we will rely on observational data while treating the solar surface as a two dimensional disk.

For observational parameters we use those found by de La Reza and Mueller [1975] using the McMath solar telescope at the Kitt Peak Observatory. These authors observed centre-to-limb spectrogram at constant solar longitude(on the rotational axis) but varying solar latitude while avoiding the potential contamination of active regions. This work allows us to represent the solar line observed at particular coordinates on the solar disk. The spatial integration used, of 34800 km in the y-direction and 174 km in the x-direction, minimising the effects of rotational broadening giving a closer representation of the underlying solar line. With only a very small observed asymmetry, a solar line at a point on the solar disk can be well described by a Gaussian absorption line with depth d, full width half maximum (FWHM) Γ, and central wavelength λ_c. The form of each Gaussian line may be expressed algebraically as

$$I_\odot(\lambda,\mu) = 1 - d(\mu)\exp\left[-4\ln 2\left(\frac{(\lambda-\lambda_c)^2}{\Gamma(\mu)^2}\right)\right], \tag{3.4}$$

where μ describes the position on the solar disk such that

$$\mu = \cos\left(\sin^{-1}\left(\frac{\sqrt{x^2+y^2}}{R_\odot}\right)\right) = \sqrt{1-\left(\frac{\sqrt{x^2+y^2}}{R_\odot}\right)^2}. \tag{3.5}$$

The results from de La Reza and Mueller [1975] for the line parameters are given in table 3.1. For the purposes of this work, the line width and depth can be sufficiently described

a_i	Γ ($\times 10^{-13}$ m)	d (%)
0	162.0	84.0
1	168.0	-0.2
2	-469.5	-0.01
3	343.9	-0.49

Table 3.2: Coefficients of a third order polynomial to describe the solar line properties as a function of position on the solar disk, r.

by fitting a third order polynomial,

$$y(r) = a_0 + a_1 r + a_2 r^2 + a_3 r^3, \tag{3.6}$$

to the presented data, where r is the radius of the position on the solar disk in units of solar radius. The resulting coefficients are given in table 3.2. The error bars on the coefficients are larger than would normally be tolerated, but here the purpose is to establish a nominal model that can be integrated into our framework in order to understand time dependent effects in the observations of an RSS.

Having stated the basic properties of the position dependent solar lines, we continue by considering the shifting of each line due to line-of-sight velocity.

3.2.2 Doppler shifts

The central wavelength of a solar line λ_c, observed at any point on the disk, may be Doppler shifted by a line-of-sight velocity between the observer and source (the Sun). The individual components contributing to a ground-based solar observers radial velocity have been discussed in section 2.3.1 on page 26. Here, ignoring velocity signals generated by the Sun, suffice to say that the total observed radial velocity is a sum of the following components: the source-observer motion v_{station}; the gravitational redshift expressed as a

velocity $v_{\rm grs}$; and the rotation of the Sun about its axis $v_{\rm rotation}$. This then is simply

$$v_r = v_{\rm station} + v_{\rm grs} + v_{\rm rotation}, \tag{3.7}$$

where the magnitude of the shift in wavelength due to Doppler shifts $\Delta\lambda$ is

$$\Delta\lambda = \lambda_{\rm rest}\frac{v_r}{c}, \tag{3.8}$$

and c is the speed of light in the medium, and $\lambda_{\rm rest}$ is the central wavelength of a solar line in a frame of rest. This gives the central wavelength of a line with Sun-observer line-of-sight motion, λ_c, as

$$\lambda_c = \lambda_{\rm rest} + \Delta\lambda \tag{3.9}$$

Substituting this into equation 3.4 gives

$$I_\odot(\lambda,\mu) = 1 - d(\mu)\exp\left[-4\ln 2\left(\frac{\left(\lambda - \lambda_c\left(1+\frac{v_r}{c}\right)\right)^2}{\Gamma(\mu)^2}\right)\right]. \tag{3.10}$$

The values of the individual components of v_r must be calculated in order to determine $I_\odot$ and to do this we require the positions and movements of solar system bodies. These values are well known and $v_{\rm station}$ may be either calculated or extracted from the JPL ephemeris. The solar gravitational redshift is commonly expressed as a velocity $v_{\rm grs} = 632\ {\rm m\ s^{-1}}$ and will be treated as a constant. We will move on to discuss the velocity contribution from solar rotation in the following section.

3.2.3 Differential Solar rotation

The radial velocity between a ground-based observer and a point on the solar disk includes a component from solar rotation. This rotation is differential over the range described by the solar latitude $\phi_{\rm lat}$. Snodgrass and Ulrich [1990] provide measured coefficients for the

sidereal solar differential rotation rate ω to fulfil the equation

$$\omega(\phi_{\rm lat}) = a_0 + a_1 \sin^2 \phi_{\rm lat} + a_2 \sin^4 \phi_{\rm lat}, \tag{3.11}$$

where the conversion from Cartesian coordinates to solar latitude is performed by

$$\phi_{lat} = \sin^{-1}\left(\frac{y}{R_\odot}\right). \tag{3.12}$$

The coefficients from Snodgrass and Ulrich [1990] are

$$a_0 = 14.713 \pm 0.0491 \ ^\circ \ \mathrm{day}^{-1}$$
$$a_1 = -2.396 \pm 0.188 \ ^\circ \ \mathrm{day}^{-1}$$
$$a_2 = -1.787 \pm 0.253 \ ^\circ \ \mathrm{day}^{-1},$$

showing that the solar equator has a greater rate of rotation than the poles.

The Earth's orbit and the solar rotation are in the same direction, and this increases the observed period of solar rotation, which when corrected for Earth's orbit, is called the solar synodic rotation period. The solar synodic rotation angular frequency $\omega_{\rm syn}$ is the difference between the solar sidereal rotation angular frequency ω and the Earth's orbital angular frequency $\omega_{\rm Earth}$ i.e.

$$\omega_{\rm syn} = \omega - \omega_{\rm Earth}. \tag{3.13}$$

Modifying the coefficients from Snodgrass and Ulrich [1990] to synodic angular frequency and expressing in units of rad s^{-1} gives,

$$a_0 = 2.972 \times 10^{-6} \ \mathrm{rad\ s}^{-1}$$
$$a_1 = -4.84 \times 10^{-7} \ \mathrm{rad\ s}^{-1}$$
$$a_2 = -3.61 \times 10^{-7} \ \mathrm{rad\ s}^{-1}.$$

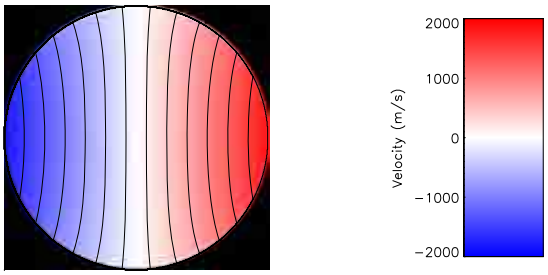

Figure 3.2: Solar differential synodic rotation map.

Finally, converting from angular frequency to units of radial velocity can be achieved by multiplying the synodic frequency by the distance in the x-direction (that is perpendicular to the axis of rotation) on the solar disk

$$v_{\text{rotation}} = \omega_{\text{syn}} x. \tag{3.14}$$

Figure 3.2 shows the differential synodic rotation map of the solar disk. The differential nature is clear with the equator rotating faster than the poles. The diagram shows the Eastern limb rotating towards the observer, and hence blue shifted, and the Western limb receding, hence red shifted. We continue to consider the orientation of the rotation axis of the solar disk.

Position and tilt angles

The introduction of solar differential rotation is more significant than just an additional component of radial velocity. The definition of an axis of rotation removes the angular symmetry of the solar disk and the orientation of the Sun is now significant. The orientation of the axis of rotation changes with respect to time, and we can define this variation. Here we introduce two common definitions to describe the orientation of the axis of rotation of the Sun that changes with Earth's orbit. The first is the solar position angle P_a defined as the position angle between the geocentric north pole and the solar rotational north pole measured eastward from geocentric north. The second, solar tilt angle B_0, is

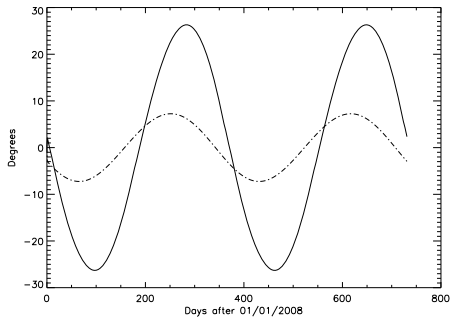

Figure 3.3: Plot showing position angle, P_a (solid line), and tilt angle, B_0 (dot-dash line), for days after 01/01/2008.

defined by the heliographic latitude of the central point of the solar disk. The positions and orientations of solar system bodies are well understood and P_a and B_0 may be calculated or extracted from the JPL ephemeris.

Figure 3.3 shows the variation of the two quantities throughout 2008 and 2009. Both quantities have a yearly period but are phase shifted with respect to each other. The amplitude of the position angle variation is 26.5 °, while the tilt angle varies between plus and minus 7.25 °.

The position angle rotates the solar rotational axis with respect to geocentric North and the tilt axis shifts in latitude. When these rotations are viewed by an RSS, the centre of rotation is the centre of the solar disk, hence we can straightforwardly implement rotation matrices. Any given position on the solar surface $[x_0, y_0, z_0]$ will be mapped to point $[x_1, y_1, z_1]$ when rotated through the angle P_a about the z-axis and B_0 about the x-axis. The rotation matrix operations are linear and can be considered sequentially giving

$$\begin{pmatrix} \cos P_a & \sin P_a & 0 \\ -\sin P_a & \cos P_a & 0 \\ 0 & 0 & 1 \end{pmatrix} \begin{pmatrix} x_0 \\ y_0 \\ z_0 \end{pmatrix} = \begin{pmatrix} x_1 \\ y_1 \\ z_1 \end{pmatrix}, \tag{3.15}$$

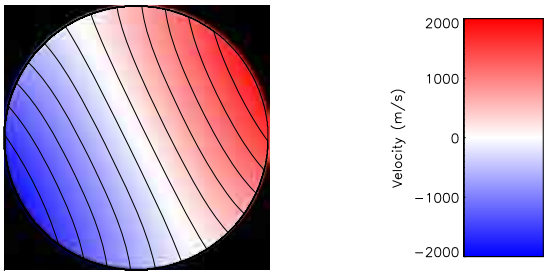

Figure 3.4: Solar differential synodic rotation map with position angle of 26.25 ° and zero tilt angle.

for position angle and

$$\begin{pmatrix} 1 & 0 & 0 \\ 0 & \cos B_0 & \sin B_0 \\ 0 & -\sin B_0 & \cos B_0 \end{pmatrix} \begin{pmatrix} x_1 \\ y_1 \\ z_1 \end{pmatrix} = \begin{pmatrix} x_2 \\ y_2 \\ z_2 \end{pmatrix}, \tag{3.16}$$

for tilt angle.

Given the variation in orientation of the solar disk we must review earlier definitions. We must redefine the input coordinates to equations 3.11 and 3.14 in terms of the rotated coordinate system to give the latitude in the rotated frame

$$\phi_{lat} = \sin^{-1}\left(\frac{y_2}{R_\odot}\right), \tag{3.17}$$

and the rotational velocity

$$v_{\text{rotation}} = \omega_{\text{syn}} x_2 . \tag{3.18}$$

Figure 3.4 shows the differential synodic rotation map of the solar disk with a position angle of $P_a = 26.25\,^\circ$ and tilt angle $B_0 = 0\,^\circ$ with respect to the cardinal points.

Having completed the discussion on components of velocity, we continue to discuss solar limb darkening.

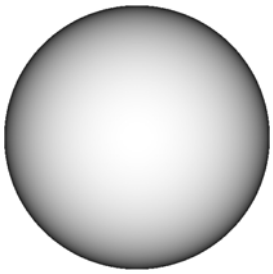

Figure 3.5: Varying intensity due to limb darkening on the solar disk at $\lambda = 770$ nm.

3.2.4 Limb darkening

Limb darkening is an effect that describes the variation in intensity across the solar disk due to variation in observed optical depth. At the centre of the solar disk an observer is looking deeper into the photosphere than at the limb. Observing at increasing depth in the photosphere reveals increasing temperature (because of the solar interior temperature gradient) which is the cause of the increased observed intensity. Hence, the limb of the solar disk is darkened with respect to the centre. Nishikawa [1990] gives an equation for limb darkening at a wavelength of 770 nm as

$$\frac{I(\mu)}{I_0} = 0.469 + 0.7525\mu - 0.2215\mu^2, \tag{3.19}$$

where μ has been defined previously in equation 3.5.

Figure 3.5 shows the intensity variation due to limb darkening on the solar disk. Once again error bars are not of concern, we are simply developing a nominal model to investigate time dependent effects. This limb darkening function is applied to the relative line intensities formed from the coefficients of the position dependent solar line model. In other words, the impact of limb darkening is multiplicative and its application can be though of as a intensity mask combined with the solar line function.

This concludes the definitions of the solar line inputs. We move on to consider how these features combine to define the RSS observations.

3.2.5 Results

Having described the components of the solar line function, we will now combine the individual effects to study the resultant weighting of the solar disk. We are interested in the weighting as a function of both position on the solar disk and wavelength. To demonstrate changes in the variation with position, we consider the intensity on the solar disk over two boxcar functions in wavelength that are narrow in comparison to the solar line and split 2600 m s^{-1} either side of the stationary central wavelength $\lambda_r = 769.898$nm. This gives two observations, one in the red wing and the other in the blue wing and is loosely analogous to the two intensity measurements made by the BiSON instrument. To show the variation in intensity as a function of wavelength we construct full disk absorption line profiles.

Figure 3.6 on the next page shows the solar line function for the combination of effects discussed in the previous section. For reference purposes, a Gaussian absorption line with depth $d = 0.84$, and FWHM $\Gamma = 18.0$pm is shown in the wavelength intensity profiles. Top of figure 3.6, the positional weightings for the solar Fraunhöfer line (only) are seen to be equal with no offset in the whole disk absorption lines central wavelength. The addition of a line-of-sight velocity shifts the central wavelength and introduces a difference in positional weighting between the two wings. The addition of solar rotation (differential) introduces a marked shift in positional weighting but also increases the width and reduces the depth of the whole disk absorption line. Rotating the axis of solar rotation by a positional angle of $P_a = 26.25°$ has only second order impact on the whole disk line, but is significant to the orientation of the positional weighting. Variation in tilt angle, up to $B_0 = 7.25°$, was tested and found to be second order in both the whole disk line and the disk weighting. The structure found at the centre of the solar disk is a consequence of the sensitivity of the solar line function to position on the solar disk, here producing an increased weighting to the centre of the disk. Finally, the change in whole disk line profile due the addition of the limb darkening function is dominated by the significant reduction in intensity across the line.

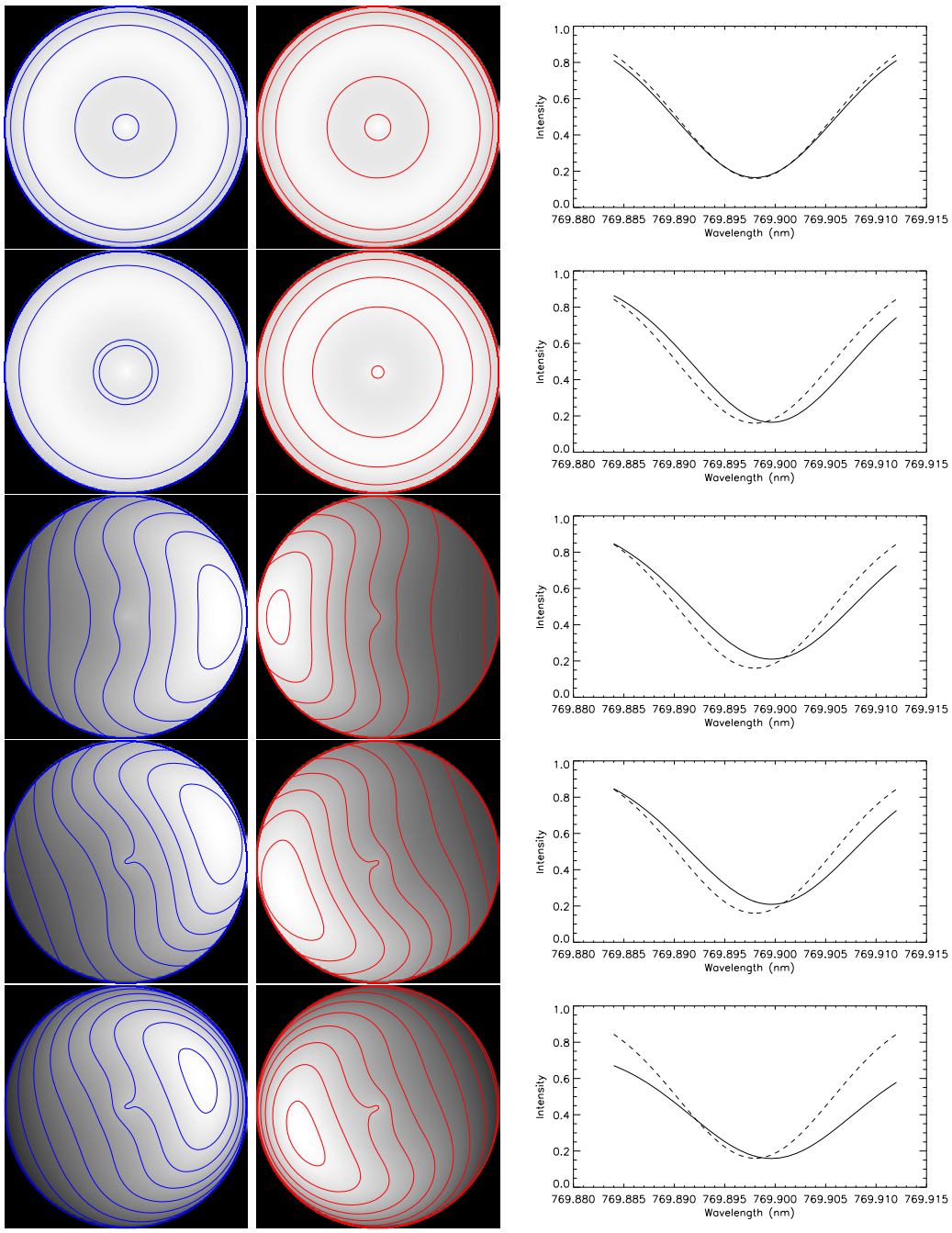

Figure 3.6: Weightings of the solar line function in position on the solar disk and wavelength. Left: blue wing positional weighting. Centre: red wing positional weighting. Right: wavelength-intensity full disk line profile with reference Gaussian absorption line (dot-dash)of depth, $d = 0.84$, and FWHM $\Gamma = 18$ pm. Top line: with solar Fraunhöfer line only. 2^{nd} line: addition of line-of-sight velocity. 3^{rd} line: including solar differential rotation. 4^{th} line: including position angle, $P_a = 26.25°$. Bottom line: with solar limb darkening.

We have demonstrated that a model of the solar line function can be produced and evaluated over both position on the solar disk and wavelength. We have considered, albeit briefly, the impact on weightings due to the individual effects input into our model, but the full value of the model cannot be appreciated until we have dealt with the other terms, atmospheric and instrumental, in the integration of equation 3.3. So we move on to consider the role of atmospheric extinction.

3.3 Atmospheric extinction

It is well known to ground-based astronomical observers that atmospheric extinction is a significant source of noise in photometric measurements. However, when an extended object, such as the Sun, is observed from Earth, two types of extinction component are present. The first, from fluctuations that are random in time and position across the solar disk, does not provide any scope for correction with current systems. However, the second is a systematic atmospheric gradient across the solar disk, often referred to as differential extinction, and we will consider this now.

Differential extinction has been studied by a number of authors with a view to correcting ground-based radial velocity Sun-as-a-star measurements (Grec and Fossat [1979], Belmonte et al. [1988], and Ehgamberdiev and Khamitov [1991]). Differential extinction appears in BiSON data as a monotonic velocity signal due to the changing orientation of the terrestrial atmospheric gradient, which rotates with respect to the solar disk's axis of rotation. The slow variation of this orientation over each day produces noise, particularly at low-frequencies. In addition, in a network of multiple and overlapping stations, such as BiSON, this spurious and changing velocity signal causes problems in the concatenation of individual station daily data. In the following section we construct an atmospheric function to include in our straight forward model given in equation 3.3 on page 38.

3.3.1 Atmospheric model

We start by defining a model of extinction due to absorption or scattering in the terrestrial atmosphere. A standard definition expresses the reduction in intensity $\frac{I}{I_0}$, as exponentially dependent on the atmospheric absorption coefficient κ_{atm}, and the airmass A giving,

$$\frac{I}{I_0} = \exp(-\kappa_{\text{atm}} A). \tag{3.20}$$

Typically the absorption coefficient would be defined as a function of wavelength. Here, the acutely narrow band of wavelengths considered allows us to treat κ_{atm} as a constant, typically around $\kappa_{\text{atm}} = 0.010 \pm 0.005$ at 770 nm. Next we will consider the variation of airmass.

3.3.2 Airmass

Airmass is defined here as the path length that light from a point on the solar disk takes through the Earth's atmosphere relative to the path length for an object at the zenith. Convention is to take the airmass at the zenith to be unity. A typical plane parallel atmosphere approximation would define airmass in terms of the secant of the zenith angle z_0 i.e.

$$A = \sec z_0. \tag{3.21}$$

A better model that includes correction for curvature of the atmosphere and refracted elevation(the shift in apparent elevation due to refraction) is given by Kasten and Young [1989]

$$A = \frac{1}{\cos(z_0) + 0.50572(96.07995 - z_0)^{-1.6364}}. \tag{3.22}$$

Taking the more complete definition as our working model, we proceed by considering the variation of the zenith angle.

Station	UTC − LT	$\phi_{\rm obs}$ (°)
Izana	0	28.30
Carnarvon	-8	-24.87
Narrabri	-10	-30.31
Sutherland	-2	-32.38
Las Campanas	4	-29.02
Mount Wilson	8	34.22

Table 3.3: Station parameters required to calculate the solar zenith angle.

3.3.3 Zenith Angle

The solar zenith angle is formed between the observers local zenith and the line-of-sight to the centre point on the solar disk. The zenith angle can be calculated from the local hour angle H, the observers latitude $\phi_{\rm obs}$, and the solar declination $\delta_\odot$. The equation to find the zenith angle is

$$\cos z_0 = \sin\phi_{\rm obs}\sin\delta_\odot + \cos\phi_{\rm obs}\cos\delta_\odot\cos H, \tag{3.23}$$

where the solar declination for any station can be calculated from the current Modified Julian Date MJD using

$$\delta_\odot = 23.44^\circ\cos\left(\frac{2\pi}{T_E}(\mathrm{MJD} - 54638.5)\right), \tag{3.24}$$

where T_E is the Earths orbital period of 365.242191 days.
The hour angle and observer latitude are dependent on the time and location of the observation. The solar hour angle can be calculated from local time LT with

$$H = 15.0^\circ(\mathrm{LT} - 12.0) \tag{3.25}$$

The difference between UTC and local time, and observer latitude for each BiSON station are given in table 3.3. The solar zenith angle varies throughout the day, in the familiar manner to produce the rising and setting of the Sun and the day-night cycle. In addition,

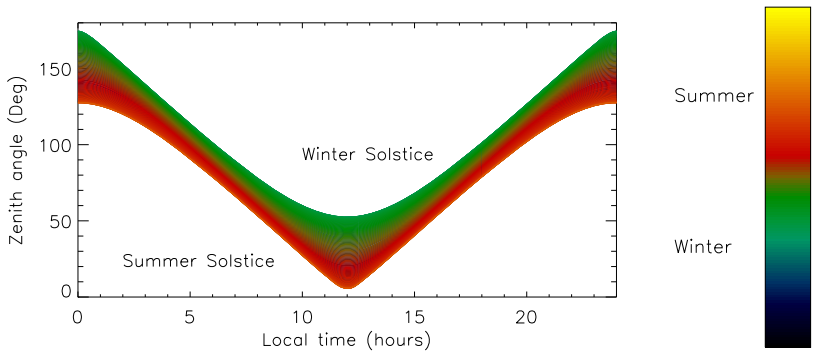

Figure 3.7: Variation of solar zenith angle with time at the BiSON Las Campanas station. The plot shows the variation with respect to local time through the day, and the variation between summer and winter solstice. Each day between summer and winter solstice is traced to give the annual variation.

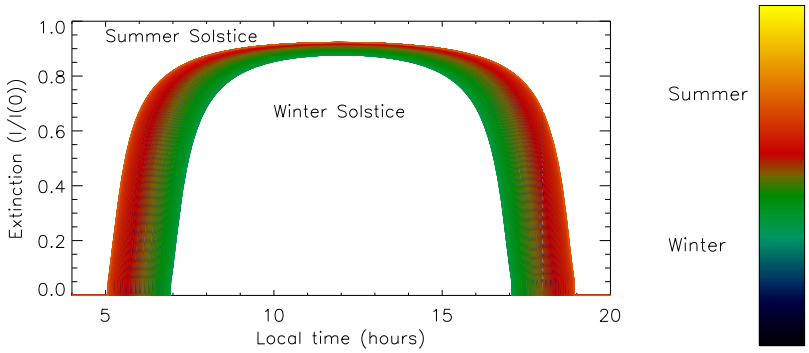

Figure 3.8: Variation of extinction with time. The plot shows the variation with respect to local time through the day, and the variation between summer and winter solstice. Atmospheric extinction coefficient set to $\kappa_{\rm atm} = 0.1$. Each day between summer and winter solstice is traced to give the annual variation.

the nature of the relative inclination of Earth's spin and orbit around the Sun produces variations in zenith angle between summer and winter solstice. Figure 3.7 shows the variation of zenith angle with respect to local time, and day of the year.

Having calculated the zenith angle, we can straight forwardly work out the airmass and in turn the atmospheric extinction. But because the zenith angle varies through the day and year, extinction does too. Figure 3.8 shows the variation of extinction with respect to time for an atmospheric absorption coefficient of $\kappa_{\rm atm} = 0.1$.

We have now dealt with the extinction of a single central point on the solar disk. We

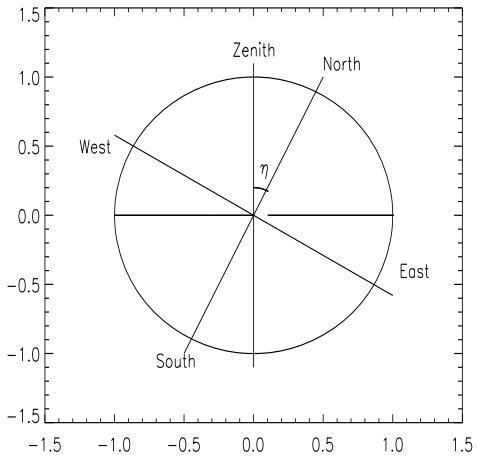

Figure 3.9: Diagram showing definition of parallactic angle on the solar disk.

will continue by considering the Sun as an extended source, the key factor in differential extinction.

3.3.4 Parallactic angle

We have seen that the Sun moves across the sky throughout a day and its position is described by the zenith angle z_0. But the solar disk is an extended source, with angular extent of 0.5 °, and therefore extinction will vary with position on the disk. To model this extinction we must consider: the angles formed between the heliographic North/South axis; the atmospheric extinction gradient; and the axis of the instrument. BiSON instruments are mounted equatorially and this maintains a constant alignment with the heliographic axis, and hence we will consider the atmosphere to be rotating with respect to this common axis.

The parallactic angle is formally the angle between the great circle through a celestial object, the zenith, and the hour circle of the object. Figure 3.9 shows the parallactic angle on the solar disk with respect to the heliographic cardinal points and zenith.

The parallactic angle of the solar disk changes through the day as the Earth spins and

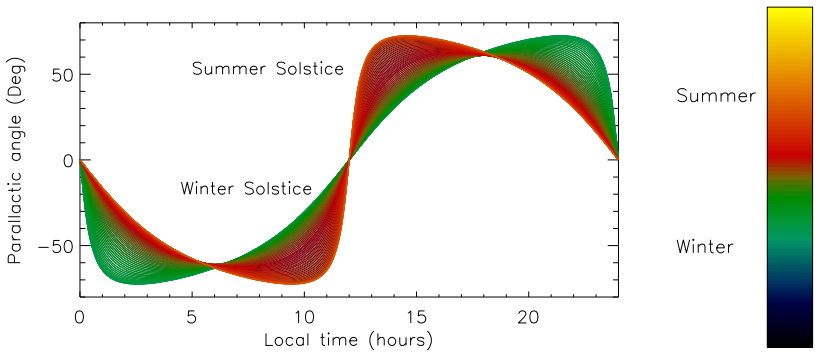

Figure 3.10: Variation of parallactic angle through the day and year. Each day between summer and winter solstice is traced to give the annual variation.

also throughout the year as the Earth orbits the Sun. The parallactic angle η can be calculated from: an observers latitude ϕ_{obs}; the solar declination $\delta_{\odot}$; and the zenith angle z_0. The dependence is expressed as [Duffett-Smith and Zwart, 2011]

$$\cos\eta = \frac{\sin\phi_{\text{obs}} - \sin\delta_{\odot}\cos z_0}{\cos\delta_{\odot}\sin z_0}. \tag{3.26}$$

Figure 3.10 shows the variation of the parallactic angle, with the abscissa in local time and a trace for each day between summer and winter solstice for the BiSON Las Campanas station.

3.3.5 Extinction across the solar disk

In this section we combine the zenith angle, parallactic angle and extinction coefficient to produce the extinction across the solar disk. We start by considering the zenith angle and define this at any point on the solar disk z_a to be the zenith angle of the disk centre plus a change in zenith angle due to position on the solar disk δz, giving

$$z_a = z_0 + \delta z, \tag{3.27}$$

where z_0 can be determined from equation 3.23 on page 52. We consider δz to act in an atmospheric frame that is aligned so that the atmospheric gradient is in the y-axis

only y_{atm}. Hence, the change in zenith angle is defined here to be the y-direction angular extent of any point away from the disk centre, giving,

$$\delta z = 0.25\,^{\circ}.\frac{y_{\mathrm{atm}}}{R_{\odot}}. \tag{3.28}$$

We must include the rotation of the atmospheric frame with respect to the heliographic coordinates (x, y) which is achieved with

$$y_{\mathrm{atm}} = y\cos\eta - x\sin\eta. \tag{3.29}$$

Using this equation and equations 3.22 and 3.20 on page 51 allows us to calculate the extinction at any point on the solar disk.

Figure 3.11 on the next page shows the modelled results for extinction across the solar disk for the BiSON Las Campanas station on 14/01/2009. The solar disks are shown with each contour line representing a 0.01% change in measured intensity due to atmospheric extinction. Results are shown for a range of times spanning the whole day. The atmospheric gradient across the disk can be seen to rotate throughout the day with respect to the stationary heliographic coordinates. The distance between contours shows the magnitude of the gradient, which is seen to be much greater at the extremes of each day.

Having considered the gradient of extinction over the solar disk we continue by studying its effect on the whole disk absorption line.

3.3.6 Results

In this section we focus on combining the spatial aspects of atmospheric extinction with the solar line function, produced from the model considered in section 3.2 on page 39. We expect to see results that produce a velocity signal that varies throughout the day due to the changing magnitude and direction of the atmospheric gradient. As BiSON instruments measure intensities at points on the solar absorption line, we must observe

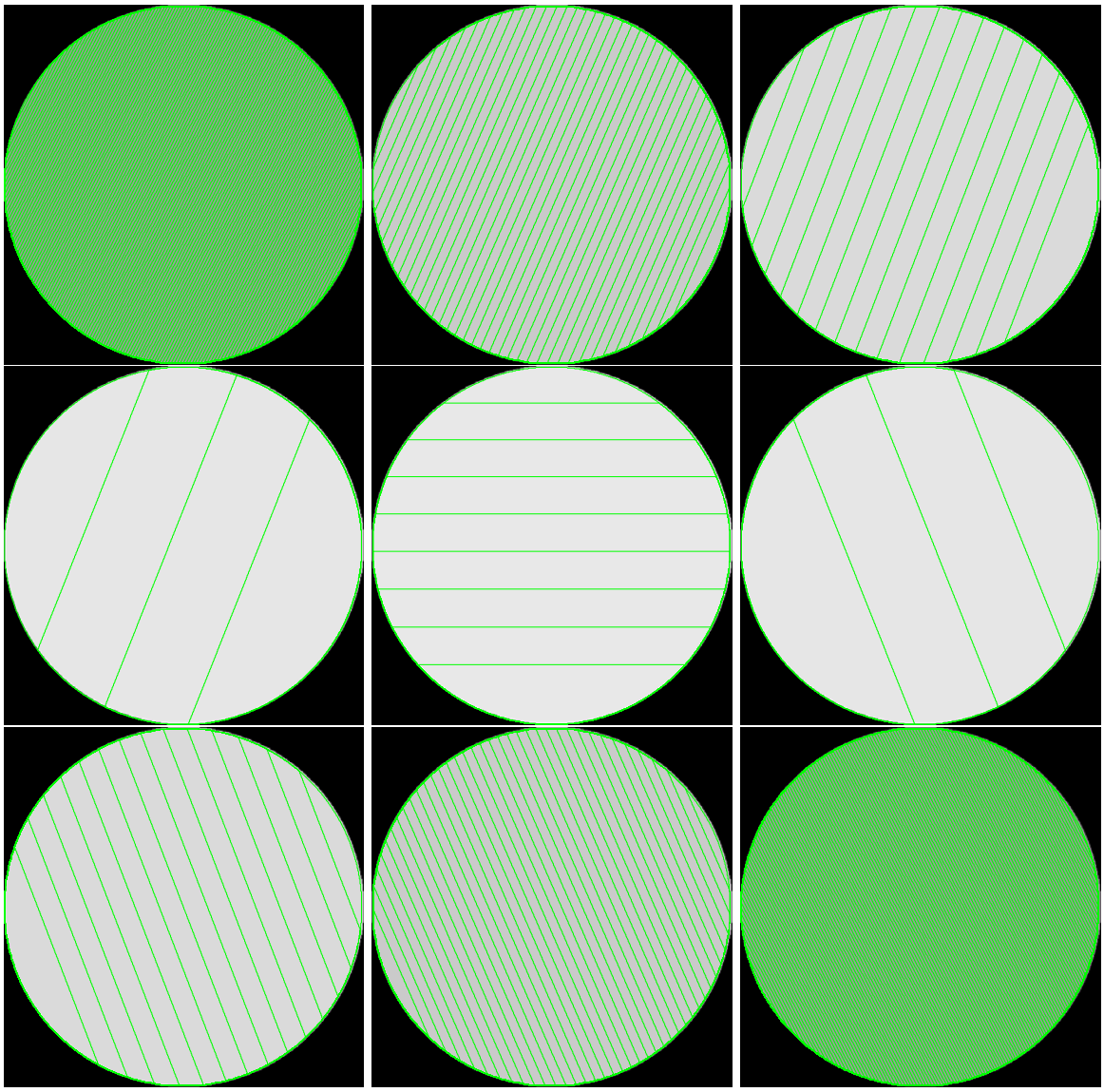

Figure 3.11: Diagrams of atmosphere showing differential extinction for the BiSON Las Campanas station on 14/01/2009. Contour lines mark changes in intensity of 0.01%, except for the central plot which has the resolution increased to changes in intensity of 0.001%. Each map shows the solar disk at different times during the day. The local time from left to right then top to bottom: 06:00; 07:00; 08:00; 10:00; 12:00; 14:00; 16:00; 17:00; and 18:00.

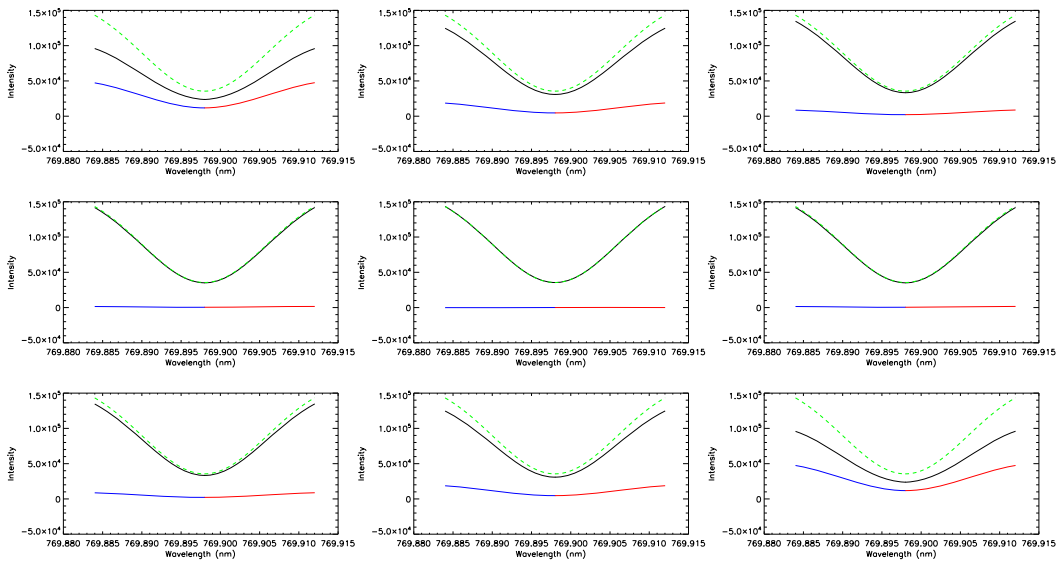

Figure 3.12: Full disk line profiles for various times through the day at the BiSON Las Campanas station on 14/01/2009. Black lines show the whole disk solar line with a referenced dashed green line not subjected to extinction. Red and blue lines show the difference between the lines with and without extinction on either side of the line. The local time from left to right then top to bottom: 06:00; 07:00; 08:00; 10:00; 12:00; 14:00; 16:00; 17:00; and 18:00.

the variation of whole disk solar line with time of day.

Figure 3.12 shows the whole disk solar absorption line shapes at different times of day for the BiSON Las Campanas station on 14/01/2009. The whole disk solar absorption lines are shown in black with a reference line without extinction displayed as a dashed green line. The blue and red lines are the difference between the green and black (atmospheric extinction) lines. The effect of extinction through the day is obvious and manifested as a reduction in intensity at the ends of each day. However, far from obvious is the action of differential extinction on the lines.

It is difficult to see the line asymmetry produced by differential extinction in figure 3.12, this effect is second order to (non-differential) extinction, and to observe it we must look more closely at the line shape. We know that differential extinction appears as a velocity signal in BiSON data but, rather than a Doppler shift of the central wavelength of the solar line, the signal is manifested as an asymmetry about the central wavelength of line. Figure 3.13 on the following page shows the modelled asymmetry (blue minus red) across

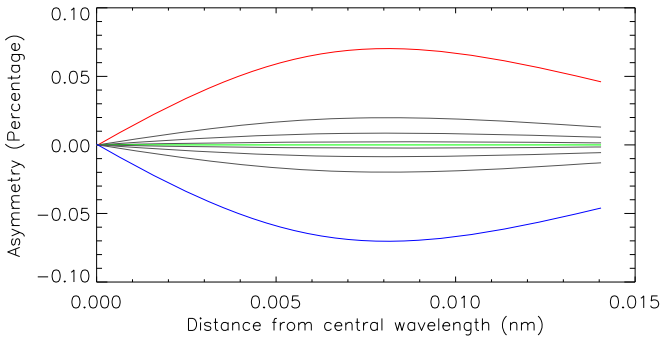

Figure 3.13: Asymmetry in full disk line for various times through the day at BiSON Las Campanas but with position angle suppressed. Variation in time (hours): 06:00 (red); 07:00; 08:00; 10:00; 12:00 (green); 14:00; 16:00; 17:00; 18:00 (blue).

the whole disk line for different times of day for the BiSON Las Campanas station on 14/01/2009. We see that the line asymmetry displays a systematic variation through the day, passing through a zero point at midday and changing signs.

Line asymmetry due to differential extinction impacts the intensities $I_{b,r}$ that BiSON instruments use to form the ratio, which is then calibrated to a velocity $v_{\rm obs}$. The calibration is defined by,

$$v_{\rm obs} = k\frac{I_b - I_r}{I_b + I_r}, \tag{3.30}$$

where k is a constant of proportionality, often referred to as the sensitivity, with typical values of 3000 $\mathrm{m\,s^{-1}}$. Assuming no variation in the denominator of the expression and that k is truly constant, then the velocity signal from differential extinction $v_{\rm de}$, is the line asymmetry ζ, multiplied by k,

$$v_{de} = k\zeta. \tag{3.31}$$

With this, the maximum asymmetry in figure 3.13 of 0.075% gives a differential extinction velocity of 2.25 $m\ s^{-1}$, which is the same order of magnitude as solar oscillations.

Figure 3.13 shows the whole disk line profile asymmetry without a contribution from position angle. So for completeness, figure 3.14 has the effects of position angle included. The position angle introduces an asymmetrical weighting, about the heliographic North/South axis, on the solar disk. The resulting asymmetry is a convolution of position angle and

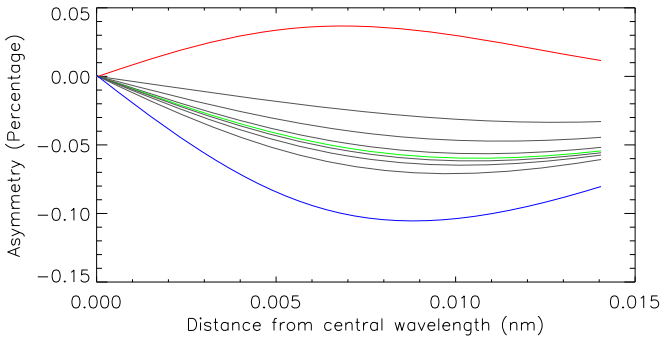

Figure 3.14: Asymmetry in full disk line for various times through the day at BiSON Las Campanas. Variation in time (hours): 06:00 (red); 07:00; 08:00; 10:00; 12:00 (green); 14:00; 16:00; 17:00; 18:00 (blue).

differential extinction. Consequently, in addition to a dependence on solar declination, the effects of differential extinction will vary throughout the year with position angle.

3.4 Instrumental weighting

We have now considered the solar line function and aspects of terrestrial atmospheric extinction pertinent to the BiSON RSS observations. Next we must consider the role of the instrumental weighting in measuring the solar radial velocity, but this is complex. To cover the required material we devote the next two chapters to the instrumental weighting, first of all describing the instrument and the scattering process, then simulating the instrumental weighting in chapter 5. Finally, we return to the model, given by equation 3.3 on page 38, in chapter 6 to generate simulated BiSON RSS data.

Chapter 4

Resonant Scattering Vapour Cells

The instrumental weighting function of a BiSON RSS, taking Sun-as-a-star radial velocity measurements, is dominated by the processes of resonant scattering that occur in the vapour cell. Because of the importance of the instrumental weighting function for simulating BiSON data, we use this chapter to set out a full description of the instrument. Starting with a description of the optical systems, we work towards a detailed presentation of resonant scattering in a magnetic field. This work forms the physical basis of the vapour cell simulation performed in the following chapter.

4.1 Geometric Description of the optical systems

In this section we describe the geometry of the optical systems with respect to the vapour cell. There are two optical systems that are dealt with independently; the primary optics that focus sunlight into the vapour cell so that a narrow wavelength band may be resonantly scattered; and the detection optics, arranged perpendicular to the primary optical axis, that collect photons that have undergone resonant scattering. Photons transported through both optical systems are counted and form the intensity measurements made by the BiSON RSS. First we consider the primary optical setup.

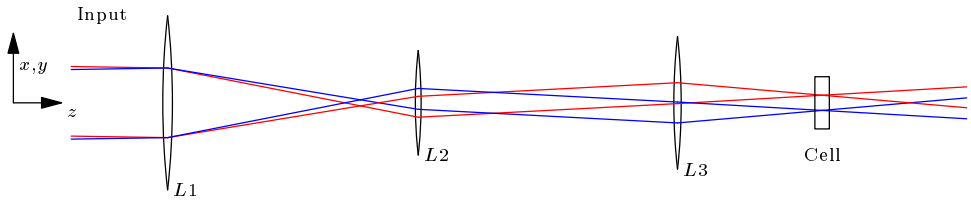

Figure 4.1: Diagram of the primary optics for a 3rd generation BiSON spectrometer.

4.1.1 Primary optical setup

The primary optics of a typical 3rd generation BiSON RSS consist of a telescope, polarisation and wavelength filters, and a resonant scattering vapour cell. Light rays entering the instrument are transported through the system to produce a twice inverted (non-inverted) image of the solar disk in the centre of the vapour cell. Light passing through the vapour cell, and with a resonant wavelength, is scattered in all directions and hence passed to the detection optics.

Figure 4.1 shows the primary optical setup to scale but magnified in the vertical axis. $L1$ is the front lens with diameter d1 = 50 mm, and a focal length f1 = 200 mm. $L2$ has a diameter d2 = 30 mm and, focal length f2 = 60 mm. These two lenses are placed so that they share a common focal plane and this creates a section of quasi-parallel light between $L2$ and $L3$ required for the optical components sensitive to off-axis angle (the Pockels cells). Finally, Lens $L3$ produces the image of the solar disk at the centre of the vapour cell. The $L3$ lens particulars are diameter d3 = 38.1 mm and focal length f3 = 150 mm.

To model the instrumental weighting we must study the scattering of photons within the cell, but this is sensitive to the geometric properties of the light path into the vapour cell. Two parameters are sufficient to specify this light path; the size of the image of the solar disk at the centre of the cell; and the solid angle of the light cone for each point in the image. Both these values can be easily calculated with knowledge of the optical setup and the angular extent of the source (the solar disk). While the angular extent of the solar disk varies slightly and systematically throughout the year, here it is considered that the full angle remains constant at one half of a degree $\theta_\odot = 0.5°$.

Image size

The size of the image of the solar disk in the centre of the BiSON RSS vapour cell is an important parameter in the simulation of an RSS [Broomhall et al., 2009b]. Using the primary optical setup described previously it is straight forward to calculate the diameter of the image from geometric optical principles. We use geometric optical principles, i.e. modelling in terms of rays, as the wavelength band width of light considered is small, and so the variation of refraction as a function of wavelength may be ignored. In addition, the paraxial approximation used is valid as off axis angles do not greatly exceed 10°, the approximate limit of validity. This geometric application is however, still a large simplification that does not consider effects due to interference, particularly diffraction. The size of the image in the common focal plane of $L1$ and $L2$, $d_{\text{image},1-2}$, is determined by the angular size of the source, in this case $\theta_\odot$, and the focal length of $L1$. Rays from the limb and centre of the solar disk, passing through the centre of $L1$, form a right angled triangle. The angle between the optic axis and the hypotenuse is half the angular extent of the source and the opposite and adjacent sides of the triangle are f1 and $0.5d_{\text{image},1-2}$ respectively. The small angle approximation of $\tan\frac{\theta_\odot}{2} = \frac{\tan\theta_\odot}{2}$ is valid giving the diameter of the image in the common focal plane of $L1$ and $L2$ as,

$$d_{\text{image},1-2} = f_1 \tan(\theta_\odot). \tag{4.1}$$

The image formed in the common focal planes of $L1$ and $L2$ is imaged into the plane orthogonal to the optical axis at the centre of the cell. The magnification from the common focal planes to the image in the cell is the ratio of the focal lengths of $L3$ and $L2$. This gives the diameter of the image in the centre of the cell as,

$$d_{\text{image,cell}} = \frac{f_1 f_3}{f_2} \tan(\theta_\odot). \tag{4.2}$$

Substituting in the values already stated gives an image with a diameter of 4.4 mm. These calculations provide a lower boundary for the true image size and to account for the geometrical nature of the calculations and imperfections in the primary optical system, a value of $\mathrm{d}_{\mathrm{image,cell}} = 5$ mm will be used in further work.

Solid angle of light into the cell

The primary optical setup places an image in good focus at the centre of the vapour cell, but away from the plane at the centre of the cell the image produced lacks focus. The solid angle of light entering the cell for a single point on the solar disk determines the dispersion of the true image at some distance away from the centre of the cell.

To calculate the solid angle of light entering the cell for a point on the solar disk, we must first define the size of the aperture at $L1$, Ξ_{L1}. The half width of the beam between $L2$ and $L3$, Ξ_{23}, is then given by,

$$\Xi_{23} = \frac{\Xi_{L1}\, f_2}{2 f_1}. \tag{4.3}$$

The value Ξ_{23} defines the opposite side of a right angled triangle with the adjacent side as the focal length of $L3$. The maximum off-axis angle in the cell θ_{cell} is then given by,

$$\theta_{\mathrm{cell}} = \tan^{-1}\left(\frac{\Xi_{L1}\, f_2}{2 f_1 f_3}\right). \tag{4.4}$$

It is common to reduce the front aperture Ξ_{L1} of BiSON instruments to reduce sensitivity to optical misalignment. A typical value for the actual aperture is $\Xi_{L1} = 30$ mm which produces a maximum off-axis angle of 0.028 rad. Converting to solid angle gives the cone as 2.46×10^{-3} sr.

While the calculations so far have avoided any discussion of diffraction it is perhaps prudent to comment on the limit of resolution. With an aperture of 50 mm, a wavelength of 770 nm, and invoking the small angle approximation, the Rayleigh criterion gives a diffraction limited angular resolution of 1.9×10^{-5} rad. For the solar disk, with angular

diameter of 8.7×10^{-3} rad, we then have a limit of around 1/460th of the solar diameter. As mentioned, in BiSON instruments the front aperture may be stopped down to as much as 30 mm, in which case the limit of resolution is 1/278th of the solar disk. Next we consider the geometry of the detector optical setup.

4.1.2 Detector optical setup

The detectors in a BiSON RSS count resonantly scattered photons propagating away from the primary optical axis. Other forms of scattering or reflection cause non-resonantly scattered light and this may be a significant source of noise. In order to maximise the ratio of resonantly scattered to non-resonantly scattered photons counted, the detectors are placed at right angles to the primary optical axis and the detectors view into the cell is limited by an aperture.

Figure 4.2 shows the optical setup for both port and starboard detectors. The lenses $L1$ and $L2$ are aspherical plano-back with a diameter of 30 mm and a focal length from the centre of 26.5 mm, this gives $f\# = 0.88$. The lenses are constructed from optical crown glass and have $n = 1.518$ at ≈ 770 nm wavelength.

Lens $L1$ is fixed in position 19 mm from the centre of the cell while $L2$ can be varied

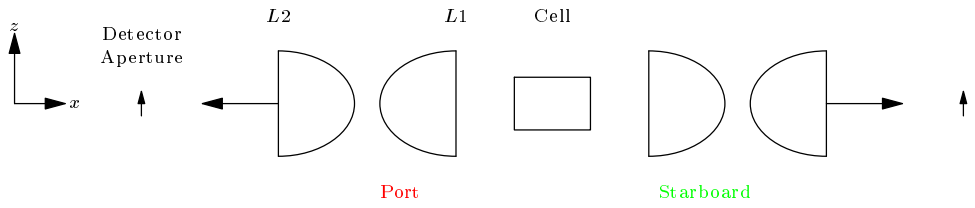

Figure 4.2: Plan view diagram of the detection optics for a 3rd generation BiSON spectrometer.

between 58 mm and 73 mm from the centre of the cell. The detector surface is placed at 81 mm from the centre of the cell and the circular aperture is of variable size ranging from 2.5 mm to 3.5 mm in radius. The radius of the aperture and position of $L2$ can be tuned for each instrument to minimise the contribution, and therefore noise, from non-

resonantly scattered light.

Non-resonantly scattered light

Non-Resonantly Scattered (NRS) photons could be a significant source of background noise in BiSON Sun-as-a-star radial-velocity measurements and hence efforts are made to minimise them. It is thought that the source of detected NRS photons is scatter from imperfections or dust on the walls of the vapour cell. To reduce the contributions from NRS light, the BiSON RSS uses an interference filter that passes light in a small band of wavelengths across the instrumental profile. As the intensity of light passing through the cell is reduced by narrowing the pass band, less non-resonant scattering occurs and the background count, with associated noise, is reduced.

In addition to the interference filter an aperture is placed over the surface of the detector to improve the signal to noise ratio. The aperture is used to mask regions of the vapour cell that contain significant amounts of NRS light. Figure 4.3 shows a composite (without normalisation) from four images of NRS light taken with a infra-red sensitive CCD from the BiSON Sutherland instrument. The intensities for each image are not continuous due to the automatic gain in the CCD, but the structure of the NRS light can be seen. The top of the image is the front of the cell and contains the majority of the NRS light. The aperture on each instrument is adjusted to maximise the resonant signal over the background noise. As a large part of the undesirable non-resonantly scattered light emanates from the front of the cell, it is clear that this volume of the cell should be masked by any aperture.

Detector optical system sensitivity

In order to simulate the BiSON RSS and its measurements of the Sun-as-a-star it is important to understand the role of the detection optical setup and its sensitivity to regions

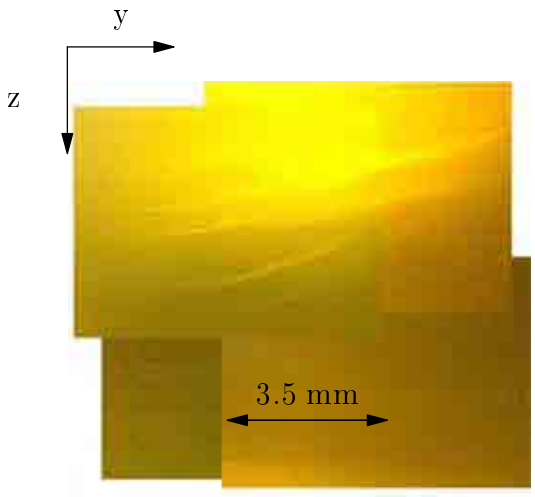

Figure 4.3: Composite images of non-resonantly scattered light for the BiSON Sutherland instrument taken in 2008 with an infra-red sensitive CCD. The front entrance of the cell is located at the top of the image (see figure 4.4 for the geometry of the observation). The majority of non-resonantly scatter light comes from the front of the cell. The scale in the focal plane, that is the zy plane at the center of the cell, is shown for reference.

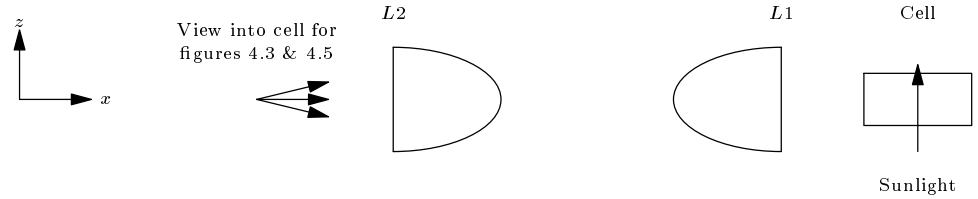

Figure 4.4: Diagram (plane view) illustrating the geometry of observation for figures 4.3 and 4.5.

of the vapour cell. To analyse the weighting in the cell produced by this detector optical setup a ray-tracing program was created.

The ray-tracing methods for a single photon in three dimensions are described fully in section 5.2.4 on page 97. Ray tracing each interaction in the detection optics system is 2D and here we consider a two dimensional xz-plane. For each point represented in the xz-plane photons are generated with systematically varying angle of propagation so that the photon crosses the diameter of the first detection lens $L1$. The photons are detected if they cross the plane of the detector within the radius of the aperture.

Figure 4.5 shows the contour map of detections from the xz-plane for different detector optics setups. The front of the cell is at the top of the map and the detector is to the right hand side. The optical setup places a greater weighting on regions of the cell, broadly

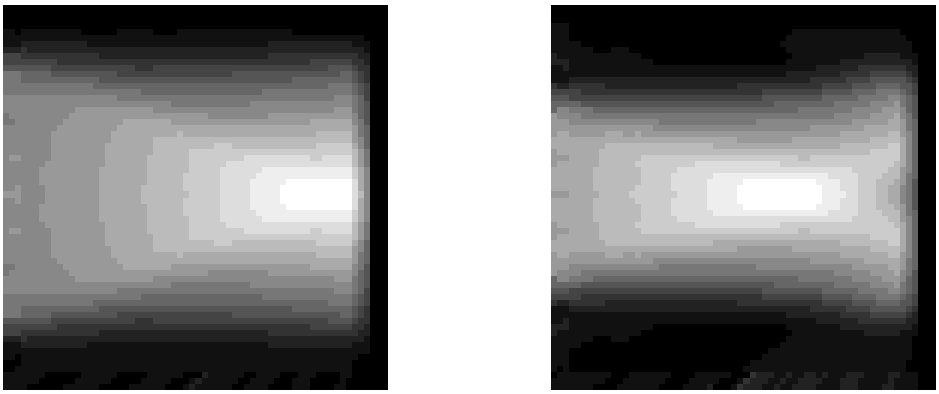

Figure 4.5: Scale maps of the detection optics weighting for a cross section of the vapour cell in the xz-plane (see figure 4.4 for the geometry of the observation). The region shown represents the full dimensions of the cell, 15 mm^2. Lens is $L2$ placed at 58 mm from the cell centre on the right hand side of the diagram. The detector has an aperture mask with radius of 3.5 mm and 2.5 mm for the left and the right plots respectively.

speaking, closer to the detector.

The weighting displayed in figure 4.5 shows that as the detector and point of scattering separation increases, the lens $L1$ presents a smaller solid angle to a particular point. This reduces the weighting of regions further from the detector. The magnitude of this effect is of course sensitive to the size of aperture placed over a detector.

In the z-direction, the aperture over the detector can be seen to minimise the weight afforded to the front and rear of the cell as required. This is expected because a point in the front or back of the cell will be completely masked if in focus at the plane of the detector but the image is outside the aperture. As the image of a point in the cell is moved out of focus so the sensitivity of the system to that point will increase.

The example weightings shown here are an important factor in how the BiSON RSS weights the image of the solar disk. In addition to the weighting from the detection optical setup there there is an optical depth effect [Broomhall et al., 2009b] that influences the instruments weighting to the solar disk. This effect is a direct result of the nature of resonant scattering and the following section sets out the physical details of resonant scattering in the vapour cell.

4.2 Resonant Scattering

As has already been discussed in Chapter 2 the BiSON RSS compares the solar absorption line with atomic transitions in the laboratory frame. The process fundamental to this technique is that of resonant scattering, sometimes called resonance radiation. Here we will discuss resonance radiation with reference to conditions in a BiSON RSS vapour cell.

4.2.1 Resonance radiation

Resonance radiation was discovered by R. W. Wood in the early part of the 20^{th} century. Much theoretical and experimental work has been carried out since then and is well described in Mitchell and Zemansky [1971]. It is established that resonant scattering occurs when the wavelength of an inbound photon matches the energy of an atomic transition. If the excited state of an atom has a short lifetime and only one lower state to de-excite into, then re-emission of a new photon, with a wavelength correlated to that of the inbound, will occur.

Experimentally, resonance radiation is produced when a broad-band continuum of light is passed through a vapour meeting the resonant scattering requirements. Scattered light over a narrow band in wavelength may be detected away from the initial light path and observations show that resonance radiation from a vapour is scattered in an isotropic manner. The explanation for such observations is obvious if we consider the excited atom as a dipole emitter with no preferential axis of alignment: emission must be isotropic. It is this property that is exploited by the RSS to transport a photon away from the optical axis to the detection optics.

Here we first consider the wavelength profile of resonantly scattered light.

4.2.2 Energy levels and line profiles

The BiSON RSS vapour cell contains potassium that is heated to around 80°C, so that vapour is placed in the path of the incoming sunlight. Figure 4.6 shows the atomic transition of potassium between the $4^2P_{\frac{1}{2}}$ and the $4^2S_{\frac{1}{2}}$ energy levels that will resonate in the BiSON RSS. The wavelength of this transition is $\lambda_c = 769.9$ nm and the lifetime of the atom in the excited state is $\tau = 2.7 \times 10^{-8}$ s. Other potassium resonant states do exist but light reaching the RSS vapour cell has been filtered to a narrow pass-band around 769.99 nm, thus suppressing detection of other lines.

The line profile of a transition is defined by the intrinsic atomic properties of the

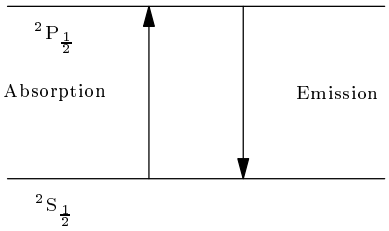

Figure 4.6: Diagram of the energy levels for potassium D1 $^2S_{\frac{1}{2}}$ to $^2P_{\frac{1}{2}}$ resonant scattering

potassium atom and the state of the scattering vapour. Within the BiSON RSS vapour cell the only independent variable is that of the vapour temperature. The vapour temperature controls the width of the line profile and the number density of the vapour. The number density of the vapour controls the optical depth and is dealt with in detail in section 4.3 on page 73. Here we concern ourselves with the width of a transition in terms of wavelength. Potassium atoms display hyperfine structure and the magnitude of this effect is determined by the quantum number for nuclear spin. The nuclear spin of the potassium atom is $I = \frac{3}{2}$ and this produces hyperfine structure with only the S or ground state significantly affected. The result is a hyperfine quartet with each component split by 88 m s^{-1} [Brookes et al., 1978]. The hyperfine splitting, natural width of 4.7 m s^{-1} and pressure broadening (less than 1 m s^{-1}) are second-order effects when compared to the Doppler width of the vapour, which is 650 m s^{-1} at a typical vapour temperature of 80°C. Therefore we will include the width of hyperfine splitting but neglect the other two effects.

Figure 4.7 shows the sum of the hyperfine quartet at the typical vapour temperature,

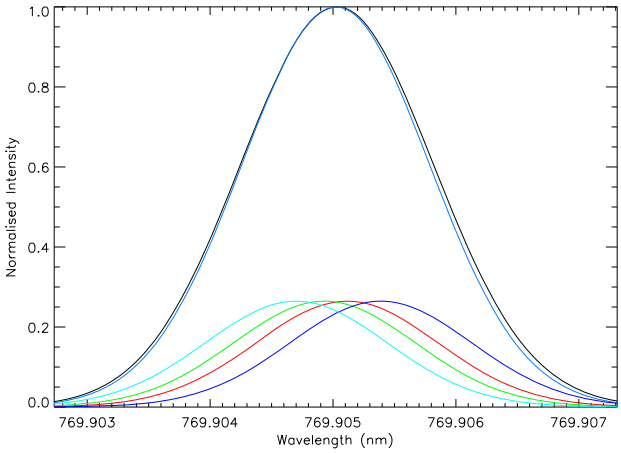

Figure 4.7: Diagram of line width with hyperfine components. The black line shows the sum of the four components. The blue line shows a Gaussian profile with FWHM of 700 ms^{-1}

80°C. The resulting line is well described by a Gaussian with a FWHM of 700 m s^{-1}. In the following work we will treat the line profile of a single resonant transition as a Gaussian with this FWHM of 700 m s^{-1}. This assumption reduces the complexity when considering the vapour under the influence of a magnetic field, described in the following section.

4.2.3 With a magnetic field

The BiSON RSS places a weak magnetic field across the potassium vapour to Zeeman split the atomic energy levels either side of the solar Fraunhofer line. This introduction of the magnetic field increases the complexity of the energy levels shown in figure 4.6 on the previous page. The Zeeman splitting of the observed spectral lines occurs because the magnetic field creates an alignment with the magnetic moment of the atom. Energy levels are then shifted creating the splitting of the resonant lines.

In the weak field approximation the external applied field is not sufficient to disrupt the coupling between orbital and spin angular moment i.e. the external applied magnetic field (0.18 T) is weaker than the potassium atoms internal magnetic field (> 2 T). The

orbital and spin angular momenta then remain coupled. In this regime, the magnitude of the shift in energy, ΔE, is given by,

$$\Delta E = m_j g_J \mu_B |\mathbf{B}|, \tag{4.5}$$

where μ_B is the Bohr magneton, g_J is the Lande g factor and m_j is the magnetic moment quantum number.

The magnetic field strength used by a typical BiSON instrument is 0.18 T, which is well within the weak field regime. For the case of the potassium D1, $^2\mathrm{P}_{\frac{1}{2}}$ to $^2\mathrm{S}_{\frac{1}{2}}$ transition, the Lande g factors are, $g_J = \frac{2}{3}$ and $g_J = 2$ respectively. For both states the magnetic quantum number may be, $m_j = \pm\frac{1}{2}$, creating a pair of doublets.

Figure 4.8 shows the shifted energy levels and subsequent splitting of the potassium

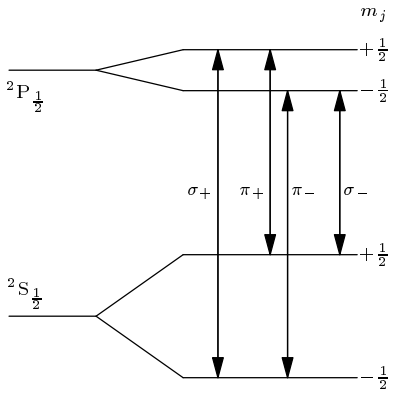

Figure 4.8: Diagram of the energy levels for potassium RSS resonant scattering with magnetic field.

atomic transitions. The components of the quartet of transitions are commonly labelled as π and σ. The labels are defined by the change in the magnetic moment quantum number with π transitions having $\Delta m_j = 0$ and σ transitions having $\Delta m_j = \pm 1$. Each transition occurs within a line profile at a well defined wavelength, but for a transition to be allowed the dipole selection rules must be satisfied.

The BiSON RSS uses a longitudinal magnetic field with respect to the incoming light. This, by design eliminates absorption taking place by a π transition because the selection rules of dipole radiation require that $\Delta m_j = 0, \pm 1$. In the transverse magnetic field

configuration all the Zeeman components are allowed transitions. However, in the longitudinal configuration, $\Delta m_j = 0$ components are polarised parallel to the magnetic field and absorption is forbidden. The two σ components remain as the two allowed transitions in the longitudinal configuration. The BiSON RSS selects only one of the σ components by the polarisation of the incoming light.

Inhomogeneity in the magnetic field adds complication to the scattering profile. In the case of a variation in the longitudinal field strength, the scattering profile is pulled and widened in the direction of the filed strength change. Measurements of the magnetic filed along the longitudinal length of the cell show the variation to be of order a few percent (private communication B. Miller). In the case of the introduction of a transverse component, the scattering profile must now include a contribution from the π component. However, a large angle away from the longitudinal axis is required before the π component is significant, because the scattering profile is sensitive to the sine of the transverse angle.

The probability of a scattering event as a photon passes through the vapour cell is determined by the optical depth. The following section works towards defining the term instrumental optical depth and showing its associated temperature dependence. This sets the platform enabling us to describe the path of a photon through the vapour cell in section 4.4 on page 77.

4.3 Instrumental Optical Depth

Now we go on to discuss the instrument at a macroscopic level, considering the optical depth of the vapour cell. This section will set out the wavelength and temperature dependence of optical depth in the vapour cell. We will show that it is too simplistic to describe the "optical depth" of the cell because a different absorption coefficient is presented across the instrumental line profile. To improve the description of the cell we introduce the term Instrumental Optical Depth(IOD), this is briefly defined as the optical

depth at the central wavelength of the resonant line profile.

4.3.1 Monochromatic optical depth

Let us start by considering monochromatic light passing through an opaque absorbing medium. The optical depth, τ_λ, is defined by the exponential reduction in the ratio of the incident and transmitted intensities through this medium

$$\frac{I}{I_0} = e^{-\tau_\lambda}. \tag{4.6}$$

The optical depth is dependent on the number density, n, of the scattering particles multiplied by the scattering cross section, σ_λ, integrated over the optical path, s, i.e.

$$\tau_\lambda = \int n\sigma_\lambda \, ds. \tag{4.7}$$

The dependence of optical depth on path length can cause confusion and a more natural parameter is the absorption coefficient, κ_λ, defined more simply by the number density multiplied by the scattering cross section

$$\kappa_\lambda = n\sigma_\lambda. \tag{4.8}$$

The state of the vapour within the cell is considered as homogeneous so the number density and scattering cross section are constant over the path taken by a photon. This allows us to compare the optical depth and absorption coefficient

$$\tau_\lambda = n\sigma_\lambda s = \kappa_\lambda s, \tag{4.9}$$

showing that the monochromatic optical depth is the absorption coefficient multiplied by the path through the absorbing medium, in this case the length of the cell.

The absorption coefficient is comprised of two terms, the number density and the scattering cross section, if both are known then the monochromatic optical depth of the cell can be calculated. We start with the number density.

4.3.2 Number Density

The BiSON RSS vapour cell contains potassium vapour which will be treated as an ideal gas under normal operating pressures, i.e. interactions between particles may be neglected. The number density of the potassium vapour can then be calculated from the familiar ideal gas law

$$pV = NkT, \tag{4.10}$$

where p is the pressure, V is the volume, N is the number of molecules, k is Boltzmann's constant, and T is the temperature of the gas.

Expressing the number density n and pressure p as a function of the temperature gives

$$n(T) = \frac{p(T)}{kT}. \tag{4.11}$$

The vapour pressure of potassium at temperatures lower than 500 K has been determined by fitting to a selection of results taken from Hicks [1962]. The selected model shows an exponential change in vapour pressure across the temperature range required, i.e.,

$$p_{\text{vapour}}(T) = 10^{-5} e^{0.085(T-312)} \text{ Pa}. \tag{4.12}$$

The number density is a function of temperature but independent of wavelength. The scattering cross section is a function of both temperature and wavelength and we consider this next.

4.3.3 Scattering Cross Section

The scattering cross section is the area of interaction presented to photons by the potassium atoms and for resonant scattering is dependent on both the vapour temperature and the photon wavelength. The temperature dependence derives from simple Doppler arguments while the wavelength dependence is introduced by the absorption line profile from Boltzmann concepts. From Mitchell and Zemansky [1971] the resonant scattering cross section $\sigma(\lambda, T)$ is given by

$$\sigma(\lambda, T) = \frac{2}{\Delta v_{\mathrm{D}}(T)} \sqrt{\frac{ln\ 2}{\pi}} \frac{\lambda_0^2\ g_2}{8\pi\ g_1} A_{2,1} \phi(\lambda), \tag{4.13}$$

where g_1 and g_2 are the degeneracy of the $^2P_{\frac{1}{2}}$and $^2S_{\frac{1}{2}}$energy levels respectively, A_{21} is the Einstein A coefficient, $\Delta v_{\mathrm{D}}(T)$ is the Doppler width of the vapour and $\phi(\lambda)$ is the resonant scattering line shape.

The resonant line shapes are the Zeeman components considered in the previous section. Doppler broadening dominates the width of the scattering line as shown in section 4.2.1 on page 69 and so $\phi(\lambda)$ can be treated as a Gaussian profile with FWHM of 700 m s^{-1}. The Doppler width is given by

$$\Delta v_{\mathrm{D}}(T) = \lambda_0 \sqrt{\frac{2kT}{m_0}}, \tag{4.14}$$

where m_0 is the atomic mass divided by Avogadro's constant.

4.3.4 A new definition: IOD

From the arguments of equations 4.13 and 4.11, the scattering cross section and number density, and so the optical depth, are functions of both vapour temperature and wavelength. When describing the vapour cell it is straightforward to refer to the temperature of the vapour. However, the wavelengths of light entering the cell are spread over a narrow pass-band determined by the interference filter. To refer to a single optical depth of the

cell becomes too simplistic and even confusing.

For the sake of clarity we introduce a new term: the Instrumental Optical Depth (IOD). The IOD is defined as the optical depth at the centre of the resonant transition line profile where $\phi(\lambda) = 1.0$. This choice means that the IOD is the maximum optical depth that a photon "sees" on entering the cell, but obviously the vast majority of photons will have a much lower optical depth presented to them than that of the IOD. The IOD is simply described by

$$\mathrm{IOD(T)} = \mathrm{n(T)}\sigma(\mathrm{T})|_{\phi(\lambda)=1}\mathrm{s}, \tag{4.15}$$

and is now only a function of vapour temperature.

The work in this chapter so far has described the optical components outside of the vapour cell, the scattering process within the cell and the IOD that provides a description of the state of the cell. We must now focus on the path that photons take to propagate through the cell. In the following section we set up a Zeeman absorption matrix in Stokes parameter space. This allows for the description of the absorption in terms of the polarisation and orientation with respect to the magnetic field. We will show that the Zeeman absorption matrix can determine the absorption and emission probabilities for light with a given wavelength, polarisation and axis of propagation through a cell with a known IOD.

4.4 The path of a photon through the cell

The simulation of the vapour cell within a BiSON RSS requires knowledge of the path taken by photons passing through the cell. Analogous to a random walk, the distance between interactions and the angle of resonant scatterings determine this path. The distance between interactions is determined by the optical depth of the potassium vapour. The distributions for angle of scattering can be determined by considering the potassium atoms as dipole oscillators rotating in a magnetic field. We start by defining the co-ordinate system.

4.4.1 Definition of axis

The angular components of spherical polar coordinates are defined in opposite ways by physicists and mathematicians, making a statement of definition prior to use necessary. Figure 4.9 shows the adopted definition - the physicists convention - in this work. Any point may be described by r the distance from the origin, θ the angle formed with respect to the z-axis, and ϕ the angle formed with respect to the x-axis. Having defined the

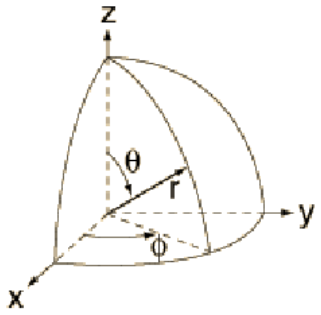

Figure 4.9: Chosen definition of spherical polar coordinates with a point described by the distance from the origin, θ the angle formed with respect to the z-axis, and ϕ formed with respect to the x-axis.

coordinate system we may move forward by considering the properties of Zeeman resonant scattering.

4.4.2 Properties of Zeeman Resonant Scattering

The resonant scattering of light in a magnetic field has been tackled already in radiative transfer theory and work heavily taken from Rees et al. [1989] will be presented here. The approach by Rees et al. [1989] is to setup a transfer equation for the Stokes vector, $\mathbf{I}$, to compare with polarimetric measurements

$$\frac{d\mathbf{I}}{dz} = -\mathbf{K}\mathbf{I} + \mathbf{j}, \tag{4.16}$$

where $\mathbf{K}$ is the total absorption matrix and $\mathbf{j}$ is the emission vector.

Stokes parameters: definition

Before tackling the application of work by Rees et al. [1989] we should start by defining what we mean by Stokes parameters. Stokes parameters provide a convenient mathematical description of the polarisation state of electromagnetic radiation. Light can be considered as a transverse wave, that is oscillations of the electric field occur perpendicular to its velocity, and the plane of this oscillation is referred to as the polarisation. And so, Stokes parameters describe the electric field in the plane of oscillation.

There are a number of ways for prescribing Stokes parameters and these vary in both nomenclature and definition, although differences rarely exceed some form of normalisation. For this reason we will take the time to write out each parameter explicitly in terms of the contribution of the electric field in the transverse directions, these being E_x and E_y if propagation is considered to be in the z-direction, and the relative phase δ of E_y with respect to E_x. We define the Stokes parameters as

$$I = \langle E_x^2 \rangle + \langle E_y^2 \rangle \tag{4.17}$$

$$Q = \langle E_x^2 \rangle - \langle E_y^2 \rangle \tag{4.18}$$

$$U = 2 \langle E_x E_y \rangle \cos \delta \tag{4.19}$$

$$V = 2 \langle E_x E_y \rangle \sin \delta, \tag{4.20}$$

where $\langle ... \rangle$ indicates the mean value over time.

Each of the Stokes parameters describes an aspect of a beam of light: the total intensity of the beam, I; the degree of linear polarisation parallel to the x-axis, Q; the degree of linear polarisation at 45° to the x-axis, U; and the degree of circular polarisation for a clockwise rotation of the electric field in a given plane when looking towards the source, defined here as right-hand circularly polarised. It is straight forward to present Stokes parameters for common states of fully polarised beams, as detailed in table 4.1. Finally for ease of presentation is it common to find Stokes parameters displayed as the "Stokes

	Q/I	U/I	V/I
linear parallel to x	1	0	0
linear parallel to y	-1	0	0
linear 45° to x	0	1	0
linear $-45°$ to x	0	-1	0
right-handed circular	0	0	1
left-handed circular	0	0	-1
unpolarised	0	0	0

Table 4.1: Stokes parameters for common states of fully polarised beams of light.

vector" $\mathbf{S}$ such that

$$\mathbf{S} = \begin{pmatrix} I \\ Q \\ U \\ V \end{pmatrix}. \tag{4.21}$$

The strength of Stokes parameters comes from the ability to describe all possible states of polarisation from unpolarised, through partially polarised, to fully polarised. We now continue to apply the radiative transfer work by Rees et al. [1989].

Zeeman absorption matrix

While Rees concerned himself with multiple types of scattering and subsequent emission, here we restrict our discussion to just resonant scattering. The resonant scattering Zeeman line absorption matrix Φ is just one component of $\mathbf{K}$ in radiative transfer theory and is given as

$$\Phi = \begin{pmatrix} \phi_I & \phi_Q & \phi_U & \phi_V \\ \phi_Q & \phi_I & \phi'_V & -\phi'_U \\ \phi_U & -\phi'_V & \phi_I & \phi'_Q \\ \phi_V & \phi'_U & -\phi'_Q & \phi_I \end{pmatrix}, \tag{4.22}$$

where ϕ and ϕ' are the line absorption and emission profiles in wavelength and the subscripts refer to the defined Stokes parameters. The individual terms are given by Rees for generalised anomalous Zeeman splitting if the following conditions are met: transi-

tions are electric dipole in nature; emission is treated as negative absorption; photons are completely redistributed on scattering; and the vapour is homogeneous. All these requirements are expected to be satisfied for potassium vapour in a BiSON RSS cell. Taking the specific case of the $4^2S_{\frac{1}{2}}$ to $4^2P_{\frac{1}{2}}$ potassium doublets, Rees formulae can be used to give the constituent terms of the absorption matrix

$$\phi_I = \frac{1}{2}\left(\phi_{\pi^+} + \phi_{\pi^-}\right)\sin^2\theta + \frac{1}{4}\left(\phi_{\sigma^+} + \phi_{\sigma^-}\right)\left(1 + \cos^2\theta\right) \tag{4.23}$$

$$\begin{aligned}
\phi_Q &= \frac{1}{2}\left[\left(\phi_{\pi^+} + \phi_{\pi^-}\right) - \frac{1}{2}\left(\phi_{\sigma^+} + \phi_{\sigma^-}\right)\right]\sin^2\theta\cos\ 2\phi & (4.24)\\
\phi_U &= \frac{1}{2}\left[\left(\phi_{\pi^+} + \phi_{\pi^-}\right) - \frac{1}{2}\left(\phi_{\sigma^+} + \phi_{\sigma^-}\right)\right]\sin^2\theta\sin\ 2\phi & (4.25)\\
\phi_V &= \frac{1}{2}\left(\phi_{\sigma^+} + \phi_{\sigma^-}\right)\cos\ \theta & (4.26)\\
\phi'_Q &= \frac{1}{2}\left[\left(\phi'_{\pi^+} + \phi'_{\pi^-}\right) - \frac{1}{2}\left(\phi'_{\sigma^+} + \phi'_{\sigma^-}\right)\right]\sin^2\theta\cos\ 2\phi & (4.27)\\
\phi'_U &= \frac{1}{2}\left[\left(\phi'_{\pi^+} + \phi'_{\pi^-}\right) - \frac{1}{2}\left(\phi'_{\sigma^+} + \phi'_{\sigma^-}\right)\right]\sin^2\theta\sin\ 2\phi & (4.28)\\
\phi'_V &= \frac{1}{2}\left(\phi'_{\sigma^+} + \phi'_{\sigma^-}\right)\cos\ \theta. & (4.29)
\end{aligned}$$

By definition the absorption and emission terms have the same form but are dependent on the absorption or emission profiles and direction of travel. In fact the absorption and emission profiles will differ due to Faraday rotation (rotation of the plane of polarisation is scrambled during absorption and subsequent emission). In further work we will ignore the impact of Faraday rotation, primarily because it is a second order effect but also because its inclusion is computationally difficult to achieve.

The Zeeman absorption matrix acts in a similar manner to a Mueller matrix but with a difference. Mueller matrices are used to describe optical components and their influence on polarised light. A Mueller matrix combined with matrix for incoming light will return the Stokes parameters of the light exiting the optical component. Here the Zeeman absorption matrix, when supplied with incoming light, will return the change in light passing through

the cell. This allows us to investigate the action of the cell on different polarisation states of light.

Polarisation

The BiSON RSS directs inbound circularly polarised light through the vapour cell in a longitudinal magnetic field. This circularly polarised light can be represented by the Stokes parameters

$$RHC = \begin{pmatrix} 1 \\ 0 \\ 0 \\ 1 \end{pmatrix}, \tag{4.30}$$

for right handedness and

$$LHC = \begin{pmatrix} 1 \\ 0 \\ 0 \\ -1 \end{pmatrix}, \tag{4.31}$$

for left handedness. The Stokes parameters of the transmitted light $\mathbf{I}_{\text{trans}}$ can be calculated from

$$\mathbf{I} - \frac{d\mathbf{I}}{dz} = \mathbf{I}_{\text{trans}}, \tag{4.32}$$

where the vapour can be represented by the resonant scattering Zeeman absorption matrix. Assuming a high opacity $\tau_\lambda >> 1$, and no emission $\phi'_{\text{j}} = 0$, the change in the Stokes vector $\mathbf{I}$, can be represented by

$$\frac{d\mathbf{I}}{dz} = \mathbf{\Phi I}. \tag{4.33}$$

Hence the we may calculate the change in the Stokes parameters for light resonantly scattered while passing through a BiSON RSS vapour cell

$$\begin{pmatrix} \phi_{dI} \\ \phi_{dQ} \\ \phi_{dU} \\ \phi_{dV} \end{pmatrix} = \begin{pmatrix} \phi_I & \phi_Q & \phi_U & \phi_V \\ \phi_Q & \phi_I & \phi'_V & -\phi'_U \\ \phi_U & -\phi'_V & \phi_I & \phi'_Q \\ \phi_V & \phi'_U & -\phi'_Q & \phi_I \end{pmatrix} . \begin{pmatrix} I \\ Q \\ U \\ V \end{pmatrix} . \tag{4.34}$$

Consistent definition of the Stokes parameter V is required to exploit the above notation Clarke [1974]. The common definition has the V parameter greater than zero for σ_+ and for σ_- the parameter must be less than zero. Using this to evaluate the previous expression for right hand circular polarisation and at the incident angle $\theta = 0$ gives

$$\begin{pmatrix} \phi_{\sigma^+} \\ 0 \\ 0 \\ \phi_{\sigma^+} \end{pmatrix} . = \begin{pmatrix} \phi_I & \phi_Q & \phi_U & \phi_V \\ \phi_Q & \phi_I & \phi'_V & -\phi'_U \\ \phi_U & -\phi'_V & \phi_I & \phi'_Q \\ \phi_V & \phi'_U & -\phi'_Q & \phi_I \end{pmatrix} . \begin{pmatrix} 1 \\ 0 \\ 0 \\ 1 \end{pmatrix} , \tag{4.35}$$

and for left hand circularly polarised light

$$\begin{pmatrix} \phi_{\sigma^-} \\ 0 \\ 0 \\ -\phi_{\sigma^-} \end{pmatrix} . = \begin{pmatrix} \phi_I & \phi_Q & \phi_U & -\phi_V \\ \phi_Q & \phi_I & -\phi'_V & -\phi'_U \\ \phi_U & \phi'_V & \phi_I & \phi'_Q \\ -\phi_V & \phi'_U & -\phi'_Q & \phi_I \end{pmatrix} . \begin{pmatrix} 1 \\ 0 \\ 0 \\ -1 \end{pmatrix} . \tag{4.36}$$

The calculations show the change in the Stokes parameters will be equal to the Stokes parameters of the input light. This means that at high optical depths, circularly polarised light is fully absorbed when incident along the magnetic field lines.

Of course the equations can be used to tackle any set of absorption parameters, or even emission parameters as the process is by design commutative. Figure 4.10 shows the angular dependence of each of the Stokes terms in $\phi - \theta$ space.

When modelling the BiSON RSS vapour cell we must know the wavelength, polarisation

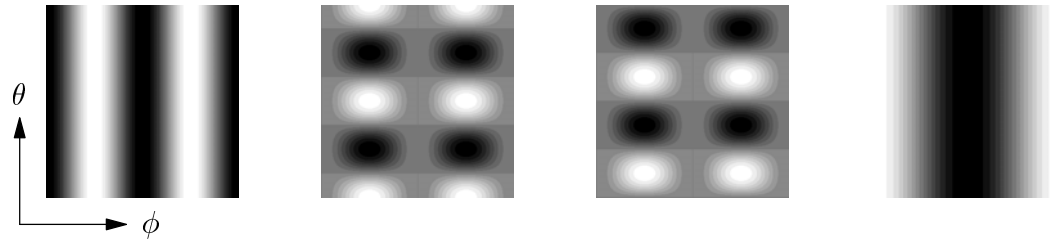

Figure 4.10: Images of the Stokes terms in $\phi - \theta$ space. Left to right: ϕ_I; ϕ_Q; ϕ_U; ϕ_V.

and direction of travel of photons to determine the probability of absorption in conjunction with IOD. Having dealt with polarisation we move on to consider the angular dependence of each transition.

4.4.3 Angular Dependence

In the absence of a magnetic field, resonantly scattered light emission is isotropic. This isotropy must be maintained over all the Zeeman transitions, but allows for anisotropic absorption and emission for an individual line. These effects can be investigated using the Zeeman absorption matrix terms.

From equation 4.23 we can isolate the angular dependency ψ of the π and σ components. We have

$$\psi_\pi = \frac{1}{2}\left(\phi_{\pi^+} + \phi_{\pi^-}\right)\sin^2\theta, \tag{4.37}$$

and

$$\psi_\sigma = \frac{1}{4}\left(\phi_{\sigma^+} + \phi_{\sigma^-}\right)\left(1 + \cos^2\theta\right). \tag{4.38}$$

The relative strengths of the lines are given in Mitchell and Zemansky [1971] and quoted as $40:20$ in the transverse direction, for the σ and π lines respectively. Again using equation 4.23 we can apply the line strengths in this direction, i.e. $\theta = 90°$. This gives

$$\phi_I = \frac{20}{2}\left(\phi_{\pi^+} + \phi_{\pi^-}\right) + \frac{40}{4}\left(\phi_{\sigma^+} + \phi_{\sigma^-}\right), \tag{4.39}$$

and shows that the components are of equal strength in the transverse direction. This is consistent with Kuhn [1962] who uses the correspondence principle to show the "equality of all four components in the transverse direction."

Figure 4.11 shows the angular distribution of the σ and π components and confirms

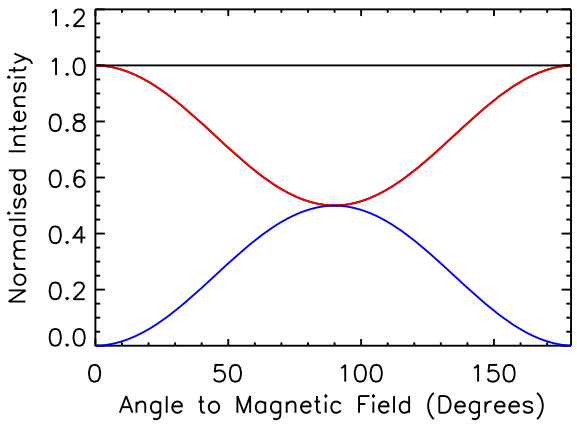

Figure 4.11: Resonant scattering angular profiles in a magnetic field. The red line represents the σ components and the blue line the π. The black line is the sum of both components showing isotropy.

their sum is isotropic as expected. The total probability of emission by either a σ or π transition can be found by integrating over θ for both components. Over all angles three times as many σ transitions as π will occur.

We have completed the required description of the instrument and the resonant scattering process, in the next chapter we implement the physics described here in a simulation of the instrument.

Chapter 5

Modelling multiple scattering

In the previous chapter we discussed the process of Zeeman split resonance radiation in a vapour. We now proceed to apply these concepts in the context of a Resonant Scattering Spectrometer (RSS) used to make radial velocity measurements of the Sun as a star. We will see that the Instrumental Optical Depth (IOD) is an important consideration in constructing a model of an RSS. Furthermore, as it is almost impossible to fully model the performance of an RSS, we show that Monte Carlo simulations are an effective method of determining the system response.

We start with a brief review of previous approaches to the problem, before motivating the need for the Monte Carlo methods including multiple (rather than single) scattering and finally present the results from the simulations. We find that the classical view of an optical depth of unity for optimal observations is flawed and show that an IOD of no less than two is advantageous.

5.1 Introduction

Optical depth in an RSS vapour cell is a well studied subject, so why should we reconsider this work? One reason is that in the context of an RSS there is inconsistency and ambiguity in the definition of optimal optical depth. We assert that the term "optimal" refers to the conditions which give the largest number of resonantly scattered photons

detected and take this as a working definition. The use of the term "optical depth" in previous work will be considered and compared to instrumental optical depth.

We will proceed by considering three different approaches to the problem which have been taken in the past: an optimal optical depth of unity; the Hoyng theoretical method; and the Broomhall empirical work on Doppler imaging. We will adjust reported values in these three works to conform to a consistent definition. We will highlight the shortcomings of the previous approaches and so make the case for a full treatment including multiple scattering.

5.1.1 Optical depth of unity

The optimal optical depth of a vapour cell in an RSS is commonly stated as having a value of unity (Boumier [1991], Chaplin [1993]), the canonical value. Why is this view so prevalent and what is its impact on vapour cell modelling? An assumption underpinning a value of unity for optical depth is that detected photons have been scattered only once. When constructing a model for the GOLF RSS, Boumier [1991] states that the optimal optical depth for the vapour cell is unity. Boumier cites Mitchell and Zemansky [1971] and private communication with H. B. van der Raay as evidence that multiple scattering in the vapour cell is negligible. The usual argument is that there should be a balance between a maximum of photons scattered into a detector and a low chance of multiple scattering. The balance point of the two opposing processes is assumed to be an optical depth of unity. But is this true?

To examine the importance of secondary scattering, we consider a cube vapour cell with an optical depth of unity and light scattered and re-emitted at the cell centre. The optical path towards a detector will then be half the length of the cell and so the optical depth seen by any photon is simply one half. We can use the equation for a beam of light with intensity I, passing through an absorbing medium with optical depth τ, and initial intensity I_0 to calculate the ratio of intensities of the passed and initial beam. Substituting

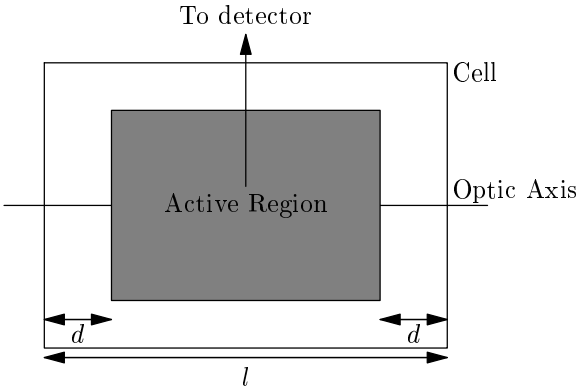

Figure 5.1: Diagram of Hoyng active region

in numbers gives

$$\frac{I}{I_0} = e^{-\tau} = e^{-0.5} = 0.61. \tag{5.1}$$

Consequently, nearly 40% of the incident photons will undergo a subsequent interaction or in other words, secondary scattering. But this calculation says nothing about the optimal optical depth which is an issue that we will explore.

5.1.2 The Hoyng Approach

Hoyng [1989] took a theoretical approach to modelling the problem of optimal optical depth in an RSS vapour cell. His work required the optimal optical depth as a parameter to estimate the noise contribution from variations in vapour temperature. Hoyng constructed an "active region" and treated the vapour as an absorbing medium. First we consider the active region. Hoyng assumed that scattered light reaching a detector originated from an "active region" in the vapour cell. This active region is controlled by the configuration of the detection optics (see section 4.1.2 on page 66). The region is assumed to be formed as a box in the centre of the cell with distance d between the front of the active region and front of the cell, and the same for the back. The total internal length of the cell is given as l. Figure 5.1 shows the Hoyng vapour cell geometry.

Having defined an active region of the cell, Hoyng proceeded by considering the fraction f of the beam absorbed in the active volume. The absorption in the active region can be

calculated as the beam intensity at the front of the active region, less the intensity at the back of the active region and gives

$$f = e^{-\kappa d}\left(1 - e^{-\kappa(l-2d)}\right) = e^{-\kappa d} - e^{-\kappa(l-d)}. \tag{5.2}$$

The point of optimal optical depth is a balance of a high enough optical depth that sufficient light is absorbed, but not so high that a large component of the scattering occurs before light reaches the active region. The optimal absorption coefficient $\kappa_{\rm opt}$, is then a (maximum) turning point of equation 5.2 i.e. $\frac{\delta \rm f}{\delta \kappa} = 0$. Differentiating and rearranging for $\kappa_{\rm opt}$ gives

$$\kappa_{\rm opt} = \frac{1}{l-2d}\log\left(\frac{l-d}{d}\right). \tag{5.3}$$

By using typical values for a BiSON spectrometer of $d = 4.0$ mm and $l = 15.0$ mm, we find that the optimal conditions are $\kappa_{\rm opt} = 0.144$ or equivalently an optical depth $\tau_{\rm opt} = 2.17$. We have seen that for optical depth greater than unity multiple scattering should be considered. There is another consideration, which is the variation of absorption coefficient with wavelength (equation 4.13 on page 76). Photons with wavelengths in the wings of the scattering line profile are subjected to a smaller scattering cross-section than those at the centre. If we were to modify the Hoyng approach to include the line profile we would find the resulting optimum IOD to be greater than 3. Therefore, not only is it sensible to consider multiple scattering but any model should be multiwavelength.

5.1.3 The Broomhall approach

Work carried out by Broomhall et al. [2009b] (from here on Broomhall) used the optical depth in the vapour cell as a parameter to estimate the RSS instrumental weighting (a new aspect of "Doppler imaging") in Sun-as-a-star observations. Constraints on the working optical depth were found to exist in the simultaneous - but subtly different - observations made by the two detectors in a single BiSON RSS.

The non-homogeneous response of the RSS across the solar disk, studied by Broomhall, is known as Doppler imaging. Solar contributions to this effect, rotation and limb darkening, had been well documented [Brookes et al., 1978] but Broomhall described an instrumental effect that was dependent on the image of the solar disk and the optical depth in the cell. This effect forms from the sensitivity of a detector that is influenced by its distance from the point on the solar image z due to the optical depth, where

$$\frac{I}{I_0} = e^{-\tau} = e^{-\kappa z}. \tag{5.4}$$

The asymmetry in the solar disk due to rotation and the instrumental weighting effect combine so that the BiSON port and starboard detectors make different observations. Hence, the two observations can be used to constrain the working value of optical depth. The value reported by Broomhall for working optical depth considered only half the length of the vapour cell. So as we can make comparison with the Hoyng work and IOD, we must double the reported result for Broomhall. In addition, Broomhall demonstrates that the reported value is sensitive to the size of the image at the centre of the vapour cell formed by the primary optics. Broomhall works consistently with an image of diameter 10 mm, but we have shown in section 4.1.1 on page 63 that the diameter for BiSON instruments is nearer 5 mm. For the corrected image size, Broomhall reports a working optical depth of 1.15, which is equivalent to $\tau = 2.3$ over the full length of the cell.

We see that the Broomhall approach is in agreement with Hoyng, which is convincing as they are testing two, quite different, concepts. However, both have common assumptions. Both ignore the changing optical depth over the scattering line profile and both treat detected photons as scattering only once. We have seen that when including the line profile the value of optimal IOD will be increased, which in turn will increase the significance of multiple scattering. Increasing multiple scattering will have the added consequence of diffusing the instrumental weighting from Doppler imaging. Therefore, it is necessary to conduct a full treatment of the system to establish the true instrumental weighting.

5.2 A Monte Carlo approach

The Monte Carlo method is a device for studying stochastic models of a physical process, in this instance a photon travelling through a vapour. The path of this photon, through the scattering medium, is simulated by 'rolling dice' (dice with many more than six sides) to determine distance and direction, absorption, and emission parameters. By repeatedly determining the path of photons through the cell, the Monte Carlo method estimates the probability that a photon, with given initial conditions, will strike a detector in an RSS. These probabilities will be used to assess the instrumental weighting over position on the solar disk and wavelength.

The transportation of photons through a scattering layer of vapour is a radiative transfer problem, particularly analogous to radiative transfer in stellar atmospheres. Monte Carlo techniques have been used for radiative transfer before (see [House and Avery, 1969] for a general but dated review). Work on radiative transfer problems has moved away from the Monte Carlo method, given development of more sophisticated numerical techniques, but in the application of the RSS, with inhomogeneous weighting from detection optics, these new techniques do not apply. In fact, the Monte Carlo method is ideal for the simulation of an RSS.

Simulation of resonant scattering, here in an RSS, using Monte Carlo methods can be described using a widely used scheme from Avery and House [1968]. To initialise the simulation, a system of coordinates, boundary's and optical components are defined to describe the RSS, and the physics of resonant scattering and the optical systems must be constructed in a probabilistic way. The method considers a single photon released to the system which is forced to traverse the cell, its motion being governed by the underlying physics sampled by quasi-random number distributions. On escaping the system the properties of the photon are recorded and assessed for detection. The release of photons continues until the statistics on the probabilities of detection are considered adequate.

5.2.1 Initialisation

Initialisation describes the state of the instrument to be used by the Monte Carlo method. Parameters that influence the propagation of a photon from the point of entry to the point of exit must be set. There are three main systems that transport photons; the primary optics that introduce a photon to the cell; the vapour in the cell that resonantly scatters photons; and the detection optics that forward a photon to the detector.

The primary optics define the range of paths a photon may take when entering the vapour cell. The parameters to be supplied to the simulation are the position of the image of a point source in the vapour cell and the maximum off-axis angle in this image. The position of the image in the cell is determined by the magnification of the primary optics. Section 4.1.1 on page 62 considered the mapping of the image of the solar disk to the image in the vapour cell, finding the image to be in the centre of the cell and have diameter $d_{\text{image,cell}} = 5$ mm. This image is inverted twice meaning that any normalised coordinate system defined on the solar disk maps $1:1$ to the image in the centre of the cell. The image in the cell is created by lens $L3$ and this defines a maximum off-axis angle of 0.028 rad. However, the off-axis angle of any individual photon is determined as a source variable, as discussed in further on in section 5.2.2. The vapour cell is described by its geometry, IOD, and the wavelength profile of the resonant potassium transition. The basic physics behind this have been discussed extensively in chapter 4, and here we will only mention a few points on application. The geometry of the vapour cell is a cube with side length of 15 mm; there will be no treatment of the stem of the vapour cell. The IOD is determined by the temperature of the vapour. And finally, the transition line profile shape is set by the underlying physics while the magnetic field determines the central wavelength of the line.

The alignment of the detection optics determines the sensitivity of the instrument to regions of the cell (see section 4.1.2 on page 66). The position of detection lens $DL2$ and the size of the aperture over the detector are variables to be set in initialisation, on top of the standard definition of the component position. Having discussed the initialisation

of the instrument we continue to discuss the parameters of the photons supplied to the system.

5.2.2 Source parameters

The parameters of a source photon must be set before it is is released to propagate through the system. Our aim for this simulation is to characterise the instrument in a way that can be integrated into the models proposed in chapter 3. If we consider the approach that would be taken with a real instrument in a laboratory, it would be ideal to present a monochromatic, circularly polarised, point source and scan through wavelength and position of source. Hence, we will follow the same approach in this simulation and so the source parameters are wavelength, polarisation, and position.

As we have defined above, wavelength is a user input into the Monte Carlo simulation (it is not determined stochastically), but the process must be repeated to cover a suitable energy range. The wavelength is important because it is combined with the IOD to produce the optical depth a photon sees when entering the cell. From earlier definitions, initial optical depth τ_i is given by,

$$\tau_i = \text{IOD} \times \phi(\lambda), \tag{5.5}$$

where $\phi(\lambda)$ is the line profile with possible values ranging from 0 to 1.

The position of an ideal point source determines the path of light through the primary optics, and hence the initial path through the vapour cell. Because the image of a point source is inverted twice through the primary optics, the position of the source maps directly to the position in the cell. The possible paths of light, from the last lens in the primary optical setup to the vapour cell, are bounded by a cone with a maximum off-axis angle of 0.028 rad defined in section 4.1.1 on page 64.

A path for each photon must be selected randomly from the distribution of off-axis angles.

A point source (or even a point on the solar disk) will emit isotropically, and hence the distribution of off-axis angles will be uniform in spherical polar coordinates over the cone bounded by the maximum off-axis angle. To achieve the required random deviates the transformation method is applied in spherical polar coordinates over the designed solid angle.

Appendix 11.2.1 on page 221 gives the derivation of the desired random deviates from two supplied uniform random deviates, u and v. The required results show the path (given in terms of θ and ϕ) within the limits of the maximum off-axis angle $\Psi_{\max}$, as

$$\theta = \cos^{-1}\left(-\cos(\pi - \Psi_{\max}) + v\left(-1 - \cos(\pi - \Psi_{\max})\right)\right), \tag{5.6}$$

$$\phi = 2\pi u. \tag{5.7}$$

Strictly speaking, the initial optical depth seen is determined by a combination of a photons wavelength, direction of travel, and polarisation. This is a slight adjustment, due to the magnetic field in the vapour cell, to the dependence given in equation 5.5. It is necessary because the Zeeman splitting of the line profiles produces a more complex situation described in detail in section 4.2.1 on page 69. However, the source condition of polarisation is determined by optical components in the instrument, which ensure circularly polarised light of either left or right handedness enters the cell. Light enters the cell parallel to the magnetic field plus or minus the off-axis angle which is a maximum of 0.028 rad. As this angle is small, we are able to state that the first absorptions to occur in the cell will be completely dominated by σ transitions, with π transitions accounting for less that 0.5% of resonant scatters. Hence in the simulation we will ignore the initial dependency on direction of travel, the impact of polarisation, and the contribution of any initial π scatter for the first absorption in the cell.

5.2.3 Propagation

The previous section details work to initialise the system and receive a photon from the primary optics. Here we deal with the process of propagating this photon through the cell and on to a detector. The movement of a photon is determined by probabilistic physical processes that are replicated here with distributions of random deviates.

The probability distribution function of distance travelled x, through a medium with absorption coefficient κ, is given by

$$P(x) = 1 - e^{-\kappa x}. \tag{5.8}$$

Using the transformation method, a random uniform deviate R, can be transformed to an exponential random deviate (see appendix 11.2 on page 221 for derivation), where the result is

$$x = \frac{1}{\kappa} |\ln R|, \tag{5.9}$$

or written in terms of seen optical depth τ, and the length of absorbing medium l,

$$x = \frac{l}{\tau} |\ln R|. \tag{5.10}$$

The seen optical depth is determined by the value of the line profile at the wavelength λ, multiplied by the IOD hence

$$x = \frac{l}{\text{IOD } \phi(\lambda)} |\ln R|, \tag{5.11}$$

where the details of $\phi(\lambda)$ from a π or σ transition have been discussed extensively in section 4.4.3 on page 84.

Absorption occurs as a resonant transition where the energies of the photon and transition match, hence the type of transition is determined by the wavelength of the photon. The magnetic field used in the BiSON instruments has magnitude large enough that there is no overlap of transitions, so a photon with wavelength within the σ line profile will only be absorbed by a σ transition. The type of absorption transition determines the excited state

of the potassium atom, and hence influences the de-excitation transition and associated emission.

Firstly, an atom may de-excite to either possible ground state, allowing both σ and π photon emission, but not with equal probability. Section 4.4.3 on page 84 shows the ratio of transitions, over all angles of emission, to be $3:1$, σ to π. This choice of transition determines the distributions of properties for the new photon emitted.

Secondly, the direction of propagation of a photon is sensitive to the type of transition, this is evident in section 4.4.3 on page 84. The random deviates giving the angle of emission required by the Monte Carlo simulation are derived in appendix 11.2 on page 221 using the transformation method. The distribution functions equated to the uniform random deviate R, are

$$R = \frac{1}{8}\left(-\cos^3\theta - 3\cos\theta + 4\right) \tag{5.12}$$

for the σ transition, and

$$R = \sin^4\left(\frac{\theta}{2}\right)(\cos\theta + 2) \tag{5.13}$$

for the π transition. These equations must be solved for theta having generated a given R, but this is non-trivial. From Press et al. [1992], we solve the previous expression by a combination of Newton-Raphson method and bisection. This yields an numerical value for θ from the uniform random deviate R.

In addition to direction of propagation, the wavelength of an emitted photon is determined by the choice of transition. As an atom de-excites through either a π or σ transition, so a photon is emitted with energy defined by the width of the transition. We approximate the transition, and so wavelength profile, as a Gaussian (section 4.2.2 on page 70). The central wavelength of the profile is set by the magnitude of the magnetic field and the width by the properties of the vapour. Here we use FWHM $= 700\text{m s}^{-1}$. A Gaussian random deviate can be generated using two uniform random variates with the 'gasdev' routine from Press et al. [1992].

Lastly, the transition type and the direction of propagation determines the polarisation

properties of photons. Previously we have treated emission and absorption through resonant transitions as dipole radiation, hence the alignment of the dipole moment is important and in fact different for σ and π transitions.

However, we are able to make a useful and valid simplification that removes polarisation from consideration. The polarisation characteristics of emission have the same dependencies (principally the alignment of the dipole) as absorption. In the absence of rotation of the axis of polarisation due to propagation through a magnetic field (Faraday effect) or other scattering processes, the polarisation of an emitted photon will give the maximum probability of absorption in that direction. For this reason, the complicated description of polarisation in terms of Stokes parameters falls out of the equations required to calculate the distance travelled before absorption. Apart from anything else this will provide a significant benefit in terms of computational efficiency, and for this reason Faraday rotation and scattering processes other than resonant scattering are ignored.

With the above physical processes, expressed in probabilistic terms, we have enough information to propagate a photon through a potassium vapour cell. After each discrete movement the photon must be tested to see if it remains in the cell. Photons still in the cell must be propagated till they are not, and photons that have left must be assessed for detection.

5.2.4 Detection

The assessment for detection will be performed by a ray tracing element of the Monte Carlo routine, in effect continuing the transfer of a photon through the instrument. For a photon leaving the cell, the point of last scatter and direction of travel are known and it is straight forward to identify photons heading towards the first detection lens. Photons not destined to meet the surface of the first detection lens can be recorded as not detected, while all others are propagated through the lens system to reach the plane of the detector. The geometric information for the detection optical setup is detailed in section 4.1.2 on

page 65.

Spencer and Murty [1962] detailed a general procedure for implementing ray tracing through an optical system with a single optical axis, as is the case for the detection optics. In brief, this procedure starts with the position of the ray source and its direction of propagation, here supplied by the vapour cell transfer element of the simulation. The point of intersection of the ray with the first optical surface is determined and the action of this surface is found. Modifying the direction of propagation of the ray completes the action of the first surface and the procedure is repeated until all surfaces are dealt with. In order to be successfully implemented into the simulation, the ray tracing element must be computationally efficient. Ray transfer matrix analysis is computationally efficient but only valid under a paraxial approximation. The detection optics accept, and detect, photons that are at a large angle ($\theta \neq \sin\theta$) to the optical axis. To fully consider the whole volume in the vapour that the detection optics are sensitive to, a ray tracing procedure is require. Ray tracing in not particularly computationally efficient but necessary. For this reason we choose to implement a simplistic and first order approach that ignores reflection from surfaces, diffraction, and dispersion. In addition, rather than using the full equation for the surface of an aspherical lens, we will substitute a computationally convenient spherical lens with the same effective focal length.

In this simplified detection optical setup there are two types of surface interaction to be considered: refraction at a planar surface; and refraction at a spherical surface. The nature of ray tracing allows us to tackle these surfaces one at a time in a repetitive nature. Typically, we find the point of intersection then apply Snell's law. In the appendix 11.3 we consider a coordinate transfer from the cell system to a convenient form for the detection optics, find a general description for the point of intersection for both planar and spherical surfaces, and finally detail the application of Snell's law at an intersection.

In our application of the ray tracing method, we must propagate a photon from the vapour cell through to the plane of the detector and then confirm detection if the photon passes inside the detector aperture. This concludes the discussion of the framework of the

simulation and we can move forward to consider the results.

5.3 Results

In this section we present results from the simulation of the RSS. These results simulate the instrument observing a distant and discrete source, constructed from $\frac{\pi}{4} \times 500^2$ white light point sources. The angular diameter of the source has been chosen to approximate that of the Sun as viewed from Earth, i.e. half a degree angular extent. This, to a reasonable approximation, is the equivalent of testing the instrument on a laboratory bench. We have asked the question "what is the optimum instrumental optical depth?" and can now ask this of the simulation. Figure 5.2 shows the gain of the instrument predicted by the simulation and by the Hoyng model as a function of IOD for a number of different detection optical setups. As an aside, to compare the two approaches we must decide on an active region for the Hoyng model and here we take the diameter of the detector aperture to define the length of the active region, thus treating the detector aperture as if imaged by the detection optics into the centre of the cell. In addition, the Hoyng results have been normalised to match the peak gain of the simulation.

First of all, we can perform a few simple checks of our understanding of the scattering in the vapour cell and its interplay with the active region.

Firstly, the greater the radius of the detector aperture, the longer the length of active region in the cell and the more counts are expected. The optimal gain results shown in figure 5.2 suggest optimal IOD as a function of aperture radius may be described by a straight line with intercept close to zero and gradient of around 1.5 (in the unusual units of % gain per mm). In other words, increasing the radius of the aperture by 1 mm is expected to produce an absolute increase of 1.5 % in gain.

Secondly, the shape of the gain curves should show two competing processes that produce the turning point at an optimal IOD. At low IOD, too much light passes through the vapour cell without interaction and so gain is low. At high IOD, too much light is

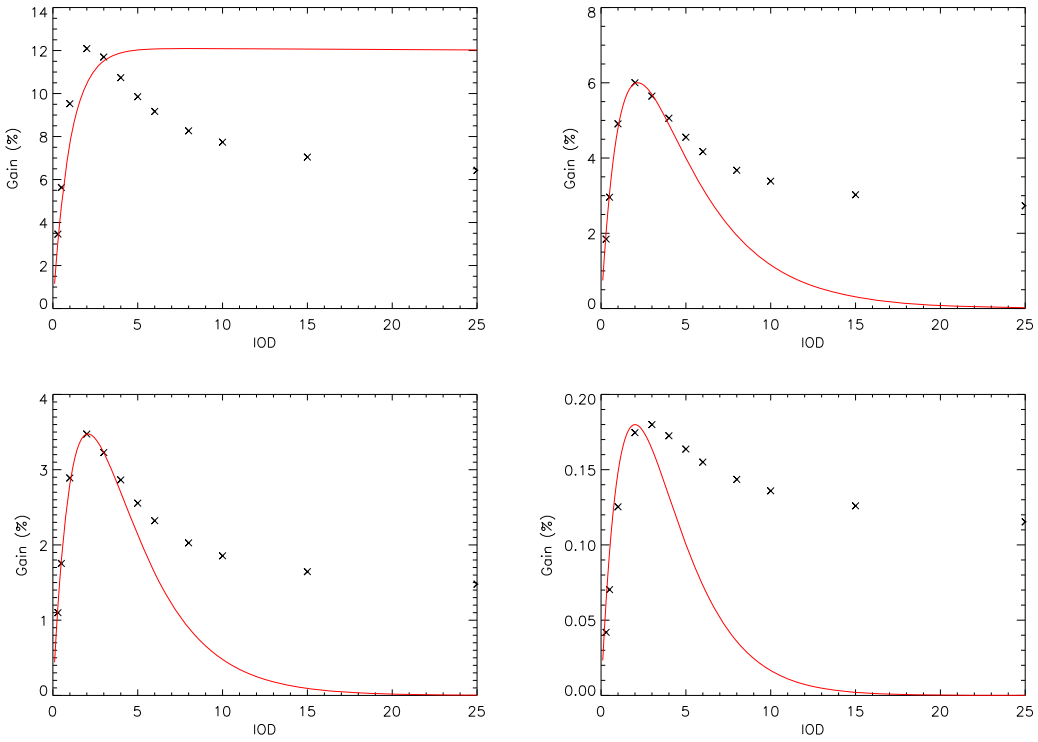

Figure 5.2: Plots of gain against instrumental optical depth for different detection optics configurations. Black crosses are results from the Monte Carlo simulation while the red lines show the Hoyng model results normalised in intensity to match the Monte Carlo results. All plots have DL2 at 73 mm from the center of the cell. The radius of the aperture at the detector varies with: top left - 7.495 mm; top right - 3.5 mm; bottom left - 2.5 mm; and bottom right - 0.2 mm.

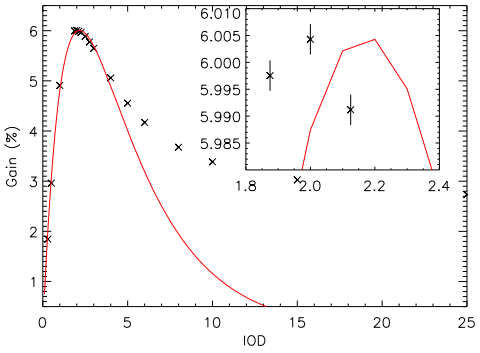

Figure 5.3: Plot of gain against instrumental optical depth for DL2 at 73 mm and detector aperture radius of 3.5 mm. The insert shows the region of optimal gain. Black crosses are results from the Monte Carlo simulation while the red lines show the Hoyng model results normalised in intensity to match the Monte Carlo results.

scattered at the front of the cell and does not reach the active volume. We can clearly see the maximum of optimal IOD in each plot and can identify the regions of too low and too high IOD. We can believe that the results presented so far are consistent with our knowledge of the RSS.

This leads us to broadly state the values of optimal IOD for each detection optics setup. The optimal IOD values differ for each setup but are predicted to lie in the range of between 2 and 3 IOD. This is then broadly consistent with the values obtained by Hoyng and Broomhall (section 5.1 on page 86). Figure 5.3 shows the gain curve, for detections optics with lens DL2 at 73 mm and a detector aperture with radius 3.5 mm, with error bars shown in the insert. We see that the optimal IOD is 2.0 ± 0.1. A conservative estimate of error corresponds to a change in vapour temperature of less than 0.5 K, which is greater than the real world resolution of the BiSON RSS temperature controllers. Having considered the absolute values of gain, optimal IOD, and the shape of the gain curve we may now consider the results in comparison to the Hoyng model. There is no useful comparison of absolute values of gain with the Hoyng model as only the fractional percentage of photons first absorbed in the active region is considered, and for this reason the Hoyng curves have been normalised to match the optimal gain of the simulation. However, the optimal IOD values and the shape of the curve contain some striking similarities and

differences.

At optical depths less than 3 and for the two intermediate aperture radii, both the optimal IOD and the shape of the curves are well matched. But at higher optical depths and more extreme detector aperture radii this agreement is lost.

The optimal IOD changes with the radius of the detector aperture for both the Monte Carlo simulation and Hoyng model. For an increase in aperture radius the simulation reports lower optimal IOD's, but for the Hoyng model the opposite is true and an increase in aperture radius produces higher optimal IOD.

In addition to the change in optimal IOD with detector aperture radius, there is a clear difference of opinion in the simulation and model at high IOD. The Hoyng model predicts very low gains for very high IOD, i.e. the absorption in the front of the cell dominates and photons do not reach the active region. The simulation is at odds with this and shows a steadying of the gain at high IOD. This can be easily explained if there is a mechanism present in the simulation, and not in the Hoyng model, that transports photons scattered at high IOD in the front of the cell into the active region, i.e. multiple scattering. The Hoyng model considers single scattering only, where as the simulation provides a full treatment for multiple scattering.

We continue this theme in the next section by considering the importance of secondary scattering at various IOD's.

5.3.1 The importance of multiple scattering

The simulation performed reveals the importance of multiple scattering by returning the number of scatters for each detected photon, and figure 5.4 shows this for a range of IOD's. The number of scatters is displayed on the abscissa, with a minimum value of one because a photon must be scattered to be detected. The ordinate shows the frequency of occurrence on a logarithmic scale. Each IOD produces an approximately straight line on this plot (an exponential dependency) with the gradient becoming less negative with increasing IOD. This shows multiple scattering to be of increasing importance at

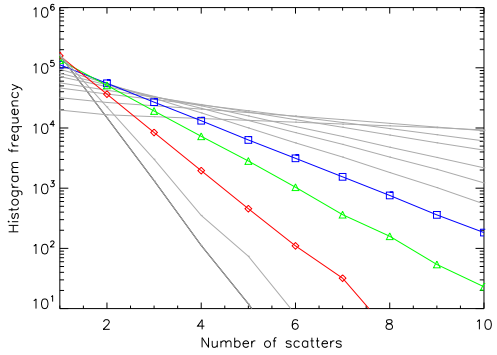

Figure 5.4: Number of scatters of detected photons for various instrumental optical depths. Detection optics setup with DL2 at 73 mm and detector aperture radius of 3.5 mm. Optical depths highlighted are: 1.0 in red; 2.0 in green; and 3.0 in blue.

increasing optical depth, which is entirely sensible.

Figure 5.5 displays the same results but as a cumulative frequency on a linear scale. In this form it is easy to identify the ratio of single to multiple scatters detected (that is single in that a photon is detected after only one scatter and multiple for more than but not including one scatter). IOD of 1 is the red line and the scatter ratio is around 3 : 1. IOD equal to 2 is shown by the green line and has a scatter ratio of around 3 : 2. Finally IOD of 3 (blue) has a scatter ratio of very nearly 1 : 1.

At this point we might consider some parameter that describes the scattering in the cell in a manner that would be familiar to the Hoyng and Broomhall approaches. The obvious choice is the mean distance between scatters in the cell, which is directly related to optical depth. However, by considering wavelengths in the wings of the resonant profile, any result will be inflated by photons that see a very small optical depth and do not interact. By weighting the mean distance between scatters by the instrumental profile, i.e. considering only inbound photon events (photons before and after scattering are not completely correlated) that are detected, we can compensate. Hence, the mean distance between scatters for detected photons for an IOD of 2 is 5.2 mm, or 0.35 times the length of the cell. We note that despite the IOD, the maximum optical depth, providing a lower limit on this value of half the cell length, the weighting created by the criteria of detection

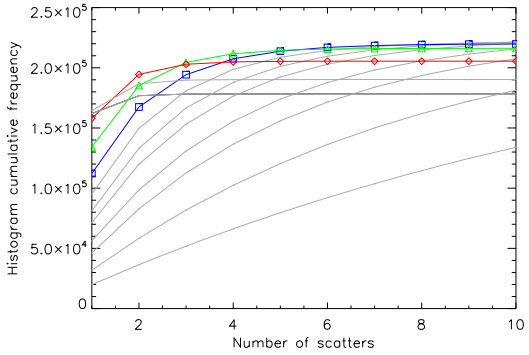

Figure 5.5: Cumulative frequency of the number of scatters of detected photons for various instrumental optical depths. Optical depths highlighted are: 1.0 in red; 2.0 in green; and 3.0 in blue. Detection optics setup with DL2 at 73 mm and detector aperture radius of 3.5 mm.

will act to lower this value, or in other words photons initially scattered at the rear of the cell are less likely to be detected. Hence greater weight is given to the photons initially scattering at the front of the cell, and the mean distance between scatters is reduced.

We have seen from the gain curves that it is important to account for multiple scattering at high IOD. We now see that multiple scattering accounts a significant fraction of the total counts at the optimum IOD of 2 and also for IOD's of 1 and 3. We continue now to consider the character of the instrument now that it is sensible to account for multiple scattering.

5.3.2 The character of the instrument

In the previous chapters we have discussed a resonant scattering spectrometer in terms of three variables: the temperature of the resonant scattering vapour that controls the instrumental optical depth; the wavelength of incident light that determines the point on the resonant profile, and hence the 'seen' absorption coefficient; and the initial path of light through the cell which is linked to the position on the solar disk. In this section we consider the response of the instrument to these variables.

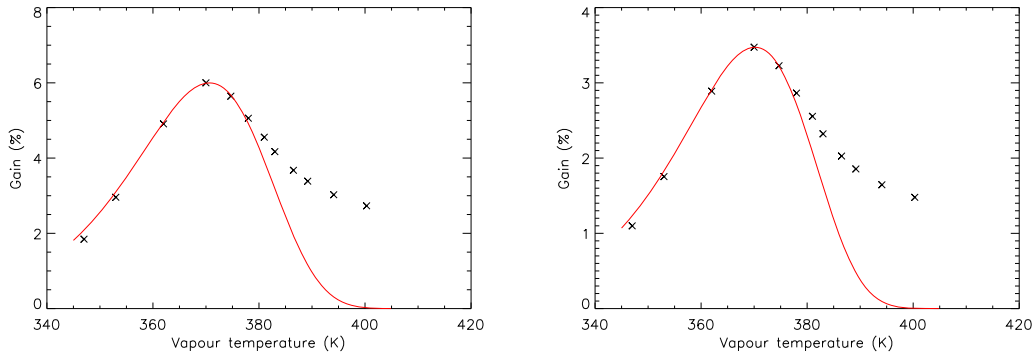

Figure 5.6: Simulated temperature curves for detection optical setups with DL2 at 73 mm and detector apertures of radius 3.5 and 2.5 mm for left and right respectively. Black crosses show the Monte Carlo results and the red line displays the Hoyng model.

Vapour temperature

A common diagnostic for tuning an RSS is the temperature curve, a plot of the intensity as a function of oven temperature. Note that we are using the distinction between: the vapour temperature, controlled by the coldest point in the stem (lower part) of the cell; and the oven temperature, the temperature of the housing surrounding the upper parts of the cell. The oven temperature and vapour temperature may differ by up to (and in extreme circumstances, over) 20 K. To aid this distinction we will refer to vapour temperature in Kelvin and oven temperature in degrees centigrade.

The temperature curves of the simulation are the gain curves as before but expressed as a function of vapour temperature rather than IOD. This conversion is achieved using equation 4.15 on page 77. The plots are shown in figure 5.6 and indicate an optimal setting to be a vapour temperature of around 370 K.

The results of the simulation can be compared with data from a real station, in this case Narrabri. S. Hale made a visit to Narrabri in February 2010 and performed a temperature scan up to nearly 170 $^{\circ}C$. This is higher than usual as normally temperature scans would avoid oven temperatures much higher than the optimal value as potassium is corrosive to the cell at very high vapour temperatures. Results from the temperature scan, originally published in the BiSON technical report series, are presented in figure 5.7.

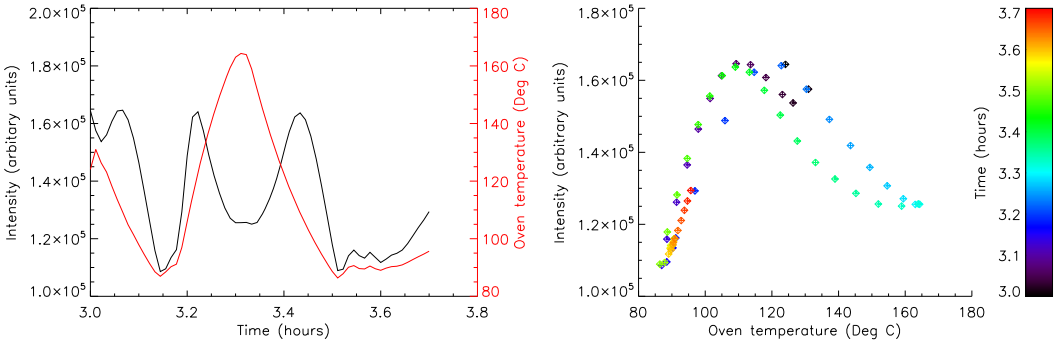

Figure 5.7: Narrabri temperature curve data from S. Hale's visit to site in February 2010. Left: intensity and oven temperature as a function of time. Right: intensity as a function of oven temperature with time indicated by the colour bar.

Results from the real data show two distinct curves for heating and cooling which emphasises the point the oven temperature is not an accurate measure of vapour temperature. However, the shape of the curves is clear and comparable to those produced by the simulation. The optimum oven temperature is around 115 $^{\circ}C$ which is around 18 degrees higher than the optimum vapour temperature, which we can regard as plausible given early statements.

The shape of the curve up to an oven temperature of 170 $^{\circ}C$, reveals the predicted importance of multiple scattering at high temperature, or as previously stated, high IOD.

We can then, be confident that the simulation provides a reasonable qualitative description of the temperature dependence of the instrument. More in depth quantitative testing of the simulation, as part of a Sun-atmosphere-instrument model, will be performed in the following chapter. Before this we examine the wavelength dependence of the instrument.

Wavelength

Figure 5.8 shows the instrumental profile in wavelength predicted by the simulation for a number of IOD's and detector apertures. For a large detector aperture, the profile at optimum IOD is approximately Gaussian in shape. This Gaussian shape is retarded with a smaller radius of detector aperture and this is due to the wavelength dependence

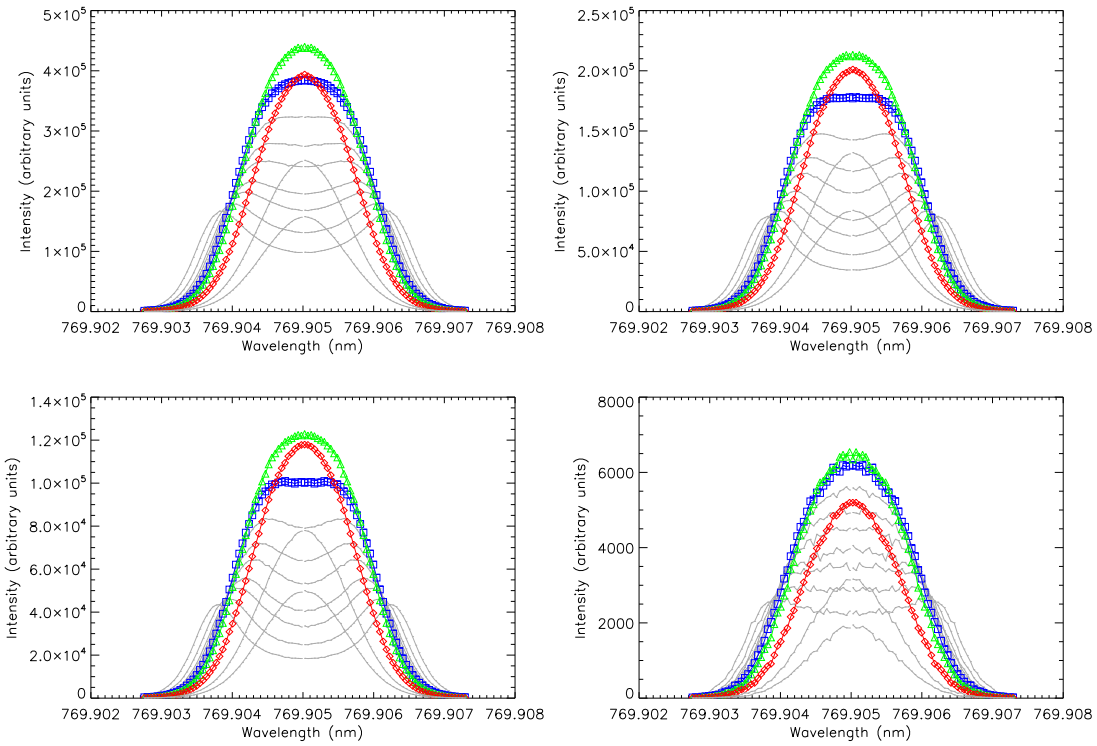

Figure 5.8: Instrumental profiles in wavelength for a simulated BiSON RSS at various IOD's and detector apertures. Optical depths highlighted are: 1.0 in red; 2.0 in green; and 3.0 in blue. Radii of detector aperture are: top left 7.495 mm; top right 3.5 mm; bottom left 2.5 mm; and bottom right 0.2 mm.

of seen optical depth. Light closer to the centre of the resonant line profile experiences a greater optical depth, than that at the wings, and this causes increased scattering in the region of the cell before the active volume. Increased scattering outside of the active region diminishes the gain of the instrument and the centre of the instrumental profile is suppressed away from its otherwise Gaussian shape.

This suppression effect can be seen when changing either the length of the active region, or the changing IOD. At higher IOD's the suppression effect starts to dominate the instrumental profile eventually producing a profile with two distinct peaks.

The wavelength dependence of seen optical depth is an effect not accounted for by either the Hoyng or the Broomhall model, yet both produce values for optical depth that are in agreement with the simulation. In addition, neither Hoyng or Broomhall give a full treatment of multiple scattering to reach their values of optical depth. We have then three

very different approaches to finding the optimum optical depth of a RSS vapour cell, each with similar superficial results. Why then have we gone to so much effort to provide a full treatment when previous results appear adequate? The answer is in the weighting of the solar image.

Weighting of the solar image

The weighting to the image of the solar disk produced by the instrument is an important consideration in any model of an RSS. The positional weighting is dependent on the vapour temperature, the wavelength of light and the impact of multiple scattering. Changes in these factors, or even alignment of the image of the solar disk in the instrument, can produce systematic and spurious velocity signals in calibrated data sets. The weighting afforded by the instrument to points on the solar disk is important.

The recent use of the optical depth in other work has been as a parameter that describes the weighting of the solar disk. We have seen already that the term optical depth ignores a variation of seen optical depth with wavelength and so we required the definition of instrumental optical depth (IOD). We have also seen that multiple scattering is an important aspect of any simulation, and while IOD could be used to describe the extent of multiple scattering, the impact on the instrumental weighting is far from obvious. Optical depth is a poor parameter for describing the response of an RSS.

The RSS is a complex system, and to model the Sun-atmosphere-instrument system we require the response of the instrument at different points in the solar disk across a range of wavelengths created by a simulation that affords a full treatment to multiple scattering. It is not sensible to parametrise this or to display weightings for all considered wavelengths created by the simulation. Through the simulation we have produced an approximation of the required information and figure 5.9 shows the instrumental weighting integrated over the wavelengths of the resonant transition. For comparison the weighting predicted by the Broomhall work is also displayed.

Direct comparison between the two instrumental weightings is difficult because Broomhall

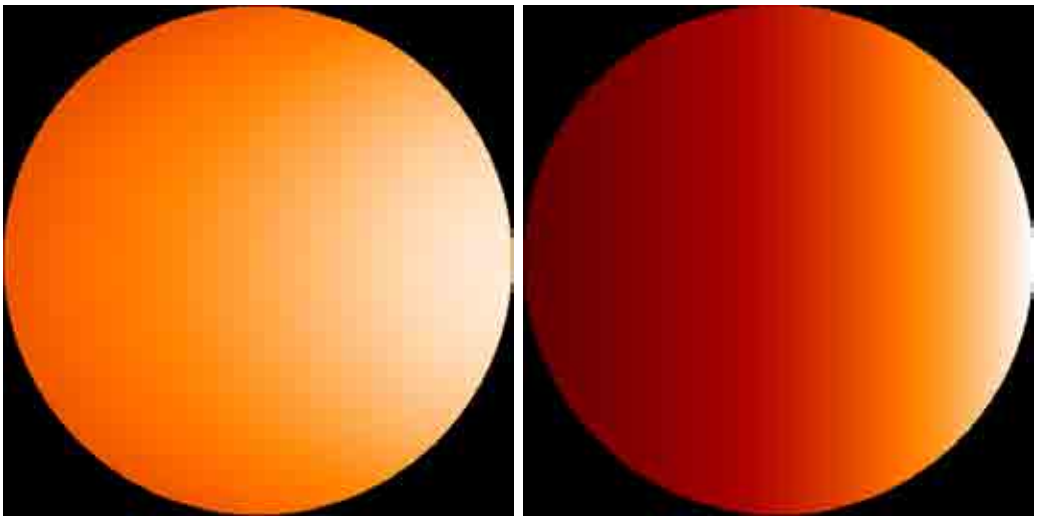

Figure 5.9: Predicted instrumental weightings to the solar disk for a detector positioned on the right hand side of the images. Left: simulated instrumental weighting integrated over the wavelength range of the resonant transition for an IOD of 2. Right: Broomhall instrumental weighting at optical depth of 2.

considered a monochromatic optical depth, while the weighting shown from the simulation is integrated over wavelength. It is however noteworthy that both weightings display the new aspect of Doppler imaging realised by Broomhall, with the gradient of extinction across the disk greater for the treatment without multiple scattering. We should expect multiple scattering to provide a diffusive effect, lowering the mentioned gradient of extinction, and this is predicted by figure 5.9. Put simply, to achieve a detailed model of a resonant scattering vapour cell multiple scattering must be considered.

We are then armed with the required information to tackle a model of the Sun-atmosphere-instrument system, and this is covered in the next chapter.

Chapter 6

Results From Sun and Instrument Simulations

The previous three chapters have developed the components of a model for the BiSON Resonant Scattering Spectrometer (RSS) that attempts to model the interaction between the Sun, atmosphere, and instrument that makes radial-velocity measurements of the solar surface. This chapter presents the model in its totality and uses the results to demonstrate the response of the instrument. Starting with the response of a single data point in time, the scope of the model is expanded to eventually produce a whole year of data from a single station. These data are studied with the aim of finding opportunity for improvement in the BiSON data reduction pipeline, specifically with respect to the reduction of low-frequency noise in long time series.

6.1 Introduction

We now have a complete but disjoint description of a model that replicates BiSON observations and we must now combine the various elements of this work. Let us refresh our memory. Chapter three has detailed the approach of the model - that we must integrate three functions(solar line function; atmospheric weighting function; and the instrumental weighting function) over the independent variables of wavelength and position on the solar

disk. The solar line function and atmospheric weightings have been covered extensively in chapter three. The third component, instrumental weighting, introduced in chapter 4 and simulated in chapter five, completes the requirements. We proceed with the numerical integration required to determine the measured intensities of an RSS.

The model of the RSS measurements will be applied as summation, rather than an analytical integration, over position on the solar disk and wavelength. This numerical approach is necessary as the instrumental weighting is simulated for 100 discrete wavelengths, each providing a unique 500×500 pixel image of the instrumental positional weighting. Hence any model must produce 500×500 pixel images of the Sun as viewed by the instrument at each of the wavelengths defined by the instrumental weighting. Each pixel in the image of the Sun is then subjected to atmospheric extinction and the modified image is combined with the instrumental weighting. The measured intensity is then the sum of the intensities at each point in each resultant image at every discrete wavelength.

Chapter five demonstrated that the optimum Instrumental Optical Depth (IOD), at least in terms of instrumental gain, occurs when IOD = 2. Hence, unless otherwise stated the reader may assume that the model has been applied using this value.

This chapter will first examine the reproducibility of the model given that the instrumental weighting is generated by a Monte Carlo method, i.e. using randomly sampled distributions. After that, we will look at the response of the instrument to specific 'pseudo' velocity inputs. We present the raw and reduced modelled data and make comparison with real data, primarily as a test of the model's sanity, before studying the effect of differential rotation and the instruments predicted long term stability. First we tackle the accuracy of the model, the upper limit of which is determined by the randomness in the simulated instrumental weighting.

6.2 Reproducibility of the model

At the heart of the model that replicates BiSON RSS radial-velocity observation is a Monte Carlo simulation that builds a weighting of the instrument to different wavelengths and position on the solar disk. The Monte Carlo method uses repeated sampling of random deviate distributions to compute this weighting, and hence by its nature will be subject to random noise. Let N be the number of random Monte Carlo photon events for a single wavelength and position on the solar disk. It is obvious that as N increases, so the random noise in the computed intensity decreases. The question is, at what N does the model return results with an acceptable random noise level?

This question requires us to state what an acceptable level of random noise in the modelled data is. In the context of low-frequency solar oscillations it is desirable to be able to measure signals perhaps as low as 1 cm/s, which approximated as a ratio of intensities is nearly 3×10^{-6}. We therefore set the requirement that the model is reproducible to - that a ratio returned for the same initial settings varies by no more than - a few parts in a million of ratio. Of course, this statement lacks some meaning without a definition of a sigma value to accompany it. However, it is not computationally realistic to generate a sufficient number of tests at high N to be able determine the returned distribution of values. Hence we choose to leave the statement as reproducible to a few parts in a million in terms of ratio.

Instead of repeating the model at computationally expensive high N with invariant initial conditions, we can borrow (and perhaps butcher) a technique from medical science for combining trials with individually low N. The so called meta-analyses reduce error or noise - due to a single effect at least - by applying a weighted combination of low N studies. Random error is reduced as the total N considered grows. Specific to this context, we can take the mean of the returned ratio, weighted by shot noise or the square root of N, to reduce the error on the true value of the ratio and compare this to the returned value.

Figure 6.1 shows the modelled ratio for N varying on a $\log_{10}$ scale with the blue line representing the weighted mean of the returned ratio for all runs. The data show convergence

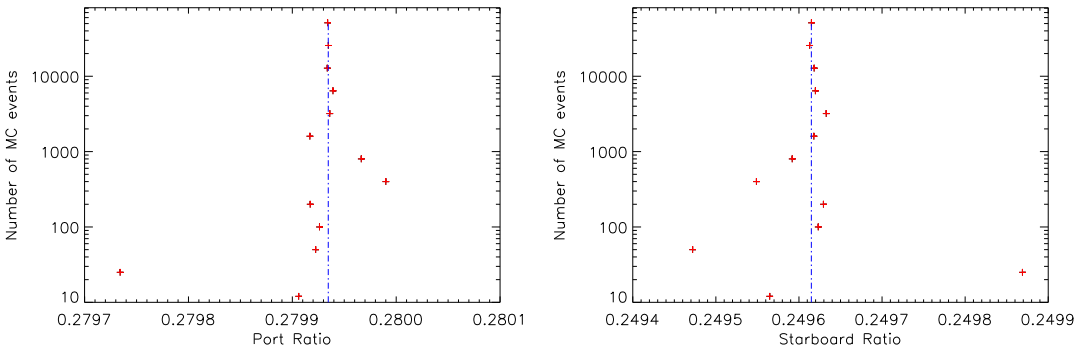

Figure 6.1: Modelled ratio for varying numbers of Monte Carlo events N in the simulation of the vapour cell. Port detector displayed on the right and starboard on the left. Weighted mean ratio for all values of N shown as blue dot-dash line.

to the averaged value with the three highest N values falling within 5 parts in a million in terms of ratio. Whilst not statistically exhaustive, we feel that this probably demonstrates that the model is self-consistent within a few parts in a million for N = 51200 , as required.

Having determined the required value for N we can proceed by considering the instrumental response to known 'pseudo' velocity signals down to a level of around 1 cm/s.

6.3 Instrument response to pseudo velocity input

The BiSON RSS measures intensities at points on a solar absorption line integrated over the whole solar disk. These intensities are by design sensitive to the Doppler shift of the solar absorption line but also by consequence, sensitive to the shape of the measured line. In the following section we investigate, through modelling, a number of effects that change the velocity measured, not through Doppler shifts but by changing the shape of the measured solar line. We test these effects on the simulated ratio at the Las Campanas simulated station on 14/01/2009 with $v_{\text{station}} = 220$ m s^{-1} in order to establish the observed magnitude of each effect. To start, we consider the alignment of the rotation axis of the Sun.

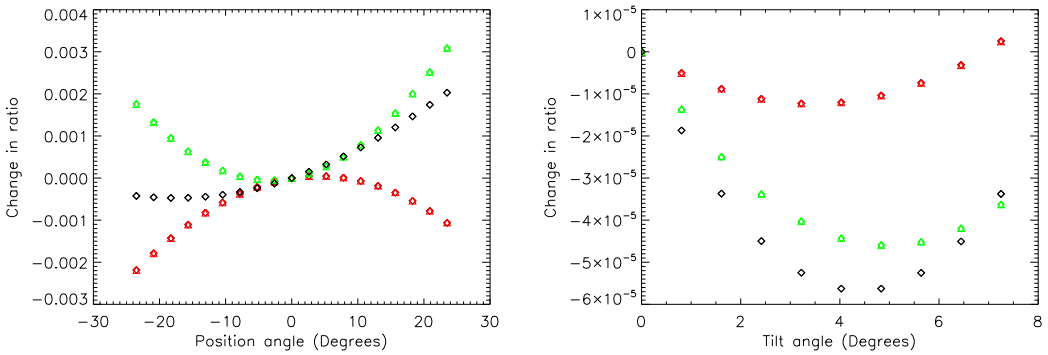

Figure 6.2: Left panel shows the modelled change in ratio as a function of the solar position angle. Right panel shows the modelled change in ratio as a function of solar tilt angle. Standard convention is applied that dictates the port detector is displayed in red, starboard in green, and the mean of the two in black.

6.3.1 Alignment of rotation axis of the Sun

The Earth orbits around the Sun with its rotation vector tilted away from orthonormal of the solar system ecliptic. In fact, the Earth's rotation vector is at an angle of 23.5° to the Earths barycentric position vector. This changes our view of the Sun - and the view from an RSS - systematically through the year. For an RSS this is important because the solar image is combined with the instrumental weighting that has a fixed alignment with respect to the RSS detectors. Or put another way, rotating the image of the Sun causes the detectors to weight the solar disk differently and measure a slightly different intensity. Chapter 3 introduces the solar position angle P_a and the solar tilt angle B_0, the two angles that describe the perceived rotation of the Sun about the z and x axis respectively. The position angle, as stated, varies by $\pm 26.3°$ and the tilt angle by 7.25°. Here we can ask questions of the modelled data as to the response of the instrument to each variation and then place an estimated value on the magnitude of the observed pseudo velocity.

Figure 6.2 shows the change in ratio for modelled data as a function of position angle (left) and tilt angle (right). Points in red represent the modelled port detector and green shows the starboard detector. The data show that the magnitude of the effect due to positional angle is is as much as 0.001 in ratio which is around 10 m s^{-1}. The effect due

to tilt angle is some 100 times smaller in magnitude and hence a second order effect.

The effect due to position angle has an approximate symmetry about the ordinate which will mean the period of the effect is seen as 6 months. There is another approximate symmetry about the abscissa that means the effect will, to some extent, cancel when considering an average of the port and starboard detector. We can say then that the position angle signal in a single detector is expected to have a magnitude of around 10 m s^{-1} with a period of around six months. For the signal of two detectors averaged together we see that this magnitude will drop by a third with an approximately annual period.

Next we consider the combined impact of dark counts and atmospheric extinction.

6.3.2 Dark counts and atmospheric extinction

BiSON RSS intensity measurements include counts from sources other than resonantly scattered light I^{res}, particularly non-resonantly scattered light I^{non}, and dark counts i. Chaplin et al. [2005] showed the effect of the contribution from these counts when intensities are combined in a ratio

$$R = \frac{I_b^{res} + I_b^{non} + i_b - I_r^{res} - I_r^{non} - i_r}{I_b^{res} + I_b^{non} + i_b + I_r^{res} + I_r^{non} + i_r}. \tag{6.1}$$

This equation can be simplified because it is sensible to assume - because all components are measured by the same detector - that the non-resonantly scattered light and dark counts are equal in both the blue and red wings, I_b and I_r. This gives the reduced equation

$$R = \frac{I_b^{res} - I_r^{res}}{I_b^{res} + I_r^{res} + 2I^{non} + 2i}, \tag{6.2}$$

where i is the mean value of i_b and i_r. This highlights the impact of the background $(I^{non} + i)$ counts that are not resonantly scattered. Background counts will act to reduce the ratio which reduces the sensitivity of the instrument and so steps are taken to minimise this impact. But background counts may impact the ratio in other ways.

It is obvious from equation 6.2 that a time varying background will add a time varying contribution to the measured ratio, i.e. the background may produce a source of noise as well a reduction in sensitivity. But how may the background vary?

A well behaved detector, such as the port detector in the Las Campanas A instrument has a dark count contribution of around 1440 counts in a total measured intensity of something like 50000 counts. These dark counts vary systematically through the year as ambient temperature changes, here described by the function $d(t)$, to produce an observed variation of a maximum of 40 in 1440 counts, or around a 3% change in dark counts. In addition, dark counts also vary through the day.

Non-resonantly scattered counts are formed from light scattered by dust or vapour cell glass imperfections and so are proportional to the total light entering the instrument. We know the input intensity varies systematically through the year due to the position of the Sun in the sky and the associated atmospheric extinction. A change in background is important in terms of its size relative to the measured resonantly scattered intensities. As the resonantly scattered counts change in the same way as the non-resonantly scattered light - intensities are increased due to seasonal effects characterised by $c(t)$ - there will be no change in the measured ratio, i.e. ignoring dark counts

$$R = \frac{I_b^{res} - I_r^{res}}{I_b^{res} + I_r^{res} + 2I^{non}} = \frac{cI_b^{res} - cI_r^{res}}{cI_b^{res} + cI_r^{res} + 2cI^{non}}. \tag{6.3}$$

But including dark counts paints a different picture

$$R = \frac{cI_b^{res} - cI_r^{res}}{cI_b^{res} + cI_r^{res} + 2cI^{non} + 2di} = \frac{I_b^{res} - I_r^{res}}{I_b^{res} + I_r^{res} + 2I^{non} + 2(d/c)i}, \tag{6.4}$$

where the d/c term has the approximate form

$$d/c(t) = \frac{1.0 + a_{\rm yr} \sin\left(\omega_{\rm yr} t + \phi_{yr}\right) + a_{\rm day} \sin\left(\omega_{\rm day} t + \phi_{day}\right)}{e^{-\kappa(t)A(t)}}, \tag{6.5}$$

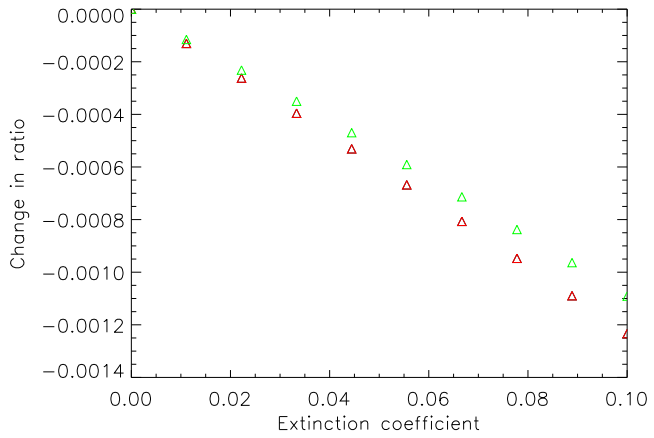

Figure 6.3: Change in modelled ratio as a function of atmospheric extinction coefficient with background counts at 2% of intensity. Port detector in red and starboard in green.

to account for yearly and daily sinusoidal variations in dark counts and the atmospheric extinction term where κ is the extinction coefficient and A is the airmass.

It is clear that background and dark counts are able to vary as a function of time. A number of efforts can be made to eliminate this variation, primarily minimisation of dark counts or failing that the minimisation of variation of dark counts. Where dark counts do exist, and even worse vary, there will be a response from the ratio when the atmospheric extinction coefficient κ varies. We can test this in the model.

Figure 6.3 shows the change in ratio as a function of the atmospheric extinction coefficient at an airmass of 1, with a fixed dark count set at 2% of the sum of the two resonantly scattered intensities. The data show a close to a linear dependence - i.e. the first to term of a series expansion of the exponential function $e^x = 1 + x + \frac{x^2}{2!} + ...$ - because the atmospheric absorption coefficient is small. The data show that a change in κ from 0.02 to 0.08 will produce a ratio change of 0.0006 or 2.1m s^{-1}. The magnitude of this effect will be sensitive to the unchanged ratio, the value of the dark counts, and airmass but this has been described in the above equations. The magnitudes given here represent a best case scenario so can be considered as a lower limit. An upper limit could conceivably be as much a 30 times greater, accounted for by a ten fold increase in A and three times

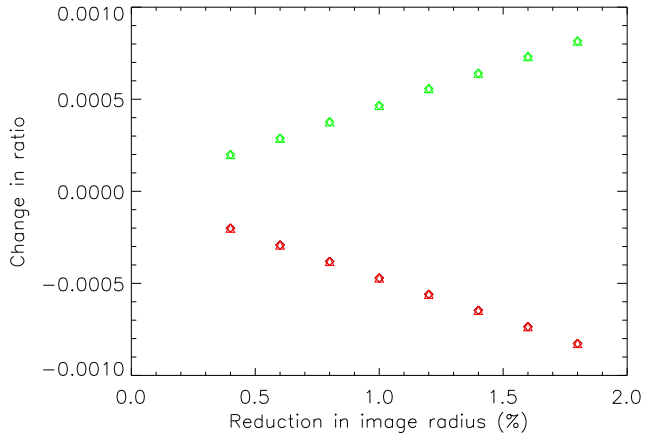

Figure 6.4: Change in ratio as a function of the image size at the centre of the RSS vapour cell. Port detector in red and starboard in green.

increase in κ.

The alignment of the solar rotation axis and atmospheric extinction effects - albeit at a constant κ - are explicitly defined in the model developed in chapter 3 and hence will appear in modelled data. But other effects are too computationally inefficient to be included. We are, however, able to study these effects as the response of a single point in time. We will now study the response of the instrument to the change of the size of the image in the solar cell and the variation in vapour cell temperature.

6.3.3 Size of solar image in cell

The angular extent of the solar disk varies with the Sun-Earth distance, which in turn influences the size of its image created at the centre of the RSS potassium vapour cell. The diameter of this image varies by $\pm 1.5\%$ throughout the year and this produces a pseudo velocity as the instrumental weighting to the solar disk is affected. This effect cannot be easily integrated into the simulation of the instrumental weighting, because it is too computationally intensive, but it is possible to generate a small number of data points to estimate the magnitude of the effect.

Figure 6.4 hints at the magnitude of the pseudo velocity signal due to variation in im-

age size. The plot shows the change in ratio as a function of the percentage change in the solar disk image diameter. The variation in image size is achieved by cropping the 500x500 images that produce the standard instrumental weighting. The crop is achieved by reducing the image size at both extremes of both axes by an integer number of pixels, so for example a crop of one pixel produces a new image of size 498x498. To maintain a consistent resolution with the other areas of the model, the instrumental weighting images are re-sized back to 500x500 using a cubic convolution interpolation method. Of course, this interpolation allows for the reduction in the size of the image but an increase would require extrapolation, and for this reason we study only the reduction in image size.

Ignoring the first point, an anomaly caused by the interpolation, the magnitude of effect due to the solar disk image size reduction is shown by the data to be a maximum of 0.0006 change in ratio, which is equivalent to around $2\,\mathrm{m\,s^{-1}}$. The data shows that the effect acts in opposite directions for port and starboard detectors, which will lead to some cancellation in the effect. As a result we can expect the value of $2\,\mathrm{m\,s^{-1}}$ to be an upper limit on the effect when considering data averaged over both detectors.

6.3.4 Potassium vapour temperature

BiSON RSS instruments are carefully temperature controlled, especially the housing of the potassium vapour, but realistic implementation of the temperature control throughout the year, in often extreme weather conditions, means that the vapour temperature is not completely stable. It is difficult to measure the vapour temperature, even more so the change in vapour temperature, of an instrument so it is difficult to assess the magnitude of the vapour temperature variation. We can though, model the response of the instrument to a change in vapour temperature by modelling the instrument at varying IOD.

Figure 6.5 shows the modelled change in ratio as a function of vapour temperature (IOD) for source-observer line-of-sight velocities of 0 and $1100\,\mathrm{m\,s^{-1}}$. The data show the ratio changing due to a shift in instrumental weighting which we have said many times is com-

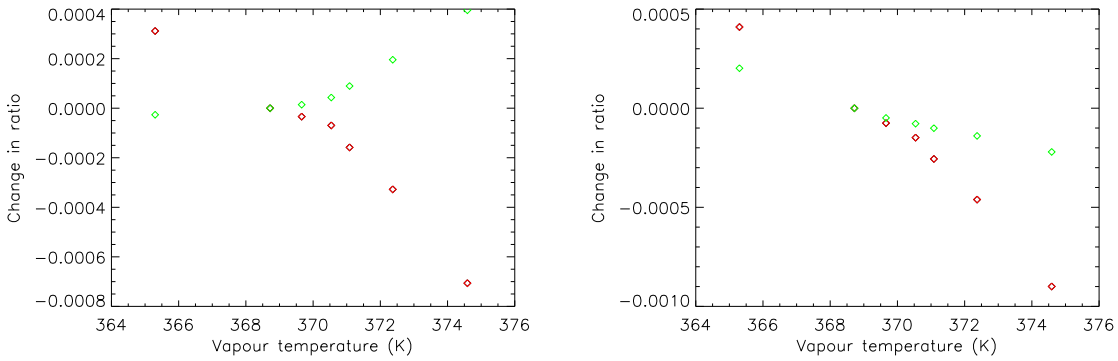

Figure 6.5: Change in ratio as a function of vapour temperature for two different line-of-sight velocities. Left panel with $v_{\rm los} = 0 \mathrm{m\,s^{-1}}$ and right panel $v_{\rm los} = 1100 \mathrm{m\,s^{-1}}$. Port detector in red and starboard in green.

bined with the solar line function. The data show that the ratio changes by around 0.0005 for a change in vapour temperature of $4K$, which is close to the upper limit of the vapour temperature change that may be expected at a BiSON station. This places the upper limit for the response of the instrument at less than $2 \mathrm{\,m\,s^{-1}}$.

We have considered four different pseudo velocity signals expected to appear in BiSON RSS data with the consequence of increased noise at low frequencies. We have found the impact of the position angle - more specifically the shift in alignment of the solar rotation axis with respect to the RSS detectors - as a signal of magnitude $7 \mathrm{\,m\,s^{-1}}$ for the average signal in both port and starboard detectors. Having studied the effects of extinction and background counts we see a minimum impact of $2 \mathrm{\,m\,s^{-1}}$ with an upper limit at some thirty times this value. We have also seen that the response of the instrument to a change in solar disk image size and vapour cell temperature variation, especially for the average of both detectors, is small over the anticipated ranges. Having considered these effects in isolation we can proceed to study modelled data for a full days single site observation.

6.4 Daily data

Having discussed the response of the RSS to pseudo velocities we can now return to the primary function of the RSS, to measure intensities that change due to the Doppler shift of the measured solar absorption line. Measured intensities are used to form a ratio which provides a good approximation of the underlying line-of-sight velocity between the observer and the source. The current model acts much like an instrument in that intensities are modelled/observed and then converted to ratios. In this section we make comparison between real data and modelled data for both intensity and ratio measurements.

6.4.1 Intensity

We have modelled a full year of data for the Las Campanas site from 01/01/2009 to 31/12/2009. To retain the effects of weather interruption, modelled data is used only where real data is free from the effect of cloud-cover. This means that modelled data will have the same fill as real residual velocities. Finally, all solar values are consistent with those defined in chapter 3 and the atmospheric extinction coefficient has been set to a constant value $\kappa = 0.03$ which is representative of the Las Campanas station.

Figure 6.6 on the next page shows simulated intensities as a function of time through the day with the real intensities plotted over the top. Two days are shown that are virtually free from weather effects, from top bottom: 11/01/2009 and 20/08/2011. The plots have been colour coded with blue lines showing the intensity measurements for the blue wing and red lines for the red wing. Real data is displayed as a solid line, modelled intensities without extinction are shown with a dashed line, and modelled intensities including extinction are shown with a dot-dash line. Ignoring arbitrary multiplicative normalisation differences (deliberately manufactured to allow the data to be displayed on the same plot) there is broad agreement in the daily shapes of real and modelled data. The effect most obvious in the difference is that of extinction and it can be seen that an extinction coefficient of 0.03 produces effects that are of the correct order of magnitude.

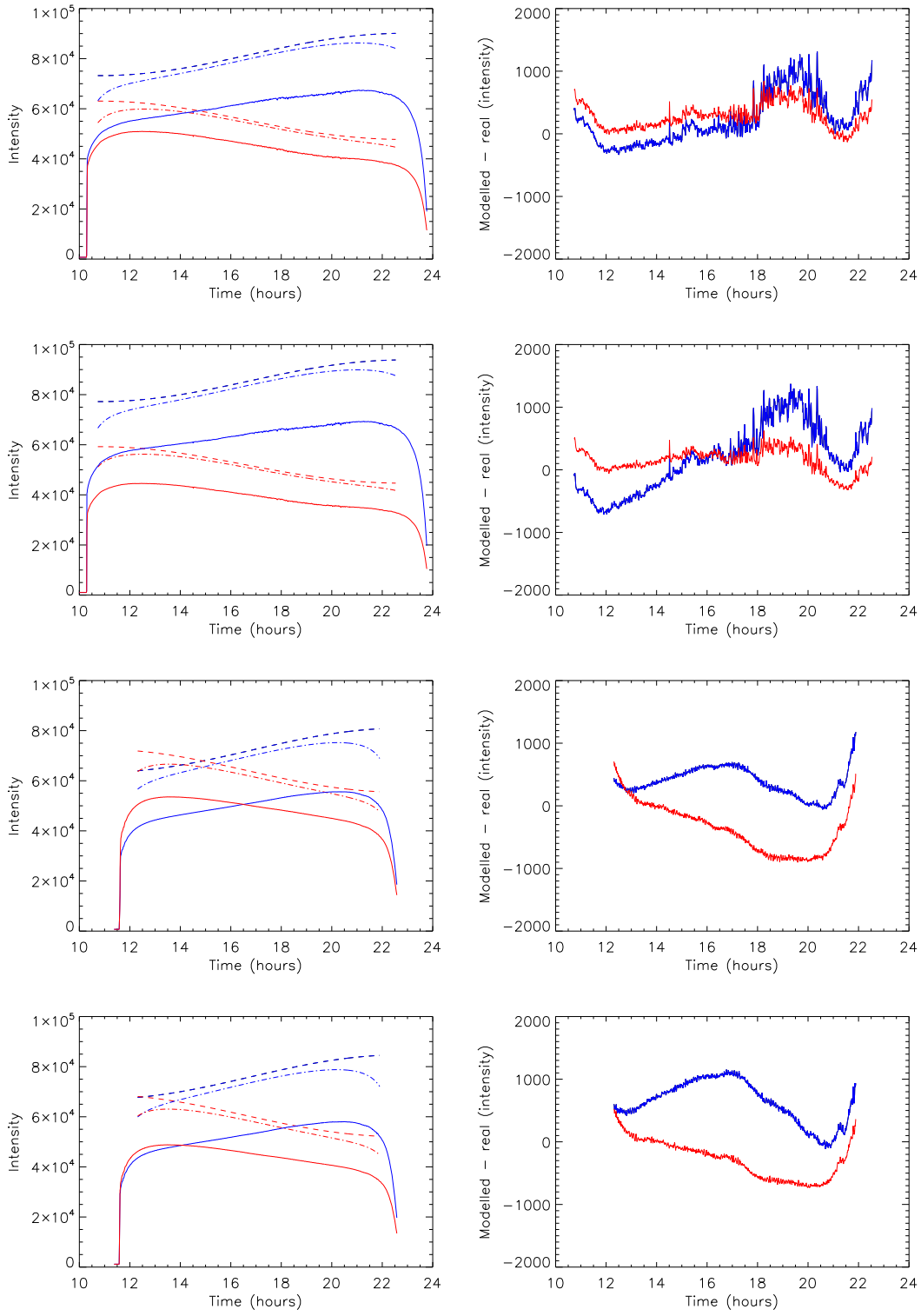

Figure 6.6: Comparison of modelled intensity data and real intensity data for the Las Campanas station on 11 January 2009 and 20 August 2009. Intensities measured in the blue wing are shown in blue and the red wing in red. Left: Intensities for real data as solid lines, modelled data without atmospheric extinction as dashed lines, and modelled data with extinction coefficient $\kappa = 0.03$. Right: Difference between the the real data and data modelled with atmospheric extinction. Top to bottom: 11/01/2011 port detector; 11/01/2011 starboard detector; 20/08/2011 port detector; and 20/08/2011 starboard detector.

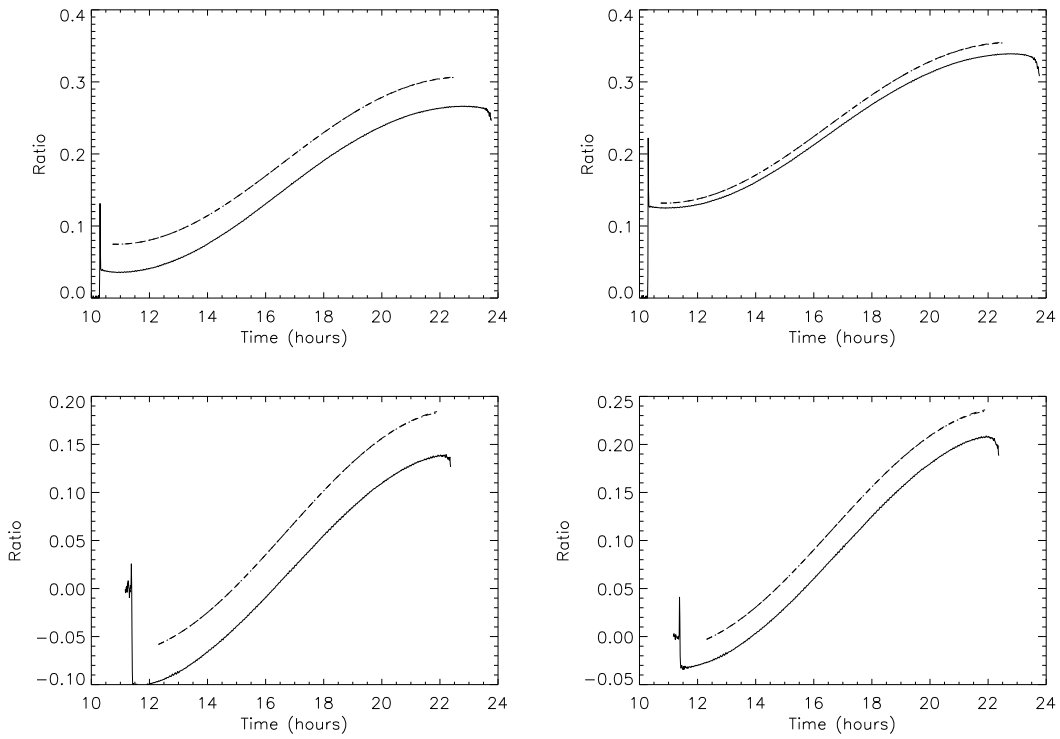

Figure 6.7: Ratios for modelled and real data for the Las Campanas station. Each panel shows real data as solid line, modelled without extinction as dashed line, and modelled data with an extinction coefficient of $\kappa = 0.03$. The modelled data with and without extinction lie over the top of each other. Left panels show port detector data and right panels starboard. Top line: 11/01/2011. Bottom: 20/08/2011.

Effects due to velocities are more easily considered by comparing modelled and real ratios and we cover this next.

6.4.2 Ratio

The intensities shown in the previous section are obviously affected by atmospheric extinction but are less sensitive to the source-observer line-of-sight velocity. In contrast the BiSON ratio is sensitive to velocity and insensitive to atmospheric extinction, which is exactly why the ratio is used. Here we present a comparison of modelled and real ratios for the four days of intensity data considered above.

Figure 6.7 shows the modelled ratio as a function of time through the day with the real ratio data plotted over the top. Again, real data is drawn as a solid line, modelled

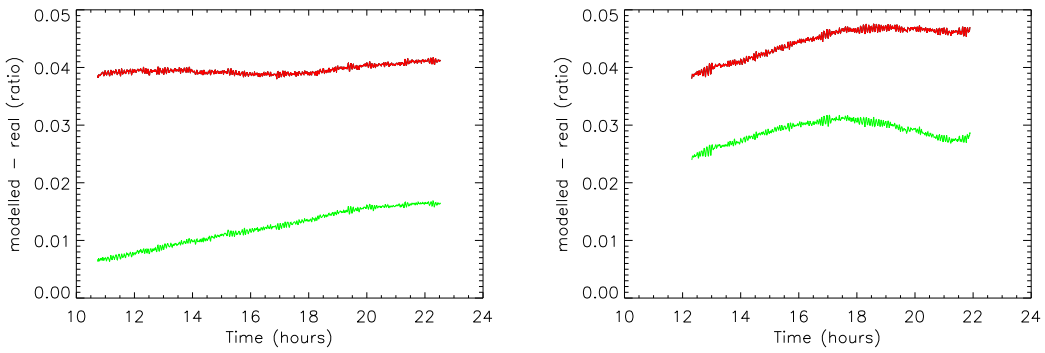

Figure 6.8: The difference between real and modelled ratios for the Las Campanas station. Port detector shown in red and starboard in green. Left: 11/01/2011. Right: 20/08/2011.

data without atmospheric extinction as a dashed line, and modelled data with extinction as a dot-dash line. There is very little difference between the modelled data with and without atmospheric extinction so these lines lie virtually over the top of each other. The difference between the signals is shown in figure 6.8. The data show the modelled ratio and real ratio to show broad agreement.

There are small but never-the-less notable departures from agreement in the modelled and real data, particularly in terms of the d.c. offset but also the gradient of the curves. Constant offsets in the values of the ratios returned can be attributed to either: a difference in position of the solar image in the cell of the instrument; different detection optics setting, i.e. the position of the first collection lens; and or inaccuracy in the underlying solar absorption line settings specified for each position on the solar disk. Changes in the gradient of the line may be explained by: again poor coefficients for the underlying solar absorption line used; and or a larger than expected contribution from background counts. It is clear from the last two sections of data considered that there is superficial agreement between the modelled and real data. It is probable that existing differences can be explained in either a failure of the model or a difference in settings in the instrument. While the model cannot hope to describe a particular instrument to a high degree of precision, we can at least use the modelled data as if it were a unique instrument and ask questions of its daily output when given a specific daily input.

6.4.3 Differential extinction

The impact of differential extinction is one such effect that can be examined using the model. We know that extinction is well corrected for by the denominator in the ratio but differential extinction is quite a different effect. Differential extinction is an artifact of the gradient of atmospheric extinction across the solar disk, the disk being a discrete source. The magnitude and alignment of this gradient causes changes in measured intensities that are different for the red and blue wings. Because the solar disk is rotating the whole disk solar line is rotationally broadened. By placing a systematic transmission gradient at some angle to the rotational axis, the seen whole disk solar line is given an asymmetry that is reflected in the intensities. By weighting more heavily to the receding limb the red wing of the solar line is enhanced as the blue wing fades, and vice versa. We can ask the simulation what signal differential extinction places in the ratio.

Figure 6.9 shows the modelled change in ratio as a function of time through the day for different values of atmospheric extinction coefficient κ, at the Las Campanas site on 14/01/2009. Lines on the chart represent values of κ with intervals of 0.01 starting at $\kappa = 0.0$. Three values of κ have been highlighted: $\kappa = 0.0$ in red; $\kappa = 0.03$ in green; and $\kappa = 0.06$ in blue. The underlying shape that results from this test is - at least to first order - the shape of differential extinction seen in real data, the effects of which are mitigated for by rejecting data from the extreme ends of each day. This signal may have a magnitude in velocity of as much as 6 m s^{-1}.

Importantly, differential extinction has a well defined shape that is defined by the gradient of the atmospheric extinction across the solar disk. While the magnitude of the change in ratio due to this effect varies with the extinction coefficient, the shape of the systematic variation remains constant. This presents the possibility of a straightforward correction, applied to data as part of the BiSON data reduction and calibration pipeline, to eliminate, or at least mitigate, the effect of differential extinction. The following chapter details this correction.

Before we proceed to the next chapter and the correction of differential extinction we must

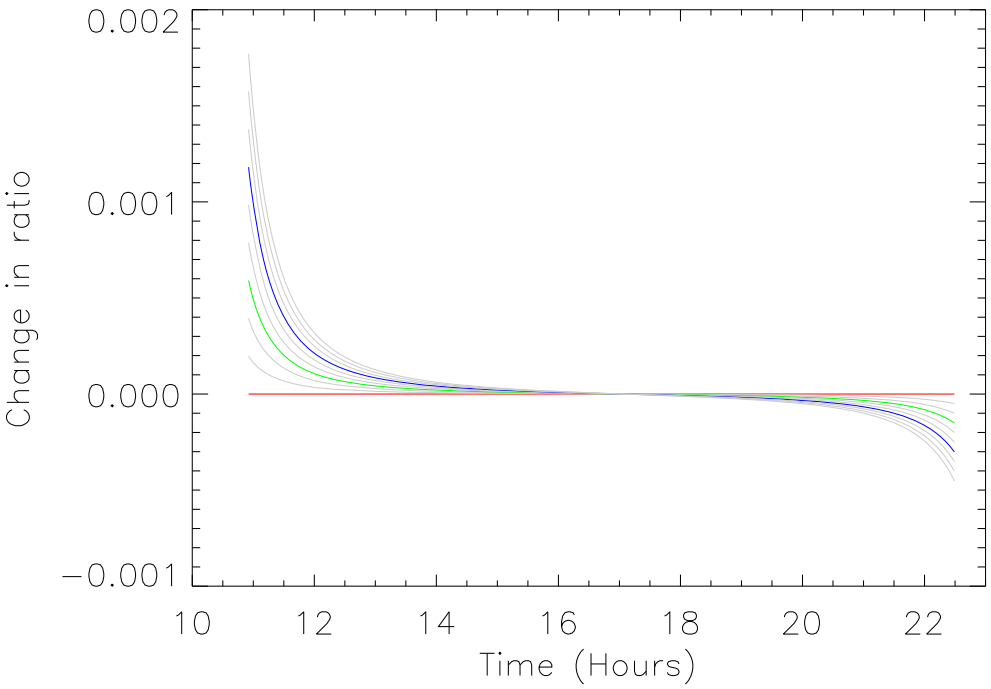

Figure 6.9: Modelled differential extinction as a function of time through the day for different values of extinction coefficient. Line shown are for extinction coefficient starting at 0.0 and increasing in steps of 0.01. Lines highlighted in colour are: $\kappa = 0.0$ in red; $\kappa = 0.03$ in green; and $\kappa = 0.06$ in blue.

conclude the work on the results of our modelling. We continue then to consider the long term stability of the modelled BiSON instrument with comparison to a real instrument.

6.5 Modelled long term stability

The BiSON RSS provides good long term stability for measuring line-of-sight velocity signals by taking measurements referenced to atomic line transitions. This high level of stability is compromised by pseudo velocity signals, like the types discussed above, with periods of a day to a year. These pseudo velocities force BiSON data calibration to be performed on a daily basis which removes very low frequency signal from the residual velocities. If the sources of pseudo velocities can be found and characterised then this would be a step towards a seasonal calibration procedure that maintains very low frequency signals of solar origin - and of other origin for that matter. We continue by comparing the yearly variation of RSS ratios for real and modelled data.

There are a number of ways of looking at the long term stability of the instrument but the most straightforward two are the ratio and the separation of the ratio created by the port and starboard detectors. First we consider the ratio.

The ratio is a data point constructed from the RSS instruments measured intensities that is a proxy for the line-of-sight velocity between the source and the observer. As this velocity changes through the day, due to the Earth's spin, and the year due to the Earth's orbit, the ratio will change too. Here we are considering the ratio over a long timescale so instead of tackling the 40 second data we consider only one point at local midday. As a result this day cadence ratio should display the Earth's orbital velocity but be insensitive to the spin velocity.

Figure 6.10 shows the modelled and real ratios taken at midday local time throughout 2009 at the Las Campanas station. Real data are displayed using solid lines and modelled data as dashed lines. Following convention, the port detector is shown in red and starboard in green. The data show reasonable agreement at this level with some offset

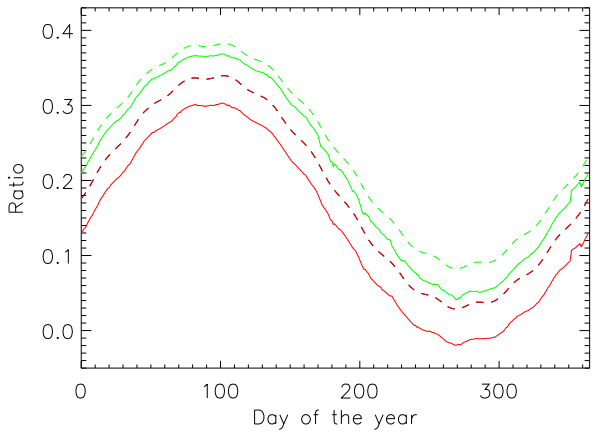

Figure 6.10: Ratios at midday local time through the year for modelled (dashed line) and real Las Campanas (solid line) data 2009. The port detector data is displayed in red and starboard in green.

and difference in sensitivity, but this is to be expected when being realistic about the approximations made in the alignment of the modelled instrument (a modelled instrument being well aligned, with the real instrument being an approximation of that setup). For completeness we mention the monthly variation seen in the ratio which is a result of the perturbations caused by the Moon.

Figure 6.11 takes the data from figure 6.10 and displays the modelled data minus real data to highlight the differences in each detector. Again, the port detector is displayed in red and the starboard in green. At first sign it is clear that there is an asymmetry in each detector for each half of the year. For the first half of the year the two detectors act in the same manner, but in the second half of the year the port detector sees effects that appear amplified in comparison to the suppressed response from the port detector. The difference in responses suggests a cause that does not act in the same manner in each detector, or put another way, the cause must generate a different response for each detector in the second half of the year.

Further to the differing response from each detector, it is notable that the difference between modelled and real data does not vary in a smooth fashion - there is some aspect of randomness or noise. Modelled data with a constant atmospheric extinction coefficient

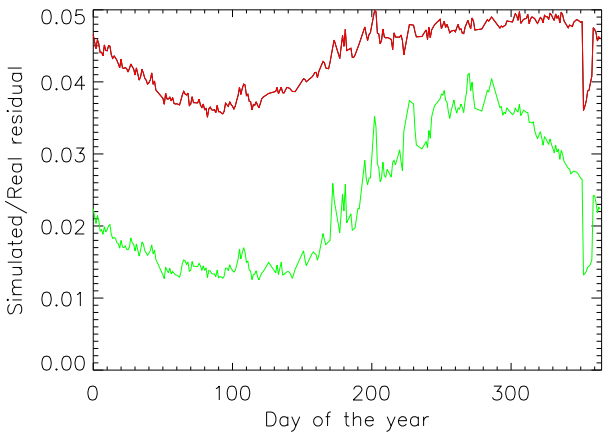

Figure 6.11: The difference between modelled and real ratios taken at midday local time for Las Campanas 2009. Port data is displayed in red and starboard in green.

and background counts does vary in a smooth fashion so the source of the noise is real data. This short timescale variation may be caused by one of instrument temperature variation, change in atmospheric extinction coefficient, guiding problems or something utterly obscure.

We see a similar noise in the port-starboard separation, the difference in ratio between the two detectors, primarily caused by the different view of the solar image each detector has.

Figure 6.12 shows the modelled (dashed line) and real data (solid line) separation of the port and starboard ratios. The data show a clear offset, again probably explained by alignment, in ratio of 0.025. In addition there is a difference, between modelled and real data, in trend in the latter half of the year. Also noise in the ratio separation is present and has the same (undetermined) source as the noise in the absolute ratio.

Figure 6.13 shows the difference between the modelled and real separation of the ratios through the year. The data show a better agreement in the first half of the year as mentioned above. We can conclude then that real data is subject to an effect that is prominent in the latter half of the year, one that reduces the separation in the port-starboard ratio, that is not included in the model.

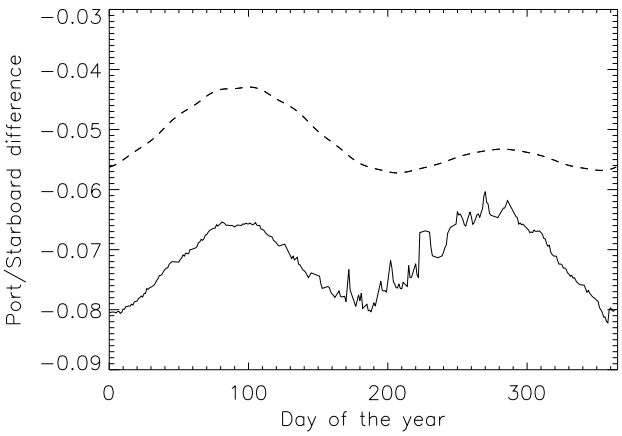

Figure 6.12: Port-starboard separation in ratio through the year for modelled (dashed line) and real (solid line) Las Campanas 2009 data.

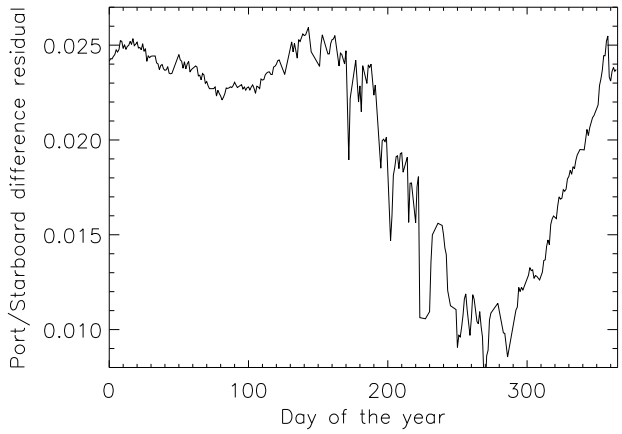

Figure 6.13: The port-starboard separation difference between modelled and real Las Campanas 2009 data.

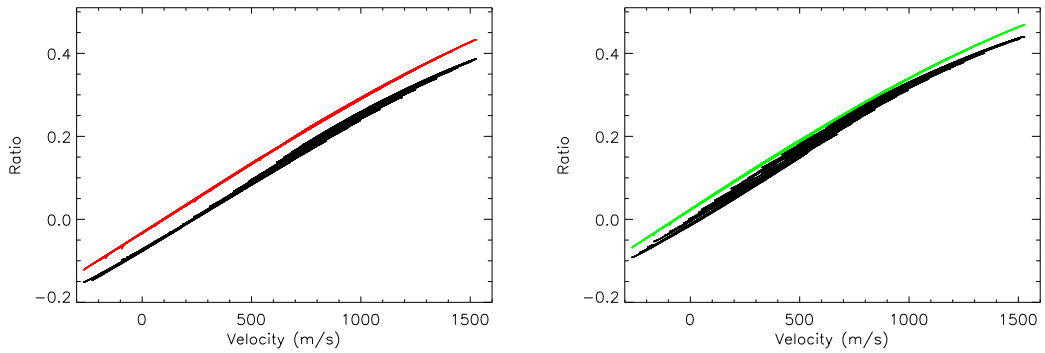

Figure 6.14: Ratio as a function of line-of-sight velocity - an RV curve - for modelled (colour) and real (black) Las Campanas 2009 data. For aesthetic purposes only every tenth day is displayed.

We have seen that the long term stability of the BiSON RSS is good but there are pseudo velocities that cause variations that impact this stability. We will consider these effects in detail in chapter 8. The last thing we will do before moving on is to demonstrate the significance of the unknown effects in a yearly RV (ratio-velocity) curve. The ratio is designed to be a measure of the line-of-sight velocity component and one would expect a well calibrated instrument to return a unique ratio for each radial velocity. In reality all of the effects discussed above lead to ambiguity in the line-of-sight velocity taken for each ratio. The yearly RV curves displays this.

Figure 6.14 shows the real and modelled ratios plotted as a function of line-of-sight velocity v_{station}. The port detector is displayed on the left and starboard on the right with modelled data in color and real data in black. The modelled ratios show a high correspondence with v_{station} - there is very little width to the line in RV space. Real data on the other hand has significant width not predicted by the model - there is reduced correspondence.

From the above we must again conclude that there are pseudo velocities acting in the real data that are either not included in the model or are expected to have much smaller magnitudes. In chapter 8 we will investigate the origin of these effects.

Chapter 7

Correcting for atmospheric effects

In the last chapter we highlighted two consequences of atmospheric extinction that introduce pseudo velocity signals into BiSON RSS measurements. The first effect, coined 'extinction coupled with dark counts', and the already familiar differential extinction are a consequence of the atmospheric terms included in our model. The atmospheric terms contain an extinction coefficient, which is an unknown variable, and the airmass, which has a well described systematic variation. If we can measure the extinction coefficient and the magnitude of the dark count contribution we may mitigate these two effects through a correction applied to the measured ratio. We start with the problem of atmospheric extinction coupled with dark counts.

7.1 Extinction coupled with dark counts

For the sake of clarity, we will recap the work of the previous chapter that linked atmospheric extinction with background counts. We demonstrated in equation 6.4 on page 116 that extinction coupled with dark counts manifests in the ratio as

$$R = \frac{cI_b^{\mathrm{res}} - cI_r^{\mathrm{res}}}{cI_b^{\mathrm{res}} + cI_r^{\mathrm{res}} + 2cI^{\mathrm{non}} + 2di} = \frac{I_b^{\mathrm{res}} - I_r^{\mathrm{res}}}{I_b^{\mathrm{res}} + I_r^{\mathrm{res}} + 2I^{\mathrm{non}} + 2(d/c)i}, \tag{7.1}$$

where c is the atmospheric transmission, a function of the extinction coefficient κ and the airmass A with standard form

$$c(t) = \frac{I(t)}{I_0} = \exp\left(-\kappa(t)A(t)\ \right), \tag{7.2}$$

and d is the time varying function that describes the instrumental dark counts. It is clear that a variation in dark counts and extinction can result in a variation in the ratio.

The ratio is designed to be a measure of the line-of-sight velocity signal between the observer and source, but here we have a clear non-solar effect that can appear as a velocity. It is desirable then that we modify the measured ratio - and hence the residual velocity - so as to minimise this effect.

From the above equations we can see a straightforward solution to the problem of extinction coupled with dark counts. If $i = 0$ i.e. there are no dark counts, we have no problem. But dark counts are unavoidable. Because dark counts are non zero and we wish to correct for the consequences, we must measure dark counts and atmospheric extinction. We will continue by discussing the measurement of extinction from the RSS intensity data and the measurement of a proxy for dark counts.

If we can measure both dark counts and atmospheric extinction, then we can construct a correction to the BiSON ratio which has form

$$R_{\text{ideal}} = R_{\text{meas}} \frac{I_b^{\text{total}} + I_r^{\text{total}}}{I_b^{\text{total}} + I_r^{\text{total}} - (2(d/c)i)}. \tag{7.3}$$

The question is, can we measure dark counts?

7.1.1 Measuring dark counts

Dark counts are straightforward to measure if the spectrometer telescope aperture is closed. Unfortunately, under such circumstances, sensitivities to solar oscillations are somewhat reduced. However, there are times in the working life of an instrument when it is necessary to have the telescope closed. For example, when the Sun is not visible at

night and during bad weather. BiSON instruments continue to collect data, albeit not velocity data, during these 'down' times and hence provide us with an opportunity. But can these measurements of dark counts provide a reliable proxy for the dark count values during 'up' time?

If, as we have argued, dark count variation is generated by temperature variations in the detector electronics, then dark counts will share similar variations to ambient or spectrometer temperature. We would expect that these variations contain a daily component and an annual component. Variation through the day(up time) is unmeasurable as we have suggested, but it could - potentially - be achieved through calibration of detectors using ambient or spectrometer temperature. We will leave this idea here as suggested further work. We will instead continue to study the variation of dark counts through the year.

In order to generate a time series of dark counts to show annual variation, we start by defining a process that gives one data point per day to represent dark counts. Using overnight intensity measurements we take a nightly value as the mean of a Gaussian distribution fitted by least squares fit to the frequency histogram. This method is preferred to a straightforward mean of the population as results are less sensitive to outliers caused by counting glitches. Using this as a working definition we may apply the technique to data from the year 2009 taken at the Las Campanas station.

Figure 7.1 shows the daily - specifically nightly - mean dark count through the year 2009 for the Las Campanas station with port data displayed on the left and starboard on the right. We instantly realise that there is a marked performance difference between the port and starboard detector. The port detector is stable to within 40 or so counts in 1440 through the entire year. The starboard detector is poorly behaved with variation occurring over the range 1700 to 2500 counts.

Putting aside the stability of the individual detectors, we still want to know if this calculated value may provide a good proxy for the day time average counts. For this purpose we have included 4 data points calculated in the same manner as night time values, but

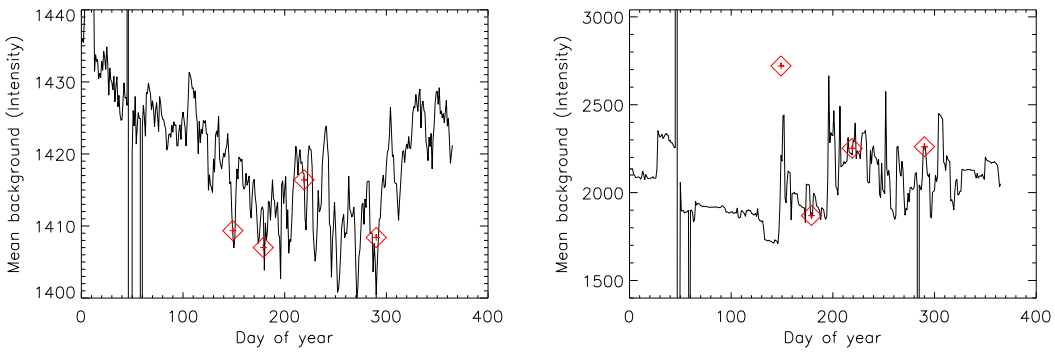

Figure 7.1: Mean overnight dark count values (black) for Las Campanas in 2009 with the port detector left and starboard right. Over plotted in red are the mean daytime dark counts for 4 days where the dome did not open.

for daytime data where the dome did not open due to bad weather. There is good agreement between the values which is encouraging. But, this ignores the fact that opening the dome will introduce additional temperature changes and of course Sunlight interaction with the spectrometer. So we accept that this measure has its limitations but provides a proxy for the variation in dark counts through the year. Next we consider the extinction coefficient.

7.1.2 Measuring atmospheric extinction coefficients

We have already stated that we require the value of the atmospheric extinction coefficient if we are to correct for its interaction with dark counts. The atmospheric extinction coefficient κ can be measured using the RSS intensity measurements, I_b and I_r, that are sensitive to, even dominated, by atmospheric extinction. But, these intensities contain a contaminating signal from the line-of-sight velocity. We can find the extinction coefficient using Bouger's method (detailed later) but first we must remove the velocity contribution. Atmospheric extinction has been modelled in earlier sections of this work simply as a reduction in intensity,

$$\frac{I}{I_0} = \exp(-\kappa A), \tag{7.4}$$

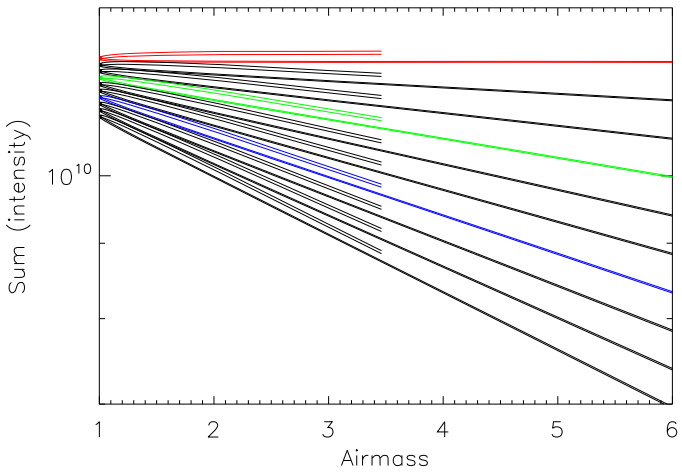

Figure 7.2: Simulated sums of $I_b + I_r$ as a function of airmass. Each line represents a different input extinction coefficient starting at $\kappa = 0.0$ and increasing in steps of 0.01, with the values 0.0,0.03,0.06 highlighted in red, green and blue respectively.

where A is the airmass. By simple manipulation we can see that

$$\ln\left(\frac{I}{I_0}\right) = -\kappa A. \tag{7.5}$$

Hence if we plot the left hand side (LHS) of this equation as a function of airmass, we expect to see straight lines where $-\kappa$ is the gradient. Figure 7.2 shows the fractional intensity for modelled data as a function of airmass through the day plotted on a log scale. Each line represents a different extinction coefficient starting at $\kappa = 0.0$ and increasing in steps of 0.01, with the values 0.0,0.03,0.06 highlighted in red, green and blue respectively. The modelled data has constant κ through the day and so the lines are expected to be straight. We see that this is true for values of airmass greater than 2. However, the station line-of-sight velocity interferes with the expected straight lines. For $A < 2$ the gradient in figure 7.2 deviates from the constant extinction coefficient input. This is caused the line-of-sight velocity bleeding into the sum during the middle part of the day. We can see this more clearly in the following plot.

Figure 7.3 shows the instantaneous value of the extinction coefficient from the gradients

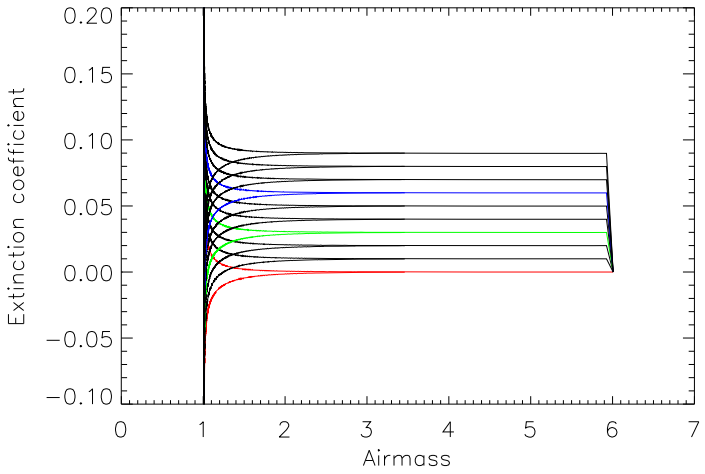

Figure 7.3: Instantaneous atmospheric absorption coefficient as a function of airmass. Each line represents a different extinction coefficient starting at $\kappa = 0.0$ and increasing in steps of 0.01, with the values 0.0,0.03,0.06 highlighted in red, green and blue respectively.

of the previous chart. We see that for $A > 2$ the returned values for κ are in good agreement with the model input. However, for $A < 2$ the interference of the velocity signal makes the returned values useless. Hence, before we measure a value for κ we should make efforts to minimise the velocity component bleeding into the sum.

To reduce the impact of the velocity component on measuring κ we consider how I varies with v_{los}. To a good first order approximation I is linear in v_{los}. Hence, we can use a straight line fit to I in terms of v_{los}, with the gradient detailing the variation in I.

By design we are using intensities that are sensitive to atmospheric extinction and relatively insensitive to v_{los}. As a result, any linear fit to intensity to account for velocity will suffer due to extinction. Most complications can be avoided if the fit of intensity to v_{los} is allowed only for regions of the day where atmospheric effects are at a minimum, which is achieved for $A < 2.0$.

In addition to the fit to velocity, we can use the reaction to the line-of-sight velocity of each intensity wing, I_b and I_r, which is nearly equal and opposite in nature. By removing the majority of the velocity component using a linear fit and then combining the two intensities as a sum, $I_b + I_r$, we have a measure that is insensitive to v_{los} but still a good

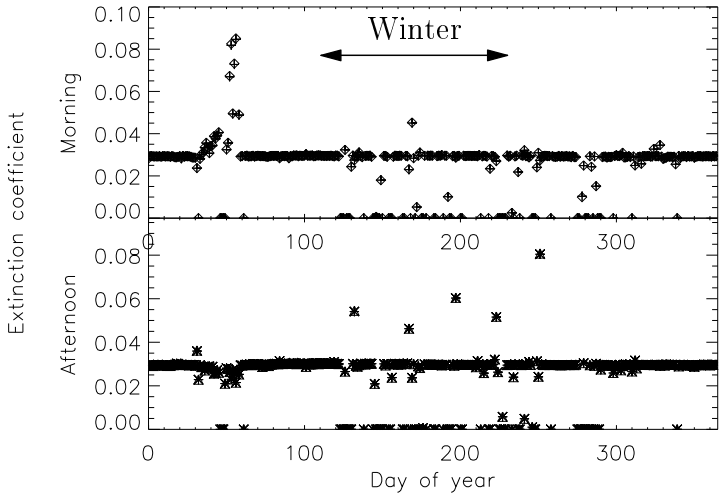

Figure 7.4: Atmospheric extinction coefficients through the year calculated from modelled RSS data with input extinction coefficient of 0.03.

measure of atmospheric extinction.

The final step in this sequence is to apply Bouger's method to the modified sum of the intensities. Bouger's method fits a straight line to the log of the measured intensity as a function of airmass. We utilise this here by applying Bouger's method separately to morning and afternoon data. We can test this method on modelled data with constant input for atmospheric extinction coefficient.

Figure 7.4 shows the atmospheric extinction coefficient determined by Bouger's method when applied to the sum of intensities modified to remove velocity components. The top plot shows morning data and the bottom afternoon, with each plot displaying both port and starboard values. The data show mostly good agreement with the model input value of $\kappa = 0.03$. Disagreement between input and returned values are due to gaps in the measured data, caused by bad (modelled) weather, that cause inaccuracies in the correction of the velocity component, particularly in the section of data at around 50 days.

This method gives us the ability to measure κ, albeit with complications due to bad weather. The types of days on which this method fails are days with shorter sections of data and for that reason have a reduced need for correction, i.e. their impact in any long time series will be reduced. We can proceed to consider real data.

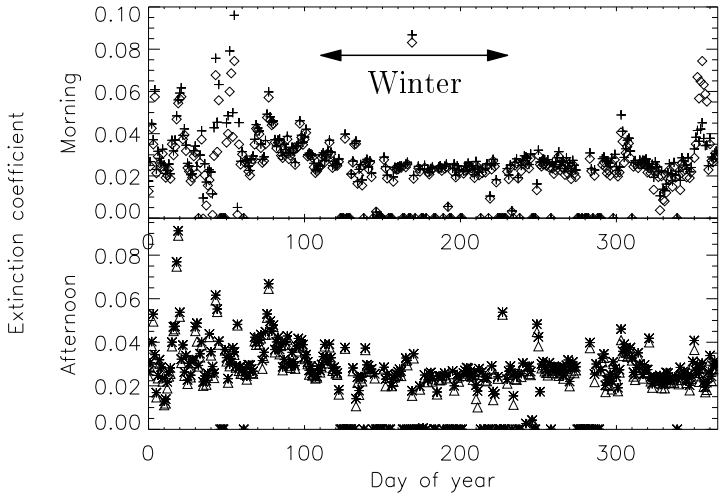

Figure 7.5: Atmospheric extinction coefficients through the year calculated from real data of Las Campanas station year beginning 01/01/2009.

Figure 7.5 shows the method under consideration applied to real data for Las Campanas 2009, i.e. the same circumstances used for modelled data. Again the top panel shows morning data and the bottom is afternoon with both port and starboard detectors shown. The data show results with good stability from day to day, ignoring the section of data around 50 days we know to be compromised. The data show better stability in winter and decreased stability during the summer months which is consistent with the anecdotal description of the stations seasonal variation. This then, provides a satisfactory measurement of κ.

We have all we need to calculate the impact of dark counts coupled with extinction in the BiSON RSS ratio. To demonstrate this effect we introduce the definition of inverse sensitivity, that is the rate of change of velocity with respect to ratio, $\mathrm{d}v/\mathrm{d}R$, given in units of m s^{-1}. This measure is then the gradient in a ratio against velocity plot and a change in sensitivity will rotate the ratio velocity curve about the origin.

Figure 7.6 on the next page shows the expected reduction in inverse sensitivity due to dark counts coupled with extinction. The data show that any changes in sensitivity are small (a few m s^{-1}) for the well behaved port detector but in excess of 12m s^{-1} for the starboard detector where dark counts contribute as much as 2% to the total count. It is

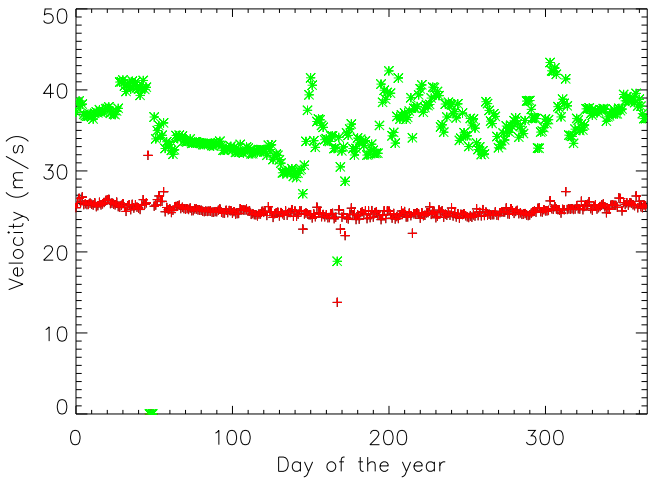

Figure 7.6: Inverse sensitivity reduction due to dark counts coupled with extinction through the year 2009 for Las Campanas A instrument, calculated at fixed ratio, $R = 0.2$.

straightforward to demonstrate what this change in sensitivity does to the ratio velocity curve.

Figure 7.7 on the following page shows the impact of dark counts as a percentage of total counts in the measured ratio. Clearly a change in sensitivity due to a change in background counts is capable of creating width in the ratio velocity curve. This width can been seen to be monotonically increasing as we move further away from the origin. However, the total width in the real data displayed in figure 6.14 of the previous chapter requires a variation in sensitivity of the order 150 and 250 $\mathrm{m\,s^{-1}}$ for the port and starboard detectors respectively. While the background counts contribute a signal, it is significantly less than that required to explain the observed lack of correspondence in the ratio velocity curve.

We have then, a signal of unknown origin that is not explained by a model of the interaction of the Sun-atmosphere and instrument. This signal prevents the application of seasonal calibration of the BiSON day - as opposed to the current daily calibration. For now we stick with matter at hand, the presence of effects of (known) atmospheric origin that manifest in BiSON measurements. We will return to the signal unidentified origin in the next chapter.

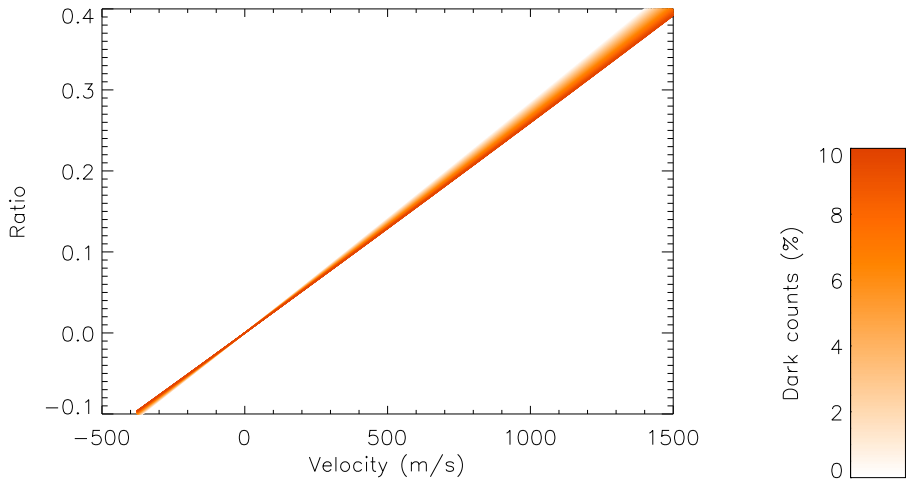

Figure 7.7: The impact of changes in inverse sensitivity due to dark counts and atmospheric extinction in a season ratio-velocity curve.

7.2 A correction for differential extinction.

Differential extinction has been detailed in a number of places in this work already (see 3.3 on page 50). To recap briefly, differential extinction is a pseudo velocity signal that enters BiSON residual velocities because atmospheric extinction varies with position on the solar disk which depends on the alignment of the extinction gradient relative to the solar axis of rotation and the magnitude of the gradient. In the previous chapter, we retrieved the form of differential extinction from modelled data. We now begin to look for a correction to this effect. First we ask the question: what is the impact in the power spectrum of differential extinction?

Figure 7.8 shows the differential extinction signal in the time and the generated residual signal in the frequency domain. The left figure shows the differential extinction shape - determined and displayed in the previous chapter (figure 6.9 on page 126) - for extinction coefficients starting at $\kappa = 0.0$ and increasing in steps of 0.01. Three cases have been highlighted with $\kappa = 0.0, 0.03, 0.06$ in red, green and blue respectively. The right figure shows the power spectrum of the residuals generated from a third-order polynomial fit and calibration to the modelled ratio for the same values of κ.

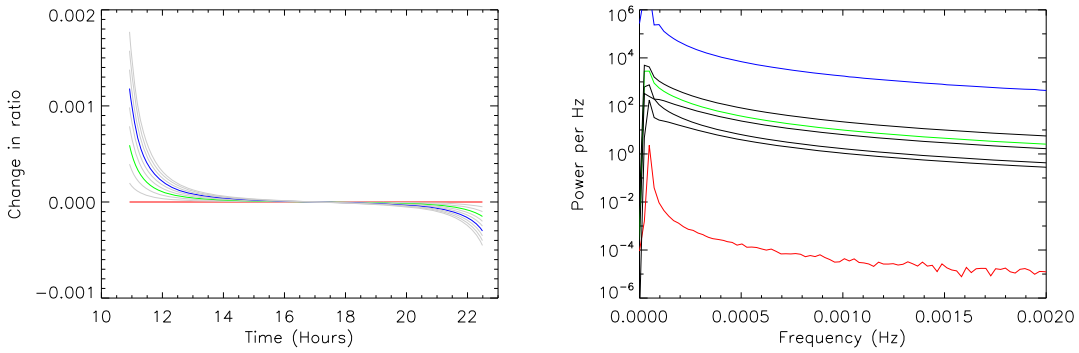

Figure 7.8: Differential extinction signal generated from modelled data. Shown in the time domain (left) and the generated residual signal in the frequency domain (right).

Figure 7.8 says two things about differential extinction. One; differential extinction introduces significant amounts of low-frequency noise, and two; the amount of noise is not linearly proportional to the amount of differential extinction. The first point is the motivation for studying a correction for differential extinction. The second point tells us something about the existing data reduction pipeline.

The BiSON pipeline typically fits a third-order polynomial to measured ratio that includes differential extinction. But the characteristic shape of a third-order polynomial is not a good fit to the differential extinction shape. One can simplify this statement by considering fitting a second or even first order polynomial to the differential extinction. As the fit acts to minimise χ^2, the resulting parameters will describe a function that scythes through the middle of the differential extinction. So fitting a third-order does not remove differential extinction, in fact it modifies the shape of the original function to satisfy a minimum in χ^2. This is why the low-frequency noise produced is not a linear function of the extinction coefficient.

From modelled data, we expect differential extinction to produce a systematic effect that varies in magnitude depending upon the atmospheric absorption coefficient. This type of effect presents an opportunity for a correction that will remove or at least minimise its impact. To achieve this we will construct a mathematical model for differential extinction that will be applied in later sections.

7.2.1 Differential extinction model

The problem of differential extinction has been studied previously (see Grec and Fossat [1979], Belmonte et al. [1988], McLeod and Isaak [1988]). It is common to seek a model for differential extinction that takes the magnitude of the atmospheric transmission gradient T'/T and multiplies this by the sine of the angle between this gradient and the rotation axis of the Sun. Including some constant, $A_{\rm inst}$, to account for the instrumental sensitivity gives a generic model for the velocity component of differential extinction as

$$v_{\rm dext} = A_{\rm inst}\frac{T'}{T}\sin(q \pm P_a), \tag{7.6}$$

where q is the parallactic angle and P_a is the position angle. The ambiguity in the plus or minus of these angles comes from an ambiguity in definition. Here we define the position angle such that the angle between the transmission gradient and the solar rotation axis is $q - P_a$.

Ehgamberdiev and Khamitov [1991] realised that the instrumental 'fudge' factor, A, would not remain constant through the year and so modelled this parameter in commendable detail. The result of this work was a complicated function containing many constants that attempted to describe the solar line function weightings but crucially not the instrumental effects. Earlier work in this thesis produced the instrumental weightings of a BiSON RSS from fundamental principles and we may now rework the modelling of differential extinction with this increased knowledge.

Here we make a subtle but necessary change to the approach of previous authors, we will derive a correction in terms of ratio not velocity. Previous work has adjusted the calibration procedure so that v_{los} includes the pseudo velocity from differential extinction. Here we will derive an additional function that may be fitted to data at the same time as a third-order polynomial. This allows for the possibility of free parameters in the fit to account for instrumental fudge factors and poorly known atmospheric extinction coefficients.

Given that we consider the existing model in velocity to be sensible, we can straightforwardly transmute previous work to suit our needs by describing differential extinction in terms of a ratio:

$$r_{\text{dext}} = A_{\text{inst}} \frac{T'}{T} \sin(q - P_a), \tag{7.7}$$

but we must expand this expression to make it meaningful.

We have a model for the atmospheric transmission function that can be expressed in terms of zenith angle (see chapter 3)

$$T = \exp\left(-\kappa A\right) = \exp\left(-\kappa \frac{1}{\cos(z) - 0.50572\left(96.07995 - z\right)^{-1.6364}}\right), \tag{7.8}$$

where the zenith angle z must be given in degrees. This gives the magnitude of the atmospheric transmission gradient with respect to z as

$$\frac{T'}{T} = \frac{\mathrm{d}T}{\mathrm{d}z} . \frac{1}{T} = -\kappa \left(\frac{0.82756}{w^{2.6364}} - \sin(z)\right) \left(\frac{0.50572}{w^{1.6364}} + \cos(z)\right)^{-2}. \tag{7.9}$$

where $w = 96.07995 - z$. For convenience we will express the above as two terms giving

$$\frac{T'}{T} = -\kappa\beta(z). \tag{7.10}$$

This then gives our model in terms of ratio as

$$r_{\text{dext}} = -A_{\text{inst}}\, \kappa\beta(z) \sin\left(q - P_a\right). \tag{7.11}$$

As we have seen in the previous section it is troublesome to measure the atmospheric extinction coefficient κ, but we require this value for equation 7.11. In addition, we require the weighting fudge factor. It is therefore sensible to combine two separate unknowns to form a single unknown, here as α. We then have a correction that is a function of zenith

angle, parallactic angle, and position angle with a single free parameter α,

$$r_{\text{dext}}(z, q, P_a) = \alpha\beta(z)\sin(q - P_a)\,. \tag{7.12}$$

This provides us with a function that can be combined with a third-order polynomial to describe the measured ratio

$$r(v, z, q, P_a) = \sum_{j=0}^{3} a_j v^j + \alpha\beta(z)\sin(q - P_a)\,. \tag{7.13}$$

It is first prudent to demonstrate the efficacy of this correction on modelled data, after this we will work with real data.

7.3 Correcting modelled data

Following on from the previous section, we now have a modelled correction to account for differential extinction. And from the previous chapter, we know the form of differential extinction from the modelling of RSS measurements. We start by comparing the two results to establish consistency.

To compare both modelled forms of differential extinction we will fit the simple approach taken in equation 7.12 to the differential extinction shape predicted by the full RSS model. Fitting is performed using the Levenburg-Marquardt routine, a robust non-linear least squares fit. We do not consider the errors in the fit parameters as the error in the modelled ratio is an unknown. We can consider just the differential extinction shape for two example days,

Figure 7.9 shows the modelled RSS data correction (black) hidden by the fitted differential extinction model (red), with the residuals of the fit shown below. Two example days are shown at opposite points in the year, 14/01/2009 and 11/06/2009, for the Las Campanas station. The data show the model to be a reasonable fit to the data with the differential extinction reduced to less than 10% of its original value.

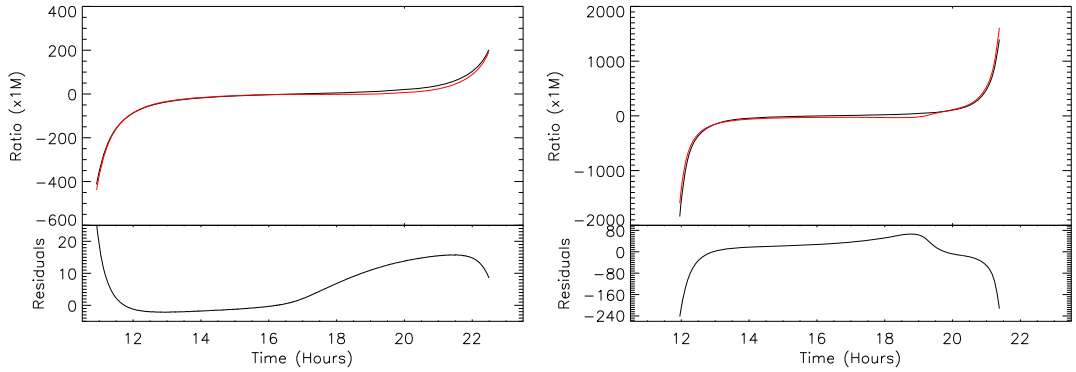

Figure 7.9: Fits of the differential extinction model to the modelled RSS differential extinction signal for the Las Campanas station 14/01/2009 (left) and 11/06/2009 (right).

Normally one would examine the fit residuals and consider a modification or addition to the model, but not here. The inclusion of a third-order polynomial fit is implicit in the final application of any correction and it is desirable to keep the interaction between the two functions - differential extinction and third-order polynomial - to a minimum. By leaving the shape of the correction tightly constrained we avoid unnecessarily increasing the number of local minima in χ^2. We can now look at how this combined fit performs when considering the modelled ratio including differential extinction.

Figure 7.10 left shows the modelled RSS ratio (black) and the third-order polynomial with differential extinction fit (red) with the residuals shown below. The right hand panel displays the power spectrum for three possibilities: the differential extinction shape uncorrected (+); differential extinction shape corrected with the differential extinction model($*$); and the modelled RSS ratio including differential extinction corrected with a combined fit of the third-order polynomial and differential extinction correction($\diamond$). The data show that the addition of the polynomial reduces the magnitude of the residual ratios. In the power spectrum, the low-frequency noise is reduced by first the correction for differential extinction and then the introduction of the polynomial. The noise-reduction at 1 mHz is at least a couple of orders of magnitude for each step. This provides an example of a best case scenario, and so we consider next a typical day.

Figure 7.11 shows the same information as 7.10 but for Las Campanas 11/06/2009.

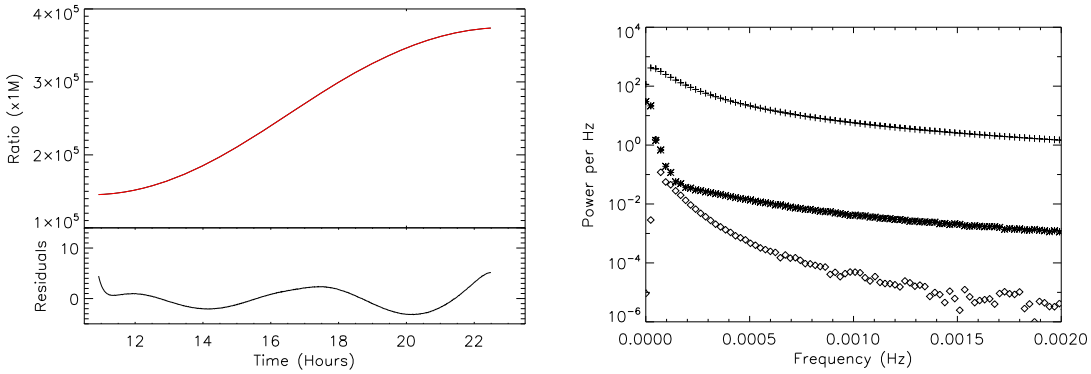

Figure 7.10: Fit of a third-order polynomial plus differential extinction correction to the modelled RSS ratio for the Las Campanas station 14/01/2009. Data and residuals in the time domain on the left and residuals in the frequency domain on the right. In the power spectrum residuals from: just the differential extinction signal (+); the fit of the correction to just the differential signal (∗); and the fit of the third-order polynomial and correction to the modelled RSS ratio including differential extinction (⋄).

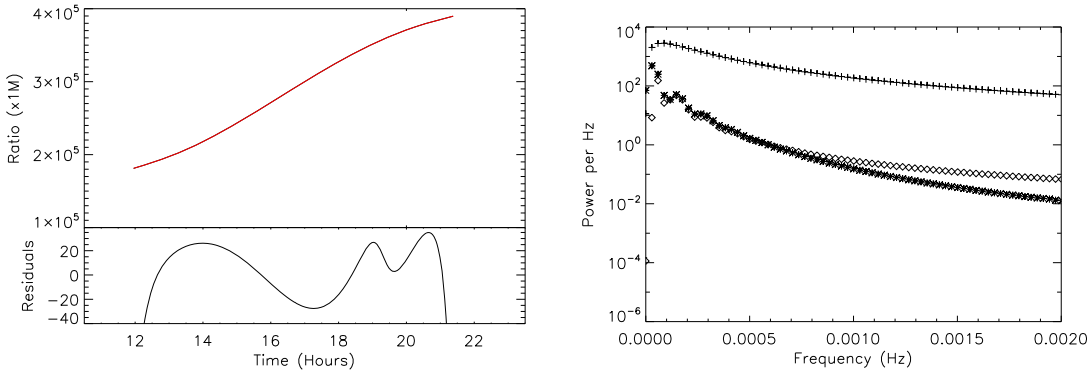

Figure 7.11: Fit of a third-order polynomial plus differential extinction correction to the modelled RSS ratio for the Las Campanas station 10/06/2009. Data and residuals in the time domain on the left and residuals in the frequency domain on the right. In the power spectrum residuals from: just the differential extinction signal (+); the fit of the correction to just the differential signal (*); and the fit of the third-order polynomial and correction to the modelled RSS ratio including differential extinction.

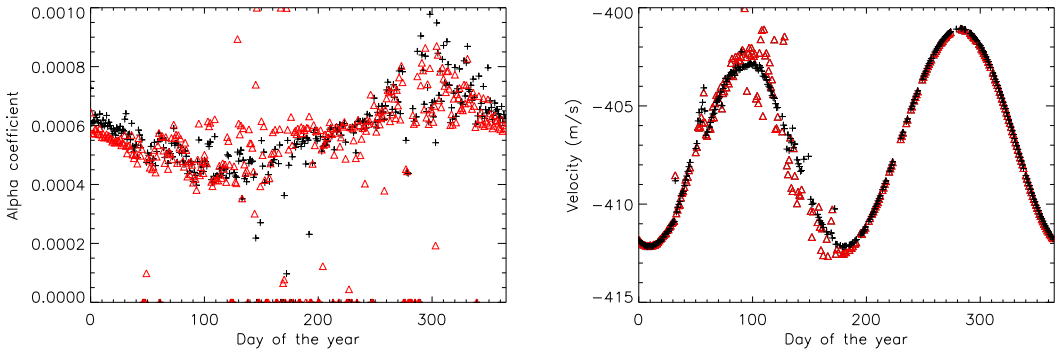

Figure 7.12: Fit coefficients for a third-order polynomial and differential extinction correction applied to simulated data. Left: The alpha coefficient for the fit to differential extinction signal only (black) and the treatment of the full ratio including differential extinction (red). Right: The δV solution to the third-order polynomial for the fit to ratio with (red) and without (black) a differential correction.

In this application the addition of the polynomial in the fit actually increases the low-frequency noise, albeit by a relatively small amount. But noise levels are still significantly reduced when compared to an uncorrected differential extinction shape. The analysis here is slightly disingenuous in that we are hinting at a comparison with uncorrected differential extinction. In reality, the noise produced by uncorrected differential extinction will be mitigated to some degree by a polynomial fit to the ratio. However, the noise due to differential extinction found in residuals from a third-order polynomial fit is very sensitive to regions of the day considered, by a number of orders of magnitude. We will give proper consideration to the reduction in noise from uncorrected to corrected data but this is best achieved when considering the noise distribution of real data. Next we consider the variation of the fit coefficients through the year.

Figure 7.12 shows the variation of the calibration fit coefficients through the year. The left chart shows the α coefficient for the differential extinction correction fitted to just the differential extinction shape (black +) and the polynomial plus correction fitted to the modelled RSS ratio (red triangle). The right chart gives δV, the velocity solution to the third-order polynomial

$$R = \sum_{j=0}^{3} a_j v^j, \tag{7.14}$$

where R is a ratio value selected such that most days through the year contain that value. This choice minimises extrapolation and for Las Campanas modelled data is set $R = 0.2$. Two δv data sets are shown, black data points for calibration with just the polynomial and red points for calibration including the differential extinction correction.

The data in figure 7.12 show a reasonable agreement in terms of the underlying trend between the calibration with correction and the control data sets. However, it is clear that there is interference between the third-order polynomial and the differential extinction correction. Days 50 to 175 show examples of the fit finding local minima around the starting estimated parameters. This can be mitigated by selecting good starting values for the fit which then return results consistent with uncorrected data, as can be seen in the second half of the year.

We have applied a differential extinction correction to modelled data that provides an opportunity for a significant reduction in noise due to this effect. We know now that the application of the correction to real data is expected to be sensitive to the fitting starting parameters. In this sense we cannot expect the correction to be perfect, instead we target a reduction in noise rather than elimination. We can now go on to apply this correction to real data.

7.4 Correcting real data

Application of a differential extinction correction to real data requires some modification to the implementation applied to sterile modelled RSS data. Of course, we are unable to isolate the differential extinction signal from velocity changes in real data which means we have no comparison for fit coefficients. The figure of merit for the correction must be the low-frequency noise observed in the power spectrum.

It is expected that the atmospheric absorption coefficient κ will vary from the morning to the afternoon and hence, so will α. Here we can take advantage of the shape of differential extinction as the model provides a significant correction at only the ends of a day - the

correction is insensitive to variations in κ during the middle of the day. Hence, we are able to define an α coefficient in the morning α_m and then a modifier coefficient $m_{\rm dex}$, such that

$$\alpha_{\rm afternoon} = \alpha_m m_{\rm dex}. \tag{7.15}$$

This adjustment is a reduction in the number of constraints on the model, but the shape of the differential extinction in each half of the day remains fixed - only the magnitude may change - which should be constraint enough. The point of transition from morning to afternoon - in terms of the alpha coefficient - is simply defined by

$$\sin\left(q - P_a\right) = 0. \tag{7.16}$$

This eliminates any discontinuity due to the discrete change in parameters.

The modifier parameter describes the change in atmospheric conditions between the morning and afternoon. Considering all BiSON stations and each of their own unique atmospheric anomalies - normally caused by dust or sand overland, or water vapour over sea - it is hard to conceive a condition where this modifier should stray from the region $0.05 \leqslant m_{\rm dex} \leqslant 20$. Therefore, the modifier parameter is constrained in the fit to these given values.

We have enough information now to apply the correction to real data. First we consider a single day of data, 14/01/2009 from the Las Campanas station. In order to display the differential extinction signal in real data we must make an adjustment to the regions of data considered. Without a correction for differential extinction, it was necessary to remove the ends of each day to minimise the noise seen in calibrated data. To show the impact of our correction we include end of day data not normally passed.

Figure 7.13 shows residual velocities (left) and their power spectra (right) for uncorrected (top) and corrected (bottom) data. The differential extinction signal is clear in the uncorrected residuals, albeit with a shape modified by the polynomial fit. The corrected residuals do not contain a differential extinction shape. A comparison of the two power

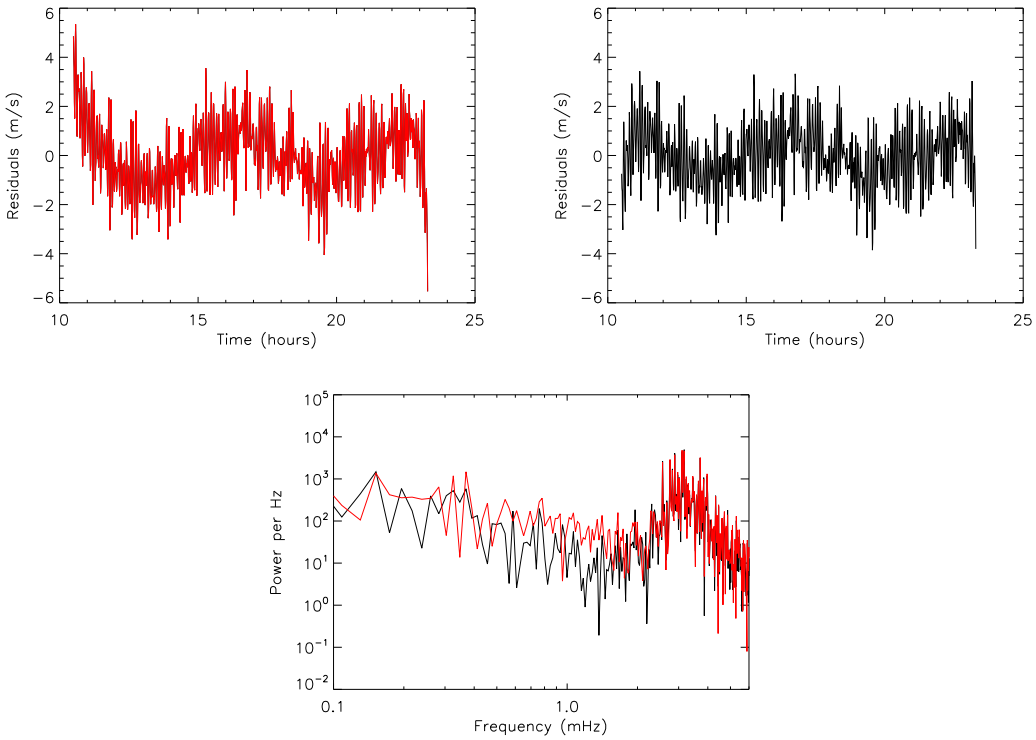

Figure 7.13: Calibrated data for the Las Campanas station 14/01/2009. Top left: residuals calibrated without the differential extinction correction and shown in the time domain. Top right: residuals calibrated with the differential extinction correction , again shown in the time domain. Bottom: Comparison of the uncorrected (red) and corrected (black) data in the frequency domain.

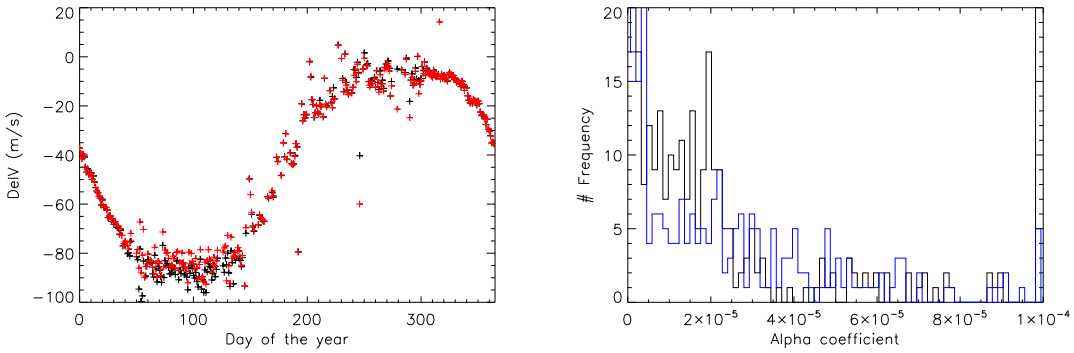

Figure 7.14: Fit coefficients for a third-order polynomial with differential extinction correction applied to real data. Left: δV the solution to the third-order polynomial, for the calibration with (red) and without the differential extinction correction. Right: histogram of the morning (black) and afternoon (blue) alpha coefficients from the calibration.

spectra shows that noise in the band $0 - 1$ mHz is significantly reduced. We will delay discussion of the noise reduction in a quantitative manner until we have considered more than a single day.

Having considered a single day we move on to apply the correction to a whole year of data. The two populations of corrected and uncorrected data can be used to show the effect of the addition of the differential correction. An important comparison between the two data sets are the fit coefficients returned. We consider these now.

Figure 7.14 shows the fit coefficients from data calibration for the year starting 01/01/2009 at the Las Campanas station. The left hand plot shows the δV formed from the third-order polynomial coefficients of the fit with the uncorrected data set shown in black and corrected in red. The right hand plot displays the histogram of the alpha coefficients for morning (black) and afternoon (blue). The data show that the polynomial fit is largely unaffected by the addition of the differential extinction correction, the exception being the region from 50 to 150 days which corresponds to the same region of disagreement in δV seen in modelled data.

The distribution of alpha coefficients show two points of interest. Firstly there are significant number of days that show values at the extreme ends allowed by the fit, zero and 1×10^{-4}. These values represent days that have little or no data at dawn and dusk that

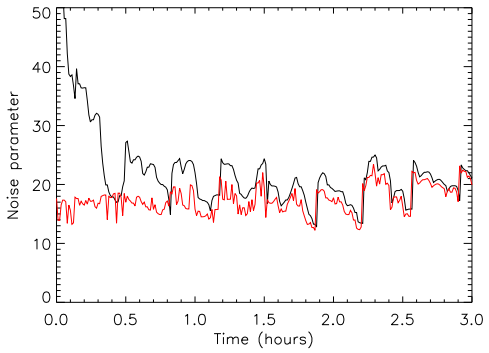

Figure 7.15: Noise parameter as a function of time from sunrise of the point of data rejection for calibration with (red) and without (black) differential extinction correction.

would otherwise provide good constraint. As we have already discussed, the fit of the differential extinction correction is sensitive to the ends of the day but insensitive to the middle of the day. On days with little constraining data, the fitting routine will allow the alpha coefficient to vary wildly without significant impact in the χ^2. This is nothing to be concerned about because of the lack of impact.

Secondly, we can compare the peak of the two distributions from real data with the values of alpha generated from simulated data. We can see there is a vague maximum in both morning and afternoon alpha values at 2×10^{-5}. The mean value generated from simulated data is 1.8×10^{-5} giving good agreement between the two. We can now move on to discuss the quantitative aspects of the reduction in noise.

When discussing a reduction in the low-frequency noise parameter - the sum of the power in the frequency band $0.8 - 1.3$ mHz - we must be cautious about our comparisons. Any observed reduction in noise is sensitive to the regions of a days data included in the analysis. We do not expect to see a reduction in noise from the addition of the proposed correction for regions of data a couple of hours either side of midday. On the other hand, if we consider a full day of data we would expect maybe a 60% reduction in noise.

Figure 7.15 shows the low-frequency noise parameter for 14/01/2009 at the Las Campanas station as a function of the length of time rejected from the start of the day. Uncorrected data are displayed in black and corrected in red. The data show an under-

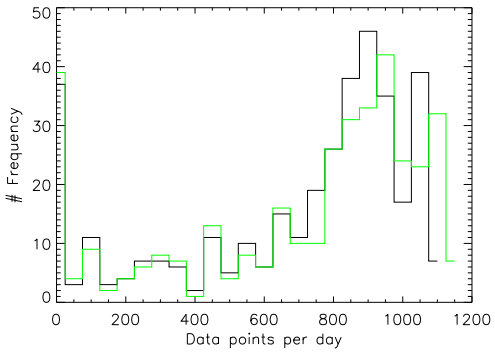

Figure 7.16: Histogram of data points per day for two regimes of regions, traditional (black) and liberal (green) over the year starting 01/01/2009 for the Las Campanas station.

lying trend with some periodic noise over the top. The 'noise' comes from end effects caused by solar oscillations producing noise in the FFT process. Ignoring this noise, we can see that low-frequency noise reduction from the addition of the correction is much greater with less data removed, as expected. The impact of the correction is significantly reduced when more that an hour of data is rejected.

We note from figure 7.15 that the corrected data are not sensitive to the length of the day considered. Each day of BiSON data has been manually processed to include regions of good data unaffected by cloud interruption or differential extinction. The introduction of a correction for differential extinction changes the requirements of the regions set for each day. Again using the year beginning 01/01/2009 and Las Campanas data, a new set of regions were created with the extreme ends of each day included rather than rejected.

Figure 7.16 shows the histogram of the number of points included in each day. Traditional regions set to exclude differential extinction are shown in black and the new liberal regions displayed in green. The increase in fill due to the extension of regions is 2.7 %. We can now compare the low-frequency noise parameters returned with and without a differential extinction correction for each day with the two different regions settings.

Figure 7.17 shows the noise distributions of a year of data starting 01/01/2009 at the Las Campanas station. The left hand chart shows the results with the traditional regions

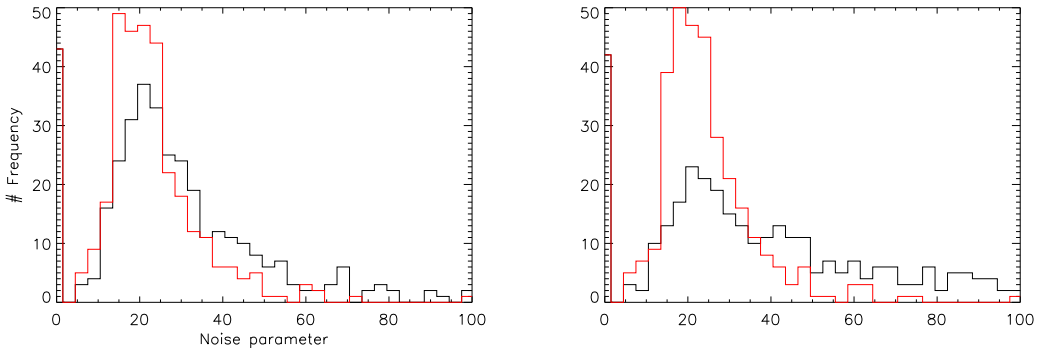

Figure 7.17: Histogram of the noise populations in two different region regimes (traditional left and liberal right) calibrated with (red) and without (black) the differential extinction correction.

and the right hand side with the liberal regions. Data without the differential extinction correction are shown in black with corrected data in red. It is clear that in both charts the data show a reduction in the mean low-frequency noise value, when corrected for differential extinction, for both populations of region data.

More than just a reduction in low-frequency noise, the correction for differential extinction produces two distributions of noise, for the different types of region used, that are not wildly dissimilar. The distribution of noise for the liberal regions is slightly shifted to higher noise than for the traditional regions but this shift is perhaps compensated for by the 2.7% increase in fill.

We will consider the fill to be a proxy for signal in a time series and hence, we can construct a parameter that describes the signal-to-noise ratio (SNR) of a long time series of data. This SNR provides a value that can be calculated and even maximised in a days region parameter space.

7.4.1 Trimming

In an effort to reduce the impact of differential extinction, prior to the advent of a correction, a technique called 'trimming' was developed to maximise the signal to noise parameter by reducing the amount of data passed through the calibration pipeline at the

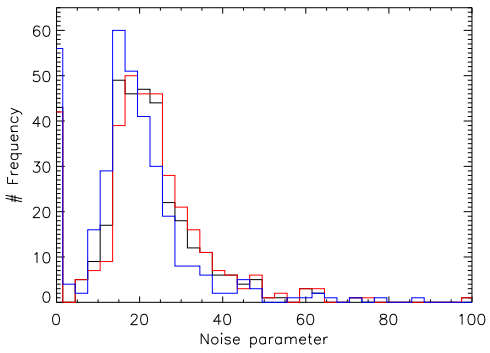

Figure 7.18: Histogram of noise populations for three different region regimes: traditional in black; liberal in red; and trimmed in blue.

extreme ends of the day. With the inclusion of the correction for differential extinction the technique of trimming has a significantly reduced impact in noise reduction. However, more data can now be included at the extreme ends of the day giving an increase in signal for a similar value of noise. Trimming it seems is still useful.

Application of the trimming procedure is a brute force method that calculates the noise - the mean value of the power in the power spectrum over the range in frequency $0.8 - 1.3$ mHz - as a function (and for all sensible values) of the number of points included. The technique is applied separately in the morning and the afternoon and as a result is computationally intensive. Numerical algorithms that would significantly optimise the path taken to a maximum value, are foiled by a number of deep local minima caused by discontinuities at the end of each day, that are of course dependent on the independent variable.

Despite being an unwieldy tool, trimming does provide a reduction in the mean value of the noise distribution through out a year.

Figure 7.18 shows the three noise distributions calibrated using the differential correction for the traditional regions(black), the liberal regions(red) and the trimmed (or optimised) regions(blue). The data show a clear shift in the distributions towards lower noise for the trimmed data set. One should be wary of over parametrisation, that is assigning a simplistic value to describe a more complex system. To sanity check the results here

we complete this chapter by presenting the three long time series produced by the three methods displayed in fig. 7.18.

7.4.2 Time series

Figure 7.19 on the next page shows three power spectra generated with a year of data (2009) from the Las Campanas A instrument. The three power spectra show the noise levels for each of the three regimes of region discussed above: traditional regions without differential extinction correction top; liberal regions middle; and optimised regions bottom. It is not important as to whether or not this mode or that mode is visible in the spectra, rather that the average noise levels are clearly distinguishable. Quantitatively, the results for each of the regions are: traditional regions with fill of 29% and noise of 29.35 $m^2\ s^{-2}\ Hz^{-1}$; liberal with a fill of 32.85% and noise of 24.64 $m^2\ s^{-2}\ Hz^{-1}$; and trimmed with a fill of 32.70% and noise of 24.13 $m^2\ s^{-2}\ Hz^{-1}$.

It is incontrovertible that the addition of the differential extinction correction reduces the low-frequency noise and allows for the acceptance of more data at the extremes of the day, which increases the fill. There is support for a reduction in noise from the addition of the trimming technique but this effect is far less dramatic.

Having satisfied ourselves that we can apply a correction for the impact of atmospheric extinction we return in the next chapter to tackle the annual velocity signal of unknown origin.

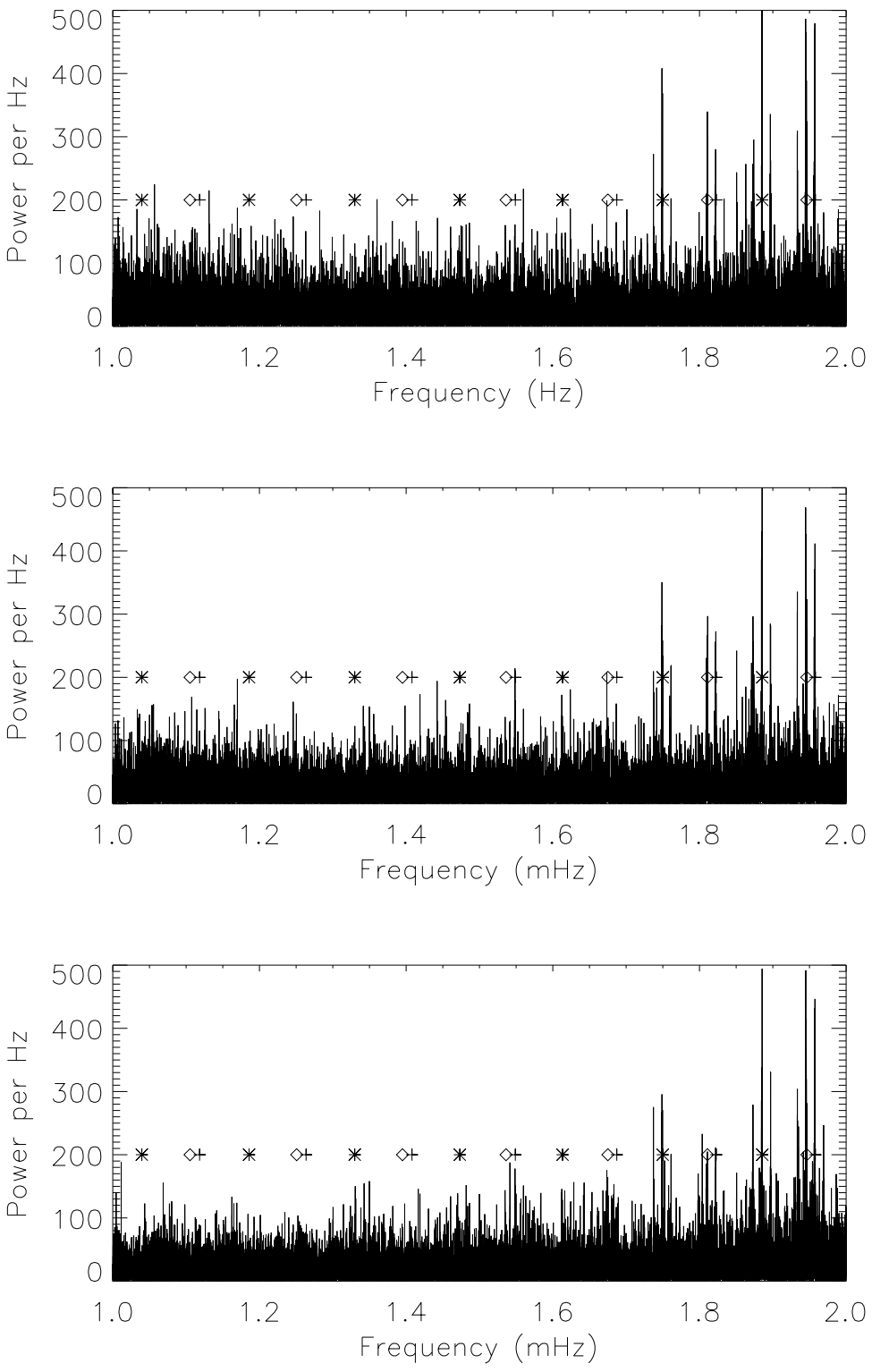

Figure 7.19: Power spectra for the three calibration regimes: Top - traditional regions without differential extinction correction; middle - liberal regions with differential extinction correction; and bottom - trimmed (optimised) regions with differential extinction correction.

Chapter 8

BiSON inference on long timescales

In Chapter 6 we presented a disagreement between the model of an RSS and the real data: there is a lack of correspondence in the ratio-velocity (RV) curve for observations not seen in modelled data. This lack of correspondence hampers efforts to produce residuals calibrated over a season rather than a single day. The motivation for a seasonal calibration is the ability to observe signals of solar origin at very low frequencies (< 0.2 mHz). Here we return to the problem of lack of correspondence to study the characteristics of the process that generates the width in the RV curve.

8.1 Introduction

When calibrating BiSON data, we assume that the measured ratio is a function of line-of-sight velocity between the spectrometer and the Sun. We would like to believe that the ratio has only this one independent variable and hence we calibrate data on a daily basis with the application of a third-order polynomial fit in velocity

$$r(v) = \sum_{i=0}^{3} a_i v^i. \tag{8.1}$$

However, studying the yearly RV curve we see that there is width, or a lack of correspondence, in the resulting line. This width is evidence of a second dependence - another

independent variable. But what is the magnitude of this width?

Figure 8.1 on the following page shows the RV curve for modelled (red and green for port and starboard respectively) and real data (black). The width of the real data curve can be expressed as a velocity - even if it is simplistic to assign the width to processes in just the velocity axis - which is of order magnitude 100 m s^{-1}. The width in modelled data can be seen to be some ten times smaller than this. In addition to the modelled observed differences, the width is of a different magnitude for the port and starboard detectors as well as the maximum width appearing at different times of the year - which is the equivalent of saying differing orbital velocities.

Given that we can clearly identify a signal of unknown origin - the cause of our lack of correspondence - and that it does not appear in modelled data, we are left with questions. Is there something missing in our model that can generate this effect? Can we explain the effect in terms of an instrumental alignment issue? And, is there a problem with a model input, perhaps the solar line function?

We will continue by investigating the properties of the signal of unknown origin, but first, it will be useful for later work to measure the integrated solar line observed by BiSON RSS.

8.2 Integrated solar line

BiSON RSS instruments make intensity measurements over a narrow band in wavelength around some wavelength on the integrated solar line. We can show the approximate shape of the mean integrated solar absorption line using an intensity-velocity (IV) curve, where each measurement of intensity, using data from many days, is displayed at the line-of-sight velocity between the observer and source. In addition, we split the two measurements I_b and I_r by the value of the magnetic field strength given in units of velocity, 2600 m s^{-1}. This IV curve traces out the shape of the solar line but is severely contaminated by the effects of atmospheric extinction. To reduce the confusion caused by atmospheric

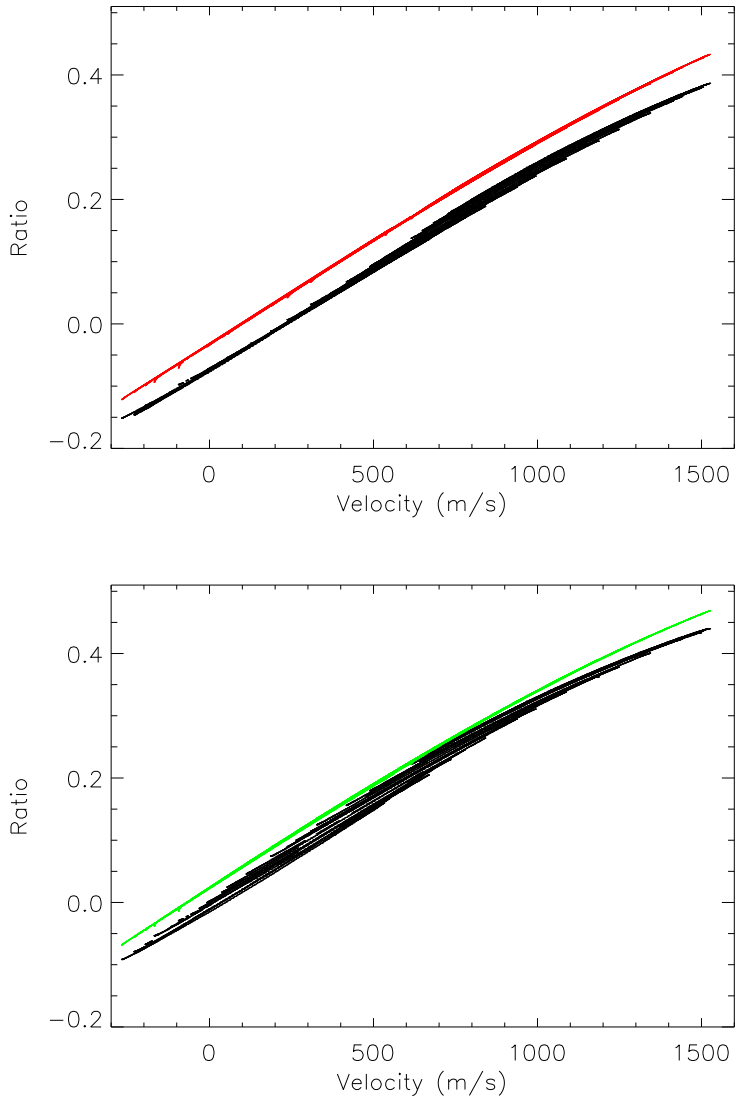

Figure 8.1: Ratio as a function of line-of-sight velocity - an RV curve - for modelled (red - port, green - starboard) and real (black) Las Campanas 2009 data. For aesthetic purposes, only every tenth day is displayed.

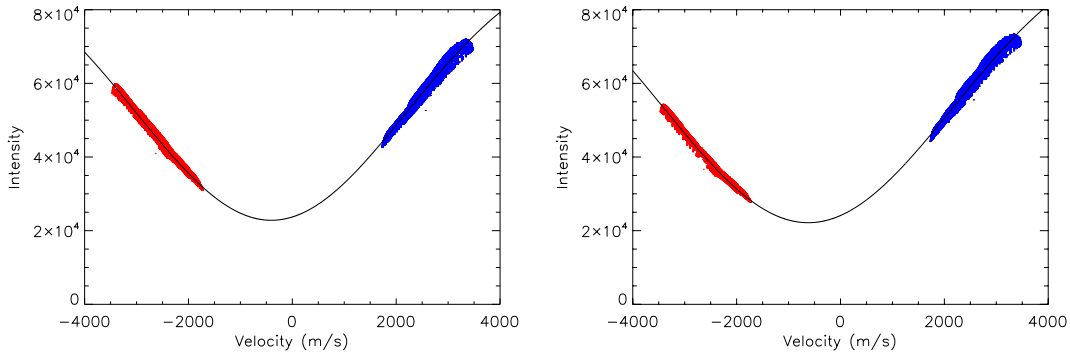

Figure 8.2: Intensity velocity (IV) curve for Las Campanas year starting 01/01/2009. Intensity wings are displayed split by the magnetic field strength, 2600 m s^{-1}, and with the fitted integrated solar line Gaussian. Right: port detector Left: starboard detector.

extinction, data are cut by passing values only where the summed intensity is within 99.99% of the daily maximum.

Given that the IV curve traces out the solar line, we can fit a basic model of the integrated solar line to the intensity data in terms of velocity v. To prevent over complication, something that would only hamper efforts in later work, we model the integrated solar line as a Gaussian with symmetry about the mean value in velocity. This model is expressed algebraically as

$$I = I_0 - \Gamma \exp\left(\frac{-z^2}{2}\right), \tag{8.2}$$

where I_0 is the intensity of the continuum away from the solar line, Γ is the depth of the solar absorption line and z is a parameter describing the mean μ and width σ of the line where

$$z = \frac{v - \mu}{\sigma}. \tag{8.3}$$

We can proceed by fitting this to the IV curve.

Figure 8.2 shows the yearly IV curve starting 01/01/2009, for the BiSON Las Campanas station. The port detector is shown on the left and starboard on the right. Plotted over the top of the intensity measurements are the symmetric Gaussian lines - fitted using the Levenburg-Marquardt robust non-linear least squares fit - to model the solar integrated

Parameter	Port	Starboard	Modelled port	Modelled starboard
Mean offset (μ m s^{-1})	-405 ± 1	-624 ± 1	-541.64 ± 0.02	-717.85 ± 0.03
Depth ($\frac{\Gamma}{I_0}$)	0.77 ± 0.01	0.78 ± 0.01	0.78056 ± 0.00001	0.78056 ± 0.00001
Width (σ m s^{-1})	2627 ± 6	2762 ± 4	2878.9 ± 0.2	2871.7 ± 0.2

Table 8.1: Returned fit parameters for a Gaussian absorption line fitted to the Las Campanas 2009 IV curve.

absorption line.

The accuracy of the fitted line is compromised both by the use of a symmetric Gaussian and the confusion created by atmospheric extinction, which generates significant systematic error. However, as a guide for the approximate values of the integrated solar line this will suffice. The same process of fitting is applied to modelled data without atmospheric effects included. The returned parameters for real data and modelled data are given in table 8.1.

The difference between the integrated solar lines of modelled and real data are significant for the mean offset and one sigma width parameters but not for the depth. Of course, the RSS model is sensitive to the input parameters for the solar line for each pixel. Comparing the returned integrated solar lines would be a sensible approach to tuning the model to suit observed data. However, generating a year of modelled data is computationally intensive which prohibits the variation of input line to match the observed outputs. The alternative, an inversion problem, could form the basis for further work.

The parameters found for the integrated solar line will be of use in the following section when studying the inverse sensitivity.

8.3 Inverse sensitivity

The lack of correspondence observed in BiSON RV curves must be described by some movement of data points, away from the underlying trend, in the ratio-velocity space. In these two dimensions, the movements must be described by a combination of translations and or rotations. Here we concentrate on a type of rotation, the variation of a spectrom-

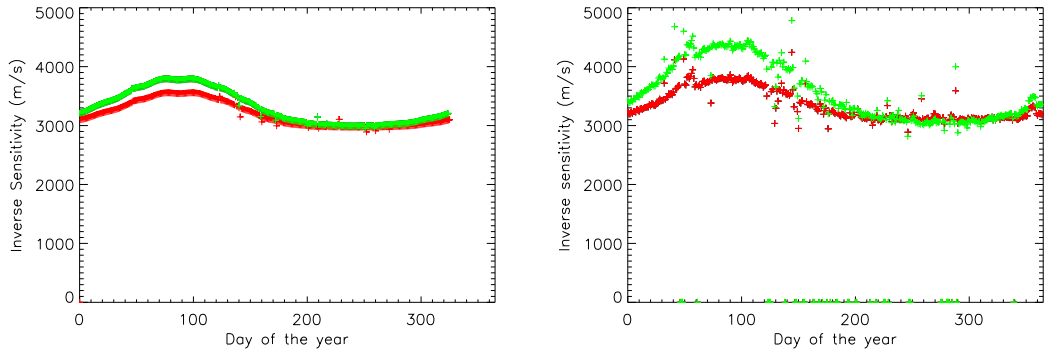

Figure 8.3: Inverse sensitivity as a function of day of the year. Left: modelled data. Right: Las Campanas station 2009. Detectors shown port (red) and starboard (green).

eter's inverse sensitivity.

The inverse sensitivity of a BiSON RSS is the rate of change of velocity with respect to ratio, or the inverse of the gradient in RV space. The inverse, rather than the sensitivity is used as this gives the familiar units of $\mathrm{m\,s^{-1}}$. Considering a change in inverse sensitivity is analogous to considering a rotation of the curve in RV space with the axis of rotation centred on the origin. Put another way, an increase in inverse sensitivity (a decrease in sensitivity) will reduce the gradient in the RV curve. The question is, can we explain the width in the RV curve with a variation in inverse sensitivity?

Figure 8.3 shows the modelled and real data inverse sensitivities as a function of day through the year 2009 for the BiSON Las Campanas A instrument. We see an underlying annual trend with some non-linear response. In fact the data can be well described by the function

$$\frac{\mathrm{d}\,V}{\mathrm{d}R}(t) = a_0 + a_1 \exp\left(\sin(\omega t + \phi)\right), \tag{8.4}$$

where the angular frequency ω and phase of the sinusoid ϕ match those of the orbital velocity signal. This simplistic application leaves a residual signal with a period of 30 days - the station velocity component due to the moon.

Figure 8.4 shows the inverse sensitivity for modelled and real data as a function of daily orbital velocity. The agreement of the curves over all velocities confirms that the independent variable is indeed orbital velocity. If the driving signal were anything else,

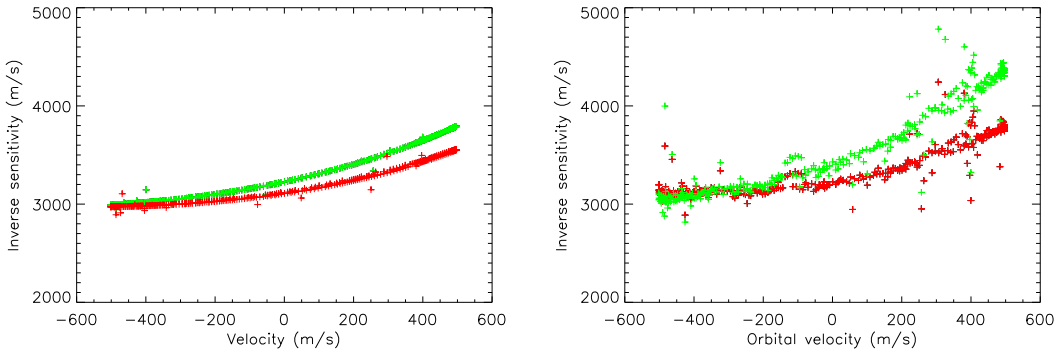

Figure 8.4: Inverse sensitivity as a function of orbital velocity. Left: modelled data. Right: Las Campanas station 2009. Detectors shown port (red) and starboard (green).

we would clearly see a disagreement due to the velocity caused by the orbit of the moon.

However, we can see that there is a significant difference in magnitude in the two data sets, real and modelled. The inverse sensitivity of modelled data varies by around half that of real data. A different inverse sensitivity function between modelled and observed data will of course produce a change in ratio's between the two, and perhaps will produce differing width in the R-V curve.

Next we consider a simple analytical treatment of the inverse sensitivity by using the integrated solar line function.

8.3.1 Analytical treatment of inverse sensitivity

Placing the mean value for the integrated solar line at zero for simplicity, the description from equation 8.2 becomes

$$I = 1 - \Gamma \exp\left(\frac{-v^2}{2\sigma^2}\right), \tag{8.5}$$

where v is now the velocity offset from the centre of the line. BiSON instruments measure intensity at wavelengths referenced by atomic transitions, in the laboratory frame, that have very narrow line widths. By considering the point of measurement to move with respect to a solar line described by a Doppler velocity v, and the BiSON measurement to be taken at a single point on the solar line, we can describe the rate of change of intensity

with respect to velocity as

$$\frac{\mathrm{d}}{\mathrm{d}v}\left(1-\Gamma\exp\left(\frac{-v^2}{2\sigma^2}\right)\right)=\frac{\Gamma v}{\sigma^2}\exp\left(\frac{-v^2}{2\sigma^2}\right). \tag{8.6}$$

BiSON RSS measure intensity but use the ratio R which gives a greater sensitivity to Doppler velocities - defined as

$$R=\frac{I_b-I_r}{I_b+I_r+b}, \tag{8.7}$$

where b is the non-resonantly scattered counts and the subscripts refer to the measurements taken in either the blue or red wing. Hence, the rate of change of the ratio with respect to velocity is then

$$\frac{\mathrm{d}R}{\mathrm{d}v}=\frac{\mathrm{d}}{\mathrm{d}v}\left(\frac{I_b(v)-I_r(v)}{I_b(v)+I_r(v)+b}\right)=\left(\frac{\mathrm{d}I_b}{\mathrm{d}v}-\frac{\mathrm{d}I_r}{\mathrm{d}v}\right)\left(I_b+I_r+b\right)^{-1}, \tag{8.8}$$

assuming that

$$\frac{\mathrm{d}}{\mathrm{d}v}\left(I_b(v)+I_r(v)+b\right)=0. \tag{8.9}$$

This assumption is valid to first order only because it relies on the velocity response of the two intensities being equal and opposite. In reality, asymmetry of the measured solar line and non-linear effects at high station velocities produce lower order effects. But for the work here the assumption is valid.

Expanding equation 8.8 in terms of the solar line function gives

$$\frac{\mathrm{d}R}{\mathrm{d}v}=\frac{\frac{\Gamma v_b}{\sigma^2}\exp\left(\frac{-v_b^2}{2\sigma^2}\right)-\frac{\Gamma v_r}{\sigma^2}\exp\left(\frac{-v_r^2}{2\sigma^2}\right)}{2-\Gamma\exp\left(\frac{-v_b^2}{2\sigma^2}\right)-\Gamma\exp\left(\frac{-v_r^2}{2\sigma^2}\right)+b}. \tag{8.10}$$

where we can describe the magnetic field strength in terms of a velocity B[1] such that $v_b=v+B$ and $v_r=v-B$.

[1]The magnetic field strength is 0.18T which acts to Zeeman split the wavelength of the potassium atomic transitions which means that we can describe the magnetic field in terms of the Doppler velocity.

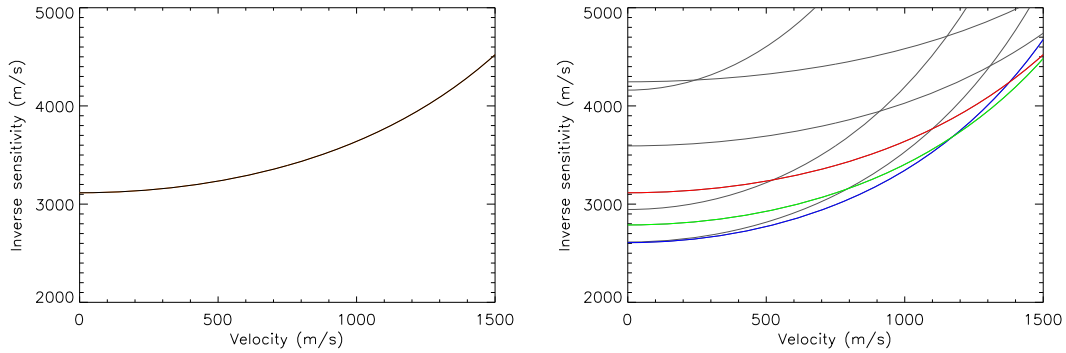

Figure 8.5: Analytical model for inverse sensitivity. Left: predicted instrumental response. Right: Response at varying magnetic field strength with interval 400 m s^{-1}. Foreground: Magnetic field strengths of 2600, 3000, and 3400 m s^{-1} in read, green, and blue respectively.

This reveals the exponential dependence observed in both real and modelled data. Without needing to simplify the expression we can plot the inverse sensitivity as a function of velocity. We use the parameters $\Gamma = 0.78$, $\sigma = 2600.0$ m s^{-1}, $B = 2600.0$ m s^{-1} and $b = 0.1$. Figure 8.5 shows this result and the results for magnetic field varying in steps of 200 m s^{-1}.

The shape of inverse sensitivity as a function of line-of-sight velocity returned by the analytical model closely resembles the both modelled and real data. Although, the magnitude of the effect throughout a year will obviously depend on any velocity offset - at greater velocities there is a greater change in inverse sensitivity. Hence, the analytical model suggests to improve agreement between RSS model and observed data we must vary one of the input parameters: magnetic field strength; background contribution; or solar line shape.

Figure 8.5 shows the inverse sensitivity as a function of velocity at varying magnetic field strengths. This plot shows us two things. Firstly, the sensitivity of an instrument may be improved by using a magnetic field strength greater than the usual $B = 2600$ m s^{-1}. The optimum sensitivity (lowest inverse sensitivity) is achieved with a magnetic field strength of $B = 3400$ m s^{-1} or $B = 0.24\,T$. Secondly, the flat part of the curves at differing magnetic field strength show, to a resolution of 200 m s^{-1}, the observed inverse sensitivity

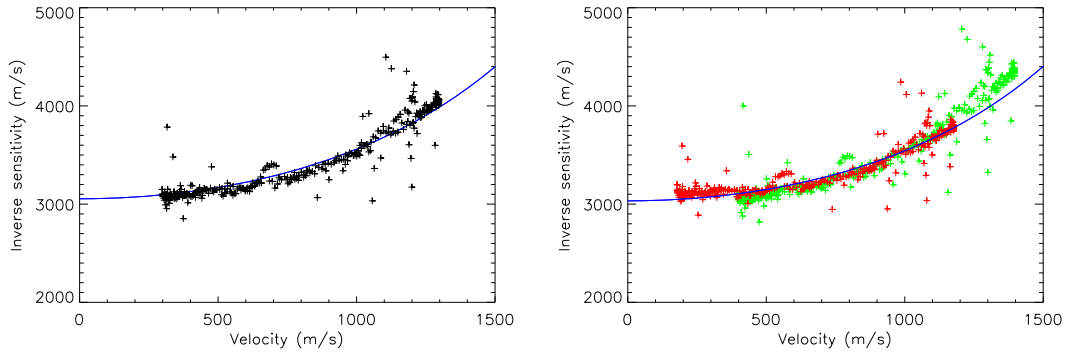

Figure 8.6: Las Campanas 2009 and analytically modelled inverse sensitivity as a function of velocity. Left: The mean of both detectors offset by 790 m s^{-1} with respect to the analytical model. Right: Port (red) and starboard (green) detectors offset by 680 and 900 m s^{-1} respectively.

matches the analytical model - and in fact the RSS model - at $B = 2600$ m s^{-1}.

Figure 8.6 shows the analytical model for inverse sensitivity with the observed data over plotted. The observed data are plotted with a velocity offset to match the analytical model curve. The offset between the port and starboard detectors, due to the imaging of the rotating sun in the cell, is a useful diagnostic. The offsets used for the port and starboard velocities are 680 m s^{-1} and 900 m s^{-1}, and while this is shifted by some 270 m s^{-1} with respect to the measured integrated line velocities, the separation of the two in in good agreement. This all suggests that inverse sensitivity is a function of line of sight velocity.

Initially we had hoped that a change in inverse sensitivity might generate width in the RV curve. But as we have seen, the observations show that inverse sensitivity is a function of line-of-sight velocity and while this will change the shape of the RV curve it does not present a method for introducing width. In order to explain the width in the RV curve we require a process that is not a function of velocity. Next we consider a parameter that describes the change in width of the RV curve to try and identify source of this signal.

8.4 The δV parameter

In this section we re-introduce the parameter δV and use its properties to examine the time dependence of the width in the RV curve. δV is defined as the velocity solution to the third-order polynomial daily calibration fit

$$r(v) = \sum_{i=0}^{3} a_i v^i, \tag{8.11}$$

where the coefficients a_i are determined by the fit to the measured ratio for each day. The following is solved either exactly, or using the Newton-Raphson technique, to give δV for each day

$$R = r(\delta V) = \sum_{i=0}^{3} a_i \delta V^i, \tag{8.12}$$

where R is a value of the ratio chosen around the middle of the yearly ratio range such that extrapolation is minimised.

Because the fit to ratio is known to provide a good description of observed ratio, δV provides a record of the calibrated velocity at R for each day. The lack of correspondence in the RV curve will manifest as a change in δV as a function of some - as yet unknown - variable. Let us consider δV for a single station over a single year.

8.4.1 Las Campanas 2009 δV

We have established that δV is a measure of the width in an RV curve. Figure 8.7 shows δV for the BiSON Las Campanas station for the year beginning 01/01/2009 for the mean and individual port and starboard detectors. The data show an annual variation with a distinct difference between the port and starboard detectors. The magnitude of the change in δV for the individual detectors is consistent with the observed magnitude of the width in the RV curve, in as much as both magnitudes are greater for the starboard detector.

We believe that the δV parameter gives a description of the width of the RV curve

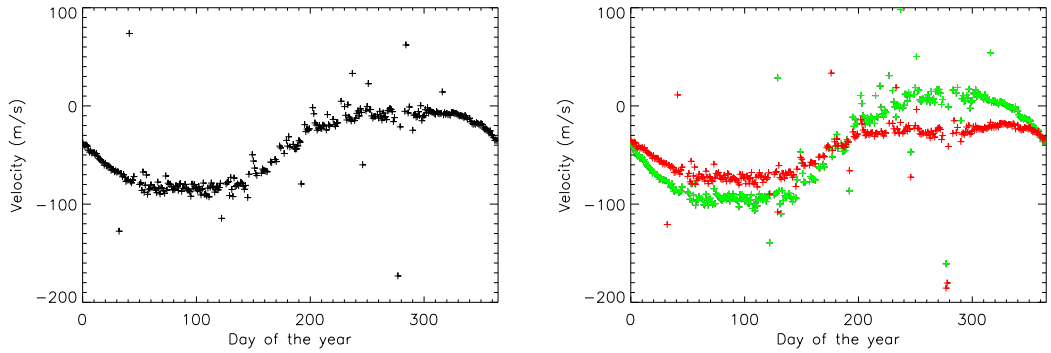

Figure 8.7: δV parameter for Las Campanas station 2009 as a function of day of the year. Left: The mean of both detectors. Right: the port (red) and starboard (green) detectors.

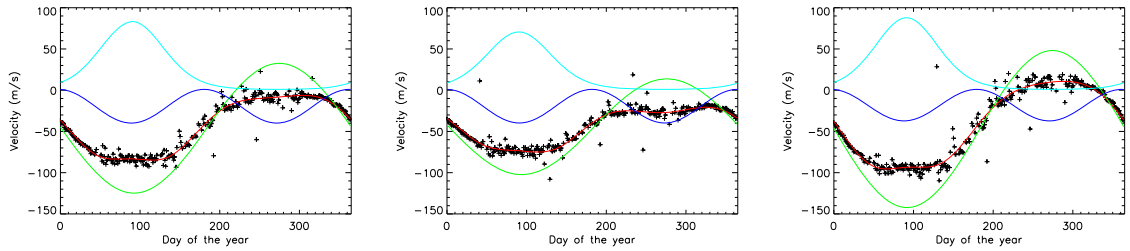

Figure 8.8: δV for Las Campanas 2009 as a function of day of the year with the fitted model (red) and individual components (green, blue, and cyan) over plotted. Left: mean detector data. Centre: port detector. Right: starboard detector.

as a function of time and we are interested in the process that is driving this width. But the shape of the δV curve indicates that there is more than one underlying process. Empirically we find that the δV curve can be well described by the model

$$\delta V(t) = a_0 + a_1 \sin(\omega t + \phi) + a_2 \sin(2\omega t + \phi) + a_3 \exp\left(\sin(\omega t + \phi)\right) \tag{8.13}$$

where ω is an angular frequency and ϕ is a phase. We will return to the justification of this model later. Figure 8.8 shows the results of the fit with each component over plotted. Fitting this model to the data shows it to provide a good description of the data but the justification for the model is less robust.

The fitted model contains three components in addition to an offset that is arbitrary. Each component should describe a process that we can identify: we see that there is a

large dominating annual trend that correlates with the negative of orbital velocity. The second component is a half yearly signal with similar magnitudes in both detectors. And the final component matches the shape of the inverse sensitivity with the sinusoid - inside the exponential - describing the orbital line-of-sight velocity (common to equation 8.10). All three components appear plausible at first sight, but let us consider each in more depth.

The first component, a sinusoid with an annual period, is of the same phase and period as the negative of orbital velocity. But we believe that our RV curve should not exhibit width due to orbital velocity; as the signal exists in both the ratio and the velocity, there should be good correlation. Any signal that is a function of velocity, in this case orbital velocity, would return the same measured ratio at a defined velocity, hence a process that is a function of velocity cannot introduce width into the RV curve, or change in the δV parameter. We might consider the input station velocities to be wrong but these are generated by the JPL ephemeris and have already been heavily scrutinised. Perhaps the annual sinusoid does not arise from negative orbital velocity.

Following exactly the same argument as in the previous paragraph, it is not obvious how the instrumental sensitivity, the second component which we have shown previously to be a function of velocity, manifests in the width of the RV curve. Of course a change in sensitivity will change the shape of the RV curve but in order to introduce width, there must be a signal that is changing as a function of something other than velocity.

The favoured explanation for the width in the RV curve relies on a change in position angle through the year, something that is not a function of velocity. The third component, a sinusoid with a period of six months, could potentially materialise from position angle. The response of the instrument to position angle has been studied already and we expect a signal with a six month period in the port and starboard detectors. However, this signal should be of opposite magnitude for each detector which causes a cancellation in the mean detector data. This is clearly not the case with the observed third component.

We are left with the following situation: we have a signal in real data that does not ap-

pear in modelled data and we lack an understanding of the source of the signal. We have modelled the δV with three components but cannot reach a conclusion as to the source of each component. It is entirely possible that the three component model is incorrect in its construction, we lack physical justification for the terms. However, it is hard to imagine - or even harder to justify - terms of any other form.

We do know that the change in sensitivity produced by our model is less than that observed in real data. We might hypothesise that the increased change in sensitivity in real data coupled with the signal produced by positional angle returns a pseudo velocity that generates a δV but have no simple method to follow this up. Instead we continue to look at methods of dealing with the width in the RV curve by introducing and then constraining an additional velocity signal, albeit one we do not understand.

8.4.2 Determining the unknown signal

So far we have studied the inverse sensitivity and δV, representing the width in the RV curve, as separate effects. Here we combine the two to generate a guess as to the underlying velocity signal ΔV that generates the lack of correspondence in the RV curve. Our parameter δV is supposed to be representative of ΔV but is assessed at only a single ratio. As ΔV changes, δV will change but so will the inverse sensitivity $\frac{\mathrm{d}V}{\mathrm{d}R}$ which impacts the rate at which δV changes. In fact, we would believe an underlying change in velocity measured as a ratio, multiplied by the inverse sensitivity produces a change in velocity or

$$\delta V \propto \Delta V \frac{\mathrm{d}V}{\mathrm{d}R}. \tag{8.14}$$

Figure 8.9 on the next page shows calculated δV divided by the calculated inverse sensitivity - less a d.c. offset of 2900 m s^{-1} chosen to match the minimum inverse sensitivity - which we expect to have the same form as ΔV. The plot shows data from the mean, port, and starboard detectors and these results display the required magnitudes, in as much as

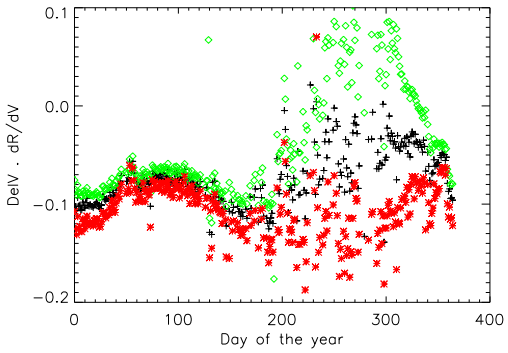

Figure 8.9: ΔV signal as a function of time predicted by the δV signal divided by the calculated inverse sensitivity.

the starboard magnitude is much greater than that of port. In addition to this , we see agreement with the temporal position of the width in the RV curve.

An RV curve contains a time dependent signal from the variation in time of velocity. Early January and late June occupy the middle of the RV curve with March at the top right and September bottom left. Looking at the progression in time of the width in the RV we see that the port detector exhibits maximum width approaching and receding from March while the starboard detector exhibits width both around March and approaching and receding from September. Studying this function, plotted in fig. 8.9, shows the same general form as the width in the RV curve. We note that the reduction in width at the extremes of the RV curve is due to a combination of smaller data sets and the turning point in the underlying velocity signal.

If we believe that the signals presented in fig. 8.9 have the same form as the underlying signal that generates the width in the RV curve, we can apply a straight forward test: the modification of velocity in the RV curve to include ΔV should significantly reduce the observed width. Rather than values generated in figure 8.9 that include various sources of noise and require some normalisation, we will explore a function that approximates the signals

$$\Delta V = A_0 \exp\left(1.0 + \sin(\omega t + \phi)\right) + A_1 \exp\left(1.0 + \sin(\omega t + \pi + \phi)\right), \tag{8.15}$$

	A_0	A_1	ϕ
Port	13.79	1.28	-0.04138
Starboard	9.76	-13.67	-0.01028

Table 8.2: Table of fitted ΔV coefficients.

where ω is the annual angular frequency, t is the day of the year, A_x is the amplitude of the component, and ϕ is the phase.

If we are to apply ΔV in addition to the station velocity we require the optimum coefficients of the above function which can be determined by minimising the width in the RV curve. The width is well described by the χ^2 returned from a fit of Ratio to a third order polynomial in velocity. We have then a minimisation problem.

Minimising the width in the RV curve is not a straight forward problem. We have a non-linear function giving a parameter space with only seven variables but with significant occurrences of local minima. The local minima are generated primarily by the third order polynomial reacting to a translation in RV space caused by the ΔV function. Systematic constraint of parameters and improved starting guesses do not alleviate these problems. Instead we resort to a rudimentary search of parameter space by varying a single coefficient of the ΔV function and then applying a linear least-squares fit of the ratio to the third order polynomial in velocity plus ΔV. This process is repeated by cycling through the ΔV coefficients until a suitable solution is found. The resulting coefficients are given in table 8.2, with the functions plotted in figure 8.10 on the following page.

Figure 8.11 shows the RV curves for port and starboard with and without the velocity corrected by the addition of ΔV. The corrected RV curves are offset by +0.1 in ratio to avoid crossing and all curves display only one in every ten days of data. It is obvious that width in the RV curve is significantly reduced and comparison with figure 8.1 on page 161 shows that the corrected curves now have width of order magnitude consistent with modelled data.

We are then able to resolve the differences displayed by the modelled and real data. Firstly, there is an additional velocity signal with period of one year that is present in

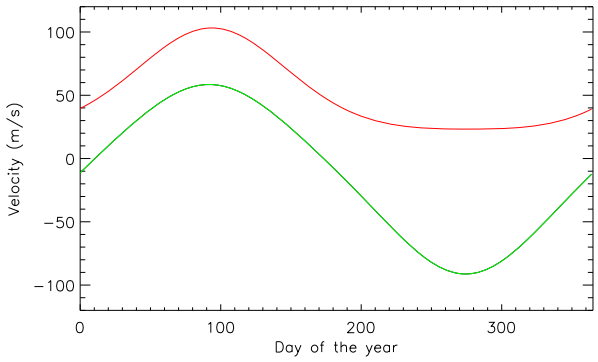

Figure 8.10: Result of fitted ΔV signal as a function of day of the year for port (red) and starboard (green) detectors.

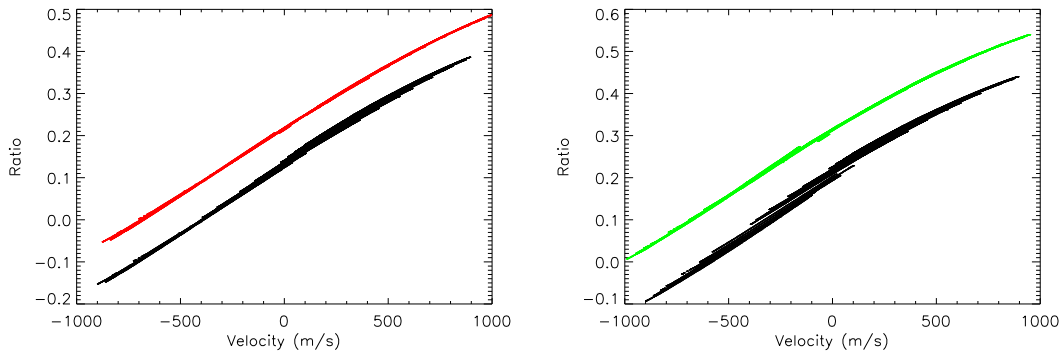

Figure 8.11: RV curves showing uncorrected (black) data and data corrected with the fitted ΔV signal. Left: port detector. Right: starboard detector.

real data but not in the model. The source of this signal remains unknown. Secondly, the integrated solar line function in the model does not match the observed integrated solar line and this impacts the sensitivity through the year. The change in sensitivity acts multiplicatively with the unexpected annual velocity and produces width in the RV curve. Further work would include a reworking of the model to tune the solar line function and the addition of the unexpected signal.

We can hypothesise about the origin of the unexpected signal. The signal has an annual period which perhaps suggests that it is of instrumental origin. A candidate that may cause a large annually varying signal is uneven weighting of the solar disk caused by obstruction - dirt or dust perhaps - in the optical system. As the weighting of the solar disk changes naturally through station velocity so an invariant weighting would generate a secondary signal and perhaps even a significant variation in the integrated solar line. With a number of opportunities for this additional instrumental weighting to occur - each optical component beyond the front lens - this hypothesis is difficult to test.

We have made a significant stride in reducing the width in the RV curve but what does this mean in terms of a seasonal calibration? Our method for reducing the width in the RV curve introduces a daily correction ΔV to the station velocity. Applying this correction and calibrating reveals systematic trends in daily data which by consequence produce the harmonics of a daily signal that dominate the low-frequency power spectrum obscuring low signal-to-noise solar oscillations. The source of the systematic variation is the implied assumption that the unexpected signal changes daily. We know that this signal contains a multiplicative sensitivity component which is a function of velocity and hence makes the corrective signal for ΔV a function of time and velocity.

In terms of implementation of a seasonal fit, an additional velocity term that is a function of time and velocity significantly increase the parameter space. Some initial success has been had with the port detector using a multi-variable non-linear least-squares fit, but application to the starboard detector has not yet been successful. Despite believing we have the required knowledge the application of a seasonal fit remains elusive.

So the long term stability of the BiSON RSS is compromised by a signal that is hypothesised to be of instrumental origin. We continue by searching for signals of solar origin in a daily cadence time series.

8.5 Long term solar signals

In the previous sections we have identified a long-term signal δV and can characterise this variation in terms of a three component model, perhaps linked to the instrumental inverse sensitivity. Here we aim to identify long-term signals of solar origin found in the δV parameter as a test of the long-term stability of the BiSON network. To accomplish this we expand our data set to include the BiSON stations: Las Campanas 1996-2010; Izana 1984-2010; Sutherland 1996-2010; and Narrabri 1996-2010 .

Figure 8.12 shows the raw δV parameter for each station calculated from the daily fit coefficients. The data sets are sensitive to interruptions from bad weather and instrumental failure. Where sensible values for δV cannot be found a value of 0 m s^{-1} is returned.

Marked on the plot of fig. 8.12 are a set of red break points that show the position of discontinuities in the δV signal. These breaks represent maintenance and upgrade visits to stations and so coincide with a modified alignment of an instrument. Typically, a site visit would include, at the least, an auto-guider scan and oven temperature scan. Changes in the guiding of an instrument will change the position of the solar image at the centre of the cell and a new vapour temperature changes both the gain of the instrument and instrumental optical depth. These variations are capable of introducing velocities offset with respect to an optimal alignment.

Discontinuities in δV show the RSS to be sensitive to its working state and this offers an explanation for the difference in integrated solar line velocity offset observed between real and modelled data. Further to this, in searching for long-term signals of solar origin we must calibrate data to account for discrete changes in alignment. Following on we consider the reduction of raw δV data by sections of constant alignment.

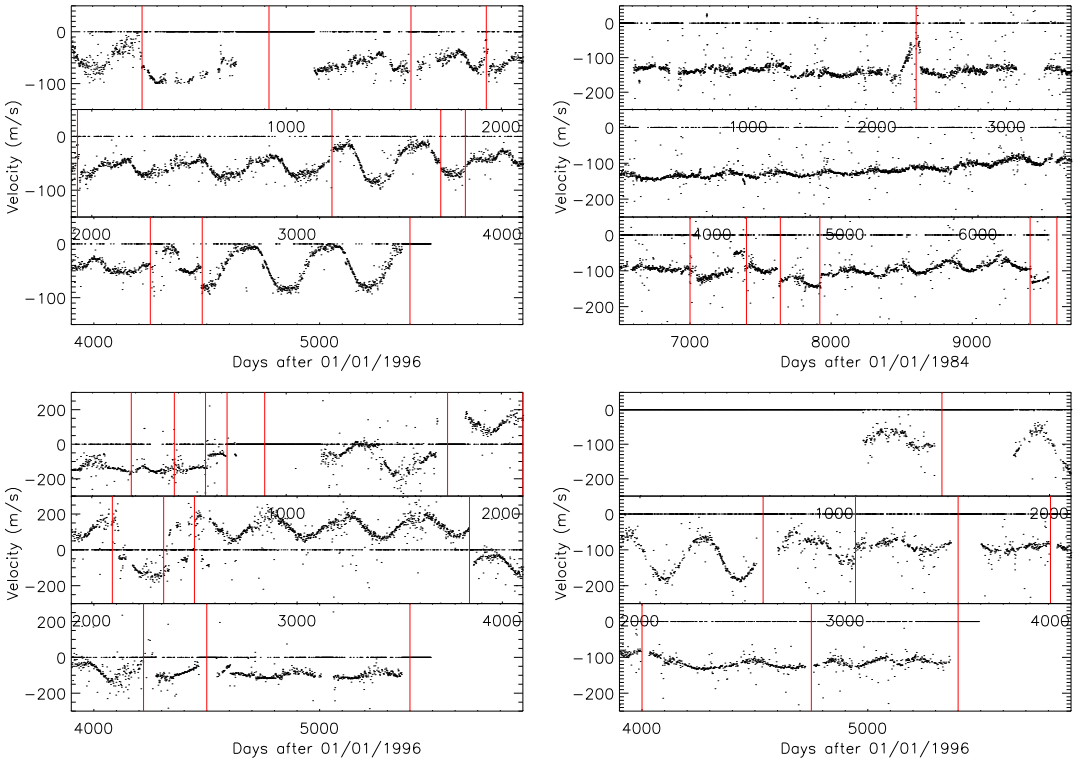

Figure 8.12: Long term δV signals. Top left: Las Campanas. Top right: Izana. Bottom left: Sutherland. Bottom right: Narrabri.

8.6 Data Reduction

The identification of signals of solar origin in the δV time series requires the removal of the dominating yearly signal. As we have seen, the magnitude and offset of this annual variation varies with what is thought to be instrumental alignment. In order to produce residuals that do not contain the annual signal, which is clearly of terrestrial origin, we consider sections of data with continuous alignment.

Removing the annual signal is accomplished by fitting the three component model of the previous section, equation 8.15 on page 173

$$\delta V(t) = A_0 \sin(\omega_0 t + \phi_0) + A_1 \exp\left(\sin(\omega_1 t + \phi_1)\right) + A_2 \sin^2(\omega_2 t + \phi_2). \tag{8.16}$$

In applying the model to long periods of data, we found an improvement in the goodness of fit by including linear terms to account for long-term drifts. Specifically, improvement came from the introduction of an additional term

$$\delta V(t) = ... + A_3 \tag{8.17}$$

and modification of each A_i term to a linear dependence in time, such that

$$A_i = m_i t + c_i. \tag{8.18}$$

Figure 8.13 shows examples of the application of the above reduction of segmented data, with the long-term residuals shown in figure 8.14 on page 181.

The residuals from the reduction of δV are expected to contain long-term solar surface velocity signals in addition to signals of instrumental origin. Of particular note are signals that may be present from the tidal distortions from Mercury and Jupiter (or in fact any planet) in addition to the the velocity signal produced as sunspots migrate across the solar disk.

Tidal distortion of stellar shape is a familiar concept in the study of binary star systems.

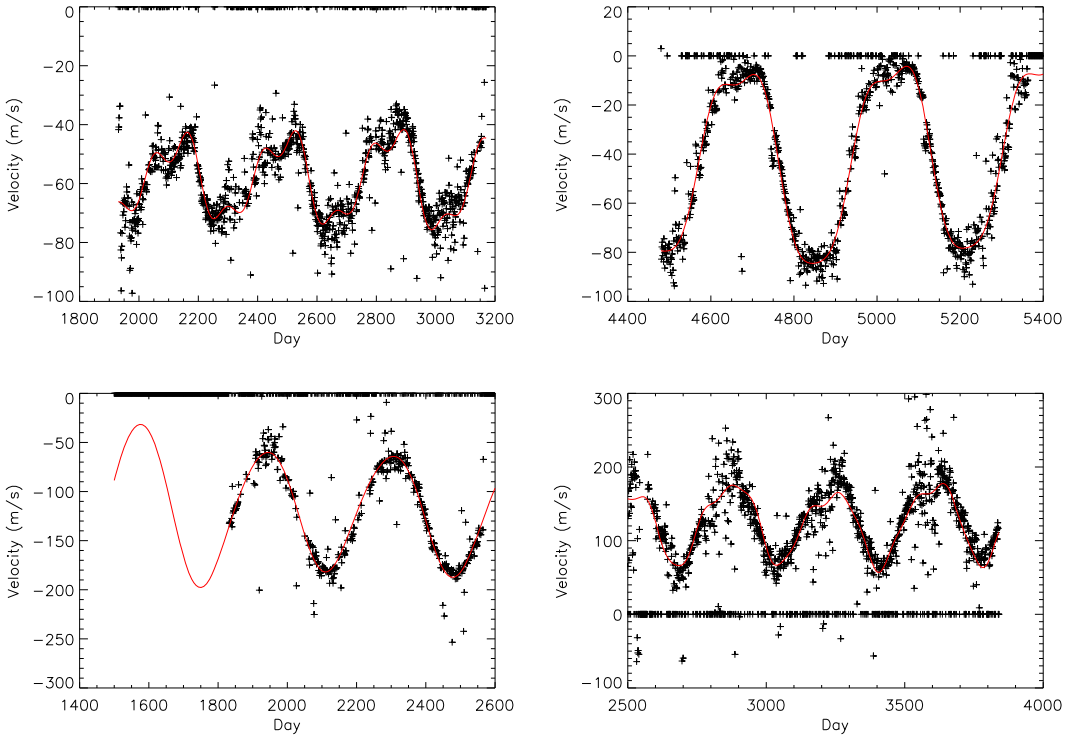

Figure 8.13: Examples of the signal fitted and removed from the long term δV results to produce δV residuals.

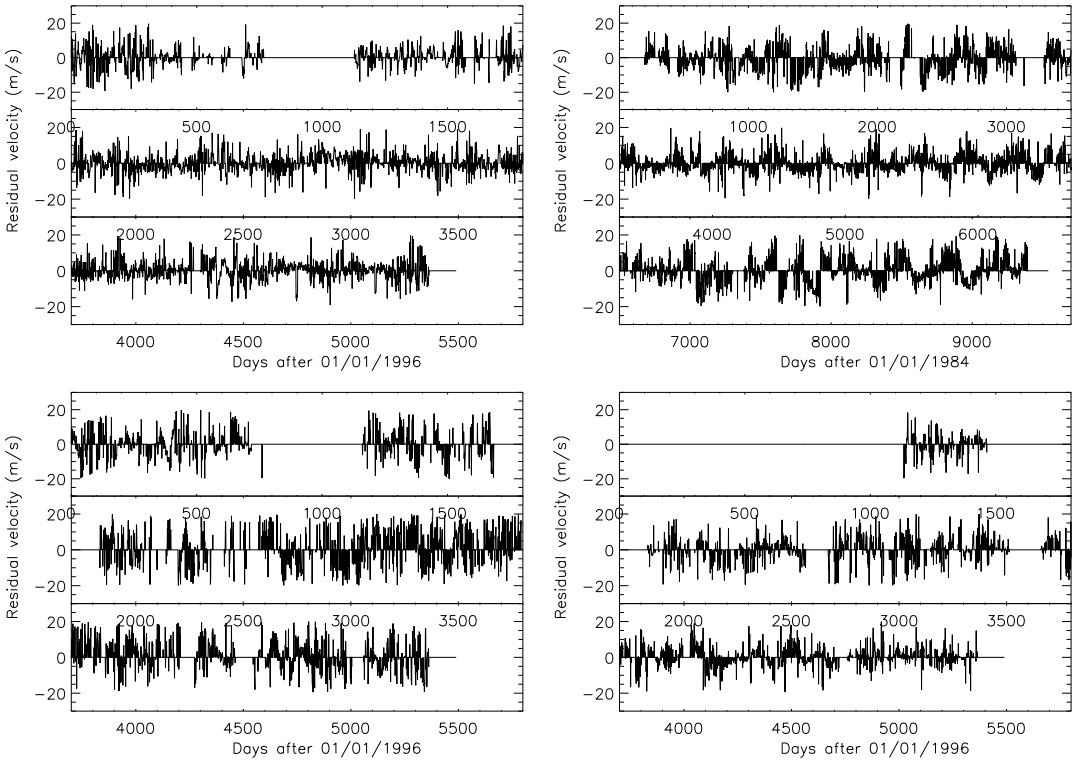

Figure 8.14: Long term δV residuals. Top left: Las Campanas. Top right: Izana. Bottom left: Sutherland. Bottom right: Narrabri.

The changing gravitational potential, due to a secondary object (here Jupiter or Mercury), across the diameter of a primary object (the Sun) causes a tidal distortion with bulges in the positive and negative direction of the secondary object. As Earth orbits the Sun a velocity signal at half the synodic period of the secondary object will appear. The synodic periods for Jupiter and Mercury are 398.9 and 115.9 days respectively, which will give signals with the frequencies 0.058 and 0.2 μHz. The magnitude of this effect is of the same order for both Jupiter and Mercury - as the force produced is proportional to the mass of the secondary object and inversely proportional to the objects separation cubed - but still relatively small.

The velocity component from sunspots is expected to appear at the solar rotation rate - the differential solar rotation rate. In the following section we use the RSS model of the previous chapters to estimated this signal.

8.7 Modelling the solar rotation signal

As sunspots pass across the face of the solar disk a net velocity signal is produced as the rotating limbs are given unequal weighting. We can demonstrate this effect using the RSS model and a single sunspot.

The spatial resolution of the RSS model is limited - by computational demands - to an image of the Sun of 500 by 500 pixels. Rather than considering sunspots of varying size and intensity, we define a spot in the model as a single pixel with no emission. An increase in the size of the spot will increase the magnitude of the effect, just as an increase in the intensity of the spot (up to normal levels) will reduce the magnitude of the effect - the two variables are interchangeable. To produce a signal we transit a spot across the surface of the solar disk at the rate of rotation associated with the specified latitude. Figure 8.15 on the following page shows the progress of a spot across the modelled solar disk at constant intervals of time.

Figure 8.16 shows the results from the RSS model with a single sunspot at various

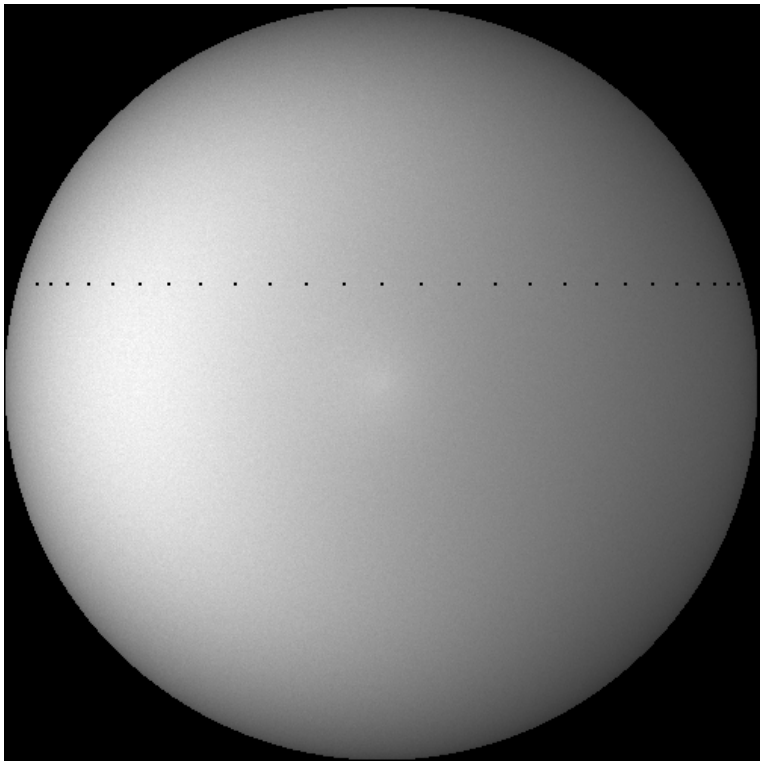

Figure 8.15: Simulated sunspot transit.

latitudes. The signal is displayed in both the time domain for the port and starboard detectors and the mean signal in the frequency domain. In order to isolate the effect of the sunspot, the frequency domain plot considers a single sunspot but with infinite life time. In reality, sunspots persist for a time period of order one full solar rotation.

The power spectra plots show the fundamental frequency signal produced at the period of the rate of solar rotation in addition to a clear harmonic structure. The fundamental and harmonics show the variation in frequency that is to be expected with latitude due to differential rotation. Given the migration of sunspots to equatorial latitudes through the solar cycle, we would expect broad excesses of power in the δV residual power spectrum at the Carrington period and its harmonics. In addition, we would expect to be able to observe a time variance in the power around the harmonics that is correlated with the international sunspot number (ISSN).

The modelling performed here of a single persistent sunspot fulfils the needs of this work: The shape of the signal in the frequency domain has been identified. Further work in this

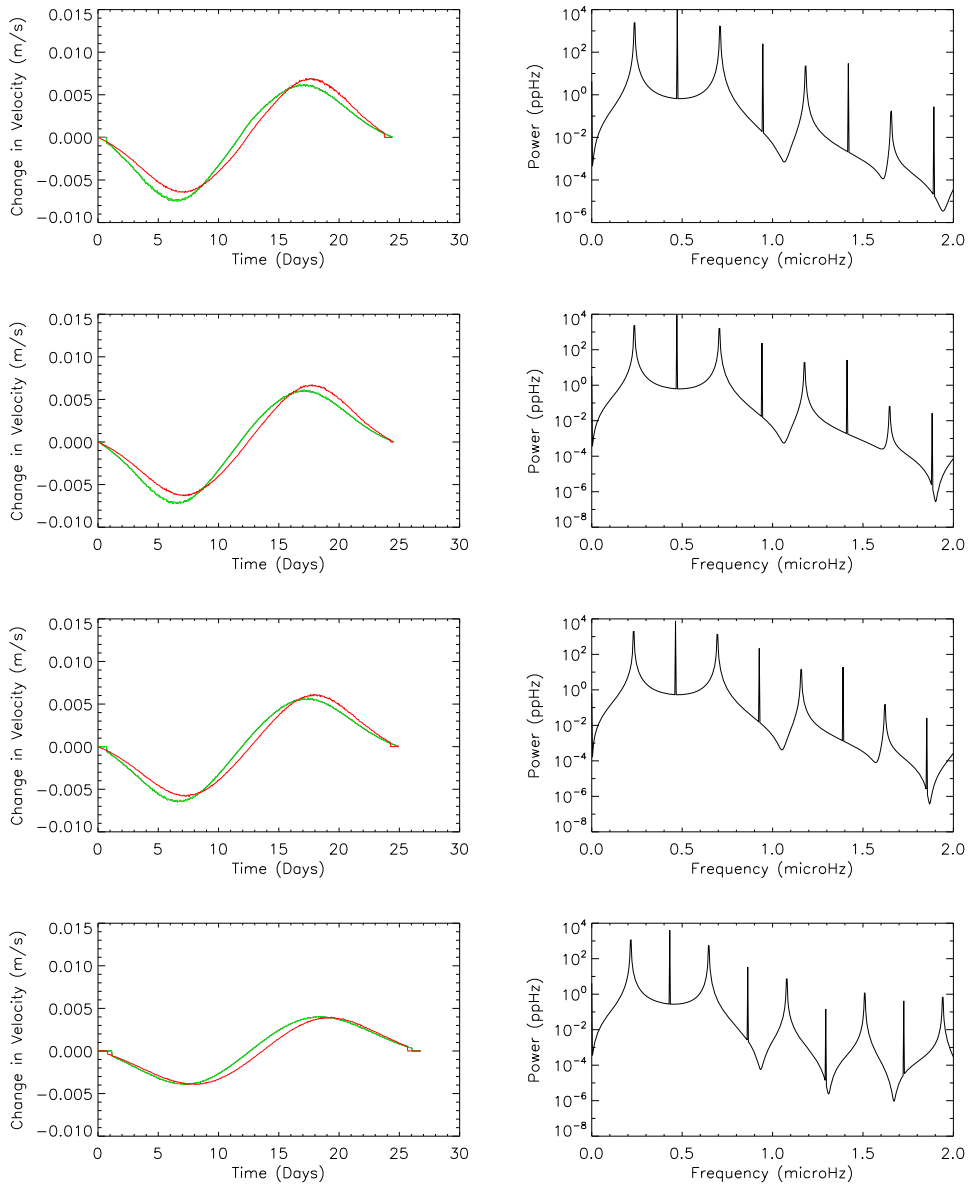

Figure 8.16: Modelled response in time and frequency domain's to a single persisting sunspot at varying latitudes on the solar disk. Latitudes top to bottom: equatorial; 15°; 25°; 45°.

area could lead to a velocity correction in the BiSON calibration pipeline to compensate for sunspots. While the magnitude of the correction would be negligible for data calibrated on a daily basis, residuals calibrated over long timer periods may benefit substantially from the removal of this effect.

We return to the measure δV signal and its residuals to examine the frequency domain for the predicted effects of planetary tidal forces and sunspots following differential rotation patterns.

8.8 Data Analysis

Figure 8.17 shows the power spectra for δV residuals for the four stations under consideration. Over plotted in red are the data with a 21 nHz boxcar smoothing filter applied. The Carrington rotation rate and some of its harmonics are visible to some degree in each of the power spectra, with Las Campanas having by far the best signal to noise. Searching for planetary tidal signals is not sensible due to the increased noise at very low frequencies and the uncertainty of source of signal around the 0.2μHz (both the Mercury tidal signal and the sunspot signal are restricted in this region).

The noise in the residual data is high compared to the small signal produce by the sunspot transits. However, Las Campanas data have just about sufficient signal to noise to allow the study of the variation of the Carrington signal as a function of time.

8.8.1 Variation signal through solar cycle

We know that sunspot activity is intrinsically linked to the 11 year solar cycle but can we see a variation in time of the sunspot signal from δV data?

Figure 8.18 shows the time variation of the δV residuals in the frequency domain. The chart is an image of Lomb periodograms with frequency on the ordinate and time on the abscissa. Each periodogram is produced using a two year data set modified by a Welch function and is presented at the midpoint in that time series. By removing data with a

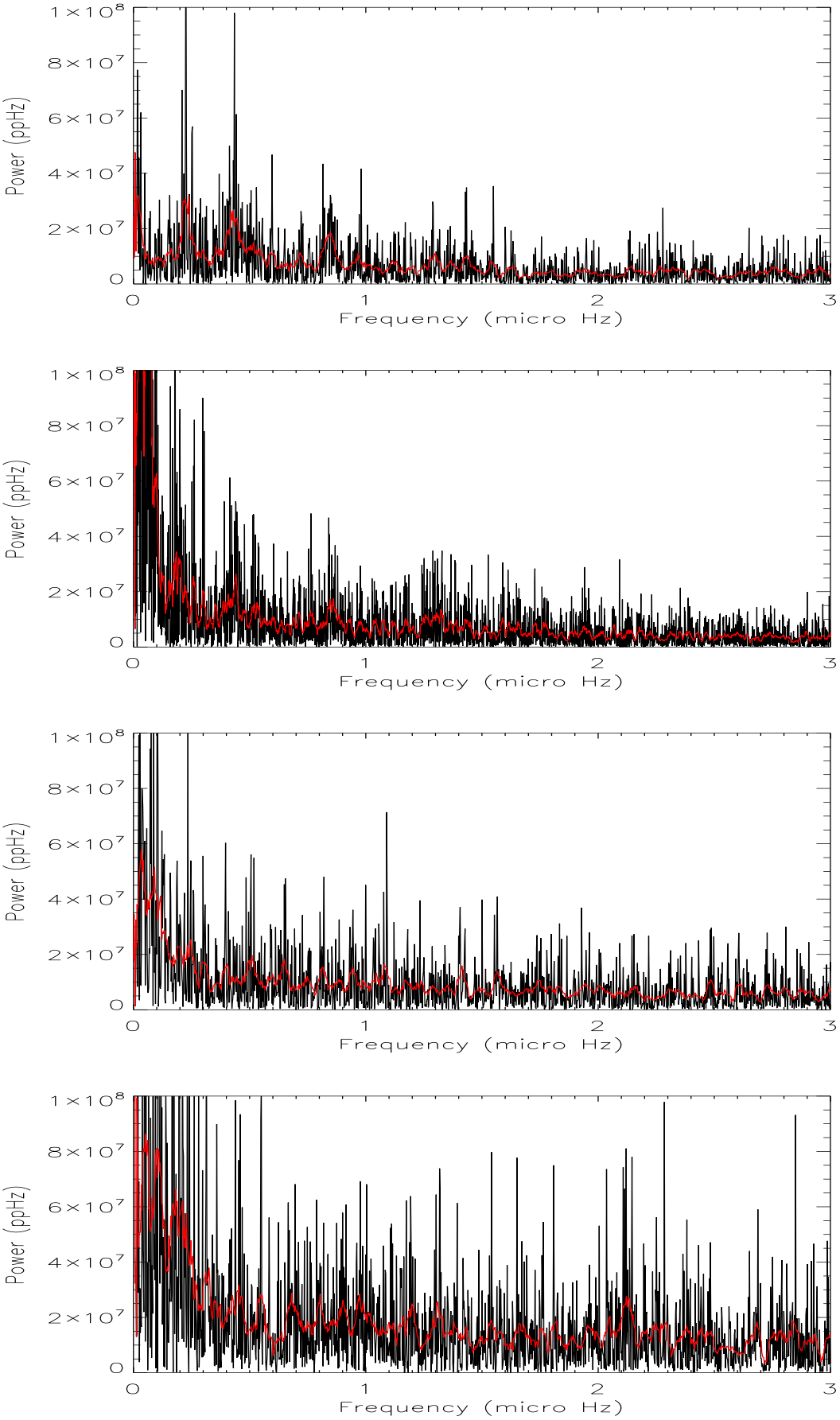

Figure 8.17: Power spectrum of the long-term δV residuals. Top to bottom: Las Campanas; Izana; Narrabri; and Sutherland.

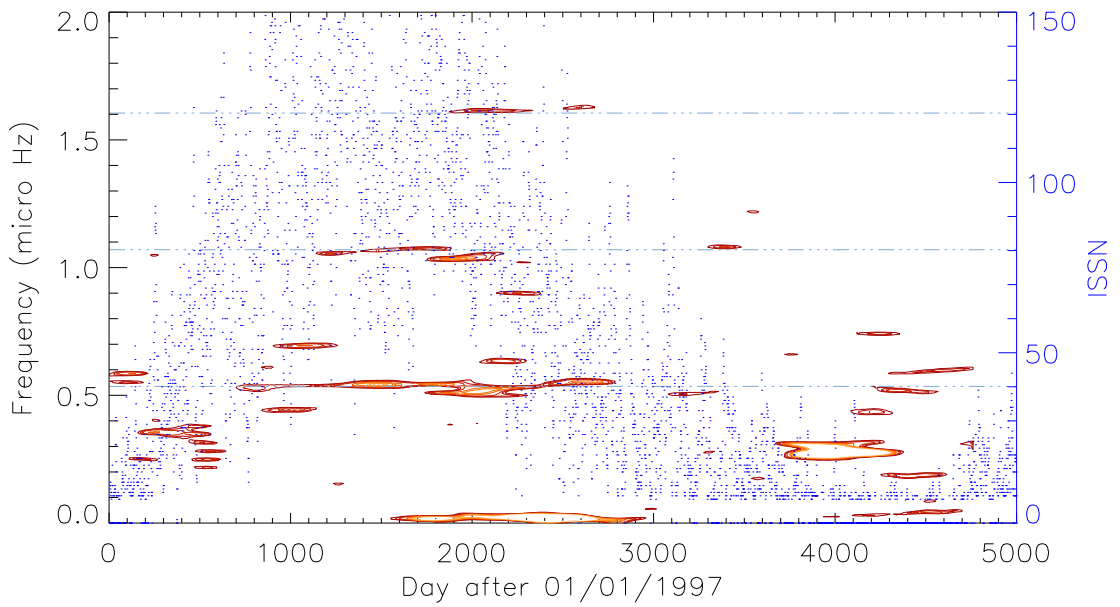

Figure 8.18: Variation in time of the Carrington harmonics with international sun spot over plotted. Horizontal blue lines show the frequency of the Carrington harmonics.

normalised Lomb value of less than 8 the sunspot signal is highlighted. The Carrington period and its first and second harmonics are shown with horizontal dot-dash lines. Over plotted in blue are the international sunspot numbers for the corresponding day. Each point in time will of course be highly correlated with its temporal neighbours but clear signals exist on timescales longer than two years for the Carrington period and the first harmonic.

Importantly the data show a tentative correlation between the ISSN and the presence of the sunspot signal. This increases our confidence that we are measuring a signal of solar origin at very low frequency in BiSON data.

8.9 Implications on BiSON RSS stability

BiSON instruments are stable over long periods in time because measurements are referenced to a laboratory-frame atomic line. The RSS's measurement of integrated solar

velocity has a number of components but is dominated by the true Doppler velocity shift of the solar surface due to Earth's obit and spin in addition to the gravitational red shift term . Other contributions to the velocity measured are second order terms and may be of solar origin - oscillations, granulation, and sunspots - or may be instrumental in origin e.g. background contributions, vapour temperature variation, and Doppler imaging.

When considering reduced and calibrated data we can consider three regimes in the frequency domain: the five minutes region, the low-frequency region (0.1 - 1 mHz), and the very low-frequency region (periods longer than a day). The five minute region is dominated by solar oscillations. The low-frequency region is dominated by solar granulation and daily harmonics introduced as a result of semi-regular gaps in the data. We have now shown that the very low-frequency region is dominated by a signal of unknown origin but probably instrumental in origin and that once this signal is removed (with varying success for different stations) we once again return to signal of solar origin in the sunspot signal.

Chapter 9

Final time series analysis

9.1 Introduction

In this final chapter we follow our analysis through to a natural conclusion: the detection of low-l, low-frequency solar oscillations. So far, this thesis has produced a description, and model, of the BiSON RSS instrument in order to improve the BiSON low-frequency data processing pipeline. Here we will apply these improvements, concatenate the resulting data and then search for modes of oscillation previously undetected in BiSON or perhaps any other data.

In the following work we apply the correction for differential extinction determined in Chapter 7. This work produces an improvement in mode signal to noise of around 25% under normal circumstances. The long-term calibration, described in Chapter 8 that is aimed at signals lower than 100 μHz, does not produce sufficient gains in signal-to-noise in the targeted region to be of interest here.

In addition to the revised calibration process, we will search for the optimum application of the existing BiSON long time series concatenation pipeline. Having processed the data, we will apply the standard power spectrum statistical tests to assess whether or not potential structure in the frequency domain is part of the background noise. Using this statistical information and the properties of a potential mode in the frequency domain, we

may make decisions on the plausibility of possible detections of modes of solar oscillations.

9.2 Data preparation

We have used BiSON unresolved Doppler velocity observations made during the period 1991 January 1 to 2010 December 31 inclusive. This period spans nearly two solar cycles including the extended solar minimum experienced at the end of solar cycle 23. The observed frequencies of p-mode oscillations vary by typically 1 part in 10,000 at 3mHz with the solar cycle. However, at low frequencies this variation is substantially lower, with no variation observed in 23 years of data for low-frequency ($\leqslant 1300$ μHz) low-l p modes [Broomhall et al., 2009a].

The data collected from all six BiSON stations are first calibrated using the radial-velocity third-order polynomial with the correction for differential extinction detailed in Chapter 7. Data are concatenated to produce a multiyear time series for analysis in the frequency domain.

A significant challenge for the concatenation process is the coherent combination of data with very different noise and duty cycle characteristics. It has been found that the selection of the best data only, determined by a low frequency noise parameter on short timescales, and rejection of other contemporaneous data, produces the optimum time series for low-frequency study. In addition, data exceeding a certain noise threshold are rejected even when this causes gaps in the time series. Consequently, this noise threshold must be chosen with some care.

To add further complication, the performance of the BiSON network has seen impressive year-on-year improvements in the quality and duty cycle of its observations. The reasons for the improvement are both changes to the spectrometer hardware, for example changing from photomultiplier tubes to solid state detectors and improving spectrometer temperature control, and modifications to the hardware and software that controls automation, allowing the network to respond quick to faults. However, this systematic improvement

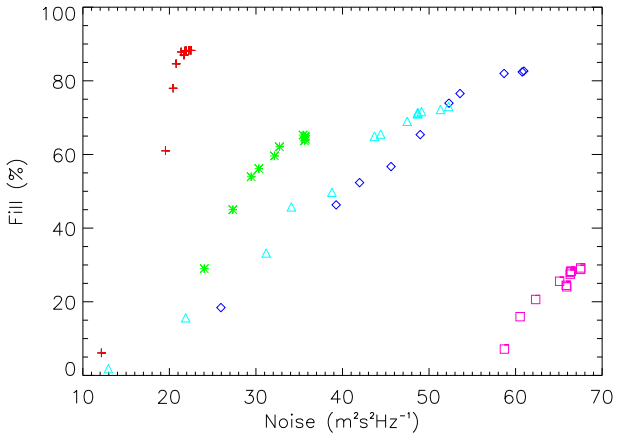

Figure 9.1: BiSON network performance described by low-frequency noise and time series duty cycle (fill) for the years: 2009 red; 2005 green; 2000 blue; 1995 cyan; 1991 pink.

in noise levels through the 20 years of BiSON data requires that any threshold be chosen to balance the low-fill and (relatively) high-noise early data, with high-fill and low-noise modern data. To emphasise the improvement in the BiSON network figure 9.1 shows the fill and noise options for 1991, 1995, 2000, 2005, and 2009, optimum performance being in the top left hand corner of the plot.

The observed signal to noise of a mode of oscillation can be described by the intrinsic signal-to-noise modified by a transfer function that is dependent on both the duty cycle of the observed time series and the local background noise. Hence we find we can describe the relative observed signal-to-noise in the low-frequency region of the power spectrum by taking the ratio of the duty cycle of the full time series to the mean power spectral density from 0.8 to 1.3 mHz. We define this as the noise parameter to which we set the rejection threshold. Varying the noise threshold used by the concatenation process allows the selection of an optimum balance of fill and noise. We find the optimum threshold value to be around 45 $\mathrm{m^2 s^{-2} Hz^{-1}}$.

Further improvements to the signal-to-noise ratio can be gained from the rejection of outlying data points. Studying the lower-frequency modes visible in a one year data set, we find that small improvements ($\approx$ 3% SNR) can be made by rejecting outlying residual

points that are more than 7 ms^{-1} away from zero.

This completes the generation of a standard time series for analysis in the frequency domain. The time series is typically transformed to the frequency domain using the FFT technique detailed in section 1.4.1 on page 11. In addition to the standard FFT, Fletcher et al. (2011) detail a new efficient method for determining weighted power spectra.

9.2.1 Weighted FFT

There are existing methods for generating power spectra from a time series with known weights but these use unrealistically computationally expensive (for a 20 year, 40 second cadence data set) sine-wave fitting (SWF) techniques. Fletcher et al. (2011) have adapted the FFT method to include weighting data in the time domain by the noise characteristics observed in the frequency domain. This method has the advantage that the adapted FFT method, substituted for the SWF, remains computationally efficient and returns results that are consistent with SWF methods.

Typically a SWF method will fit

$$A_i \sin\left(2\pi f_i t_k\right) + B_i \cos\left(2\pi f_i t_k\right), \tag{9.1}$$

to the data, y_k, at each frequency f_i, where t_k is the time of the kth observation. Normally A_i and B_i would be evaluated by least squares fitting. Fletcher et al. show that it is possible to rewrite expressions for A_i and B_i in terms of an FFT and a summation over the observational weighting:

$$A_i = \frac{-\mathrm{Im}\left(\mathrm{FFT}(\mathrm{w_k y_k})\right)}{\sum\left(\frac{w_k}{2}\right)}, \tag{9.2}$$

and

$$B_i = \frac{\mathrm{Re}\left(\mathrm{FFT}(\mathrm{w_k y_k})\right)}{\sum\left(\frac{w_k}{2}\right)}, \tag{9.3}$$

where w_k is the weight for each data point.

The weighting of the data is determined by one over the low-frequency figure of merit used elsewhere in this thesis, i.e. the inverse of the mean of the power in the frequency domain over the range 0.8 to 1.3 mHz. Fletcher et al. tested this weighted FFT technique against simulated and real data and found evidence of a useful increase in signal to noise.

9.2.2 Bin shifting

Bin shifting offers the opportunity for optimising signal to noise by maximising the height of a mode in a single bin together with producing different realisations of background noise. For modes with a narrow width compared to the frequency bin width, it is possible that power is distributed over a couple of bins and so increased relative height may achieved by moving much of the power to a single bin. By varying the length of a time series by small amounts, the centre of a bin in frequency can be shifted and perhaps in the above case this would confine more power to a single bin. In addition, slightly 'different' realisations of the background noise are generated when bins are arranged slightly differently in frequency. A change in the noise may be all that is required to achieve a new detection.

The necessity of performing an FFT on a long data set many times, each time bin shifting, requires that any systematic search must select modified lengths of time series that provide computational efficiency. Here we apply 25 shifts, for each of which the length of data set is determined to optimise the FFT routine. Data points are removed from the start of the time series up to a maximum number of 1500 points.

Bin shifting achieves slightly different realisations of the background noise using a single data set in the time domain. However, the spectra obtained are not independent and there will be correlations between prominent noise spikes in each of the shifted sets. While the different realisations of the noise are correlated meaning we cannot use the probabilities independently from each spectrum, we do still retain a different realisation of a mode of oscillation against a slightly different noise background. Chaplin et al. [2002a] find that if

the likelihood of uncovering a mode in an unshifted data set is small, then the probability of finding significance in all 25 bin-shifted sets is increased by a factor of around 3.
In the following section we consider the techniques of searching for significant structure in the frequency domain of data sets that are optimised for maximum signal to noise and also bin shifted.

9.3 Searching the power spectrum

At low frequencies in the p-mode spectrum, modes are manifested in the frequency domain as prominent discrete peaks with narrow width. The peaks show a regular structure in both the regular spacing of modes with the same l (i.e. degree) and regular spacing, due to rotational splitting, in the m components (i.e. azimuthal order). In addition, the width and total power of modes measured in the power spectrum varies with frequency in a definable manner [Houdek, 2002]. These properties allow peaks to be identified as resonant modes of solar oscillation.
However, small signal to noise in these low-frequency regions increases the possibility that noise may be confused with observed structure, particularly single peaks. Hence, any search for low-frequency p modes must include an understanding of the probability of an occurrence of different structures. We must remember that that the probabilities we obtain do not describe the probability that structure is due to a mode, but only describe the probability that a structure is part of the background noise. For this reason we require a concerted effort to produced more than just the significance of a spike.
Searching the power spectrum for resonant modes of oscillation requires us to extract all available information and use the sum of this information to inform our belief that a peak or structure is due to a mode of oscillation. As such, significance testing is an important part of any strategy.

9.3.1 Significance testing

The basic method of single peak significance testing has been introduced in an earlier section of this thesis (section 2.5 on page 33). The process of calculating the probability that a single peak is part of the background noise is standard practise with the only choice arising being the width of the power spectrum over which to assess the probability. Here we select this range in frequency (determining N bins from the earlier notation) to be $\Delta p = 100$ μHz.

In addition to searching for single peaks, it is sensible to search for collections of power produced by the width of resolved modes. In this instance, the same calculations are repeated as for a single spike but in a averaged power spectrum. Here adjacent bins are combined to produce a new single bin and hence bins in the smoothed spectrum do not lose their statistical independence. Thus the modification required to the above process is only that, rather than before with a χ^2 2 d.o.f, the underlying distribution is now χ^2 $2k$ d.o.f where k is the number of bins over which smoothing takes place [Anderson et al., 1990, Appourchaux, 2003].

A third test is possible that relies on the near constant rotational splitting of multiplets for $l \geqslant 1$ modes of oscillation.

Testing for multiplets

We start by defining the nature of the multiplet structure that is observed due to rotational splitting. Solar rotation lifts the degeneracy of modes with $l \geqslant 1$ into $2l + 1$ components. But the nature of our full-disc helioseismic data and our near equatorial view of the Sun means in reality we only observe $l + 1$ components where $l - m$ is even. Modes in the frequency region of interest are expected to have components that are split by the rotation of the solar interior where the synodic frequency splitting for $|\Delta m| = 1$ is expected to be close to 0.4 μHz.

Asymmetries in the frequency splittings between each multiplet may be introduced by the presence of a magnetic field. This effect is not anticipated in $l = 1$ modes but may

be present in modes of higher l [Chaplin et al., 2002b]. To account for this possibility we introduce an uncertainty in the m component splitting of $\delta\nu = 0.1$ μHz. Hence, our definition of multiplet structure is a prominent spike in the spectrum with other prominent spikes separated by multiples of 0.4 ± 0.1 μHz appropriate for that l.

A test for a multiplet is initiated when a single peak is located and found to be in excess of the $P \leqslant 0.1$ threshold. We can then proceed to determine the probability of observing a pair or triplet[1] in the defined multiplet region of frequency.

We start by calculating the probability of observing at least one spike by chance with a relative height above $s_{\nu 2}$ over the uncertainty range $2N_\delta$, i.e.

$$P_\delta = P[1; p(s_{\nu 2}), 2N_\delta] = 1 - [1 - p(s_{\nu 2})]^{2N_\delta} \, . \tag{9.4}$$

Hence the probability of finding 2 spikes as part of a multiplet above $s_{\nu 2}$ is

$$P_{\rm m} = p(s_{\nu 2}) P_\delta = p(s_{\nu 2}) \left(1 - [1 - p(s_{\nu 2})]^{2N_\delta}\right) . \tag{9.5}$$

The number of possible arrangements of the multiplet over the range in the power spectrum under consideration, Δ_p, is dependent on the splitting $N_{\rm split}$ associated with 0.4 μHz and the uncertainty allowed, N_δ associated with 0.1 μHz. In a power spectrum assessed over $\Delta_p = 100$ μHz and produced by a time series of 20 years at 40 second cadence, both $N_{\rm split}$ and N_δ are much smaller than the number of bins in Δ_p, N. Hence, the number of arrangements can be approximated as N. So the probability of observing at least one multiplet pair can be approximated as

$$P_{\rm multi} \approx P\left[1; P_{\rm m}, N\right] = 1 - \left[1 - P_{\rm m}\right]^N \, . \tag{9.6}$$

[1] We do not expect to observe the quartet from $l = 3$ modes in the region 0.8 to 1.3 mHz due to the significantly reduced signal to noise compared with $l = 0, 1$ or 2.

It is possible to search for triplets, where by $P_{\rm m}$ is replaced by $P_{\rm t}$ which is given by

$$P_{\rm t} = p(s_{\nu 2})P_{\delta}^{2}. \tag{9.7}$$

There is no straightforward analytical expression to calculate $s_{\nu 2}$ but given the normalised height of the spikes in the power spectrum, the probability that the structure is due to noise may be calculated.

We have now considered the techniques required to identify unusual structure in the frequency domain. We move on to discuss the preliminary results found from these statistical tests.

9.4 Preliminary results

Figure 9.2 shows the structure found by the statistical tests of the previous section with the $P = 0.1$ and $P = 0.01$ thresholds displayed in red and blue respectively, together with the predicted frequencies from the Saclay seismic model [Turck-Chièze et al., 2001] assuming a rotational splitting of 400 nHz. To avoid repetition of the same region in frequency, only a single instance is shown, even when more combinations of signal to noise appear significant. While it would appear that the majority of peaks barely pass above the $P = 0.01$ threshold it must be remembered that smoothing a power spectrum can increase signal to noise, but this also increases the bin width and this in turn increases the uncertainty in the central frequency of any structure. Therefore, structure is displayed at the minimum smoothing necessary to lift a peak, where possible, above the $P = 0.01$ threshold. Or in other words, in many cases where $P \geqslant 0.01$, more signal to noise can be found by increasing the number of bins over which the power spectrum is smoothed.

Table 9.1 shows the results from the search for structure in the power spectra for frequencies from 900 μHz to 1300 μHz. Some structure at very low frequency was found to be significant but has been rejected on the basis that it is not plausibly a frequency of oscillation. Possible detections are listed by l, n, and m with the frequencies given

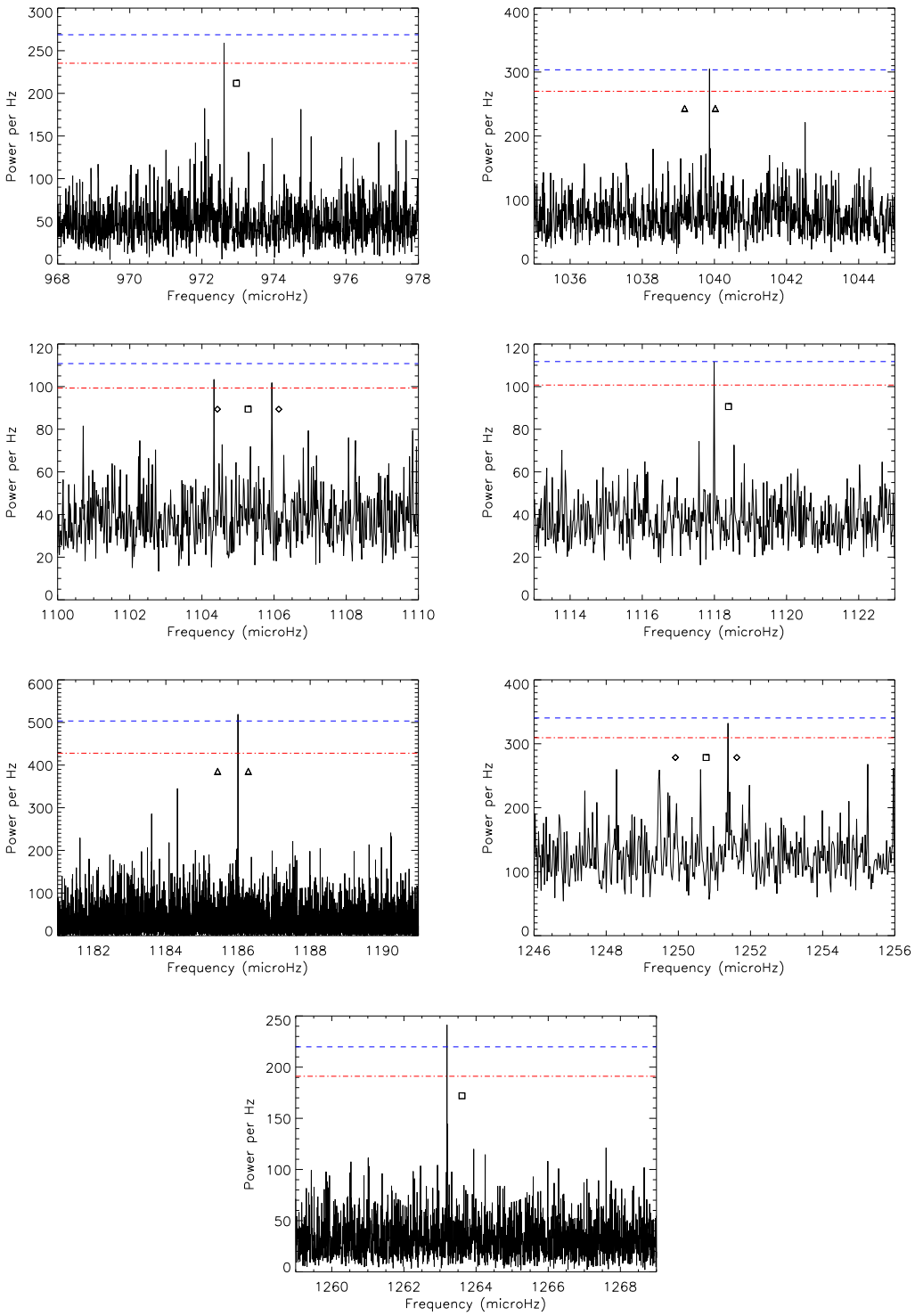

Figure 9.2: Selected smoothed power spectra for structure near a predicted frequency of oscillation and $P \leqslant 0.1$. The number of bins over which the spectra are smooth are (in ascending frequency): 4,7,11,12,1,15,and 3. Over plotted are the $P \leqslant 0.01$ and $P \leqslant 0.1$ significance levels in blue and red respectively together with the predicted frequencies from Turck-Chièze et al. [2001]. Predicted frequencies are displayed by m value with $m = 0, 1$, and 2 displayed with squares, triangles and diamonds respectively.

l	n	m	Frequency (μHz)	Probability (P) structure due to noise	Smoothed	Outlier	WFFT
0	6	0	972.614 ± 0.003	0.0197	4	7	No
1	6	+1	1039.864 ± 0.006	8.79×10^{-3}	7	-	Yes
		mean	1039.463 ± 0.006				
2	6	-2	1104.335 ± 0.009	0.134	11	8	No
		+2	1105.938 ± 0.009	0.141	11	8	No
		multiplet		0.015	11	8	No
		mean	1105.136 ± 0.006				
0	7	0	1117.992 ± 0.010	9.60×10^{-3}	12	20	No
1	7	-1	1185.196 ± 0.006	4.97×10^{-3}	8	10	No
		+1	1185.999 ± 0.001	6.05×10^{-3}	1	10	No
		multiplet		5.11×10^{-5}	8	10	No
		mean	1185.598 ± 0.003				
2	7	-2	1249.758 ± 0.011	0.302	14	-	Yes
		+2	1251.377 ± 0.012	0.015	15	-	Yes
		multiplet		1.61×10^{-4}	14	-	Yes
		mean	1250.567 ± 0.008				
0	8	0	1263.193 ± 0.002	1.70×10^{-3}	3	8	No

Table 9.1: Results from significance testing.

for the center of the bin with the greatest relative height. Frequencies are listed together with a conservative estimate of the error which is half the width of the bin containing the peak. The probability that a structure is part of the background noise is given together with the number of bins over which the power spectrum is smoothed, the outlier rejection threshold, and whether or not a weighted FFT (WFFT) is used (in which case outlier rejection is not used). In addition, where multiplet structure is expected we give the mean value of frequency, with the exception of the $l = 1$, $n = 6$ structure where only a single component is found. In this case we take the mean value of rotational splitting for modes nearby, $\delta\nu = 401$ nHz, to calculate a pseudo mean.

We find that structure is identified by the statistical tests close to predicted frequencies of modes of oscillation given by the Saclay helioseismic model for all but $l = 1$, $n = 6$, $m = -1$. Any structure further than 1 μHz away from a predicted frequency has been discarded.

The structures listed in table 9.1 are not necessarily regarded yet as detections. We will

continue by investigating the properties of the observed structure.

9.5 Going beyond statistical significance

As we have stressed previously, we wish to use the sum of all available information to guide our decision as to whether or not structure seen in the frequency domain is a mode of solar oscillation. Here we extract detailed information on observed structure and compare results to modelled results and other observations.

9.5.1 Fitting individual modes

We continue by attempting to fit a basic Lorentzian model to the observed structure in the power spectrum. This fitting is applied for two reasons. Firstly, attempting to fit a well constrained model to structure that is in fact noise will produce returned parameters that are not consistent with expectations, in which case would undermine any detection. Secondly, the earlier use of the central frequency of the most prominent bin is not necessarily a good measure of the frequency of a mode of oscillation (the background noise will exist on top of any mode structure). Fitting a sensible model, where possible, will give more robust estimates of both the frequency and the associated errors.

At higher frequencies ($\geqslant 1300$ μHz) and hence higher signal to noise ratios it is sensible to fit modes as sets or even better use a pseudo global fitting technique [Fletcher et al., 2009]. At lower frequencies and hence lower signal to noise, this approach fails to return sensible parameters with the height of the mode often being iterated to zero. We find that the solution is to fit individual components using a simple model over only a narrow band in the frequency domain ($\delta\nu_{\text{fit}} = 1$ μHz).

Modelling the power spectrum

We make the reasonable assumption that the narrow band in frequency under consideration, $\delta\nu_{\rm fit}$, has a flat background noise that is well described by the χ^2_{2k} probability distribution. The observed unsmoothed spectrum, O_i, whose probability distribution is described by

$$P_i(O_i) = \frac{1}{\langle O_i \rangle} \exp\left(\frac{1}{\langle O_i \rangle}\right) \tag{9.8}$$

which over $\delta\nu_{\rm fit}$ is represented by the joint probability density:

$$L = \prod_i P_i, \tag{9.9}$$

where L is the likelihood function. Substituting the probability distribution into equation 9.9 gives a function S that can be minimised to give maximum likelihood estimates of the model's, $M_i(a)$, parameters,

$$S = -\ln(L) = \sum_i \left[\ln(M_i(a)) + \frac{O_i}{M_i(a)}\right]. \tag{9.10}$$

While this limit is derived for a single spectrum with χ^2_2 distribution. Appourchaux [2003] showed that for fitting to k mean averaged spectra, there is no approximation in minimising the same function, S, but resulting errors must be normalised by $\sqrt{k}$.

For fitting of individual low-frequency solar oscillations we choose a model containing a symmetric Lorentzian together with a flat background term, i.e.

$$M_i(a) = \frac{A(w/2)^2}{(\nu_i - \nu_0)^2 + (w/2)^2} + b, \tag{9.11}$$

where A is the maximum signal power, w is the full width at half maximum, ν_0 is the mode frequency, and b is the background level. The function S is minimised using the Powell multi-variable minimisation procedure [Press et al., 1992].

To calculate errors on the model parameters Anderson et al. [1990] detail that if the

maximum likelihood function is expressed in terms of the logarithms of the parameters A and w, then for small changes in the model parameters, the shape of the hyper-surface near the maximum value is approximately Gaussian. This means the errors on the fitted parameters can be determined using the identity elements of the inverse Hessian matrix. Of course as already stated, this must be scaled by the square root of the number of bins by which the power spectra has been smoothed.

To complete the method of individually fitting low-frequency modes we define a figure of merit for the goodness of fit. Anderson et al. [1990] define the "merit" function as

$$M_{\text{merit}} = \frac{\sum_i \left(\frac{O_i - M_i(a)}{M_i(a)}\right)^2}{d.o.f.} \tag{9.12}$$

where the degrees of freedom, d.o.f., are the number of points less the number of free parameters in the fit. Figures of merit less than or equal to unity suggest the fitting function is a good approximation of the observed spectra over $\delta\nu_{\text{fit}}$. Some care is required here as low signal-to-noise means that poorly fitting functions may still exhibit a low merit figure but we may expect this to still return MERIT $\geqslant 1$. As such the merit figure is only a guide.

For structures at higher frequency that have higher signal to noise and greater width in the frequency domain, it is essential to consider the asymmetry of a mode and also the window function convolved with the true signal that causes diurnal side lobes. At low frequency, the narrow widths of modes with respect to the bin size and small asymmetries [Chaplin et al., 1999], combined with the narrow region of the power spectrum considered means that fitting a symmetric Lorentzian function without considering the diurnal side lobes - which exist outside of the region considered - is valid.

The technique of fitting individual modes over a narrow region in the frequency domain was tested against a simulated time series of 20 years length that comprised a single symmetric mode, granulation, and white noise. The method consistently produced results within 2σ error of the input parameters with varying resolved mode lifetimes.

l	n	m	Frequency (μHz)	ln width (μHz)	ln height ($m^{-2}\ s^{-2}\ Hz^{-1}$)	Merit/d.o.f.
0	6	0	972.613 ± 0.004	-5.7 ± 0.7	5.8 ± 0.5	1.09
0	7	0	1117.992 ± 0.005	-4.6 ± 0.7	4.7 ± 0.8	0.94
1	7	-1	1185.193 ± 0.004	-4.8 ± 0.6	4.8 ± 0.7	0.96
1	7	+1	1185.997 ± 0.004	-5.1 ± 0.8	5.1 ± 0.9	0.97
2	7	-2	1249.743 ± 0.011	-3.6 ± 0.6	3.6 ± 0.7	0.98
2	7	+2	1251.373 ± 0.010	-3.2 ± 0.5	3.7 ± 0.5	1.14
0	8	0	1263.197 ± 0.004	-4.8 ± 0.5	5.0 ± 0.6	0.98
1	8	-1	1329.232 ± 0.004	-4.1 ± 0.4	5.5 ± 0.5	1.08
1	8	+1	1330.035 ± 0.005	-3.9 ± 0.3	5.3 ± 0.4	0.93
0	9	0	1407.471 ± 0.006	-3.5 ± 0.3	5.0 ± 0.4	0.91

Table 9.2: Results from fitting individually to structure observed in the power spectrum near a predicted frequency of oscillation.

Fitting results

The results of the fitting procedure can be seen in table 9.2. We see that the fitting method returns sensible error values and acceptable values for the goodness-of-fit merit function.

The fact we fit our model to the listed power spectrum structure and that this returns useful parameters adds significant weight to the conclusion that we are observing modes of solar oscillation. However, in addition we should check the returned properties of these potential modes with modelled data and other observation programs.

Comparison of observed frequency with models

We can use the difference between the frequency of an observed structure and the frequency from modelled theoretical mode values to guide our decision on plausibility of a detection. Figure 9.3 gives this difference using the modelled frequencies of the Saclay seismic model [Turck-Chièze et al., 2001] for values of $l = 0$, 1, and 2. Although by no means confirmation, the presence of a clear trend in the difference between observations and modelled results lends weight to the plausibility of detections.

Comparison of frequency with other observers

A comparison of the potential modes detected with other work (table 9.3 on page 207) shows a satisfactory level of agreement. Comparisons are drawn between two previous BiSON publications (Broomhall et al. [2009a] and Chaplin et al. [2002a]), as well as with results using data from Solar and Heliospheric Observatory (SOHO) instruments, i.e. GOLF [García et al., 2001], GOLF and MDI [Bertello et al., 2000], and MDI and SPM [Toutain et al., 1998].

Despite good general agreement, there a number of cases where returned frequencies show variation beyond the ubiquitous 3σ limit. Firstly, $l = 2$, $n = 6$ shows nearly a 0.4 μHz difference with the value reported by Toutain et al. [1998]. We note that the observed structure does not meet our own significance criteria ($P \leqslant 0.01$) but suggest that the difference between the modelled frequency and the Toutain result would not pass one of our first cuts.

Secondly, the $l = 1$, $n = 7$ mode shows good agreement with the existing BiSON detection but a significant difference with other results. The error on the Toutain result is too large to make sensible comparison with but the Garcia and Bertello result differences are significant. Garcia et al. report this mode using a number of techniques throughout the paper sometimes with and sometimes without confidence levels in the detection (what we would describe here as the significance test result). Where significance levels are quoted, the maximum value returned is $> 95\%$ so do not meet the requirements stated here of $P \leqslant 0.01$. It is difficult to justify any conclusion on the validity of a frequency based on a significance level but we may consider the length of the time series used (20 years to 3.5 years) as adding plausibility to the BiSON detection.

Finally the $l = 0$, $n = 8$ mode shows differences across all reported results. There is very little in the data to suggest the prevalence of one result over any other but we do note that the mean value of all the presented results is in some sort of agreement with the

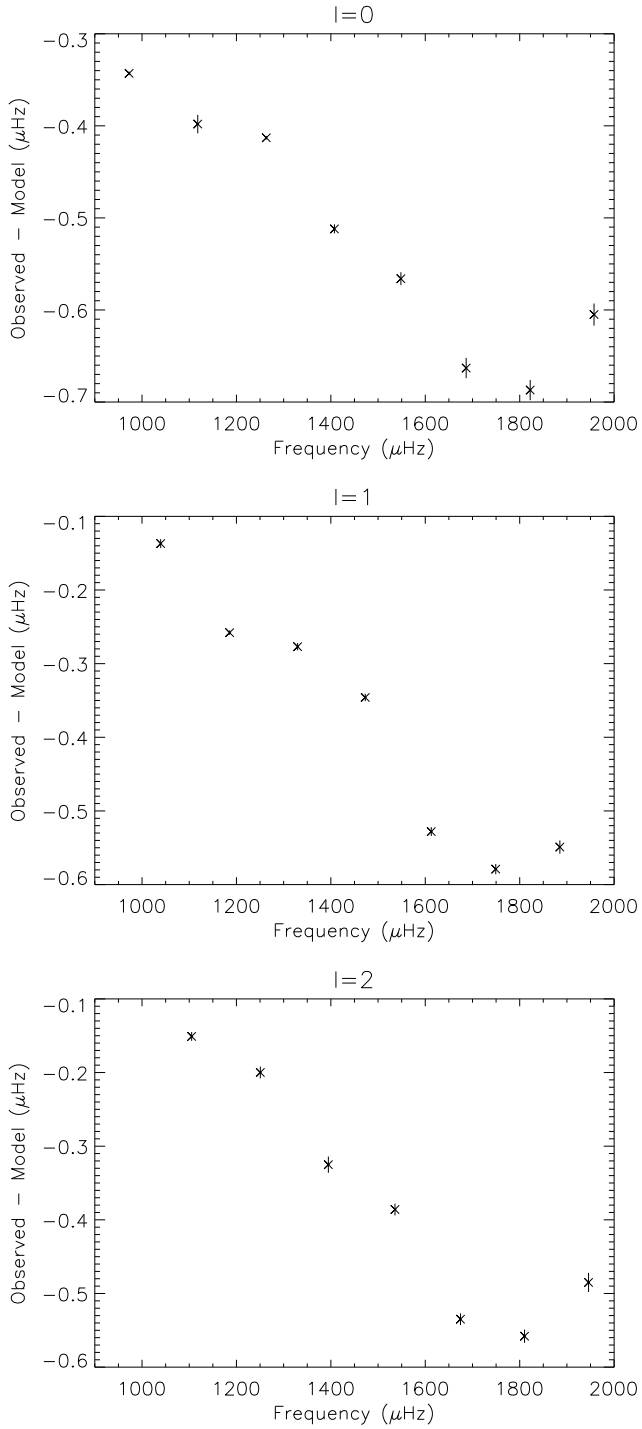

Figure 9.3: Frequency differences between the modelled predicted mode frequencies of Turck-Chièze et al. [2001] and the observed frequency of structure detected in power spectra.

result published in this thesis. The disparate results presented here suggest that perhaps reported error bars - all here being calculated in the same or very similar manner - are under-estimated.

Fitted widths

Our main aim in evaluating the width of structure in the power spectra is to establish a frequency dependent relation that lends weight to the conclusion that the observed structure is generated from a mode of solar oscillation. But further to this, any relation describing mode width as a function of frequency can be extrapolated to lower frequencies to provide information about the possibility of detections at lower frequency and lower mode width.

Determining the mode width in the low-frequency region with low signal-to-noise is difficult and the results returned by the fitting procedure may be subject to bias [Chaplin et al., 2008]. This bias manifests as an underestimate in returned line width caused by the tails of the Lorentzian peaks becoming dominated by background noise. This effect is prominent when the length of a time series used is of order a few (perhaps as many as 5) lifetimes of the mode or less. In addition, the magnitude of the effect is sensitive to the signal to noise of a mode which means that making corrections for the effect is difficult. Here we attempt no correction but must remember that the returned width of structure in the power spectrum will be an underestimate of the true width of a mode of oscillation with bias increasing at lower frequency.

To establish a frequency dependence at low-frequency we have used the individually fitted frequencies of this thesis together with results returned at higher frequency using a pseudo global fit. We have rejected frequencies above 2000 μHz in order to avoid the 'flattening out' of line widths around the 5 minute region. Using the weighting of the errors returned by the fitting routine we fit a linear function to the natural log of frequency versus the natural log of the line width, i.e. a power law. The fit and results can be seen in figure 9.4 and table 9.4.

l	n	Thesis	Broomhall et al. [2009a]	Chaplin et al. [2002a]	García et al. [2001]	Bertello et al. [2000]	Toutain et al. [1
0	6	972.613 ± 0.004	972.613 ± 0.002	972.613 ± 0.002	972.609 ± 0.003	972.616 ± 0.005	-
1	6	1039.463 ± 0.006	-	-	-	1039.465 ± 0.003	1039.463 ± 0.0
2	6	1105.136 ± 0.006	-	-	-	-	1104.768 ± 0.0
0	7	1117.993 ± 0.005	-	-	-	-	-
1	7	1185.598 ± 0.003	1185.592 ± 0.004	-	1185.549 ± 0.003	1185.536 ± 0.003	1185.336 ± 0.1
2	7	1250.567 ± 0.008	-	1250.564 ± 0.025	-	-	1250.563 ± 0.0
0	8	1263.193 ± 0.002	1263.162 ± 0.012	1263.162 ± 0.012	1263.215 ± 0.002	1263.213 ± 0.003	1263.187 ± 0.0
1	8	1329.631 ± 0.005	1329.629 ± 0.004	1329.630 ± 0.004	1329.662 ± 0.010	1329.634 ± 0.003	1329.645 ± 0.0
2	8	1394.683 ± 0.011	1394.680 ± 0.011	1394.683 ± 0.011	1394.671 ± 0.003	1394.684 ± 0.002	1394.678 ± 0.0

Table 9.3: Reported mode frequencies from this and other work.

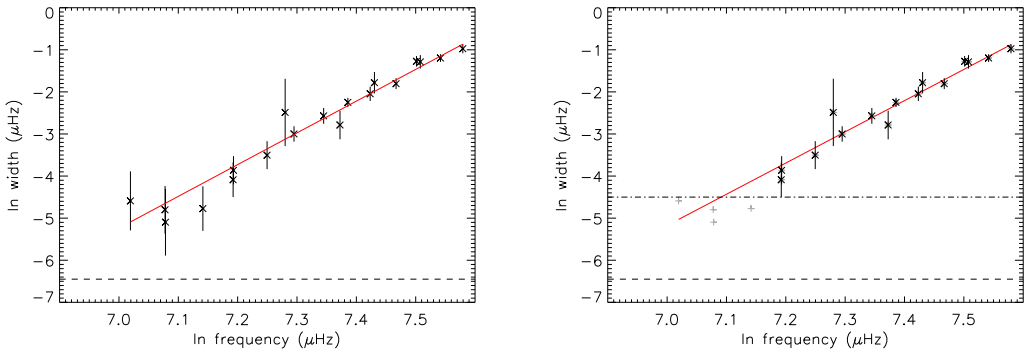

Figure 9.4: Mode widths as a function of frequency plotted on a ln-ln scale. Over plotted in red is the least squares fit linear model with the dashed line showing the (bin width) resolution limit. Right: Same plot but rejecting data with small line widths (cut off at dot-dash line).

The gradient of the frequency dependence of line width is returned as 7.5±0.4. Remembering that this is an underestimate due to the fitting bias that increases the underestimate of mode width at decreasing frequency. This value then presents a lower limit of the frequency dependence of line width. Theoretical calculations from atmospheric radiative transfer models predict the gradient to be 8.0 [Balmforth, 1992] meaning that results here are consistent with this.

At narrow line widths the shape of the structure observed in the frequency domain becomes increasingly dominated by a sinc component in the mode structure generated by the use of a finite time series. Through simulation and modelling we find that the impact of the finite time series can be described in three regimes specified by the ratio of the length of the time series to the lifetime of a mode (T/τ). Firstly, where $T\ \tau \geqslant 5$ we find the error in the fitted width to be less than 1/100 of a bin width i.e. there is little cause for concern. Secondly, for $5 > T/\tau > 2$ we find returned widths to be slightly underestimated by no more than 1/10 bin widths. Finally, at $T/\tau \leqslant 2$ the spectral structure is increasingly dominated by the sinc component and returned widths show the behaviour associated with attempting to fit a Lorentzian to a sinc function, i.e. erratic results.
To check for any impact on returned line widths from the use of a finite time series, we repeat the above fit but reject data where $T/\tau \leqslant 7$. This has the added benefit of

reducing possible bias, discussed above, due to low signal-to-noise. The revised results give the gradient of the fitted line as 7.4 ± 0.4 and the intercept of the frequency axis as -57.1 ± 3.2, which agrees with the original result.

A correction for the determined effects due to the increasing importance of the sinc component may be considered but the error on any correction becomes large at points where the correction may be useful. Future work may consider fitting a model that includes the sinc function which can be easily obtained from the Fourier transform of a decaying sine wave evaluated from 0 to T.

As part of our assessment of the plausibility that observed structure is a mode of oscillation we note that the goodness of fit (χ^2/d.o.f. $= 0.6$) shows there to be good agreement between the data and the linear fit in ln-ln space model. This then does lend weight to the plausibility of our observed structure being modes of solar oscillation. The unusually low value of χ^2 suggests that we have been too conservative in our errors assigned to the values of width, but given our concerns over systematic bias it not sensible to revisit these values.

Calculated power

We can follow a similar path to assess the plausibility of a mode by studying the pattern of mode amplitude as a function of frequency. The amplitude of a mode may be calculated from the height and width of a mode in the frequency domain and this calculation is insensitive to the width fitting bias detailed above.

If a mode can be resolved then its amplitude squared, V^2, is $\pi/2$ times height, H, times width, $\Delta\nu$, i.e.

$$V^2 = \frac{\pi}{2} H \Delta\nu. \tag{9.13}$$

We assume that the structure detected here is sufficiently well resolved for this to be valid, or at least an acceptable approximation, and apply the fitted width and height of a mode

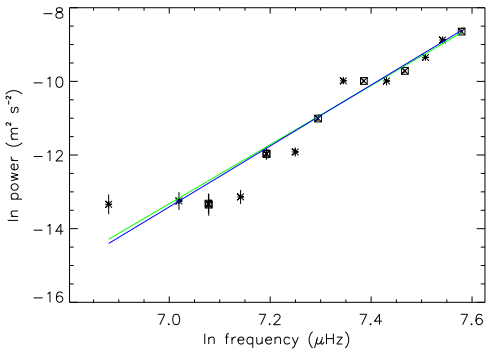

Figure 9.5: Observed mode power as a function of frequency on a ln-ln scale. Over plotted are the least squares fit linear models for $l = 0$ green and $l = 1$ blue.

to determine the power. Expressing the relationship in logarithmic form gives

$$\ln V^2 = \ln \frac{\pi}{2} + \ln H + \ln \Delta\nu, \tag{9.14}$$

where the variance of the amplitude squared is given by

$$\sigma^2_{\ln V^2} = \sigma^2_{\ln H} + \sigma^2_{\ln \Delta\nu} - 2 \operatorname{cov}\left(\sigma_{\ln \mathrm{H}}, \sigma_{\ln \Delta\nu}\right), \tag{9.15}$$

where $\operatorname{cov}\left(\sigma_{\ln \mathrm{H}}, \sigma_{\ln \Delta\nu}\right)$ is the covariance of the log with and height. The width and height of a mode have a high negative correlation, so the covariance acts to reduce the error in $\ln V^2$.

The calculated mode amplitude plotted as a function of frequency on a ln-ln scale is shown in figure 9.5 together with the best fit linear models for $l = 0$ and $l = 1$. The coefficients of the fit are given in table 9.4.

It is clear from the plot of log power as a function of log frequency that a linear model is not a good fit to the data. The error bars for the calculated power provide very good constraint which is not fulfilled by the linear model. This then is not information that can add significantly to our confidence in the detection of modes. We do note however, that the departure from the linear occurs at high frequency (≈ 1600 μHz) where we are already confident that the observed structures are modes. This then does not positively

Method	l	Gradient	Intercept	χ^2/d.o.f.
width	all	7.5 ± 0.4	-57.5 ± 2.7	0.60
power	0	8.0 ± 0.2	-69.5 ± 1.8	18.9
	1	8.3 ± 0.2	-71.3 ± 1.7	8.4

Table 9.4: Coefficients of the linear models fit to observed mode width and power in ln-ln space.

or negatively impact our assessment of the plausibility of structure as modes of solar oscillation.

The good constraint provided by the small error bars in the amplitude squared and the anticipated lack of bias provides the low-frequency regime with an interesting diagnostic on the noise generation rate from turbulent excitation but this is beyond the scope of this thesis.

9.6 Detections

We now discuss the claims of detections for modes of solar oscillations. We have presented the probability that a structure is due to the background noise, compared the frequency of structure to modelled predictions, fitted Lorentzian shapes, and extracted mode parameters. The sum of this information leads us to conclude that structure that has a probability of being part of the background noise of less than 1% and that has been successfully fit and returned plausible parameters may be considered as a detection of a mode of solar oscillation. These cases are listed in table 9.5 on the following page in black. The remaining two instances (in red in table 9.5) of possible detection do not offer such convincing evidence.

The $l = 1$, $n = 6$ mode at 1039.463 ± 0.006 μHz is detected with $P \leqslant 0.01$ but the low signal to noise prevents fitting. Consequently we must look to the work of others and the comparison with modelled predicted frequencies. Remarkable agreement in frequency is found with the work of Bertello and Toutain and hence we can gain confidence

Radial order n	Mode frequency (μHz) $l = 0$	$l = 1$	$l = 2$
6	972.613 ± 0.002	1039.463 ± 0.006	1105.136 ± 0.006
7	1117.992 ± 0.005	1185.598 ± 0.003	1250.567 ± 0.008
8	1263.193 ± 0.002	1329.631 ± 0.005	1394.683 ± 0.011
9	1407.473 ± 0.005	1472.848 ± 0.005	1535.861 ± 0.008

Table 9.5: BiSON table of mode frequencies.

that structure at this frequency is perhaps present in data sets from 4 different instruments (GOLF, MDI, SPM, and BiSON). However, the common use of MDI in the work of Bertello and Toutain allows the possibility that the detected signal is only present in MDI data and then detected here in this work too. Further to this, comparison with predicted frequencies is inconclusive as extrapolation from confirmed modes does not provide enough information to allow absolute confirmation or rejection. We feel confident that with increasing signal to noise, this structure will soon reveal itself to be a mode of oscillation.

Finally we consider the $l = 2$, $n = 6$ mode at 1105.136 ± 0.006. The structure found here is a pair multiplet with each component giving $P \leqslant 0.1$ and the multiplet $P \leqslant 0.02$. Comparison with the detection of Toutain has nearly 0.4 μHz disagreement in frequency. Using the comparison with modelled predictions we note there is better agreement, both in terms of absolute value and the difference trend, with the value found in this thesis. Without sufficient signal to noise to be able to fit to this mode no further information is available. We therefore suggest that more work is required here before a firm detection is made.

With the year-on-year increase in quality of the BiSON network it should not prove to be long before a sufficient increase in signal to noise naturally occurs to allow the fitting of the $l = 1, 2$, $n = 6$ modes. This should provide the required information to form a decision on detection of a mode of solar oscillation. We finish this thesis by attempting to draw conclusions on the future for the detection of low-frequency p modes.

9.7 Future Prospects

Given our estimates for the power and life times of the low-frequency p modes we can attempt to draw some inference on the possibility of future detections by considering the estimated height of a bin in the frequency domain. We start by reaffirming our symmetrical Lorentzian model,

$$M(a) = \frac{A(w/2)^2}{(\nu_i - \nu_0)^2 + (w/2)^2}, \tag{9.16}$$

and stating the maximum height observed in the power spectrum of a single bin as

$$H = \int_{\nu_0 - \frac{\delta\nu}{2}}^{\nu_0 + \frac{\delta\nu}{2}} M \, \mathrm{d}\nu, \tag{9.17}$$

where $\delta\nu$ is the bin width. Applying the integration gives

$$H = \left[\frac{2A(w/2)^2 \tan^{-1}\left(\frac{2(\nu-\nu_0)}{w}\right)}{w} \right]_{\nu_0 - \frac{\delta\nu}{2}}^{\nu_0 + \frac{\delta\nu}{2}}. \tag{9.18}$$

Evaluating this expression and substituting

$$A = \frac{V^2}{w}\frac{2}{\pi}, \tag{9.19}$$

gives the height in a single bin as

$$H = \frac{V^2}{\pi}\left(\tan^{-1}\frac{\delta\nu}{w} - \tan^{-1}\frac{-\delta\nu}{w}\right). \tag{9.20}$$

Given that we have frequency dependent relations for both the amplitude squared and the width of a mode, we see that the observed height of a bin in the frequency domain is determined by the bin width. Of course, we operate in a region with low signal to noise, hence a significant impact of the background distribution, which elevates the observed height.

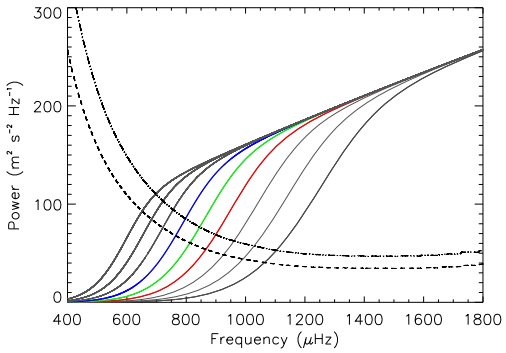

Figure 9.6: Predicted heights of low-frequency p modes for different lengths of observation time series. 20 year background levels displayed, prior to this thesis as a dot-dot-dash line and following the work done in this thesis as a dashed line. Each time series displayed is twice the length of the previous starting at 1 year with 8,16, and 32 years displayed in red, green, and blue respectively.

Figure 9.6 shows the predicted heights as a function of frequency at different bin widths described by the length of time series used. The time series lengths of 8, 16, and 32 years are displayed in red, green, and blue respectively. The background level from the 20 year time series is over plotted to give a sense of scale.

Figure 9.6 clearly shows that the advantage of a longer time series is to move the apex, marking the transition from the linear dependence of clearly resolved to unresolved, to lower frequencies. However, doubling the length of time series each time produces less than a linear decrease in the low-frequency limit. Consequently, the limit of future detections at low frequency will be the background noise levels. In this sense the year-on-year improvement of BiSON data will have a significant impact on future detection limits.

Chapter 10

Conclusion

The aim of this thesis was to study low-frequency p-mode oscillations using the Birmingham Solar Oscillation Network (BiSON). Through the introduction of an improved correction and calibration procedure for raw data, we have demonstrated that we are able to achieve significant gains in the signal-to-noise ratio at frequencies below 1.3 mHz. These gains in the BiSON data set have allowed us to detect new modes of oscillation and, very importantly, determine their properties.

We started by constructing a model for the observations made by a resonant scattering spectrometer (RSS). This model consists of three distinct components to describe three categories of phenomena: the solar absorption line function; terrestrial atmospheric extinction; and the RSS instrumental response. Nominal models describing the first two components were constructed from existing observations. The determination of the instrumental response necessitated a multifaceted approach.

To elucidate the instrumental response required that we detailed the physics of resonant scattering that allows an RSS to make high-precision radial velocity observations. We constructed a Monte Carlo simulation based on these principles to uncover the response of the instrument in terms of both wavelength and position on the solar disk. Using this simulation we demonstrated that the optimal Instrumental Optical Depth (IOD) for

an RSS is very close to 2 and that, contrary to canonical belief, at this IOD multiple scattering in the RSS vapour cell is an important consideration.

By combining the three completed components of our model (the Sun, the atmosphere, and the instrument) we were able to produce modelled radial velocity observations taken by an RSS. Modelled data was compared to real observations and found to be consistent, at least within expectations given that a real instrument is only an approximation of the ideal setup found in the modelled data. This then allowed for the opportunity to study the impact of the terrestrial atmosphere in real observations.

We isolated the impact of the terrestrial atmosphere by studying the difference between modelled data both with and without an atmosphere. The resulting signal is dominated by a process, well known to the community of helioseismologists, referred to as "differential extinction". Previous attempts at a correction for differential extinction had been able to demonstrate a function that could be applied to a single day of data. However, a general correction that could be applied to more than a single day remained illusive. This prevented any previous corrections from having any impact a the long time series. We demonstrated a novel approach to the correction that could be applied to a whole year of data, and hence could be applied to all BiSON stations over a long time period to generate a time series with a significant improvement ($\approx 25\%$) in low-frequency signal to noise.

We applied the new correction for differential extinction to 20 years of BiSON observations and generated a time series optimised for good low-frequency noise. We then applied a frequentist statistical approach to produce a list of possible modes of oscillation for study. Further to this, we have fitted where possible, Lorentzian profiles to the modes, using a likelihood maximisation technique. This allowed for the determination of the modes parameters and served as check on the validity of the detections. We categorise 2

new modes as high confidence detections (n=7, l=0,2), with 2 further modes showing a good level of statistical significance but insufficient signal to noise to allow robust fitting (n=6, l=1,2). Importantly, the frequencies of these new modes were determined with small error bars. In addition, the improved signal to noise produced a reduction in error bars on frequencies for modes already observed.

Finally, fitting of the detected modes allowed for the estimation of the linewidth ($\Delta\nu$) and power. Over the frequency range $972 \geqslant \nu \geqslant 1850$ μHz we find the frequency-linewidth dependence to be $\Delta\nu \propto \nu^{7.5\pm0.4}$ which is close to agreement with theoretical predictions of $\Delta\nu \propto \nu^{8.0}$, thereby extending the range over which the physics of mode excitation can be tested.

Appendices

Chapter 11

Appendix

11.1 Modelling the solar velocity field

The varying solar surface velocity field has components due to oscillations and granulation. Here we describe the process - taken from De Ridder et al. [2006] - of modelling these as integrated velocity signals to produce a timeseries.

11.1.1 Stochastic oscillations

Solar oscillations are stochastically excited and intrinsically damped by turbulent convection. This process continually injects energy into the modes of oscillation producing observable amplitudes. The process is often compared to a bell in a sandstorm, continually ringing due the constant excitation from the particles of sand. Hence we model the stochastic oscillations $v(t)$ as a damped and re-excited oscillator.
We start with a harmonic oscillator

$$v(t) = A(t)\sin\left(2\pi\nu_0 t + \phi(t)\right), \tag{11.1}$$

where $A(t)$ and $\phi(t)$ are the time-dependent amplitude and phase. The oscillator experiences exponential damping with rate η, but re-excitation occurs before dying out. This re-excitation is simulated by 'kicking' the amplitude at small and regular intervals $\Delta t_{\rm kick}$. Between two kicks the oscillation is damped with a factor of $e^{-\eta\Delta t_{\rm kick}}$, so the kicking equation is [De Ridder et al., 2006]

$$A_{n+1} = e^{-\eta\Delta t_{\rm kick}} A_n + \epsilon_{n+1}, \tag{11.2}$$

where ϵ is a normally distributed random number with zero mean. Equation 11.2 is a first-order autoregressive process.
In addition to the amplitude, the phase of oscillation is time dependent, and in order to account for this De Ridder et al. [2006] model $v(t)$ as a sum of a sine and a cosine term with amplitudes B and C respectively. Each amplitude is modelled independently using the prescribed autoregressive technique. Hence to calculate the $v(t)$ of a single mode, amplitudes B_n and C_n are evolved using equation 11.2 so that $n\Delta t_{\rm kick} \leqslant t < (n+1)\Delta t_{\rm kick}$.

The velocity amplitude of the oscillation is then

$$v(t) = e^{-\eta(t-n\Delta t_{\rm kick})}\left[B_n \sin(2\pi\nu_0 t) + C_n \cos(2\pi\nu_0 t)\right]. \tag{11.3}$$

In order to model solar oscillations input parameters must be chosen sensibly. The kick step-time should be sufficiently small with respect to the damping time η^{-1}. The discrete modelling process better approximates a continuous system with decreasing kick-step and De Ridder et al. [2006] report a sensible choice as 1/100th of the damping time. In addition, the variance of the randomly distributed variable ϵ and the damping rate control the power and the Lorentzian width of a mode in the power spectrum, and so must be chosen to match solar values.

11.1.2 Granulation

Granulation and super-granulation provide significant contributions to integrated solar velocity observations, especially at low frequencies. When detecting solar oscillations, granulation provides a source of noise that prevents detection of the scientifically interesting low-frequency p and g modes. Here we describe a model, presented by Palle et al. [1995] and references therein, of the solar 'background' velocity signal.
Palle et al. [1995] use a model of multiple components to describe the solar 'background' velocity field. The frequency domain description of each component is described by the power spectral density $P(\nu)$ where

$$P(\nu) = \frac{4\sigma^2\tau}{1+(2\pi\nu\tau)^2}, \tag{11.4}$$

σ is the amplitude scale of the velocity variation, and τ is the characteristic time-scale. For frequency ranges above 50 μHz, only the components due to granulation (G) and super-granulation (SG) are significant, the meso-granulation and active region component signals falling off rapidly above this frequency limit. Hence, we can consider BiSON observations in this regions of interest as a sum of two components

$$P_{\rm total} = P_{\rm G} + P_{\rm GR}. \tag{11.5}$$

This power spectral density can be modelled by the sum of two random walks, or more formally two autoregressive processes, see equation 11.2. To recap,

$$G_{n+1} = e^{-\Delta t/\tau} G_n + \epsilon_{n+1}, \tag{11.6}$$

where ϵ is a normally distributed random number with zero mean and standard deviation $\sigma\sqrt{\Delta t/\tau}G_n$ that is the velocity variation due to granulation.
To compute the granulation amplitude at a time t, G_n is evolved until step n such that $n\Delta t \leqslant t < (n+1)\Delta t$ so that

$$G(t) = e^{\delta/\tau} G_n + \epsilon, \tag{11.7}$$

where $\delta = t - n\Delta t$ and $\epsilon \approx N(0, \sigma\sqrt{\delta/\tau})$.
Again one must make sensible choices for the input parameters. The time-step Δt should

be selected so that it is 1/100th of the smallest time-scale τ. The parameters for the rms amplitudes and time-scales are taken from Lefebvre et al. [2008].

11.2 The transformation method

The transformation technique transforms the probability distribution of y, $p(y)\ dy$ to a function that can be sampled by inputting a uniform random variate. The Monte Carlo method detailed in chapter 5 uses the transformation technique to produce a number of non-uniform distributions. This appendix contains the derivations.

11.2.1 Uniform deviates in spherical polar coordinates over a limited solid angle

The Monte Carlo simulation of chapter 5 determines the initial direction of propagation of a photon by randomly selecting the angle of propagation from within a cone determined by the primary optics. This selection of off-axis angle requires a distribution that is uniform in spherical polar coordinates over a limited solid angle, Ω, with axis in the z direction. Here the maximum off-axis angle is given as x and the polar angles θ and ϕ are taken with respect to the z and x axis respectively. We can start by writing the area element,

$$\mathrm{d}\Omega = \sin\theta\ \mathrm{d}\theta\ \mathrm{d}\phi. \tag{11.8}$$

Expressing the integral and substituting for the variable of integration gives,

$$\int \mathrm{d}\Omega = \int_{\cos\theta=\cos(\pi-\mathrm{x})}^{\cos(\pi)} \int_{\phi=0}^{2\pi} -\,\mathrm{d}\phi\ \mathrm{d}(\cos\theta), \tag{11.9}$$

which is evaluated to,

$$\Omega = -\left[\phi\right]_0^{2\pi}\left[\cos\theta\right]_{\cos(\pi-x)}^{1} \tag{11.10}$$

We see that ϕ varies uniformly from 0 to 2π and θ varies from $\cos(\pi - x)$ to -1 and is non-uniform. The distribution, uniform in spherical polar coordinates, can be achieved with two random variables u and v that are uniform and vary from 0 to 1. Using the transformation technique gives,

$$\phi = 2\pi u \tag{11.11}$$

$$\theta = \cos^{-1}\xi, \tag{11.12}$$

where ξ is a function that transforms the range of v to the required range. That function is,

$$\xi = -\cos(\pi - x) + v\left(-1 - \cos(\pi - x)\right). \tag{11.13}$$

11.2.2 Exponential random deviates

Adapted from Avery and House [1968], it is straight forward to generate a distribution of distances along the photon path before absorption by utilising the transformation

method. The probability of an absorption between x and x + δx along a path follows the exponential absorption law which gives a probability density function,

$$p(x)\mathrm{dx} = \mathrm{e}^{-\kappa \mathrm{x}}\kappa \mathrm{dx}, \tag{11.14}$$

and a corresponding distribution function,

$$P(x) = 1 - e^{-\kappa x}. \tag{11.15}$$

The distance to absorption can be determined by equating a uniform random deviate, R to the distribution function,

$$R = 1 - e^{-\kappa x}. \tag{11.16}$$

Solving for x gives,

$$x = \frac{-1}{\kappa} |\ln(1 - R)|. \tag{11.17}$$

Since R is equally distributed on $0.0 \geq \mathrm{R} < 1.0$ then $1 - \mathrm{R}$ will also be equidistributed. Neglecting the minus sign gives,

$$x = \frac{1}{\kappa} |\ln R| = \frac{l}{\tau} |\ln R|. \tag{11.18}$$

This is the distance a photon will advance before absorption.

11.2.3 Random deviates for the σ transition angular dependence

Absorption or emission probabilities for σ transitions show dependence over the angle θ, taken with respect to the z axis, of

$$\psi_\sigma(\theta) = 1 + \cos^2\theta, \tag{11.19}$$

see section 4.4.2 on page 80 for details. This gives the dependence over unit area of $\mathrm{d}\Omega$ as,

$$\mathrm{d}\Omega = (1 + \cos^2\theta)\sin\theta \ \mathrm{d}\theta \ \mathrm{d}\phi \tag{11.20}$$

The probability over all angles must be unity,

$$\int_{\theta=0}^{\pi} \int_{\phi=0}^{2\pi} p(\Omega) \ \mathrm{d}\Omega = 1, \tag{11.21}$$

and normalising to satisfy this gives the probability distribution function,

$$P(\Omega) = P(\theta') = \int_{\theta=0}^{\theta'} p(\theta)\mathrm{d}\theta = \frac{3}{8} \int_{\theta=0}^{\theta'} \left(1 + \cos^2\theta\right) \sin\theta \mathrm{d}\theta. \tag{11.22}$$

Integrating and invoking the transformation technique, by setting $P(\theta') = R$, gives,

$$R = \frac{1}{8}\left(-\cos^3\theta - 3\cos\theta + 4\right). \tag{11.23}$$

The transformation technique requires that we solve for θ, but this is non-trivial and requires a numerical approach. From [Press et al., 1992], we solve the previous expression by a combination of Newton-Raphson method and bisection. This yields an numerical value for θ from the uniform random deviate R.
The σ transition is uniform in ϕ and ranges between 0 and 2π. As shown earlier in this section, this gives,

$$\phi = 2\pi R. \tag{11.24}$$

11.2.4 Random deviates for the π transition angular dependence

Absorption or emission probabilities for π transitions show dependence over the angle θ, taken with respect to the z axis, of

$$\psi_\sigma(\theta) = \sin^2\theta, \tag{11.25}$$

see section 4.4.2 on page 80 for details. This gives the dependence over unit area of $\mathrm{d}\Omega$ as,

$$\mathrm{d}\Omega = \sin^3\theta \; \mathrm{d}\theta \; \mathrm{d}\phi \tag{11.26}$$

The probability over all angles must be unity,

$$\int_{\theta=0}^{\pi}\int_{\phi=0}^{2\pi} p(\Omega)\,\mathrm{d}\Omega = 1, \tag{11.27}$$

and normalising to satisfy this gives the probability distribution function,

$$P(\Omega) = P(\theta') = \frac{3}{4}\int_{\theta=0}^{\theta'} sin^3\theta \mathrm{d}\theta, \tag{11.28}$$

which when integrated and $P(\theta')$ set to R we have,

$$R = \sin^4\left(\frac{\theta}{2}\right)(\cos\theta + 2)\,. \tag{11.29}$$

Once again this must be solved for θ but is non-trivial. The numerical techniques mentioned earlier of Newton-Raphson and bisection are used, and the random deviate θ is calculated. Once again the ϕ dependence is uniform over 0 to 2π.

11.3 Ray tracing through the detection optics

The details of propagating a photon through the detections optics, starting with a transformation from the coordinates of the vapour cell to the coordinates of the detection optics.

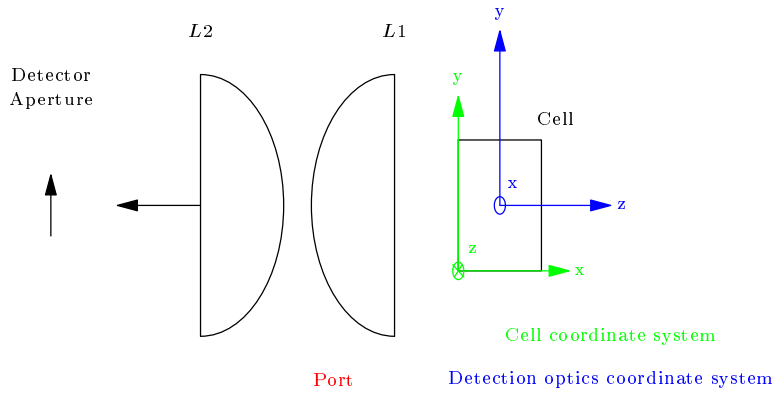

Figure 11.1: Diagram showing both cell and detection optics coordinate systems along with the cell and detection optics.

Coordinate system transfer

The transition of a photon from the Monte Carlo radiative transfer of the vapour cell, to the optical transfer of the detection optics makes it sensible to change our coordinate system from that of the cell to one that suits the detection optics. The sensible choice of detection optics coordinate system is one that places the origin at the centre of the cell, hence giving an axis along the detection optical axis. It is of course arbitrary which coordinate axis this is, but here we choose the z-axis of our system to match the detection optical axis.

Figure 11.1 shows the two chosen coordinate systems. To transfer from one system to the other we are required to perform a translation followed by a rotation. The translation moves the origin of the system from the bottom left hand corner of the cell, the double primed coordinate system, to the centre of the cell, the primed system. This action on any point P can be achieved with

$$P' = P'' - \frac{l}{2}, \tag{11.30}$$

where l is the length of the cell.
The rotation of the coordinate system is through 90° about the y-axis in the primed system. The rotation matrix $\mathrm{R}_2(\beta)$ describes the rotation of a point about the y-axis and is given by

$$\mathrm{R}_2(\beta) = \begin{pmatrix} \cos\beta & 0 & -\sin\beta \\ 0 & 1 & 0 \\ \sin\beta & 0 & \cos\beta \end{pmatrix}, \tag{11.31}$$

where β is the angle of rotation. Applying $\beta = 90°$ gives

$$\mathrm{P} = \mathrm{R}_2(90°)P' = \begin{pmatrix} 0 & 0 & -1 \\ 0 & 1 & 0 \\ 1 & 0 & 0 \end{pmatrix} \begin{pmatrix} X' \\ Y' \\ Z' \end{pmatrix} = \begin{pmatrix} -Z \\ Y \\ X \end{pmatrix}. \tag{11.32}$$

This coordinate transfer must be applied to both points provided by the Monte Carlo vapour radiative transfer element of the simulation. The two points in question are: the

point of last scatter inside the cell P_0''; and the last known point outside the cell P_f''.

Planar intersect

Using our knowledge of P_0 and P_f we must find the point of intersection with the planar surface of the first detection lens P_1.
Here we generalise the description of known points such that P_{n-1} is a known photon position before the surface in question, P_{n+1} is an extrapolation of position beyond the surface in question taken from the knowledge of P_{n-1} and the direction of propagation of the photon, and P_n is the point of intersection on the surface. The position of the centre of the lens is given by $P_{\mathrm{L_n}}$.
In our system photons travel in straight lines until reaching an optical surface, hence we can describe a ray trace with the equation of a straight line. The point of intersection may be found using a parametrisation of these equations in s, i.e.

$$P_n = P_{n-1} + s\left(P_{n+1} - P_{n-1}\right). \tag{11.33}$$

The value of s can be found because we know P_{n-1}, P_{n+1}, and that the planar surface satisfies $Z_n = Z_{\mathrm{L_n}}$. Stating this with s as the solution gives

$$s = \frac{Z_{\mathrm{L_n}} - Z_{n-1}}{Z_{n+1} - Z_{n-1}}. \tag{11.34}$$

It is then trivial to find the elements of a point of intersection on the planar surface

$$X_n = X_{n-1} + s\left(X_{n+1} - X_{n-1}\right) \tag{11.35}$$
$$Y_n = Y_{n-1} + s\left(Y_{n+1} - Y_{n-1}\right) \tag{11.36}$$
$$Z_n = Z_{\mathrm{L_n}}. \tag{11.37}$$

Spherical intersect

Using the same general definitions as before we may calculate the point of intersection with a spherical surface, with the centre of the lens and the centre from the equation of the sphere coinciding. Again we must parametrise the equation of a straight line representing the propagation of the light ray. Here, to avoid confusion with the previous section, we parametrise in u, i.e.

$$P_n = P_{n-1} + u\left(P_{n+1} - P_{n-1}\right). \tag{11.38}$$

The equation for a spherical surface to represent the lens is defined as

$$R_{\mathrm{L_n}}^2 = \left(x - X_{\mathrm{L_n}}\right)^2 + \left(y - Y_{\mathrm{L_n}}\right)^2 + \left(z - Z_{\mathrm{L_n}}\right)^2, \tag{11.39}$$

where $R_{\mathrm{L_n}}$ is the radius of the spherical surface and so by earlier definition, also the radius of the lens.
We wish to solve the combination of the two equations to determine u. By substituting the expansion of equation 11.38 into 11.39 we obtain a quadratic equation of the form,

$$au^2 + bu + c = 0, \tag{11.40}$$

where,

$$a = (X_{n+1} - X_{n-1})^2 + (Y_{n+1} - Y_{n-1})^2 + (Z_{n+1} - Z_{n-1})^2 \tag{11.41}$$

$$\begin{aligned} b = {} & 2\,(X_{n+1} - X_{n-1})\,(X_{n-1} - X_{\mathrm{L_n}}) \\ & + 2\,(Y_{n+1} - Y_{n-1})\,(Y_{n-1} - Y_{\mathrm{L_n}}) \\ & + 2\,(Z_{n+1} - Z_{n-1})\,(Z_{n-1} - Z_{\mathrm{L_n}}) \end{aligned} \tag{11.42}$$

$$\begin{aligned} c = {} & X_{\mathrm{L_n}}^2 + Y_{\mathrm{L_n}}^2 + Z_{\mathrm{L_n}}^2 + X_{n-1}^2 + Y_{n-1}^2 + Z_{n-1}^2 \\ & - 2\,[X_{n-1}X_{\mathrm{L_n}} + Y_{n-1}Y_{\mathrm{L_n}} + Z_{n-1}Z_{\mathrm{L_n}}] - R_{\mathrm{L_n}}. \end{aligned} \tag{11.43}$$

Solving the quadratic equation using the familiar formula

$$u_{1,2} = \frac{-b \pm \sqrt{b^2 - 4ac}}{2a}, \tag{11.44}$$

yields two solutions, provided the light ray passes through the sphere (two same value solutions if the ray only grazes the sphere). Substituting $u_{1,2}$ back into equation 11.38 gives the two points of intersection. Because the detection lenses are semi-spheres only one solution u provides the correct point of intersection, but this is easily obtained when the alignment of the lens is known.
Now we can determine the points of intersection in our system so we move on to consider the application of Snell's law at these points.

Snell's law

Snell's law describes the refraction of light at a boundary between two media with different refractive indices. The law is commonly expressed as

$$n_i \sin\theta_i = n_f \sin\theta_f, \tag{11.45}$$

where n is the refractive index and θ is the angle of the light path with respect to the normal of the boundary. This equation appears to operate in 2 dimensions, so how can it be applied in the simulation of 3 dimensional ray tracing?
Ray tracing may propagate through the 3 dimensions we have defined for the detection optics, but the application of Snell's law is an intrinsically 2D operation. In order to maintain this simplification it is necessary to transform the coordinate frame of the detection optics into a frame in which neither the incident ray nor the normal to the media boundary have any ϕ component, that is to say no component in the y-axis. This is nothing more than a transformation between two coordinate systems but one that allows the application of equation 11.45.
To realise this straight forward application of Snell's law, we define two coordinate systems, the system of the detections optics $O = (l_1, l_2, l_3)$, and the system to suit Snell's law $O' = (k_1, k_2, k_3)$. (Note: the prime notation has nothing at all to do with the prime notation of the previous section.) Figure 11.2 on the next page shows the definition of the O' coordinate system. To proceed we write Snell's law in a vector form that is valid for either of our defined coordinate systems. Here we define the incident ray as $\mathbf{S}$, the refracted ray as $\mathbf{T}$, and the unit vector normal to the boundary as $\hat{\mathbf{r}}$, giving

$$n_i \mathbf{S} \times \hat{\mathbf{r}} = n_f \mathbf{T} \times \hat{\mathbf{r}}. \tag{11.46}$$

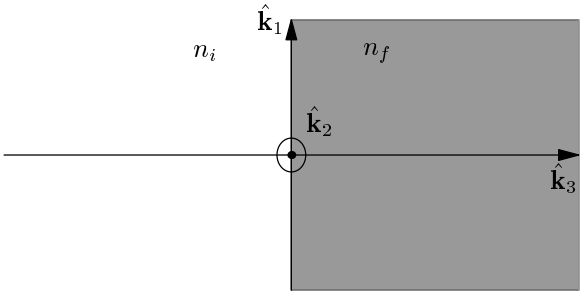

Figure 11.2: Diagram showing definition of the O' coordinate system.

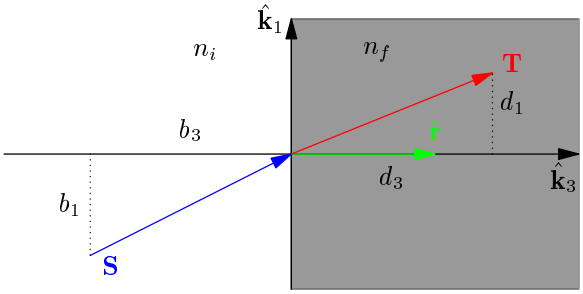

Figure 11.3: Diagram showing vectors $\mathbf{S}$, $\mathbf{T}$, and $\hat{\mathbf{r}}$ in the O' coordinate system. b and d are the representations of $\mathbf{S}$ and $\mathbf{T}$ in this, the O', system.

In essence, we must transform the $\mathbf{S}$ into $\mathbf{S}'$, calculate $\mathbf{T}'$ and then transform to $\mathbf{T}$. To achieve this we define representations of the vectors in both coordinate systems

$$\mathbf{S} = \sum a_i \hat{\mathbf{l}}_i \tag{11.47}$$

$$\mathbf{S} = \sum b_i \hat{\mathbf{k}}_i \tag{11.48}$$

$$\mathbf{T} = \sum c_i \hat{\mathbf{l}}_i \tag{11.49}$$

$$\mathbf{T} = \sum d_i \hat{\mathbf{k}}_i \tag{11.50}$$

$$\hat{\mathbf{r}} = \sum e_i \hat{\mathbf{l}}_i \tag{11.51}$$

$$\hat{\mathbf{r}} = \sum f_i \hat{\mathbf{k}}_i. \tag{11.52}$$

Figure 11.3 shows the three vectors $\mathbf{S}$, $\mathbf{T}$, and $\mathbf{r}$ as well as the two representations b and d in the O' coordinate system.

From the above definitions we can calculate the transformation matrices A_{kl} and A_{lk} such that

$$b_i = \sum \left(\mathrm{A}_{lk}\right)_{ij} \; a_j \tag{11.53}$$

$$c_i = \sum \left(\mathrm{A}_{kl}\right)_{ij} \; d_j. \tag{11.54}$$

Deriving the transformation matrix A_{kl} is covered in appendix 11.4 on the next page. Here we state the most convenient form

$$\mathrm{A}_{kl} = \begin{pmatrix} \hat{\mathbf{r}}\times\left(\frac{\hat{\mathbf{r}}\times\mathbf{S}}{|\hat{\mathbf{r}}\times\mathbf{S}|}\right) & \frac{\hat{\mathbf{r}}\times\mathbf{S}}{|\hat{\mathbf{r}}\times\mathbf{S}|} & \hat{\mathbf{r}} \end{pmatrix}, \tag{11.55}$$

this is possible because we have chosen the primed frame such that $f = (0, 0, 1)$ and $b_2 = d_2 = 0$. To be meaningful to the simulation the transformation should be represented in terms of a and e, and it is, but in the appendix. To solve for c, the representation of $\mathbf{T}$ in O, we use equation 11.54 and so require the transformation matrix above A_{kl} and d, the representation of $\mathbf{T}$ in O'. Using the geometry from figure 11.3 we see that

$$d = \begin{pmatrix} \sin\theta_f \\ 0 \\ \cos\theta_f \end{pmatrix}. \tag{11.56}$$

It follows from our original definition of Snell's law and a trigonometric relationship that

$$d = \begin{pmatrix} \frac{n_i}{n_f}\sin\theta_i \\ 0 \\ \sqrt{1-\left(\frac{n_i}{n_f}\sin\theta_i\right)^2} \end{pmatrix}. \tag{11.57}$$

By definition $\mathbf{S}$ and $\hat{\mathbf{r}}$ are vectors separated by the angle θ_i, which means that θ_i can be found from the cross product of the two

$$\frac{\hat{\mathbf{r}}\times\mathbf{S}}{|\hat{\mathbf{r}}\times\mathbf{S}|} = \sin\theta_i\ \hat{\mathbf{k}}_2. \tag{11.58}$$

Having dealt with the mathematics of the process we need only determine the vectors $\mathbf{S}$ and $\hat{\mathbf{r}}$ in order to calculate c. $\mathbf{S}$ is the incident ray moving from a point P_{n-1} to the surface of a lens at point P_n. Hence, $\mathbf{S}$ in full is

$$\mathbf{S} = \begin{pmatrix} X_n - X_{n-1} \\ Y_n - Y_{n-1} \\ Z_n - Z_{n-1} \end{pmatrix}. \tag{11.59}$$

The normal to the surface of the lens is described by $\hat{\mathbf{r}}$ and has been defined so that its direction is away from the cell and towards a detector. For a planar surface, $\hat{\mathbf{r}}$ is given by

$$\hat{\mathbf{r}} = \begin{pmatrix} 0 \\ 0 \\ \pm 1 \end{pmatrix}, \tag{11.60}$$

and for a spherical surface

$$\hat{\mathbf{r}} = \begin{pmatrix} \pm X_n \mp X_{L_n} \\ \pm Y_n \mp Y_{L_n} \\ \pm Z_n \mp Z_{L_n} \end{pmatrix}. \tag{11.61}$$

Finally we wish to determine the direction of propagation of a refracted ray in spherical polar coordinates, which can be achieved with

$$\theta = \cos^{-1}\left(\frac{c_3}{\sqrt{c_1^2 + c_2^2 + c_3^2}}\right) \tag{11.62}$$

$$\phi = \tan^{-1}\left(\frac{c_2}{c_1}\right). \tag{11.63}$$

11.4 Orthogonal transformation matrix

In section 11.3 on the preceding page we transform from a detection optics coordinate system into a coordinate system that allows the application of Snell's law. The transformation is a rotoinversion, which is a type of orthogonal transformation. An orthogonal transformation is a linear transformation that maps l to k, $T : l \to k$ and preserves the lengths of vectors and the angles between vectors,

$$\langle\, l, k \,\rangle = \langle\, T\, l, T\, k \,\rangle\,, \tag{11.64}$$

where $\langle\, \cdot, \cdot \,\rangle$ is an inner product.
An orthogonal transformation, T, can be realised using an orthogonal matrix, A. As we are transforming in Euclidean space from real vector space $\mathbb{R}^3$ to $\mathbb{R}^3$, A is a 3×3 matrix which has elements a_{ij}. For any linear transformation in three dimensions,

$$x_1' = a_{11}x_1 + a_{12}x_2 + a_{13}x_3 \tag{11.65}$$

$$x_2' = a_{21}x_1 + a_{22}x_2 + a_{23}x_3 \tag{11.66}$$

$$x_3' = a_{31}x_1 + a_{32}x_2 + a_{33}x_3, \tag{11.67}$$

which can be expressed more succinctly as,

$$x_i' = \sum a_{ij}\ x_j. \tag{11.68}$$

Using the notation defined in section 11.3 we wish to perform a transformation from a to b, apply Snell's law to get d and then transform back to c. Expressing this,

$$b_i = \sum \left(\mathrm{A}_{kl}\right)_{ij}\ a_j \tag{11.69}$$

$$\mathbf{T}\times\hat{\mathbf{r}} = \frac{n_i}{n_f}\mathbf{S}\times\hat{\mathbf{r}} \tag{11.70}$$

$$c_i = \sum \left(\mathrm{A}_{lk}\right)_{ij}\ d_j. \tag{11.71}$$

We could apply all steps sequentially but that would require more calculations than are necessary. We remember that equation 11.70 is valid in both our frames and we choose the primed coordinate system such that $f = (0, 0, 1)$ and $b_2 = d_2 = 0$. We can now start to describe the coordinate system. As f is the representation of $\hat{\mathbf{r}}$ in the primed frame,

$$\hat{\mathbf{k}}_3 = \hat{\mathbf{r}}, \tag{11.72}$$

and because $b_2 = d_2 = 0$, $\mathbf{r}\times\hat{\mathbf{S}}$ can be defined as in the $\hat{\mathbf{k}}_2$ direction, which means that we can define,

$$\hat{\mathbf{k}}_2 = \frac{\mathbf{r}\times\hat{\mathbf{S}}}{|\mathbf{r}\times\hat{\mathbf{S}}|}. \tag{11.73}$$

Finally we can complete the $\mathbb{R}^3$ space with $\hat{\mathbf{k}}_2\times\hat{\mathbf{k}}_3$ so that,

$$\hat{\mathbf{k}}_1 = \left(\frac{\mathbf{r}\times\hat{\mathbf{S}}}{|\mathbf{r}\times\hat{\mathbf{S}}|}\right)\times\hat{\mathbf{r}}. \tag{11.74}$$

Our transformation matrix A_{lk} is then,

$$\mathrm{A}_{lk} = \begin{pmatrix} \left(\frac{\hat{\mathbf{r}}\times\mathbf{S}}{|\hat{\mathbf{r}}\times\mathbf{S}|}\right)\times\hat{\mathbf{r}} & \frac{\hat{\mathbf{r}}\times\mathbf{S}}{|\hat{\mathbf{r}}\times\mathbf{S}|} & \hat{\mathbf{r}} \end{pmatrix}, \tag{11.75}$$

but we must express $\mathbf{S}$ and $\hat{\mathbf{r}}$ in terms of their representations in the original frame, a and e, so

$$\mathbf{S} = \begin{pmatrix} a_1 \\ a_2 \\ a_3 \end{pmatrix}, \tag{11.76}$$

and

$$(\mathrm{A}_{lk})_{3j} = \hat{\mathbf{r}} = \begin{pmatrix} e_1 \\ e_2 \\ e_3 \end{pmatrix}. \tag{11.77}$$

Which makes $(\mathrm{A}_{lk})_{2j}$,

$$\frac{\hat{\mathbf{r}}\times\mathbf{S}}{|\hat{\mathbf{r}}\times\mathbf{S}|} = \frac{1}{\sqrt{(a_3e_2 - a_2e_3)^2 + (a_1e_3 - a_3e_1)^2 + (a_2e_1 - a_1e_2)^2}} \begin{pmatrix} a_3e_2 - a_2e_3 \\ a_1e_3 - a_3e_1 \\ a_2e_1 - a_1e_2 \end{pmatrix}, \tag{11.78}$$

which for simplicity in the next step we will write as,

$$\frac{\hat{\mathbf{r}}\times\mathbf{S}}{|\hat{\mathbf{r}}\times\mathbf{S}|} = \begin{pmatrix} m_1 \\ m_2 \\ m_3 \end{pmatrix}. \tag{11.79}$$

Finally we can write $(\mathrm{A_{lk}})_{1j}$ as

$$\left(\frac{\hat{\mathbf{r}}\times\mathbf{S}}{|\hat{\mathbf{r}}\times\mathbf{S}|}\right)\times\hat{\mathbf{r}} = \begin{pmatrix} m_3a_2 - m_2a_3 \\ m_1a_3 - m_3a_1 \\ m_2a_1 - m_1a_2 \end{pmatrix}. \tag{11.80}$$

This completes the transformation matrix. The values for d are determined in section 11.3 on page 228.

Bibliography

E. R. Anderson, T. L. Duvall, Jr., and S. M. Jefferies. Modeling of solar oscillation power spectra. ApJ, 364:699–705, December 1990.

H. M. Antia and S. Basu. Solar Rotation Rate During the Cycle 24 Minimum in Activity. ApJ, 720:494–502, September 2010.

H. M. Antia, S. Basu, and S. M. Chitre. Solar Rotation Rate and Its Gradients During Cycle 23. ApJ, 681:680–692, July 2008.

T. Appourchaux. On Maximum Likelihood Estimation of averaged power spectra. A&A, 412:903–904, December 2003.

T. Appourchaux, K. Belkacem, A.-M. Broomhall, W. J. Chaplin, D. O. Gough, G. Houdek, J. Provost, F. Baudin, P. Boumier, Y. Elsworth, R. A. García, B. N. Andersen, W. Finsterle, C. Fröhlich, A. Gabriel, G. Grec, A. Jiménez, A. Kosovichev, T. Sekii, T. Toutain, and S. Turck-Chièze. The quest for the solar g modes. A&A Rev., 18:197–277, February 2010.

M. Asplund, N. Grevesse, M. Guedel, and A. J. Sauval. The solar model problem resurrected. *ArXiv Astrophysics e-prints*, October 2005a.

M. Asplund, N. Grevesse, and A. J. Sauval. The Solar Chemical Composition. In T. G. Barnes III & F. N. Bash, editor, *Cosmic Abundances as Records of Stellar Evolution and Nucleosynthesis*, volume 336 of *Astronomical Society of the Pacific Conference Series*, pages 25–+, September 2005b.

L. W. Avery and L. L. House. An Investigation of Resonance-Line Scattering by the Monte Carlo Technique. 152:493, May 1968.

N. J. Balmforth. Solar pulsational stability. I - Pulsation-mode thermodynamics. MNRAS, 255:603–649, April 1992.

S. Basu and H. M. Antia. Constraining Solar Abundances Using Helioseismology. ApJ, 606:L85–L88, May 2004.

S. Basu and H. M. Antia. Characteristics of Solar Meridional Flows during Solar Cycle 23. ApJ, 717:488–495, July 2010.

S. Basu, W. J. Chaplin, Y. Elsworth, R. New, A. M. Serenelli, and G. A. Verner. Solar Abundances and Helioseismology: Fine-Structure Spacings and Separation Ratios of Low-Degree p-Modes. ApJ, 655:660–671, January 2007.

J. A. Belmonte, Y. P. Elsworth, G. R. Isaak, R. New, P. L. Palle, and T. Roca Cortés. Effect of atmospheric extinction on solar radial velocity measurements. In E. J. Rolfe, editor, *Seismology of the Sun and Sun-Like Stars*, volume 286 of *ESA Special Publication*, pages 177–179, December 1988.

L. Bertello, F. Varadi, R. K. Ulrich, C. J. Henney, A. G. Kosovichev, R. A. García, and S. Turck-Chièze. Identification of Solar Acoustic Modes of Low Angular Degree and Low Radial Order. ApJ, 537:L143–L146, July 2000.

P. Boumier. *These: Astrophysique et Techniques Spatiales.* L'Universite De Paris VII, 1991.

J. R. Brookes, G. R. Isaak, and H. B. van der Raay. A resonant-scattering solar spectrometer. *MNRAS*, 185:1–17, 1978.

A. M. Broomhall, W. J. Chaplin, Y. Elsworth, and T. Appourchaux. Needles in haystacks: how to use contemporaneous data in the search for low-frequency modes of oscillation of the Sun. MNRAS, 379:2–10, July 2007.

A.-M. Broomhall, W. J. Chaplin, G. R. Davies, Y. Elsworth, S. T. Fletcher, S. J. Hale, B. Miller, and R. New. Definitive Sun-as-a-star p-mode frequencies: 23 years of BiSON observations. MNRAS, 396:L100–L104, June 2009a.

A. M. Broomhall, W. J. Chaplin, Y. Elsworth, and R. New. New aspects of Doppler imaging in Sun-as-a-star observations. MNRAS, 397:793–801, August 2009b.

W. C. Chaplin, Y. Elsworth, G. R. Isaak, R. Lines, C. P. McLeod, B. A. Miller, R. New, and H. B. van der Raay. Observing the sun with the Birmingham Solar-Oscillations Network (BISON). *The Observatory*, 116:32–33, February 1996a.

W. J. Chaplin. *High-precision velocity and magnetic measurements of bright stars with a magneto-optical filter.* Ph.D. Thesis, University of Birmingham, 1993.

W. J. Chaplin, Y. Elsworth, R. Howe, G. R. Isaak, C. P. McLeod, B. A. Miller, H. B. van der Raay, S. J. Wheeler, and R. New. BiSON Performance. Sol. Phys., 168:1–18, September 1996b.

W. J. Chaplin, Y. Elsworth, R. Howe, G. R. Isaac, C. P. McLeod, B. A. Miller, and R. New. Techniques used in the analysis of the data collected by the birmingham solar-oscillations network (bison). *Astron. Astrophys. Suppl Ser.*, 125:195–205, 1997.

W. J. Chaplin, Y. Elsworth, G. R. Isaak, B. A. Miller, and R. New. Skew-symmetric solar P modes in low-l BiSON ˆ* data. MNRAS, 308:424–430, September 1999. doi: 10.1046/j.1365-8711.1999.02719.x.

W. J. Chaplin, Y. Elsworth, G. R. Isaak, K. I. Marchenkov, B. A. Miller, R. New, B. Pinter, and T. Appourchaux. Peak finding at low signal-to-noise ratio: low-l solar acoustic eigenmodes at n¡= 9 from the analysis of BiSON data. MNRAS, 336:979–991, November 2002a.

W. J. Chaplin, Y. Elsworth, G. R. Isaak, K. I. Marchenkov, B. A. Miller, R. New, B. Pinter, and S. Thiery. Observation of, and variations in, multiplet frequency asymmetries at low l. In A. Wilson, editor, *From Solar Min to Max: Half a Solar Cycle with SOHO*, volume 508 of *ESA Special Publication*, pages 71–73, June 2002b.

W. J. Chaplin, Y. Elsworth, G. R. Isaak, B. A. Miller, R. New, and B. Pintér. Noise characteristics of full-disc helioseismic observations made by resonant scattering spectrometers. MNRAS, 359:607–614, May 2005.

W. J. Chaplin, A. M. Serenelli, S. Basu, Y. Elsworth, R. New, and G. A. Verner. Solar Heavy-Element Abundance: Constraints from Frequency Separation Ratios of Low-Degree p-Modes. ApJ, 670:872–884, November 2007.

W. J. Chaplin, Y. Elsworth, B. A. Miller, R. New, and G. A. Verner. Uncovering the Bias in Low-Degree p-Mode Linewidth Fitting. Sol. Phys., 251:189–196, September 2008.

W. J. Chaplin, T. Appourchaux, Y. Elsworth, R. A. García, G. Houdek, C. Karoff, T. S. Metcalfe, J. Molenda-Żakowicz, M. J. P. F. G. Monteiro, M. J. Thompson, T. M. Brown, J. Christensen-Dalsgaard, R. L. Gilliland, H. Kjeldsen, W. J. Borucki, D. Koch, J. M. Jenkins, J. Ballot, S. Basu, M. Bazot, T. R. Bedding, O. Benomar, A. Bonanno, I. M. Brandão, H. Bruntt, T. L. Campante, O. L. Creevey, M. P. Di Mauro, G. Doğan, S. Dreizler, P. Eggenberger, L. Esch, S. T. Fletcher, S. Frandsen, N. Gai, P. Gaulme, R. Handberg, S. Hekker, R. Howe, D. Huber, S. G. Korzennik, J. C. Lebrun, S. Leccia, M. Martic, S. Mathur, B. Mosser, R. New, P.-O. Quirion, C. Régulo, I. W. Roxburgh, D. Salabert, J. Schou, S. G. Sousa, D. Stello, G. A. Verner, T. Arentoft, C. Barban, K. Belkacem, S. Benatti, K. Biazzo, P. Boumier, P. A. Bradley, A.-M. Broomhall, D. L. Buzasi, R. U. Claudi, M. S. Cunha, F. D'Antona, S. Deheuvels, A. Derekas, A. García Hernández, M. S. Giampapa, M. J. Goupil, M. Gruberbauer, J. A. Guzik, S. J. Hale, M. J. Ireland, L. L. Kiss, I. N. Kitiashvili, K. Kolenberg, H. Korhonen, A. G. Kosovichev, F. Kupka, Y. Lebreton, B. Leroy, H.-G. Ludwig, S. Mathis, E. Michel, A. Miglio, J. Montalbán, A. Moya, A. Noels, R. W. Noyes, P. L. Pallé, L. Piau, H. L. Preston, T. Roca Cortés, M. Roth, K. H. Sato, J. Schmitt, A. M. Serenelli, V. Silva Aguirre, I. R. Stevens, J. C. Suárez, M. D. Suran, R. Trampedach, S. Turck-Chièze, K. Uytterhoeven, R. Ventura, and P. A. Wilson. The Asteroseismic Potential of Kepler: First Results for Solar-Type Stars. ApJ, 713:L169–L175, April 2010.

J. Christensen-Dalsgaard. Helioseismology. *Reviews of Modern Physics*, 74:1073–1129, November 2002.

J. Christensen-Dalsgaard and D. O. Gough. Is the sun helium-deficient. Nature, 288: 544–547, December 1980.

J. Christensen-Dalsgaard, W. Dappen, and Y. Lebreton. Solar oscillation frequencies and the equation of state. Nature, 336:634–638, December 1988.

J. Christensen-Dalsgaard, D. O. Gough, and M. J. Thompson. The depth of the solar convection zone. ApJ, 378:413–437, September 1991.

D. Clarke. Nomenclature of polarized light: elliptical polarization. Appl. Opt., 13:222–224, 1974.

A. Claverie, G. R. Isaak, C. P. McLeod, H. B. van der Raay, and T. R. Cortes. Solar structure from global studies of the 5-minute oscillation. Nature, 282:591–594, December 1979.

D. T. Cumberbatch, J. A. Guzik, J. Silk, L. S. Watson, and S. M. West. Light WIMPs in the Sun: Constraints from helioseismology. Phys. Rev. D, 82(10):103503–+, November 2010.

R. de La Reza and E. A. Mueller. The potassium abundance in the solar photosphere. Sol. Phys., 43:15–32, July 1975.

J. De Ridder, T. Arentoft, and H. Kjeldsen. Modelling space-based high-precision photometry for asteroseismic applications. MNRAS, 365:595–605, January 2006.

P. Delache and P. H. Scherrer. Detection of solar gravity mode oscillations. Nature, 306: 651–653, December 1983.

P. Duffett-Smith and J. Zwart. *Practical Astronomy with your Calculator or Spreadsheet*. 2011.

S. Ehgamberdiev and I. Khamitov. On the calculation of spurious velocity signal produced by atmospheric differential extinction in whole-disk oscillation measurements. Sol. Phys., 133:81–88, May 1991.

Y. Elsworth, R. Howe, G. R. Isaak, C. P. McLeod, and R. New. Evidence from solar seismology against non-standard solar-core models. Nature, 347:536–539, October 1990.

Y. Elsworth, R. Howe, G. R. Isaak, C. P. McLeod, B. A. Miller, R. New, and S. J. Wheeler. Techniques used in the analysis of solar oscillations data from the BiSON (University of Birmingham) network. I. Daily calibration. A&AS, 113:379–+, October 1995.

Y. P. Elsworth, S. M. Jefferies, C. P. McLeod, R. New, P. L. Palle, H. B. van der Raay, C. Regulo, and T. R. Cortes. The 160 minute solar oscillation - an artifact? ApJ, 338: 557–562, March 1989.

S. T. Fletcher, W. J. Chaplin, Y. Elsworth, and R. New. Efficient Pseudo-Global Fitting for Helioseismic Data. ApJ, 694:144–150, March 2009.

S. T. Fletcher, A.-M. Broomhall, D. Salabert, S. Basu, W. J. Chaplin, Y. Elsworth, R. A. García, and R. New. A Seismic Signature of a Second Dynamo? ApJ, 718:L19–L22, July 2010.

A. H. Gabriel, G. Grec, J. Charra, J.-M. Robillot, T. Roca Cortés, S. Turck-Chièze, R. Bocchia, P. Boumier, M. Cantin, E. Cespédes, B. Cougrand, J. Crétolle, L. Damé, M. Decaudin, P. Delache, N. Denis, R. Duc, H. Dzitko, E. Fossat, J.-J. Fourmond, R. A. García, D. Gough, C. Grivel, J. M. Herreros, H. Lagardère, J.-P. Moalic, P. L. Pallé, N. Pétrou, M. Sanchez, R. Ulrich, and H. B. van der Raay. Global Oscillations at Low Frequency from the SOHO Mission (GOLF). Sol. Phys., 162:61–99, December 1995.

A. H. Gabriel, F. Baudin, P. Boumier, R. A. García, S. Turck-Chièze, T. Appourchaux, L. Bertello, G. Berthomieu, J. Charra, D. O. Gough, P. L. Pallé, J. Provost, C. Renaud, J.-M. Robillot, T. Roca Cortés, S. Thiery, and R. K. Ulrich. A search for solar g modes in the GOLF data. A&A, 390:1119–1131, August 2002.

R. A. García, C. Régulo, S. Turck-Chièze, L. Bertello, A. G. Kosovichev, A. S. Brun, S. Couvidat, C. J. Henney, M. Lazrek, R. K. Ulrich, and F. Varadi. Low-Degree Low-Order Solar p Modes As Seen By GOLF On board SOHO. Sol. Phys., 200:361–379, May 2001.

R. A. García, S. Turck-Chièze, S. J. Jiménez-Reyes, J. Ballot, P. L. Pallé, A. Eff-Darwich, S. Mathur, and J. Provost. Tracking Solar Gravity Modes: The Dynamics of the Solar Core. *Science*, 316:1591–, June 2007.

R. A. García, D. Salabert, J. Ballot, K. Sato, S. Mathur, and A. Jimenez. The acoustic low-degree modes of the Sun measured with 14 years of continuous GOLF & VIRGO measurements. *ArXiv e-prints*, December 2010.

D. O. Gough. A new measure of the solar rotation. MNRAS, 196:731–745, September 1981.

D. O. Gough, editor. *Seismology of the sun and the distant stars; Proceedings of the NATO Advanced Research Workshop, Cambridge, England, June 17-21, 1985*, 1986.

D. O. Gough and M. J. Thompson. *The inversion problem*, pages 519–561. 1991.

G. Grec and E. Fossat. Calculation of pseudo solar narrow band oscillations produced by atmospheric differential extinction. A&A, 77:351–353, August 1979.

G. Grec, E. Fossat, and M. A. Pomerantz. Full-disk observations of solar oscillations from the geographic South Pole - Latest results. Sol. Phys., 82:55–66, January 1983.

N. Grevesse and A. J. Sauval. Standard Solar Composition. Space Sci. Rev., 85:161–174, May 1998.

W. T. Hicks. Evaluation of vapor-pressure data for mecury, lithium, sodium and potassium. *The Journal of Chemical Physics*, 38-8:1873–1880, 1962.

G. Houdek. Stochastic Excitation in Solar-Type Stars (invited paper). In C. Aerts, T. R. Bedding, & J. Christensen-Dalsgaard, editor, *IAU Colloq. 185: Radial and Non-radial Pulsationsn as Probes of Stellar Physics*, volume 259 of *Astronomical Society of the Pacific Conference Series*, pages 447–+, 2002.

L. L. House and L. W. Avery. The Monte Carlo technique applied to radiative transfer. *Journal of Quantitative Spectroscopy and Radiative Transfer*, 9:1579–1591, 1969.

R. Howe, J. Christensen-Dalsgaard, F. Hill, R. Komm, J. Schou, and M. J. Thompson. A Note on the Torsional Oscillation at Solar Minimum. ApJ, 701:L87–L90, August 2009.

P. Hoyng. On the sensitivity of resonant scattering spectrometers for whole-disk solar velocity oscillation measurments. *ApJ*, 345:1088–1103, 1989.

C. A. Jones, M. J. Thompson, and S. M. Tobias. The Solar Dynamo. Space Sci. Rev., 152:591–616, May 2010.

C. Karoff, W. J. Chaplin, T. Appourchaux, Y. Elsworth, R. A. García, G. Houdek, T. S. Metcalfe, J. Molenda-Zakowicz, M. J. P. F. G. Monteiro, M. J. Thompson, J. Christensen-Dalsgaard, R. L. Gilliland, H. Kjeldsen, S. Basu, T. R. Bedding, T. L. Campante, P. Eggenberger, S. T. Fletcher, P. Gaulme, R. Handberg, S. Hekker, M. Martic, S. Mathur, B. Mosser, C. Regulo, I. W. Roxburgh, D. Salabert, D. Stello, G. A Verner, K. Belkacem, K. Biazzo, M. S. Cunha, M. Gruberbauer, J. A. Guzik, F. Kupka, B. Leroy, H. -. Ludwig, S. Mathis, A. Noels, R. W. Noyes, T. Roca Cortes, M. Roth, K. H. Sato, J. Schmitt, M. D. Suran, R. Trampedach, K. Uytterhoeven, R. Ventura, and P. A. Wilson. Asteroseismology of Solar-type Stars with Kepler I: Data Analysis. *ArXiv e-prints*, May 2010.

F. Kasten and A. T. Young. Revised optical air mass tables and approximation formula. Appl. Opt., 28:4735–4738, November 1989.

H. Kjeldsen, T. R. Bedding, and J. Christensen-Dalsgaard. Correcting Stellar Oscillation Frequencies for Near-Surface Effects. ApJ, 683:L175–L178, August 2008.

V. A. Kotov. The 160 minutes oscillations. Sol. Phys., 100:101–113, October 1985.

H. G. Kuhn. *Atomic Spectra*. Longmans, Green and Co. LTD, London and Harlow, 1962.

S. Lefebvre, R. A. García, S. J. Jiménez-Reyes, S. Turck-Chièze, and S. Mathur. Variations of the solar granulation motions with height using the GOLF/SoHO experiment, November 2008.

J. W. Leibacher and R. F. Stein. A New Description of the Solar Five-Minute Oscillation. Astrophys. Lett., 7:191–192, 1971.

R. B. Leighton. In R. N. Thomas, editor, *Aerodynamic Phenomena in Stellar Atmospheres*, volume 12 of *IAU Symposium*, pages 321–325, 1960.

D. B. McLeod and G. R. Isaak. A detector of small gradients of transparency of the terrestrial atmosphere. In E. J. Rolfe, editor, *Seismology of the Sun and Sun-Like Stars*, volume 286 of *ESA Special Publication*, pages 223–225, December 1988.

A. Mitchell and M. Zemansky. *Resonance Radiation and Excited Atoms*. Cambridge University Press, Cambridge, 1971.

J. Nishikawa. A new system of precise full-disk solar surface photometry. ApJS, 74: 315–323, September 1990.

P. L. Palle, A. Jimenez, F. Perez Hernandez, C. Regulo, T. Roca Cortes, and L. Sanchez. A measurement of the background solar velocity spectrum. ApJ, 441:952–959, March 1995.

W. H. Press, S. A. Teukolsky, W. T. Vetterling, and B. P. Flannery. *Numerical Recipes in C++*. Cambridge University Press, Cambridge, 1992.

D. E. Rees, G. A. Murphy, and C. J. Durrant. Stokes profile analysis and vector magnetic fields ii: Formal numerical solutions of the stokes tranfer equations. *ApJ*, 339:1093:1106, 1989.

E. J. Rhodes, Jr. and R. K. Ulrich. The Use of p Mode Oscillations to Measure the Solar Rotation Rate. In *Bulletin of the American Astronomical Society*, volume 9 of *Bulletin of the American Astronomical Society*, pages 336–+, March 1977.

D. Salabert, R. A García, P. L Palle, and A. Jimenez. Global p-mode oscillations throughout the complete solar cycle 23 and the beginning of cycle 24. *ArXiv e-prints*, November 2010.

A. M. Serenelli, S. Basu, J. W. Ferguson, and M. Asplund. New Solar Composition: The Problem with Solar Models Revisited. ApJ, 705:L123–L127, November 2009.

A. B. Severnyi, V. A. Kotov, and T. T. Tsap. Observations of solar pulsations. Nature, 259:87–89, January 1976.

H. B. Snodgrass and R. K. Ulrich. Rotation of Doppler features in the solar photosphere. *Apj*, 351:309–316, March 1990.

G. H. Spencer and M. V. R. K. Murty. Genral ray-tracing procedure. *Journal of the Optical Society of America (1917-1983)*, 52:672–+, June 1962.

M. Stix. *The Sun: an introduction*. Springer-Verlag, Heidelberg, Germany, 2002.

M. J. Thompson. A new inversion of solar rotational splitting data. Sol. Phys., 125:1–12, January 1990.

T. Toutain, T. Appourchaux, C. Fröhlich, A. G. Kosovichev, R. Nigam, and P. H. Scherrer. Asymmetry and Frequencies of Low-Degree p-Modes and the Structure of the Sun's Core. ApJ, 506:L147–L150, October 1998.

S. Turck-Chièze, S. Couvidat, A. G. Kosovichev, A. H. Gabriel, G. Berthomieu, A. S. Brun, J. Christensen-Dalsgaard, R. A. García, D. O. Gough, J. Provost, T. Roca-Cortes, I. W. Roxburgh, and R. K. Ulrich. Solar Neutrino Emission Deduced from a Seismic Model. ApJ, 555:L69–L73, July 2001.

S. Turck-Chièze, R. A. García, S. Couvidat, R. K. Ulrich, L. Bertello, F. Varadi, A. G. Kosovichev, A. H. Gabriel, G. Berthomieu, A. S. Brun, I. Lopes, P. Pallé, J. Provost, J. M. Robillot, and T. Roca Cortés. Looking for Gravity-Mode Multiplets with the GOLF Experiment aboard SOHO. ApJ, 604:455–468, March 2004.

R. K. Ulrich. The Five-Minute Oscillations on the Solar Surface. ApJ, 162:993–+, December 1970.